Universidade de Aveiro Secção Autónoma de Ciências da Saúde
2015

ERIKA JUDITH CARDOSO RODRIGUES DAVIM

AUMENTO DA REACTIVIDADE SUPERFICIAL DE SUPORTES POROSOS VITROCERAMICOS À BASE DE SÍLICA

SURFACE REACTIVITY ENHANCEMENT OF SILICA-BASED GLASS-CERAMIC SCAFFOLDS

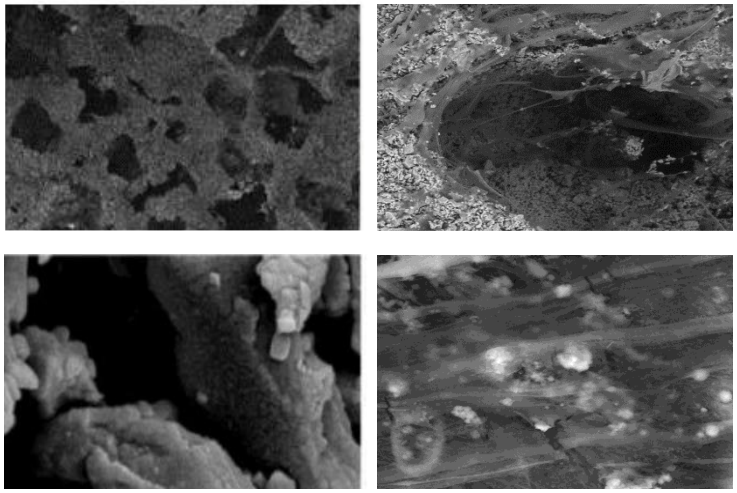

Universidade de Aveiro Secção Autónoma de Ciências da Saúde
2015

ERIKA JUDITH CARDOSO RODRIGUES DAVIM

AUMENTO DA REACTIVIDADE SUPERFICIAL DE SUPORTES POROSOS VITROCERAMICOS À BASE DE SÍLICA

SURFACE REACTIVITY ENHANCEMENT OF SILICA-BASED GLASS-CERAMIC SCAFFOLDS

dissertação apresentada à Universidade de Aveiro para cumprimento dos requisitos necessários à obtenção do grau de Doutor em Engenharia Biomédica, realizada sob a orientação científica da Doutora Maria Helena Figueira Vaz Fernandes, Professora Associada do Departamento de Engenharia de Materiais e Cerâmica da Universidade de Aveiro e da Doutora Ana Maria Oliveira da Rocha Senos, Professora Associada do mesmo departamento

Apoio financeiro da FCT e do FSE no âmbito do III Quadro Comunitário de Apoio.

…To Filipe, Denise and Tiago

o júri

presidente

Prof. Doutor Vitor Brás de Sequeira Amaral
professor catedrático da Universidade de Aveiro

Prof. Doutora Julia Asunción Serra Rodríguez
professora titular da Universidade de Vigo

Prof. Doutora Regina da Conceição Corredeira Monteiro
professor associado da Universidade Nova de Lisboa

Prof. Doutora Maria Pia de Melo Alvim Ferraz Tavares
professor associado da Universidade Fernando Pessoa

Prof. Doutor Rui Ramos Ferreira e Silva
professor associada da Universidade de Aveiro

Prof. Doutora Maria Helena Figueira Vaz Fernandes
professora associada da Universidade de Aveiro (Orientadora)

Acknowledgments

This thesis would not be possible without the help of several persons and Institutions, to whom I am and will be very grateful.

First and foremost I would like to thank to my main supervisor, prof. Helena Fernandes for their continued support, guidance and encouragement throughout this thesis. I owe my sincere gratitude to for her constant enthusiasm throughout the course of the past 8 years. Thank you for providing me with the unique opportunity to join the Biomaterial group and the freedom to pursue my research interests and to collaborate with other research groups.
I would not have accomplished the things I have up to now, without your unconditional support.

I also would like to thanks to prof. Ana Senos for given me a lot of help to my research work, not only to review this work but also for their support during all these years.

I would also like to express my thanks to Professor Maria Helena Raposo Fernandes and her group - School of Dental Medicine, University of Porto – for their collaboration in studies of in vitro biocompatibility.

I am very grateful to my colleagues and friends in my research group, without forgetting those that are not working with us anymore, for the constant support and motivation. Thank you for sharing all the laughter and tears! An especial thanks to Filipe, Daniela, Diogo, Nathalie, Ana Margarida, José Carlos, Rui, Marisa, Nuno and Patricia for making the final stage of writing this thesis so much more fun!

I want also to acknowledge the technical support given by Célia, Ana Sofia and Maria João. I would like also to acknowledge the technical staff of the Laboratório Central de Análises of the University of Aveiro, Dr. Rosário Soares and Dr. Eugénio Soares, for all the support with the HT-XRD and ICP analysis. Thanks to both Bruno and Marta for their help and advice conducting the SEM analysis.

I would like to thanks my family for always respecting and for supporting my choices in life. I would like to give special thanks to my husband, Filipe Davim, for always listening to my complaints about the difficulty of research. Thanks for your understanding and support, especially all the times I worked odd or long hours. I know that without your constant encouragement I could not have done this.

To all who are left without mentioning, that with their generous and enthusiastic collaboration, both directly and indirectly, facilitated the development and implementation of this thesis.

I am gratefully acknowledged to the financial support for this doctoral research given by FEDER funds through the Operational Programme Competitiveness Factors - COMPETE and National Funds through FCT - Foundation for Science and Technology under the project SFRH / BD / 48357 / 2008.

Palavras-chave

Estruturas porosas, vidro, vitrocerâmicos, cristalização, funcionalização

Resumo

Na chamada cirurgia reconstrutiva decorre, presentemente uma notável mudança de paradigma em que se tende a passar da utilização de tecidos transplantados e implantes sintéticos, para uma abordagem de engenharia de tecidos que tem como objetivo regenerar tecidos danificados, usando para isso células do corpo e biomateriais porosos, que orientam o crescimento do novo tecido.

O foco central desta tese foi a produção de estruturas porosas vitreas ou vitroceramicas, que exibem um comportamento bioativo e biocompativel, com reatividade superficial específica em fluidos fisiológicos sintéticos e interações célula-matriz alteradas pela composição e tratamentos térmicos aplicados.

Entender o comportamento de sinterização e da interação entre os processos de densificação e cristalização do vidro foi fundamental para avaliar as condições de sinterização ideais para a obtenção de uma estrutura porosa para aplicações em engenharia de tecidos. Foi realizado um estudo abrangente da sinterização, identificando o efeito da distribuição de tamanho de particula do pó de vidro e das variáveis do ciclo de sinterização na produção de scaffolds de vidro com microestruturas funcionais.

As estruturas porosas desenvolvidas, preparadas pelo método de sinterização com sal usando o sistema vitreo $3CaO.P_2O_5$ - SiO_2 - MgO, com adições de Na_2O e um porogéneo, NaCl, apresentam uma elevada porosidade, interconectividade, distribuição de tamanho de poros e resistência mecânica apropriada para aplicações em estratégias de regeneração óssea.

A substituição de 6 % de MgO por Na_2O na rede vitrea permitiu adequar a taxa de dissolução e bioactividade dos suportes porosos de vidro. Quanto à avaliação biológica, da incorporação de sódio na composição ocorreu uma inibição da resposta celular para períodos curtos. No entanto, foi demonstrado que, após 21 dias, a resposta celular é semelhante para ambas as composições. O comportamento *in vitro* dos suportes de vidro foi testado através da introdução destes em fluido corporal simulado (SBF) durante 21 dias. A espectroscopia por energia dispersiva de raios-X e as análises de SEM provaram a existência de precipitados de fosfato de cálcio sobre ambas as composições.

A cristalização de whitlockite por ceramização das matrizes vítreas afectou o comportamento de dissolução em SBF. Em consequência dos diferentes tratamentos térmicos efectuados, foi possível produzir diferentes estados de cristalização e alterar a bioactividade e biocompatibilidade dos suportes porosos.

Para recuperar e ajustar a bioatividade dos vitrocerâmicos com 82 % de fase cristalina foram aplicados diferentes métodos de modificação superficial incluindo a funcionalização com 3-aminopropil-triethoxysilane (APTES). A superfície do vitrocerâmico modificado exibiu a formação de uma camada de hidroxiapatite cristalina após 21 dias de imersão em SBF, enquanto que no vitrocerâmico base não se detetou a formação de fosfato de cálcio até 5 meses.

As estruturas porosas ceramizadas apresentaram uma resistência mecânica adequada à sua aplicação em engenharia do tecido ósseo e degração a uma taxa adaptável. Considerando-se a avaliação biológica, as estruturas porosas demonstraram um efeito indutivo sobre a proliferação celular, cujas células apresentaram uma morfologia normal e elevada taxa de crescimento.

Este estudo abre novas possibilidades de utilização de vidros do sistema $3CaO.P_2O_5$-SiO_2-MgO para o fabrico de várias estruturas, ajustando simultaneamente a sua bioactividade e controlando o teor da fase cristalina. Além disso, o comportamento in vitro destas estruturas em contacto com células indicia o seu elevado potencial para utilização no campo da regeneração do tecido ósseo.

Keywords Scaffold, Glass, glass-ceramic, crystallization, functionalization

Abstract

A paradigm shift is taking place from using transplanting tissue and synthetic implants to a tissue engineering approach that aims to regenerate damaged tissues by combining cells from the body with highly porous scaffold biomaterials, which act as templates, guiding the growth of new tissue.

The central focus of this thesis was to produce porous glass and glass-ceramic scaffolds that exhibits a bioactive and biocompatible behaviour with specific surface reactivity in synthetic physiological fluids and cell-scaffold interactions, enhanced by composition and thermal treatments applied.

Understanding the sintering behaviour and the interaction between the densification and crystallization processes of glass powders was essential for assessing the ideal sintering conditions for obtaining a glass scaffolds for tissue engineering applications. Our main goal was to carry out a comprehensive study of the bioactive glass sintering, identifying the powder size and sintering variables effect, for future design of sintered glass scaffolds with competent microstructures.

The developed scaffolds prepared by the salt sintering method using a $3CaO.P_2O_5$ - SiO_2 - MgO glass system, with additions of Na_2O with a salt, NaCl, exhibit high porosity, interconnectivity, pore size distribution and mechanical strength suitable for bone repair applications.

The replacement of 6 % MgO by Na_2O in the glass network allowed to tailor the dissolution rate and bioactivity of the glass scaffolds. Regarding the biological assessment, the incorporation of sodium to the composition resulted in an inibition cell response for small periods. Nevertheless it was demonstrated that for 21 days the cells response recovered and are similar for both glass compositions. The in vitro behaviour of the glass scaffolds was tested by introducing scaffolds to simulated body fluid for 21 days. Energy-dispersive X-ray spectroscopy and SEM analyses proved the existence of CaP crystals for both compositions.

Crystallization forming whitlockite was observed to affect the dissolution behaviour in simulated body fluid. By performing different heat treatments, it was possible to control the bioactivity and biocompatability of the glass scaffolds by means of a controlled crystallization.

To recover and tune the bioactivity of the glass-ceramic with 82 % crystalline phase, different methods have been applied including functionalization using 3-aminopropyl-triethoxysilane (APTES). The glass ceramic modified surface exhibited an accelerated crystalline hydroxyapatite layer formation upon immersion in SBF after 21 days while the as prepared glass-ceramic had no detected formation of calcium phosphate up to 5 months.

A sufficient mechanical support for bone tissue regeneration that biodegrade later at a tailorable rate was achievable with the glass–ceramic scaffold. Considering the biological assessment, scaffolds demonstrated an inductive effect on the proliferation of cells. The cells showed a normal morphology and high growth rate when compared to standard culture plates.

This study opens up new possibilities for using $3CaO.P_2O_5$–SiO_2–MgO glass to manufacture various structures, while tailoring their bioactivity by controlling the content of the crystalline phase. Additionally, the in vitro behaviour of these structures suggests the high potential of these materials to be used in the field of tissue regeneration.

Table of Contents

List of Abbreviations

ATR	Attenuated Total Reflectance
ALP	Alkaline Phosphatase
a.u.	Arbitrary Units
BET	Brunauer–Emmett–Teller method
BO	Bonding/bridging oxygen
CaP	calcium phosphates
Ca/P	Calcium-phosphorus ratio
CAD	Computer aided design
CLSM	Confocal laser scanning microscopy
DCPD	Dicalcium phosphate dehydrate (Brushite)
DSC	Differential Scanning Calorimetry
DTA	Differential Thermal Analysis
ECM	Extracellular Matrix
EDS	Energy Dispersive Spectroscopy
Endo	Endothermic
Exo	Exothermic
FTIR	Fourier Transform Infrared Spectroscopy
FWHM	Full width at half-maximum
HT-XRD	High temperature X-ray diffraction
HA	Hydroxyapatite
HCA	Hydroxycarbonate apatite
HOC	Human osteoblast-like cells
ICP-OES	Inductively Coupled Plasma Optical Emission Spectroscopy
IUPAC	International Union of Pure and Applied Chemistry
μ-CT	Micro-computed tomography analysis
MPa	Mega Pascal
NA	Not available
NBO	Non bonding oxygen
OCP	Octacalcium phosphate
P	Porosity
pH	Potential of Hydrogen
SBF	Simulated body fluid
SEM	Scanning electron microscopy
SSA	Specific surface area
SFF	Solid freeform fabrication
SA/V	Surface area per volume ratio
3D	Three-dimensional
TRIS	Tris(hidroximethyl)aminomethane
wt.%	Weight percent
XRD	X-Ray Diffraction

List of Symbols

Eg	Activation energy associated with glass transition
Ec	Activation energy for crystallization
Q/Es	Activation energy for sintering
K	Anisotropy factor
ρ_a	Apparent density
N	Avrami exponent
Q’	Constant of viscous fluid
ρ_{sal}	Density of salt
ρ_{fr}	Density of glass powder
x	Fraction of crystallization
R	Gas constant (8.314 J K^{-1} $Mole^{-1}$)
Tg	Glass transition temperature
β	Heating rate
Q^n	Local configuration around each silicon atom where n is the number of bridging oxygen ranging from 0 to 4
$Ec_{(x)}$	Local activation energy
E	Linear module (GPa)
mm	Micrometers
Tc	Onset of crystallization temperature
εx	Perpendicular strain
εy	Parallel strain
Tp	Peak crystallization temperature
KBr	Potassium bromide
ppm	Parts per million (10^6), mg/l
ppb	Parts per billion (10^9), µg/l
P	Porosity
T	Temperature (°C)
α	Thermal expansion coefficient
H	Viscosity
λ	Wavelenght

List of Figures

Chapter II

Literature review

Chapter III

Materials and methods

Chapter IV

Effect of particle size in the anisotropic sintering of the $3CaO.P_2O_5$–SiO_2–MgO glass powder

Chapter V

Crystallization kinetics of a Si-Ca-P-Mg bioactive glass by non-isothermal methods

Chapter VI

Increased surface area during sintering of calcium phosphate glass and sodium chloride mixtures

Chapter VII

Effect of glass composition on the processing and properties of Ca-P-Mg-Si scaffolds

Chapter VIII

Effect of glass composition on the in vitro bioactivity and biocompatibility of Ca-P-Mg-Si-Na scaffolds

Chapter IX

Crystallization effect in the in vitro bioactivity and biocompatibility of a Calcium-Phosphate-based glass bulk and scaffold

Chapter X

Surface functionalization of Si-Ca-P-Mg glass-ceramic: a bioactivity study

List of Tables

Chapter II

Literature review

Chapter III

Materials and Methods

Chapter IV

Effect of particle size in the anisotropic sintering of the 3CaO.P2O5–SiO2–MgO glass powder

Chapter V

Effect of particle size in the anisotropic sintering of the 3CaO.P_2O_5–SiO_2–MgO glass powder

Chapter VI

Increased surface area during sintering of calcium phosphate glass and sodium chloride mixtures

Chapter VII

Effect of glass composition on the processing and properties of Ca-P-Mg-Si scaffolds

Chapter VIII

Effect of glass composition on the in vitro bioactivity and biocompatibility of Ca-P-Mg-Si-Na scaffolds

Chapter IX

Crystallization effect in the in vitro bioactivity and biocompatibility of a Calcium-Phosphate-based glass bulk and scaffold

Chapter X

Surface modification of Si-Ca-P-Mg glass-ceramic: a bioactivity study

Chapter I

"What we anticipate seldom occurs: but what we least expect generally happens."

Benjamin Disraeli (1804 – 1881)

CHAPTER I

PREFACE

I.1. Introduction

Advances in medicine have provided the man not only an increase in life expectancy, as well as the desire for a better quality of life. This has generated an increase in demand and consequently the development of new materials for use in grafts to restore function, remodel or even enhance bone structures.

The restrictions related with the used of biological graft has led to the development of a newly emerging field of biomaterials called 'tissue engineering'. One approach is to use three-dimensional, porous, degradable scaffolds, which provide support while allowing the ingrowth of new bony tissue as the scaffold degrades.

The developed biomaterials for bone regeneration are intended to interact with the tissue in a specific way, through the cellular and molecular stimuli, combining bioabsorption and bioactivity properties in the same material. The use of bioactive glasses has proved advantageous because it rapidly bonds to bone and degrades over time, releasing soluble products that are thought to stimulate osteoprogenitor cells. There are several methods which can be utilized to obtain porous scaffolds, and one of the simplest is the particulate leaching technique after the salt sintering method.

I.1.1. *Research Objectives*

The central focus of this thesis is to develop porous glass and glass-ceramic scaffolds using the salt sintering method.

To achieve these goals, the following issues were addressed:

- Development and optimization of the sintering processes tailoring specific scaffold parameters affecting microstructural architecture, namely pore size, pore network geometry, hierarchical microstructures, and anisotropy of internal pore structures.

- Changement of the base glass composition in the $CaO–P_2O_5–SiO_2$ system by suitable additives (such as Na_2O as modifier and MgO as stabilizer), aiming to obtain glass melts of controlled viscosity and workability to enlarge the "working window" for sintering.

- Evaluation of the characteristics of surface reactivity and mechanical resistance of selected compositions.

- Understanding of the effect of crystallization and functionalization on the surface reactivity in acellular medium and in cell cultures to allow assessing the best compromise in the fabricated scaffolds.

I.1.2. *Structure of the thesis*

This dissertation is structured in eleven chapters. Chapter I provides a succinct introduction, the research objectives and an outlook of the content of each chapter. Chapter II presents an extensive literature review that range from bone structure, to bioactive glasses, sintering and crystallization procedures and functionalization. Chapter III outlines the research methods used in testing the goals presented in Chapter I.

The outcome of the experimental work is divided in the next seven chapters and correspond to the manuscripts resulted from the research activity that had been published or submitted to ISI journals. Finally, Chapter XI present the overall conclusions of the dissertation and describes potential future directions.

Chapter II

"The process of scientific discovery is, in effect, a continual flight from wonder."

Albert Einstein (1879 – 1955)

CHAPTER II

LITERATURE REVIEW

II.1. Bone Repair

II.1.1. Bone tissue

Bone tissue is a specialized connective tissue, which composition, organization and dynamics allow to participate in the mechanical functions of support, protection and mobility and mineral homeostasis in the body. According to the macroscopic structure, the bone may be divided into two categories, trabecular bone, also known as cancellous or spongy bone and cortical (or compact) bone. The major difference between these two types of bone is on the basis of porosity and the unit microstructure [1]. Cortical bone tissue is denser with low porosity (10 %) and surrounds the marrow space, whereas trabecular bone is composed of a honeycomb-like network of trabecular plates and rods interspersed in the bone marrow compartment, with an interconnected porosity between 50 and 90 %. Both cortical and trabecular bone are composed of osteons, Fig. II.1. The osteon consists of a central canal called the osteonic (haversian) canal, which is surrounded by concentric rings (lamellae) of matrix. The osteonic canals contain blood vessels that are parallel to the long axis of the bone. These blood vessels interconnect, by way of perforating canals, with vessels on the surface of the bone [2].

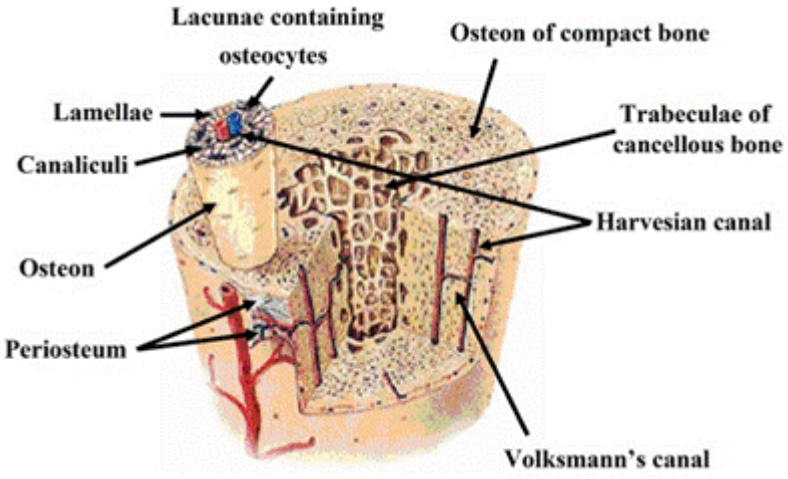

Fig.II.1. The structure of bone [3]

The bone mechanical loading functions and protection are achieved by both, the bone mineral phase which confers strength and stiffness while the organic phase, collagen, is responsible for

bone toughness and ductility. The cancellous bone works mainly in compression while cortical bone must withstand compressive forces, tensile and shear. The mineral component of bone are calcium phosphates, being the most important constituent, hydroxyapatite, $Ca_{10}(PO_4)_6(OH)_2$. The association of the hydroxyapatite crystals with a size between 10-100 nm, with the collagen fibres is responsible for the hardness and strength characteristics of the bone tissue. The bone apatite structure also contains small amounts of fluorine, chlorine, sodium and magnesium [4].

II.1.2. Bone cells

The bone cells are responsible for producing, maintaining and modifying the structure of bone tissue. Distributed as a layer over the bone matrix are the osteoblasts, lining cells and osteoclast whereas osteocytes permeate the mineralised interior of the bone, as shown in Fig.II.2.

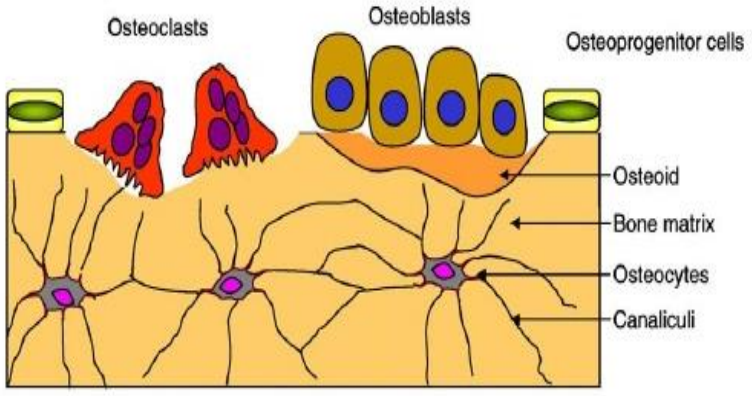

Fig.II.2. Schematic diagram of bone structure at cellular level [5]

II.1.2.1. Osteoblasts

The osteoblasts are considered responsible for the synthesis and mineralization of bone during both initial bone formation and later bone remodelling. [6]. They produce many cell products, including the enzymes alkaline phosphatase and collagen, part of the organic unmineralized component of the bone called osteoid. Eventually the osteoblast is surrounded by the growing bone matrix, and, as the material calcifies, the cell is trapped in a space called lacuna. Thus entrapped, it becomes an osteocyte.

II.1.2.2. Osteocytes

The osteocyte is the most common cell. As mentioned before, they derive from osteoblasts which become enclosed within the bone matrix during bone formation. Each osteocyte communicates with its neighbours by means of gap junctions, through small channels in the bone matrix called

canaculi. Osteocytes are therefore in close communication with osteocytes and osteoblasts, supplying nutrients [7,8]

II.1.2.3. Osteoclasts

Osteoclasts are multinucleated cells as they are formed from two or more cells that fuse together, which can resorb bone. They come from the bone marrow and are related to white blood cells. They are found on the surface of the bone mineral next to the dissolving bone [9].

II.2. Bone tissue regeneration

The bone has the ability to promote its spontaneous regeneration and remodel its micro and macrostructure, through processes of osteogenesis (bone formation) and bone resorption [10]. However, when bone regeneration is required in large quantity, such as for skeletal reconstruction of large bone defects created by fracture or diseases, alternatives to complement the 'insufficient' bone-regeneration process are on demand. Autologous bone (bone removed from the patient) are still being considered as the "gold standard" bone-grafting material [11]. Since this kind of grafts is osteoconductive (provides a scaffold on which bone cells can proliferate), osteoinductive (induces proliferation of undifferentiated cells and their differentiation into osteoblasts), and osteogenic (provides a reservoir of skeletal stem and progenitor cells that can form new bone). Allografts obtained from human cadavers or living donors, is an alternative allogeneic bone grafting, which bypasses the problems associated with harvesting and quantity of graft material present in autologous bone [12]. Although bone repairs are still mostly performed by grafting, there are issues of immunogenicity and rejection reactions, possibility of infection transmission, and cost [13]. Due to the numerous constraints that such grafts exhibit bone graft substitutes were developed. Scaffolds made of synthetic or natural biomaterials, where developed to promote the migration, proliferation and differentiation of bone cells for bone regeneration [14–19]. While various biomaterials have been introduced to respond to this need, it is considered impossible to develop a biomaterial to fulfil the requirements to all desired applications [20–22].

One of the great challenges that biomaterials science faces today stems from the increasingly need of implants use, coupled with the significant increase in Human life expectancy. In fact, an increasing fraction of patients live beyond the expected life of your implants, so that new materials should present a durability of around 20 to 30 years, twice that found in materials used until the present.

The target of tissue engineering is to restore structure and function to a defect and not only for replacement thereof [23], using the body's natural healing response in addition to treatment with one or more of three elements: cells, signalling molecules and scaffolds [24]. There are two general strategies in the field of tissue engineering: the first focuses on *in vitro* seeding and

culturing specific cell types in a scaffold. The cells grow outside the body, become differentiated, and mimic naturally occurring tissues. These tissue-engineered constructs are then implanted into patients to replace diseased or damaged tissues. With time the scaffolds are resorbed and replaced by host tissues. The second strategy involves using the scaffold as a growth factor/drug delivery device using the body's own systems, where regeneration of tissues is induced *in vivo*. After implantation cells from the body are recruited to the scaffold site and form tissue upon and throughout the matrices. These two approaches are not mutually exclusive and can be easily combined [25].

II.3. Scaffolds – Requirements

Scaffolds are three dimensional (3D) structures that should exhibit tailored porosity, pore size and interconnectivity, providing an environment and architecture specific to favour tissue integration and vascularisation [26]. The material composition and structural characteristics such as the internal and external architecture are of crucial importance for the success of the tissue engineering strategies [27,28]. Ideally, scaffolds should favour cell attach, growth and differentiation [29]. The scaffolds must be constructed in order to allow the mimic of the regeneration process and should have an external shape adapted to the size and geometry of the defect [25]. After implantation, the scaffold should allow neovascularization, stimulate bone tissue formation and must be biodegradable or resorbable to allow for replacement of newly formed tissue [2]. It is desirable that in addition to the features previously mentioned, the matrix mechanical behaviour presents compatibility with the bone [4]. These properties should be maintained as matrix degrades and new tissue growth occurs [30]. Finally, the synthetized material and fabricated scaffold should be suitable for sterilization and the production technology must be scalable and cost-effective. These requirements will further be developed in the next points.

II.3.1. Porosity

Ideally scaffolds should have a high interconnected porosity to allow tissue and cell ingrowth and also vascularization of tissue, significant diffusion of nutrients and metabolic waste resulting from the activity of cells which will grow, meantime, in the scaffold [28, 31–33]. However, the degree of porosity also influences other properties, such as mechanical stability, and should therefore be balanced with the needs of mechanical deployment location, for use *in vivo*. The pore size is also of great importance, especially the implementation of the bimodal porosity for the effective scaffold vascularization and for bone ingrowth [34]. If the pores have a reduced size, pore occlusion occurs with the anchor of cells, which in turn will prevent cell penetration, production of extracellular matrix and neovascularization of the internal area of the scaffold.

To discuss the pore morphologies of the scaffolds it is necessary to stablish the size classification of pores. The International Union of Pure Applied Chemistry (IUPAC) classification of pore size for Catalysis application is micropores < 2 nm, mesopores 2-50 nm and macropores > 50 nm [35]. The follower pore size classification [33,36,37], is commonly used for scaffolds to be employed in bone regeneration, 1–20 μm as micropores and macropores > 100 μm, even though the scale range of these dimensions are higher than those of IUPAC.

Regarding the ideal size of pores, most authors consider advisable a diameter larger than 100-150 μm to allow host cell components and extra-cellular bone tissue and blood vessels. Ensuring the supply of blood and providing a more effective and healthy growth of bone tissue (osteogenesis without preceding cartilage formation) [33,38–40], and micropores (≈ 2–10 μm) for cell adhesion, migration and osteointegration [41]. However, other authors [42] believe that bone reconstruction is obtained only through a 3D matrix with temporary interconnected macropores in the range of 1.2–2.0 mm. The latter approach reduces the mechanical resistance limiting the *in vivo* applications of these matrices [43].

II.3.2. Surface

The superficial properties of the materials namely chemical and topographical determine the ionic exchange dynamics and the protein adsorption. They also can control and provoke cellular adhesion, proliferation and differentiation [44–46]. A bioactive material induces the formation of a carbonate apatite layer biologically active on its surface, creating a compatible environment with osteogenesis. This mineralized interface assures the linking between the material and the bone tissue, resulting in the tissue regeneration [44]. Roughness mainly improves mechanical cell attachment, although the correlation of this event – increasing roughness – with cell attachment remains unknown [47–50]. Increasing the specific surface area and pore volume of bioactive glass may greatly accelerate the apatite formation and therefore enhance the bioactive behaviour [51].

II.3.3. Mechanical Properties and Biodegradability

Strength is another important property of scaffolds considered for the replacement of load-bearing bone. The mechanical properties of the scaffold is strongly influenced by internal architecture [39,52–54] and must be carefully designed [55,56] to be suitable for bone regeneration. Ideally, it should be equivalent to bone in terms of the characteristics shown in Table II.1.

Table II.1. Mechanical properties of bone under compression [57].

	σ (MPa)	E (GPa)	K_{IC} (MPa $m^{1/2}$)
Trabecular bone	2–12	0.05–0.5	-
Cortical bone	80–120	3–30	2–12

In addition to strength and elastic modulus, other mechanical properties such as fracture toughness are of crucial importance when implanted in load-bearing bone defects. The intrinsic brittleness and low fracture toughness limits the use of some materials in load-bearing implants. The mechanical properties should allow scaffolds to resist the pressure and maintain the porosity needed for cell growth and matrix production [4,21,52].

At the same time, scaffolds should not only have similar mechanical properties to that of the host tissue, but also be able to degrade with time *in vivo*, preferably at a controllable biodegradation/ bioresorption rate (chemical dissolution or decomposition of biomaterials under physiological environments), without the need for surgical removal. The rate of degradation should vary based on its application and can be affected by several factors. Generally, it depends upon the chemical composition of the scaffold, the solubility of degraded products and the local pH of the surrounding environment. It also depends on the scaffolds crystallinity and physical arrangements like porosity pore size and distribution.

The maintenance of the strength and stability of the interface during the breakdown and reconstruction of natural host tissue and the matching of the degradation rate of the support with the growth rate of new bone tissue are some of the difficulties in the development of scaffolds materials [53,58,59].

II.3.4. Biocompatibility

One of the primary requirements of any bone scaffolds is biocompatibility a term that has been described in many ways. Biocompatibility of a scaffold is described in the William dictionary of biomaterials [60] as its ability to perform its desired function, that is, to support normal cellular activity with an appropriate response in a specific application.

An ideal bone scaffold must be osteoconductive where the scaffold allows the bone cells to adhere, proliferate, and form extracellular matrix on its surface and pores. The scaffold should also be able to induce new bone formation through biomolecular signalling and recruiting progenitor cells, a property known as osteoinduction [61,62].

II.4. Bioactive Glasses

Several materials have been used with the aim of producing scaffolds mostly polymers of natural or synthetic origin and some ceramics/glasses [37,63–65]. Of all materials used in the manufacture of scaffolds, we will focus on glasses, the object of study of this thesis.

The first glass to be approved for biomedical use, in 1985, was developed by Hench for use in middle ear surgery and is commercially available as Bioglass®, also designated as 45S5. The name ‘45S5’ refers to both the SiO_2 content (45 wt. %) and the Ca/P molar ratio. Developed in

1969 it was produced like conventional glass in which the basic components are SiO_2, Na_2O, CaO and P_2O_5. The *bioactivity* of these materials refers to the special response that they induce upon contact with the physiological environment.

Bioactive glasses develop on its surface a biologically active hydroxycarbonate apatite (HCA) layer which provides a bonding interface with the tissue, chemically and structurally equivalent to the mineral phase in bone [64,66–68].

According to Hench [69,70], the process of apatite formation on silica-based bioactive glasses surfaces is divided into five stages, Fig. II.3:

- Rapid exchange of Na^+ and/or K^+ from glasses with H^+ or H_3O^+ from solution, leading to a high pH local environment (stage I)

$$Si–O–Na^+ + H^+ \rightarrow Si–OH + Na^+ \quad \text{(Eq. II.1)}$$

- Loss of soluble silica in the form of $Si(OH)_4$ and Si–OH, due to breaking of Si–O–Si bonds by the attack of H^+ (stage II)

$$Si–O–Si + H_2O \rightarrow Si–OH + OH–Si \quad \text{(Eq. II.2)}$$

- Condensation and repolymerization of silanols $Si(OH)_4$ to form a SiO_2-rich layer depleted in alkali and alkaline-earth cations (stage III)

- Precipitation of Ca^{2+} and PO_4^{3-} ions on the silica-rich layer to form an amorphous calcium phosphate-rich layer (stage IV)

- Crystallization of the amorphous film by incorporation of OH^- and CO_3^{2-} anions (stage V)

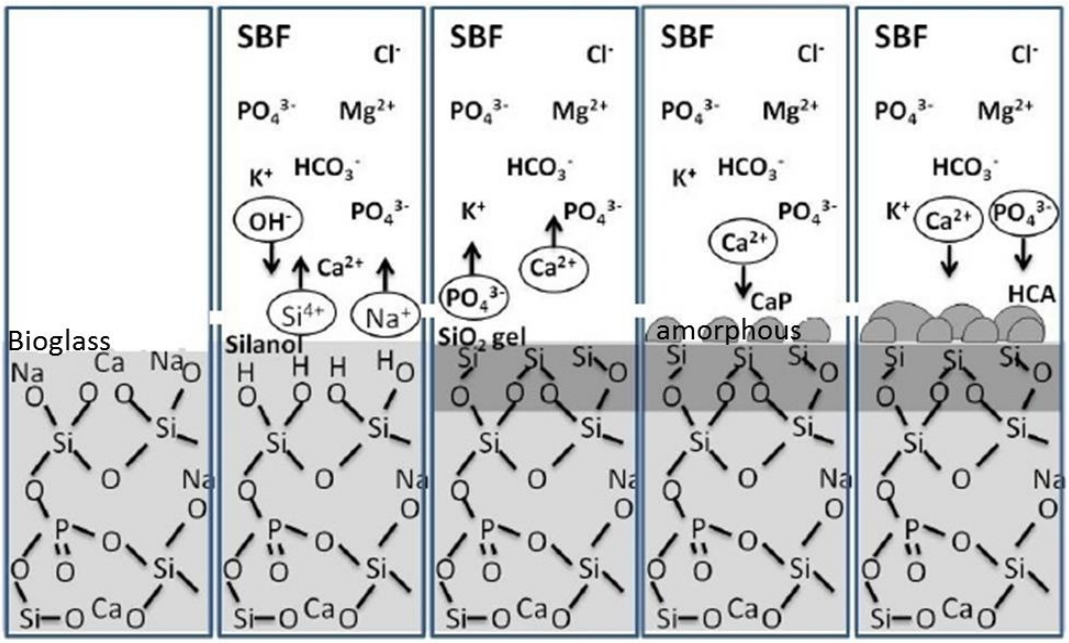

Fig.II.3. Schematic representation of the process of apatite formation on bioactive surfaces in contact with SBF [71]

The presence of this HCA layer is considered to be useful but not critical for bone mineralization [72,73]. Bioactive glasses [68,74,75] typically contain less than 60 wt. % of SiO_2 and large amounts of alkali and alkaline-earth oxides. The alkali and alkaline-earth ions are exchanged with H^+ (or H_3O^+) ions from the solution, leading to the hydrolysis of the silica groups and the creation of silanol (Si−OH) groups on the glass surface. The increase in pH (or OH^- concentration) leads to attack of the SiO_2 glass network, and the dissolution of silica, in the form of silicic acid, $Si(OH)_4$, into the solution, and the continued formation of Si−OH groups on the glass surface, which decreases the leaching of ions. At this stage, Ca^{2+} and PO4 groups migrate from the fluid to the silica-rich layer, and finally a CaP-rich layer is deposited on top of the glass which crystallizes to hydroxycarbonate apatite (HCA) [2].

The 45S5 composition consists of a silicate network (45 wt. % SiO_2) incorporating 24.5%Na_2O, 24.5%CaO and 6 % P_2O_5 (wt. %). The high amounts of Na_2O and CaO, as well as the relatively high CaO/P_2O_5 ratio make the glass surface highly reactive in physiological environments. Over the years other compositions were developed with additional elements incorporated in the silicate network, (table II.1) such as fluorine [76], magnesium [77,78], strontium [79–81], iron [82], silver [83–86], boron [87–91], potassium [92] or zinc [18,93,94]. The development of new biomaterials has recently concentrated on SiO_2-free glasses [91,95–98].

The first materials incorporating magnesium oxide were Ceravital glasses (40–50 SiO_2, 10–15 P_2O_5, 5–10 Na_2O, 0.5–3.0 K_2O and 2.5–5 MgO (wt. %)) and the resulting glass-ceramic materials. Kokubo et al. [43] worked with glasses of SiO_2–CaO–P_2O_5-MgO. Vogel and Holand [99] developed the Bioverit family of glass ceramic in which MgO content is in the range 6 – 28 mol. %.

Regarding to MgO, its contribution to the bioactivity is controversial [100]. MgO has been documented to decrease apatite formation in SBF [101] but also, on the other hand, to improve the early stages of mineralization [102] and contribute to an intimate contact with living tissue, showing that it is possible to design glasses with high MgO content (~ 18 %) without loss of bioactivity [103].

The development of phosphate glasses for biomedical application in the early 80's, introduced by Gilchrist [104], allowed an adjustment of the chemical composition to the mineral phase of bone, and a wide range of degradation rates as a function of this composition, adaptable to the required application [58,59].

Recent studies have shown that the ionic products, resulting from glass dissolution, enhance osteogenesis by regulating osteoblast proliferation, differentiation, and gene expression [7,25,68,80,105,106]. *In vitro* testing of biomaterials is used to provide rapid data on the biological interaction of materials with cells. This *in vitro* and also the *in vivo* tests showed that there is a sequence of bioactive glass reaction with tissues [2,107], and 6 more stages were added to the 5 presented before:

- Adsorption of biological moieties in the SiO_2-hydroxycabonate apatite layer from surrounding tissues (stage VI)

- Action of macrophages to remove debris from the site allowing cells to occupy the space (stage VII)

- Attachment of stem cells on the bioactive glass surface (stage VIII)

- Differentiation of stem cells to form bone growing cells, such as osteoblasts (stage IX)

- Generation of extra cellular matrix (stage X)

- Mineralization of matrix through crystallisation of inorganic calcium phosphate matrix to enclose bone cells in living structure (stage XI)

II.5. Bioactive Glasses Applications

The first clinical applications of a bioactive glass were solid plates [43] for replacing the bones of the middle ear, 1985, but most current applications are based on particulates [64,74]. The first particulate material cleared for sale was PerioGlas®, in 1993 in USA and in Europe in 1995. Their initial clinical applications were to restore bone loss resulting from periodontal disease [64,108] and in middle ear surgery [109]. Bioglass® particulate is also used for the treatment of dentinal hypersensitivity, incorporated into toothpaste, or used with an aqueous vehicle and applied to the tooth surface around exposed root dentin [110]. Building on the successes of PerioGlas®, a Bioglass® particulate for orthopaedic bone grafting, in non-load-bearing sites, was introduced in

clinical applications in the European market in 2000, under the trade name NovaBone®. In orthopaedic applications, the development and improvement of these glasses were directed mainly to the enhancement of the mechanical properties, through the preparation of glass-ceramics (section II.8).

In the form of scaffolds, the porosity allows new bone tissue to grow into the porous structure, providing an adequate biological fixation [111–114]. The interest in bioactive glasses has been expanded since their initial discovery and now it is also focused on tissue engineering applications. All compositions, in Table II.2, were or are being used in scaffold production.

Table II.2. Compositions of some glasses used on scaffolds production

Glass	Ref.	SiO_2	CaO	Na_2O	P_2O_5	B_2O_3	CaF	K_2O	MgO	ZnO	TiO
45S5 wt.%	[115–119]	45	24.5	24.5	6.0	-	-	-	-	-	-
45S5-B wt.%	[88,120]	15.37	26.9	24.4	2.6	30.73	-	-	-	-	-
BG1 wt.%	[121]	53.6	13.2	11.9	2	1	-	15.1	3.2	-	-
S53P4 wt.%	[122]	53	20	23	4	-	-	-	-	-	-
G5 wt.%	[123]	-	44.5	6	44.5	-	-	-	-	-	5
6P53B wt.%	[124]	52.7	18	10.3	6	-	-	2.8	10.2	-	-
58S wt.%	[125]	58	33	-	9	-	-	-	-	-	-
PIG wt.%	[126]	-	60	7	30	-	-	-	-	-	3
SCNPBT wt.%	[127]	58.6	23.66	9.32	3.38	1.78	-	-	-	-	1.26
70S30C wt.%	[128]	70	30	-	-	-	-	-	-	-	-
13-93 wt.%	[129–131]	53	20	6	4	-	-	12	5	-	-
13-93B3 wt. %	[91]	-	20	6	4	53	-	12	5	-	-
HZ5 wt. %	[132]	42.6	23.4	23.4	5.7	-	-	-	-	5	-
SNCM mol.%	[78]	50	16	25	-	-	-	-	9	-	-
D-Alk-B mol.%	[122]	18	22	6	2	36	-	8	8	-	-
CEL2 mol.%	[133]	45	26	15	3	-	-	4	7	-	-
Fa-GC mol.%	[134]	50	18	7	6	-	9	7	3	-	-
CSK mol.%	[135]	50	44	-	-	-	-	6	-	-	-

II.6. Scaffolds processing methodologies

A variety of methods has been used to fabricate bioactive glass scaffolds. Table II.3, summarises the current developments in the creation of scaffolds with the structure and properties suitable for bone tissue engineering.

Table II.3. Overview on recent studies performed to obtain scaffolds

Fabrication technique	Particle size/ fibre diameter(§) (µm)	Pore size (µm)	Porosity (%)	Compressive strength (MPa)	Glass composition/ system
Polymer foam replication	< 5 [115,117]	200-600 350-800	90-95	n.d	45S5
	≈ 5 [118]	510-720	89-92	0.41±0.1	
	5-10 [118,136]	510–720	89-92	0.27-0.42	
	≈ 10 [119]	510-720	92-94	n.d	
	10-20 [137]	> 400	91-93	0.1-0.15	
	< 30 [77,138]	100-500	70-75	1±0.4	13-93
	CEL2 [139]		54-73	1±0.4	
	5 – 10 [131]		85±2	11±1	
	<53 [88] < 150 [120]	200-500 100-500	68-87 78-82	10 5-7	13-93B3
	≈ 4 [122]	200-500 200-300	70-88 67.7±2.3	3.8-1 9.7±1.3	D-Alk-B
	< 32 [76]	> 100	74.6±3.4	2±0.6	Fa-GC
Glass fibers	75 § [140]	n.d	45-50 55-60	18 12	13 - 93
	25-40 [129,141]		44.3±3.6	5.3±2	
	75 § [132]	n.d	70	n.d	HZ5
	75 § [121]	300-400	70	n.d	BG1
	45 – 90 [119]	20-100	40	6±1	45S5
Slip casting	255-325 [142,143]	100-300	40 - 45	22±1	13 - 93
Freezing	<150 [143]	90-110	53-57	25±3	13 - 93
	1.0 ± 0.5 [130]	60-120	50-55	27±8	
Robocasting	<73 [124,144]	60	500	136±22	6P53B

Foam glass	Sol* [123]	20-500	40-55	n.d	G5
	Sol* [56]	100-500	82-88	2.25	70S30C
Burning out organic	< 106 [134]	100-300	24.50	1	Fa - GC
	38 – 75 [146]	200-300	21	n.d	45S5
	45 – 90 [147]	100	n.d	n.d	
	<25 [148]	100	60-70	117 - 123	
	25 – 75 [149]	n.p	43.5	6.8 ± 2.7	
	<25 [149]	n.p	47.2	5.4 ± 2.3	
	n.a. [125]	20 - 200	60 - 70	n.d.	58S
	<125 [126]	30 - 600	77	n.p.	PIG
	<106 [135]	>100; 200-500	60-62	1.5 - 6	SCK
	<100 [78]	50 - 100	40	6 ± 1	SNCM
Solution combustion	[127,150]	14 - 160	38.6	2.25	SNCPBT
Leaching particle	< 20 [151,152]	200-300	76.5	0.29	Na_2O – CaO –B_2O_3
Solid freeform fabrication	[153]	150-200	50	140 ± 70	13 - 93
	[124]	500 - 1000	60	136	6P53B

The large range of compressive strength values reported (0.3–140 MPa) can be interpreted by the differences in the fabrication method, glass composition, pore morphology and size distribution, and thickness of the struts, as well as on the mechanical test parameters employed (sample geometry, size and loading speed).

Generally, Bioglass® composition is unsuitable for the production of glass scaffolds, because a sintering process is employed in all known methods for the processing of scaffolds. The sintering process requires temperatures above the glass transition temperature of the glass, in order to initiate the densification of the powder and, the Bioglass® crystallises immediately above its glass transition. Even after crystallization, most of the compressive strength values are out of the range obtained for trabecular bone, as can be seen in Table II.1.

The following section is a short review of the common scaffold fabrication methods presented on Table II, including the advantages and disadvantages of each.

II.6.1. Polymer foam replication

The replication method involves the preparation of glass green bodies' foams by coating a polymer foam with a glass slurry. The polymer, having the desired pore structure, simply serves as a sacrificial template for the glass coating. The polymer template is immersed in the slurry and the excess slurry squeezed out leaving a more or less homogeneous coating on the foam struts. After drying, the polymer is slowly burned out in order to minimise damage to the glass coating. Once the polymer has been removed, the glass network is sintered to a desired density. Their microstructure depends on the initial morphology of the preformed foam. The foam replica technique has the ability to produce foams with a highly porous structure and adjustable pore dimensions. Moreover irregular shapes can be produced to match the size and shape of the bone defect.

By using the described method, different types of scaffolds with tailored gradient of porosity were fabricated. Chen et al. [118] were able to prepare a porous 45S5 bioactive glass-ceramic scaffold with 89 to 90 % porosity by using a polyurethane template. With the introduction of magnesium and potassium, a 13–93 glass-ceramic scaffold was prepared by the same method with similar porosity and a compressive strength of 11 ± 1 MPa [131], which match the highest values reported for human trabecular bone (Table I). These compressive strengths values are more than 10 times higher than the reported for 45S5 Bioglass® based scaffolds [118] as a result of the glass composition that improves the viscous flow characteristics of 13–93 glass and the glass densification prior to crystallization.

II.6.2. Glass fibers

Sintering bioactive glass fibers is also an interesting method to achieve a scaffold with interconnecting porosity. In this process, the scaffold is formed by thermally bonding a loose and random packing of fibers in a mold. The relative porosity, pore size and strength of these scaffolds can be controlled by changing certain parameters such as the size of the fibers, temperature and sintering time [154,155]. Pirhonen et al. [155] used the glass system $53SiO_2$–$6Na_2O$–$12K_2O$–5MgO–20CaO–4 P_2O_5 (wt. %) to obtain fibers with 100 mm in diameter and 3 mm length. Through the glass fiber technique, scaffolds were obtained with 80 % porosity and pore average size of 420 μm, by sintering at 690 °C. Porosity in the form of interconnected pore space is provided by the pore space between the glass fibers. With the increase of sintering temperature, the densification of the structure increases, reducing the relative porosity and pore size with consequent loss of pore interconnectivity.

II.6.3. Foam glass

The use of foaming agents to the sol-gel has been studied by several authors [123,128,156,157]. Yuan, et al. have adopted H_2O_2 as a foaming agent to prepare and manufacture 45S5 bioactive glass scaffolds, with pore sizes ranging from 100–600 μm [157]. The H_2O_2 decomposition process leads to a random distribution of interconnected pores. An increment in the porosity, pore size and interconnectivity degree was observed by Navarro et al. [123] with the increase of H_2O_2 content. The hydrogen peroxide lead to the formation of pores with a particular morphology, elongated at lower concentrations and more spherical at higher concentrations. The scaffold with higher porosity (55 %) obtained with the addition of 60 % H_2O_2 showed pore size greater than 500 μm.

The produced scaffolds belongs to the porous SiO_2 (100S), SiO_2–CaO (70S30C) and CaO–P_2O_5 –SiO_2 (58S) systems, have a specific surface area between 106 to 283 m^2 g^{-1} because of the nanopores in the glass that are inherent to the sol–gel process, mechanical strength of 2.2 – 2.4 MPa, similar to spongy bone and porous hydroxyapatite used clinically [128,156]. Consequently they are suitable for substituting defects in low-load sites only. In the foam glass technique, as the temperatures increase the glasses become substantially crystallized and their degradability will decrease. It is also difficult to control the percentage and pore size, and the interconnectivity of the prepared materials making it challenging to obtain geometries and porosity appropriated to the desired application.

II.6.4. Burning out method

As a porosity promoter, it is also possible to use organic particles such as sucrose [126], gelatin [158], naphthalene [159], polyethylene [135], corn, potatoes and rice starches [78,149]. The organic phase can be added to ceramic powders and subsequently it is thermally removed during sintering. PEG-glycol particles of different sizes and amounts were used to retrieve a porous bioactive glass after sintering [160]. The sintering occurs only at temperatures higher than the firing temperature of the porogen. This approach presents low production costs, however controlling the composition of the finished products is difficult because of glass tendency to crystallize during thermal treatment, resulting in problems of homogeneity and reproducibility. In addition, it is difficult to achieve highly porous samples with adequate mechanical properties. A porosity value between 50 and 70 vol.% has been reported for glass-ceramic scaffolds based on a SiO_2–CaO–K_2O system [126,135]. However, lower porosity values are often reported [78,149]. Macroporous glass-ceramics of the CaO–P_2O_5–Na_2O–TiO system were obtained by pressing and sintering a mixture of glass particles with sucrose (particle diameter > 500 μm). Low sintering temperature, high sucrose glass ratio, and small glass particles size provide high porosity, approximately 80 to 90 %. However, the use of low sintering temperatures, impairs the

mechanical strength of the structure [126]. Another similar process consists in mixing particles of camphor ($C_{10}H_{16}O$) with Bioglass® 45S5 [146]. Macropores were obtained with a diameter between 200 – 300 μm. However, this technique yielded only 21 % of the total porosity with isolated pores, not being thus possible to simulate the intertrabecular bone. Soundrapandian et al [159] have produced 63 – 66 % porous bioactive glass scaffolds based on SiO_2–Na_2O–ZnO–CaO–MgO–P_2O_5 system (BGZ and MBG) for drug delivery using naphthalene as a porogen. The naphthalene was evaporated from the samples via very slow drying up to 80 ºC, followed by sintering at approximately 725 ºC.

Li Nas et al. [125] prepared macroporous sol–gel bioglasses using granular polyethylene glycol (PEG) as pore former with 60 – 70 % porosity. The pore diameter was distributed around 10 – 200 μm containing mesopores of 2 – 50 nm. The volume and size of pore former can control the porosity and the macropore diameter.

II.6.5. Leaching particle/Salt sintering process

This is a simple way to make a porous scaffold using water-soluble particles such as salts NaCl, K_2SO_4 and $MgSO_4$ that are dissolved leaving pores of the same size as the salt. The pore structures can easily be manipulated by controlling the size and fraction of the porogen. Unless sufficient porogen is used it may be difficult to leach it from the glass, and at high percentages, the mechanical properties of the scaffold are substantially reduced. The most common porogen used is NaCl. Depending upon the glass / salt ratio, this technique allows to obtain values of porosity of about 75 % [151,152]. The scaffolds thus obtained have a very low mechanical strength of 0.29 MPa [151].

The selected salt must have a suitable particle size, melting temperature higher than the temperature of densification of the glass and a high solubility in a solvent in which the glass is insoluble. The added salt should not induce the formation of new phases in the glass composition during sintering. Regarding this technique, it can be established that the densification of the sintered material is greater, the smaller the size of the glass particles with respect to the salt.

This technique has the advantage of being quite simple, but the results were still not satisfactory since the control of processing variables and their effect on sintering characteristics of the supports has not been investigated. Further studies are necessary and will be performed in this thesis.

II.6.6. Solid freeform fabrication

Solid freeform fabrication (SFF), also referred to as rapid prototyping (RP), describes a group of techniques used to manufacture 3D objects from a computer aided design (CAD) file, without the use of traditional tools such as dies or molds. The technique can be used to predesign the scaffold

architecture structure on a computer. Several SFF techniques have been used for scaffold fabrication, but there is little information on the production of glass scaffolds based on these techniques. Recently, scaffolds of apatite–mullite glass–ceramics, 13–93, and 6P53B glasses have been manufactured using freeze extrusion, selective laser sintering and robocasting methods [124,153]. In the last method, an aqueous paste of 6P53B bioactive micron-sized glass powder is extruded through a fine nozzle, printing lines as thin as 30 μm, and deposited over the previous layer, obtaining a scaffold with a compressive strength of 136 MPa, comparable to human cortical bone [65].

II.6.7. Freeze *casting of suspensions*

The freeze casting route involves rapid freezing of a ceramic slurry, poured into a mould and subsequent freeze drying to sublimate the solvent under vacuum, avoiding the drying stresses and shrinkage that may lead to cracks and warping during normal drying. After drying, the compacts are sintered in order to fabricate a porous material with improved strength, stiffness and desired porosity. The result scaffold has a complex and often anisotropic porous microstructure. By controlling the growth direction of the ice crystals, it is possible to impose a preferential orientation for the porosity in the final material. A benefit of the oriented microstructure is higher scaffold strength in the direction of orientation, compared to the strength of a scaffold with a randomly oriented microstructure. Unidirectional freezing of aqueous suspensions has been used recently to produce oriented bioactive glass scaffolds. The process commonly results in the formation of porous constructs with a lamellar microstructure. However, the width of the slot-like pores (10 – 40 μm) is considered to be too small to support tissue ingrowth. Both 45S5 and 13–93 glass scaffolds have been prepared using this technique [129,141]. Bioactive glass 13–93 was used in the fabrication of scaffolds with pore diameters of 100 – 150 μm and oriented columnar microstructures by unidirectional freezing of camphene-based suspensions. It has also been shown that the addition of an organic solvent such as 1, 4 - dioxane to the aqueous solvent, results in a change of the lamellar microstructure to a columnar microstructure with an increase in the pore width.

II.7. Sintering

In all the methods used for the production of 3-D structures from glass particles it is necessary to resort to sintering. During the heat treatment the viscosity of glass dramatically decreased. Because of surface tension effects, that vary as a function of surface curvature, material flows are driven toward the particle necks, thus densifying a powder compact into a ceramic solid.
The overall sintering process was roughly divided in three steps, fig. II.4, that have been analyzed by Frenkel (initial stage) [161,162], Scherer (intermediate stage) [163,164], and Mackenzie –

Shuttleworth, MS model (final stage) [165,166]. These stages are defined according to the porosity and grains morphology.

The initial stage consists of fairly rapid interparticle neck growth by diffusion, vapour transport, plastic flow, or viscous flow. For a powder system with an initial density of 50 – 60 % of the theoretical density, this corresponds to a linear shrinkage of 3 to 5 % or to a relative density of 65 %. In the intermediate stage pores form a network of channels between the interconnected particles. This stage ends when the relative density reaches about 94 %, that is, when the open pores gives rise to closed pores. During the final stage, all the porosity becomes isolated and the increase in density of the compact is not as high as in previous stages. The number of pores tends to decrease. In some cases, these closed pores may trap gases, making their elimination difficult.

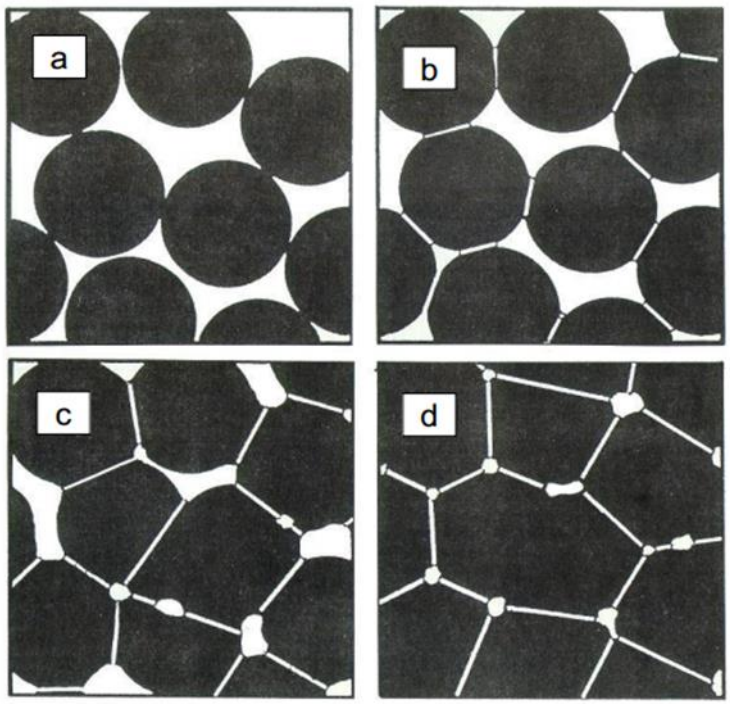

Fig.II.4. Illustrations of the stages of sintering: initial package (a), initial stage (b), intermediate stage (c) and final stage (d) [167]

A few models and a variety of experiments have been proposed and conducted on viscous flow sintering. The first work on the sintering of glass was originated from the theory of viscous sintering by Frenkel. Using a simple energy balance (the energy dissipated by viscous flow is equal to the energy gained by the reduction of surface area during sintering), the Frenkel classical model for the isothermal densification successfully described parts of the sintering process. After a sintering time t, the linear shrinkage (ΔL) of the sample relative to the original length, L_0, is given by Eq.II.3

$$\frac{\Delta L}{L_0} = \left[\frac{3\gamma}{8\eta(T)r}\right]t \qquad \text{Eq. II.3}$$

Where η(T) is the temperature-dependent shear viscosity, γ is the glass-vapor surface energy (whose temperature dependence is very weak), and r is the initial particle radius. Eq.II.3 demonstrates that the initial shrinkage rate is inversely proportional to the viscosity and particle size.

The non-isothermal sintering investigation has been performed by dilatometry, using a variety of heating rates, in order to expand beyond the isothermal mechanistic approach to initial stage sinter modeling.

Venkatu [168] developed an initial stage sintering model which includes the heating rate. The focus of the work was to determine which of the six sintering mechanisms were the cause of dimensional change during heating, Eq. II.4.

$$y^p = \frac{A}{\beta}\exp\left[\frac{-(Q+Q')}{RT}\right] \qquad \text{Eq. II.4}$$

where Q' is a constant with the value of 24.27 kJ mol^{-1}, for the viscous flow, β is a constant that only depends on the material and of the sintering mechanism and p is the sintering exponent, which presents the values of p = 1 for viscous flow, p = 2 for volume diffusion and p = 3 for the diffusion mechanism by grain contour.

An inhibition source of densification is the crystallization of the particles. In the optimum sintering process, glass full densification should occur before the onset of crystallization. In the glass sintering, densification occurs in the interval between glass transition temperature and the onset of crystallization. If this interval is too small, the glass may not have time to fully densification prior to initiating crystallization [174]. Crystallization brings a marked reduction in the densification by viscous flow, for approximately 10 % of crystals formed, the apparent viscosity increases about 100 times, resulting in a sudden reduction in the viscous flow with stop of the shrinkage, which can be observed in dilatometric curves [175].

The densification prior crystallization of 10 μm glass particles is affected by the heating rate as showed by Boccaccini et al. [176] in the Ba–Mg–Al–Si–O system. They used two heating rates, one at 15 and another at 1 ºC min^{-1}. The crystallization was delayed to higher temperature in the sample heated at a faster heating rate, and a full densification was obtained. However, at 1 ºC min^{-1}, a densification of 89 % was obtained at the same final temperature.

Shrinkage is also affected by the initial particle size factor [169,170] and consequent degree of particle orientation. Glass particles with mixed size distribution sintered about five times faster than glasses with equivalent average particle size and spherical uniform size distribution. In

general, the particle orientation contributes to inhomogeneous green packing and consequent anisotropic shrinkage behaviour [171,172]. The effects of particle shape (ball-milled and spheroidized), uniaxially pressed powders effects on shrinkage anisotropy during sintering of cordierite-type glass [173], showed that both types of particle compacts exhibited around 0.7 anisotropy factor, but that spheroidizing reduced the shrinkage rate.

Anisotropy of shrinkage is a common phenomenon in the sintering practice. When sintering a cylindrical sample, for example, it can be observed that the shrinkage in the axial direction differs from that in the radial direction [171,172,174]. Anisotropic shrinkage appears not to be a simple particle shape effect but may be related to particle packing and size distribution in the axial and radial directions [175,176].

II.8. Crystallization

Despite the discovery of Bioglass in 1971, there is still no vitreous scaffold structure successfully produced [177]. Bioglass crystallizes immediately above the glass transition temperature, yielding a glass ceramic scaffold, resulting in the formation of $Na_2Ca_2Si_3O_9$ as the main crystalline phase [178,179]. A secondary minor phase, $Na_2CaSi_3O_8$, is sometimes suggested [180]. Glass-ceramics are obtained by using an appropriate thermal treatment on the parent glass [57,64,181,182]. The composition of the crystalline phases and the crystallite sizes, within the residual vitreous matrix, define the properties of the final material [182].

Many bioactive glass-ceramics have reached commercial success (table II.4). Ceravital (apatite-devirrite) was the first glass-ceramic material for clinical applications, developed in 1973 [109]. Clinical use of this bioactive material was limited, due to instability of the crystal phase boundaries in the glass-ceramic.

One of the glass-ceramics of higher clinical success is Cerabone ® A-W (apatite-wollastonite), introduced by Kokubo in 1982 [43]. So far, the clinical use in vertebral replacement and spinal repair has provided acceptable results [183]. In 1983, Holand et al. [70,99], of the University of Jena, developed a new series of bioactive glass-ceramics, called Bioverit® I (mica–apatite) and Bioverit® II (mica).

Table II.4. Composition and selected properties of glass-ceramics with clinical applications as compared to those of Bioglass 45S5 [184]

Composition (wt. %)	Bioglass 45S5	Ceravital [109]	Cerabone A/W [183]	Bioverit [70,99]
Na_2O	24.5	5-10	0	3-8
K_2O	0	0.5-3.0	0	0
MgO	0	2.5-5	4.6	2-21
CaO	24.5	30-35	44.7	10-34
Al_2O_3	0	0	0	8-15
SiO_2	45.0	40-50	34.0	19-54
P_2O_5	6.0	10-50	6.2	2-10
CaF_2	0	0	0.5	3-23
Phases	Glass	Apatite + glass	Apatite + β - wollastonite + glass	Apatite + Mica
Flexural Strength MPa	42	100 - 150	220	100-160
Compressive strength (MPa)	n.d.	500	1060	500
Young's modulus GPa	35	n.d.	117	70-88
Clinical Application	middle ear alveolar ossicular chain replacement	middle ear ossicular chain replacement	vertebral replacement, iliac crest prostheses, bone defect fillers	Orthopaedic, head and neck surgery

The effect of crystal phases in the bioactive mechanisms is still under debate. The mechanism of apatite formation on glass-ceramic A-W is essentially the same as that on Bioglass in the Na_2O–CaO–SiO_2–P_2O_5 system. However, glass-ceramic A-W forms an apatite layer on its surface without forming a silica gel layer first as showed by Kitsugi et al. [185].

The effect of crystallinity on the apatite formation on Bioglass® surfaces *in vitro* [186] revealed that the crystal phase $Na_2Ca_2Si_3O_9$ slightly decreased the formation kinetics of such layer on the glass sample surface but it did not totally suppress it [118,149,187]. It has been suggested that the precipitation of the apatite layer depended on the presence of a residual glassy phase in the glass-ceramic [188]. On the contrary, it was found [189] that fully crystallized samples could also develop a crystalline HCA layer, but that the reaction rate significantly reduce with the degree of crystallization, for crystallization values higher than 60 vol. % [190,191]. It is possible that the bioactivity is due to the presence of the $Na_2Ca_2Si_3O_9$ [118], since this crystal phase is bioactive

by itself [70,192], through the transformation of the crystalline phase into a reactive amorphous phase.

Boccaccini et al. [193] modelled the degradation mechanisms of 45S5 glass-ceramics in three basic steps:

(i) Preferential dissolution takes place at the interface between $Na_2Ca_2Si_3O_9$ crystallites and residual glassy phase. The so-produced gaps allow the physiological solution to penetrate into the material and to promote a diffused ion leaching from the crystalline phase.

(ii) Crystallites progressively break down into very fine grains and the amorphous matrix is dissolved as a consequence of the ion exchange.

(iii) As a consequence, in the end, the crystalline phase changes into an amorphous phase.

If the crystallization slowed down the bioactivity, it is possible to adjust this parameter through controlled crystallization to match the natural healing rate of bone tissue, through low dissolution rates as well as low resorptions, according to the requirements of the application. If the bioactive behaviour is hindered due to crystalline phases, it is possible to improve the resorption behaviour by modifying the surface of the material.

II.9. Functionalization

The surface properties of the glass ceramics are sometimes different from those required by biomedical applications. Several approaches have been investigated to optimize the performance of biomaterials, namely glass ceramics in contact with living tissues [194]. The biomaterial surface can be modified by mechanical, physical, chemical or biological treatments, in order to induce an appropriate tissue response. Indeed, the variation in chemical functional groups is known to affect hydrophobicity, Fig. II.5, which in turn affects protein adsorption and conformation, subsequently affecting various cellular responses [195].

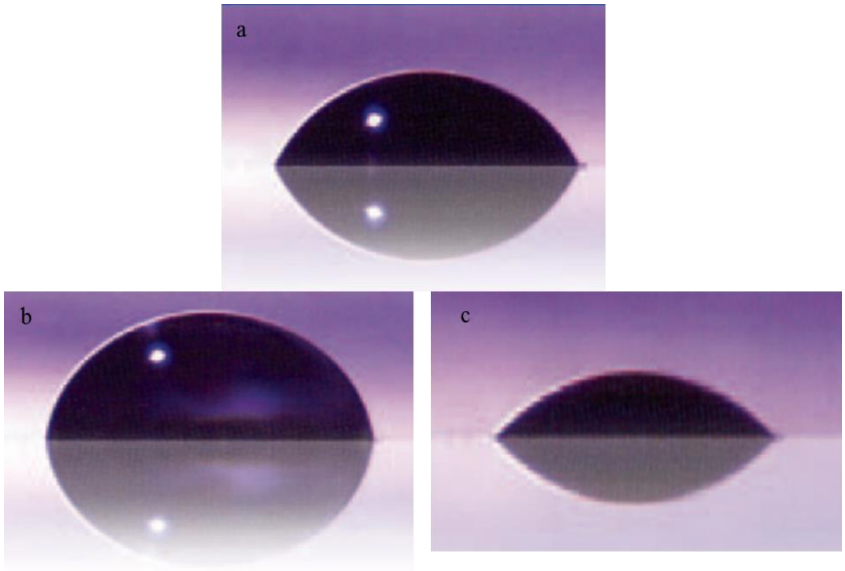

Fig.II.5. Illustrations of the surface wetting types a) Ordinary Surface "typical wetting, b) Hydrophobic "poor wetting" and c) Hydrophilic "good wetting" [196]

Among the variety of methods, silanization has been recently investigated [119,197–201]. Silica surface interacts with the silane reagent to form a covalent bond with the surface, Fig. II.6.

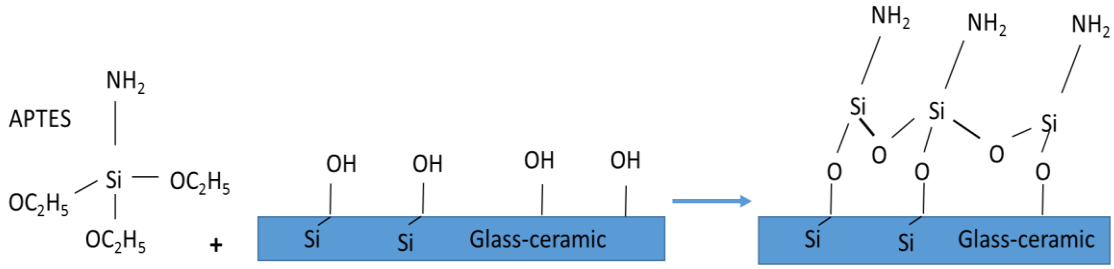

Fig.II.6. Schematic of APTES adsorption to the glass-ceramic surface [202,203]

This attachment, of functional organosilanes to silica and glass substrates, has proven to be an efficient means of immobilizing antibodies and cellular receptors [201,204]. Successful and reproducible conditions require a silane uniform monolayer deposition on the glass surface that requires a cleaned surface. The cleaning treatment process is important to promote both surface removal of contaminants and exposure of reactive hydroxyls. Several cleaning methods have been proposed in the literature, such as the use of acetone [205,206], acids or alkali treatments [207]. The acids commonly used include hydrochloric acid, sulphuric acid, hydrofluoric acid, and nitric acid. Alkali treatment involves immersion of the implants in either sodium or potassium hydroxide followed by heat treatment and rinsing in distilled water.

After surface activation silanization can be performed. The most common silane coupling agent used is 3-aminopropyltriethoxysilane (APTES) [208,209], which reacts with the free hydroxyl groups of activated carriers to generate silane modified surfaces, Fig. II.6. The amine groups of

the silane modified surface react with a dialdehyde cross linker forming an aldehyde derivatized surface, which further reacts with the free amino groups of the antibody/protein to be immobilized. Since bioactive glasses have the ability to undergo ion-exchange processes which, in contact with simulated body fluid (SBF) [210–213], leads to the formation of silanols, and then to the further steps of hydroxyapatite formation, it seems to be possible to pre-activate the surface to enhance the cell responses [194,206]. However, the fast condensation of silanols to silica gel imposes a deep control of surface cleaning and activation to preserve the presence of free -OH groups on it. The Bioglass® derived glass-ceramic scaffold [206] was exposed to surface functionalization (acetone + APTES) and further grafting with alkaline phosphatase, to disrupt the stable $Na_2Ca_2Si_3O_9$ crystalline phase, further enhancing the formation of the calcium phosphate phase in SBF.

References

[1] J. Behari, Biophysical Bone Behaviour: Principles and Applications, John Wiley & Sons, 2009.

[2] L.L. Hench, J. Wilson, An Introduction to bioceramics, World Scientific, 1993.

[3] P.D.H. and C.W. Alireza Nouri, Biomimetics Learning from Nature, InTech, 2010.

[4] K.F. Leong, C.M. Cheah, C.K. Chua, Solid freeform fabrication of three-dimensional scaffolds for engineering replacement tissues and organs, Biomaterials. 24 (2003) 2363–2378.

[5] J.-H. Jang, O. Castano, H.-W. Kim, Electrospun materials as potential platforms for bone tissue engineering, Adv. Drug Deliv. Rev. 61 (2009) 1065–1083.

[6] S. Serrano, M.L. Mariñoso, A. Torres, V. Lorenzo, U. Keysers, J. Lloreta, et al., Osteoblastic proliferation in bone biopsies from patients with end-stage chronic renal failure, J. Bone Miner. Res. 12 (1997) 191–9.

[7] T. Komori, Functions of the osteocyte network in the regulation of bone mass, Cell Tissue Res. 352 (2013) 191–8.

[8] S.C. Miller, W.S.S. Jee, The bone lining cell: A distinct phenotype?, Calcif. Tissue Int. 41 (1987) 1–5.

[9] G.D. Roodman, Osteoclast Differentiation, Crit. Rev. Oral Biol. Med. 2 (1991) 389–409.

[10] F. Barrère, C.A. van Blitterswijk, K. de Groot, Bone regeneration: molecular and cellular interactions with calcium phosphate ceramics, Int. J. Nanomedicine. 1 (2006) 317–32.

[11] C.T. Laurencin, M. Attawia, B. M, Advencements in tissue engineered bone substitutes, Curr. Opin. Orthop. 10 (1999) 445–451.

[12] W. Enneking, Transplanting allografts, J. Am. Coll. Surg. 201 (2005) 5–6.

[13] N.N. Hung, Basic knowledge of bone grafting, InTech, 2012.

[14] Q. Fu, E. Saiz, M.N. Rahaman, A.P. Tomsia, Bioactive glass scaffolds for bone tissue engineering: state of the art and future perspectives, Mater. Sci. Eng. C. 31 (2011) 1245–1256.

[15] E.L. Chaikof, H. Matthew, J. Kohn, A.G. Mikos, G.D. Prestwich, C.M. Yip, Biomaterials and scaffolds in reparative medicine, Ann N Y Acad Sci. 961 (2002) 96–105.

[16] S.-W. Yook, H.-D. Jung, C.-H. Park, K.-H. Shin, Y.-H. Koh, Y. Estrin, et al., Reverse freeze casting: A new method for fabricating highly porous titanium scaffolds with aligned large pores, Acta Biomater. 8 (2012) 2401–2410.

[17] A.G. Mikos, J.S. Temenoff, Formation of highly porous biodegradable scaffolds for tissue engineering, Electron J Biotechnol. 3 (2000) 114–119.

[18] S. Shruti, A.J. Salinas, G. Lusvardi, G. Malavasi, L. Menabue, M. Vallet-Regi, Mesoporous bioactive scaffolds prepared with cerium-, gallium- and zinc-containing glasses, Acta Biomater. 9 (2013) 4836–4844.

[19] M.N. Collins, C. Birkinshaw, Hyaluronic acid based scaffolds for tissue engineering-A review, Carbohydr. Polym. 92 (2013) 1262–1279.

[20] M. Navarro, A. Michiardi, O. Castaño, J.A. Planell, Biomaterials in orthopaedics, J. R. Soc. Interface. 5 (2008) 1137–58.

[21] D.W. Hutmacher, Scaffolds in tissue engineering bone and cartilage, Biomaterials. 21 (2000) 2529–2543.

[22] M.I. Sabir, X. Xu, L. Li, A review on biodegradable polymeric materials for bone tissue engineering applications, J. Mater. Sci. 44 (2009) 5713–5724.

[23] J.F. Mano, G.A. Silva, H.S. Azevedo, P.B. Malafaya, R.A. Sousa, S.S. Silva, et al., Natural origin biodegradable systems in tissue engineering and regenerative medicine: present status and some moving trends, J. R. Soc. Interface. 4 (2007) 999–1030.

[24] M. Yaszemski, Evolution of bone transplantation: molecular, cellular and tissue strategies to engineer human bone, Biomaterials. 17 (1996) 175–185.

[25] S.P. Bruder, B.S. Fox, Tissue engineering of bone: Cell based strategies, Clin. Orthop. Relat. Res. (1999) S68–S83.

[26] S. Wu, X. Liu, K.W.K. Yeung, C. Liu, X. Yang, Biomimetic porous scaffolds for bone tissue engineering, Mater. Sci. Eng. R Reports. 80 (2014) 1–36.

[27] L. Meinel, S. Hofmann, V. Karageorgiou, L. Zichner, R. Langer, D. Kaplan, et al., Engineering cartilage-like tissue using human mesenchymal stem cells and silk protein scaffolds, Biotechnol. Bioeng. 88 (2004) 379–91.

[28] B. Sharma, J.H. Elisseeff, Engineering Structurally Organized Cartilage and Bone Tissues, Ann. Biomed. Eng. 32 (2004) 148–159.

[29] E.S. Place, N.D. Evans, M.M. Stevens, Complexity in biomaterials for tissue engineering., Nat. Mater. 8 (2009) 457–70.

[30] R. Langer, J. Vacanti, Tissue engineering, Science. 260 (1993) 920–926.

[31] M. Mastrogiacomo, S. Scaglione, R. Martinetti, L. Dolcini, F. Beltrame, R. Cancedda, et al., Role of scaffold internal structure on in vivo bone formation in macroporous calcium phosphate bioceramics, Biomaterials. 27 (2006) 3230–7.

[32] M. Navarro, M.-P. Ginebra, J. Clément, M. Salvador, A. Gloria, J.A. Planell, Physicochemical Degradation of Titania-Stabilized Soluble Phosphate Glasses for Medical Applications, J. Am. Ceram. Soc. 86 (2003) 1345–1352.

[33] V. Karageorgiou, D. Kaplan, Porosity of 3D biomaterial scaffolds and osteogenesis, Biomaterials. 26 (2005) 5474–5491.

[34] I.O. Smith, F. Ren, M.J. Baumann, E.D. Case, Confocal laser scanning microscopy as a tool for imaging cancellous bone, J. Biomed. Mater. Res. B. Appl. Biomater. 79 (2006) 185–92.

[35] International Union of Pure and Applied Chemestry (IUPAC), IUPAC, USA.

[36] X.P. Wang, X. Li, A. Ito, Y. Sogo, Synthesis and characterization of hierarchically macroporous and mesoporous CaO-MO-SiO2-P2O5 (M=Mg, Zn, Sr) bioactive glass scaffolds, Acta Biomater. 7 (2011) 3638–3644.

[37] M. López-Álvarez, C. Rodríguez-Valencia, J. Serra, P. González, Bio-inspired Ceramics: Promising Scaffolds for Bone Tissue Engineering, Procedia Eng. 59 (2013) 51–58.

[38] V. Olivier, N. Faucheux, P. Hardouin, Biomaterial challenges and approaches to stem cell use in bone reconstructive surgery, Drug Discov. Today. 9 (2004) 803–11.

[39] A. Bignon, J. Chouteau, J. Chevalier, G. Fantozzi, J.-P. Carret, P. Chavassieux, et al., Effect of micro- and macroporosity of bone substitutes on their mechanical properties and cellular response, J. Mater. Sci. Mater. Med. 14 (2003) 1089–97.

[40] T.M. Freyman, I.V. Yannas, L.J. Gibson, Cellular materials as porous scaffolds for tissue engineering, Prog. Mater. Sci. 46 (2001) 273–282.

[41] K.A. Hing, B. Annaz, S. Saeed, P.A. Revell, T. Buckland, Microporosity enhances bioactivity of synthetic bone graft substitutes, J. Mater. Sci. Mater. Med. 16 (2005) 467–75.

[42] C.E. Holy, M.S. Shoichet, J.E. Davies, Engineering three-dimensional bone tissue in vitro using biodegradable scaffolds: investigating initial cell-seeding density and culture period, J. Biomed. Mater. Res. 51 (2000) 376–82.

[43] T. Kokubo, A/W glass-ceramic: processing and properties, An Introd. to Bioceram. (1999) 75–88.

[44] C. Cassinelli, M. Morra, G. Bruzzone, A. Carpi, G. Di Santi, R. Giardino, et al., Surface chemistry effects of topographic modification of titanium dental implant surfaces: 2. In vitro experiments, Int. J. Oral Maxillofac. Implants. 18 (2003) 46–52.

[45] R. Lange, F. Lüthen, U. Beck, J. Rychly, A. Baumann, B. Nebe, Cell-extracellular matrix interaction and physico-chemical characteristics of titanium surfaces depend on the roughness of the material, Biomol. Eng. 19 (2002) 255–261.

[46] W. He, K.E. Gonsalves, N. Batina, D.B. Poker, E. Alexander, M. Hudson, Micro/nanomachining of Polymer Surface for Promoting Osteoblast Cell Adhesion, Biomed. Microdevices. 5 (2003) 101–108.

[47] M.H.P. da Silva, G.A. Soares, C.N. Elias, J.H.C. Lima, H. Schechtman, I.R. Gibson, et al., Surface analysis of titanium dental implants with different topographies, Mater. Res. 3 (2000) 61–67.

[48] K. Gomi, B. Lowenberg, G. Shapiro, J.E. Davies, Resorption of sintered synthetic hydroxyapatite by osteoclasts in vitro, Biomaterials. 14 (1993) 91–6.

[49] J.S. Temenoff, L. Lu, A.G. Mikos, Bone Tissue Engineering Using Synthetic Biodegradable Polymer Scaffolds, Bone Eng. (2000) 454–461.

[50] H. Yuan, Z. Yang, Y. Li, X. Zhang, J.D. De Bruijn, K. De Groot, Osteoinduction by calcium phosphate biomaterials, J. Mater. Sci. Mater. Med. 9 (1998) 723–726.

[51] M. Vallet-Regí, C.V. Ragel, A.J. Salinas, Glasses with Medical Applications, Eur. J. Inorg. Chem. 2003 (2003) 1029–1042.

[52] G. Piotrowski, L.L. Hench, W.C. Allen, G.J. Miller, Mechanical studies of the bone bioglass interfacial bond, J. Biomed. Mater. Res. 9 (1975) 47–61.

[53] J. Zhao, S. Xiao, X. Lu, J. Wang, J. Weng, A study on improving mechanical properties of porous HA tissue engineering scaffolds by hot isostatic pressing, Biomed. Mater. 1 (2006) 188–192.

[54] J.M. Kemppainen, S.J. Hollister, Tailoring the mechanical properties of 3D-designed poly(glycerol sebacate) scaffolds for cartilage applications, J Biomed Mater Res A. 94 (2010) 9–18.

[55] L.G. Griffith, Emerging design principles in biomaterials and scaffolds for tissue engineering, Ann N Y Acad Sci. 961 (2002) 83–95.

[56] Q. Chen, C. Zhu, G. Thouas, Progress and challenges in biomaterials used for bone tissue engineering: bioactive glasses and elastomeric composites, Prog. Biomater. 1 (2012) 2.

[57] J.S. Temenoff, L. Lu, A.G. Mikos, Bone tissue engineering using synthetic biodegradable polymer scaffolds, Bone Eng. (2000) 455–462.

[58] X. Lu, Y. Leng, Theoretical analysis of calcium phosphate precipitation in simulated body fluid, Biomaterials. 26 (2005) 1097–1108.

[59] J.R. Jones, L.M. Ehrenfried, L.L. Hench, Optimising bioactive glass scaffolds for bone tissue engineering, Biomaterials. 27 (2006) 964–73.

[60] D.F. Williams, On the mechanisms of biocompatibility, Biomaterials. 29 (2008) 2941–53.

[61] L.M. Mukundan, R. Nirmal, D. Vaikkath, P.D. Nair, A new synthesis route to high surface area sol gel bioactive glass through alcohol washing: a preliminary study, Biomatter. 3 (2013) 1–10.

[62] S. Bose, M. Roy, A. Bandyopadhyay, Recent advances in bone tissue engineering scaffolds, Trends Biotechnol. 30 (2012) 546–554.

[63] L.S. Nair, C.T. Laurencin, Biodegradable polymers as biomaterials, Prog. Polym. Sci. 32 (2007) 762–798.

[64] J.R. Jones, E. Gentleman, J. Polak, Bioactive Glass Scaffolds for Bone Regeneration, Elements. 3 (2007) 393–399.

[65] Q. Chen, J.A. Roether, A.R. Boccaccini, Tissue engineering scaffolds from bioactive glass and composite materials, Topics in Tissue Engineering [chapter 6], 2008.

[66] L.L. Hench, Bioceramics: From Concept to Clinic, J Am Ceram Soc. 81 (1998) 1705–1728.

[67] I.D. Xynos, A.J. Edgar, L.D. Buttery, L.L. Hench, J.M. Polak, Gene-expression profiling of human osteoblasts following treatment with the ionic products of Bioglass 45S5 dissolution, J. Biomed. Mater. Res. 55 (2001) 151–7.

[68] I.D. Xynos, M. V Hukkanen, J.J. Batten, L.D. Buttery, L.L. Hench, J.M. Polak, Bioglass 45S5 stimulates osteoblast turnover and enhances bone formation In vitro: implications and applications for bone tissue engineering, Calcif. Tissue Int. 67 (2000) 321–9.

[69] P. Saravanapavan, J.R. Jones, R.S. Pryce, L.L. Hench, Bioactivity of gel-glass powders in the CaO-SiO2 system: a comparison with ternary (CaO-P2O5-SiO2) and quaternary glasses (SiO2-CaO-P2O5-Na2O), J. Biomed. Mater. Res. A. 66 (2003) 110–9.

[70] O. Peitl, E. Dutra Zanotto, L.L. Hench, Highly bioactive P2O5–Na2O–CaO–SiO2 glass-ceramics, J. Non. Cryst. Solids. 292 (2001) 115–126.

[71] T. Kokubo, H.M. Kim, M. Kawashita, Novel bioactive materials with different mechanical properties, Biomaterials. 24 (2003) 2161–2175.

[72] T. Kokubo, H. Takadama, How useful is SBF in predicting in vivo bone bioactivity?, Biomaterials. 27 (2006) 2907–2915.

[73] M. Bohner, J. Lemaitre, Can bioactivity be tested in vitro with SBF solution?, Biomaterials. 30 (2009) 2175–9.

[74] L.L. Hench, The story of Bioglass, J. Mater. Sci. Mater. Med. 17 (2006) 967–78.

[75] L.L. Hench, Genetic design of bioactive glass, J. Eur. Ceram. Soc. 29 (2009) 1257–1265.

[76] C. Vitale-Brovarone, M. Miola, C. Balagna, E. Verné, 3D-glass–ceramic scaffolds with antibacterial properties for bone grafting, Chem. Eng. J. 137 (2008) 129–136.

[77] C. Vitale-Brovarone, E. Verné, L. Robiglio, P. Appendino, F. Bassi, G. Martinasso, et al., Development of glass-ceramic scaffolds for bone tissue engineering: characterisation,

proliferation of human osteoblasts and nodule formation, Acta Biomater. 3 (2007) 199–208.

[78] C. Vitale-Brovarone, E. Vernè, M. Bosetti, P. Appendino, M. Cannas, Microstructural and in vitro characterization of SiO2-Na2O-CaO-MgO glass-ceramic bioactive scaffolds for bone substitutes, J. Mater. Sci. Mater. Med. 16 (2005) 909–17.

[79] M.D. O'Donnell, R.G. Hill, Influence of strontium and the importance of glass chemistry and structure when designing bioactive glasses for bone regeneration, Acta Biomater. 6 (2010) 2382–5.

[80] E. Gentleman, Y.C. Fredholm, G. Jell, N. Lotfibakhshaiesh, M.D. O'Donnell, R.G. Hill, et al., The effects of strontium-substituted bioactive glasses on osteoblasts and osteoclasts in vitro, Biomaterials. 31 (2010) 3949–56.

[81] H.B. Pan, X.L. Zhao, X. Zhang, K.B. Zhang, L.C. Li, Z.Y. Li, et al., Strontium borate glass: potential biomaterial for bone regeneration, J. R. Soc. Interface. 7 (2010) 1025–31.

[82] C.-S. Hsi, H.-Z. Cheng, H.-J. Hsu, Y.-S. Chen, M.-C. Wang, Crystallization kinetics and magnetic properties of iron oxide contained 25Li2O–8MnO2–20CaO–2P2O5–45SiO2 glasses, J. Eur. Ceram. Soc. 27 (2007) 3171–3176.

[83] J.J. Blaker, S.N. Nazhat, A.R. Boccaccini, Development and characterisation of silver-doped bioactive glass-coated sutures for tissue engineering and wound healing applications, Biomaterials. 25 (2004) 1319–29.

[84] A.M. El-Kady, R.A. Rizk, B.M. Abd El-Hady, M.W. Shafaa, M.M. Ahmed, Characterization, and antibacterial properties of novel silver releasing nanocomposite scaffolds fabricated by the gas foaming/salt-leaching technique, J. Genet. Eng. Biotechnol. 10 (2012) 229–238.

[85] A. Balamurugan, G. Balossier, D. Laurent-Maquin, S. Pina, A.H.S. Rebelo, J. Faure, et al., An in vitro biological and anti-bacterial study on a sol-gel derived silver-incorporated bioglass system, Dent. Mater. 24 (2008) 1343–51.

[86] J.R.J. Delben, O.M. Pimentel, M.B. Coelho, P.D. Candelorio, L.N. Furini, F. Alencar dos Santos, et al., Synthesis and thermal properties of nanoparticles of bioactive glasses containing silver, J. Therm. Anal. Calorim. 97 (2009) 433–436.

[87] X. Liu, Z. Xie, C. Zhang, H. Pan, M.N. Rahaman, X. Zhang, et al., Bioactive borate glass scaffolds: in vitro and in vivo evaluationn for use as a drug delivery system in the treatment of bone infection, J. Mater. Sci. Mater. Med. 21 (2010) 575–582.

[88] X. Liu, W. Huang, H. Fu, A. Yao, D. Wang, H. Pan, et al., Bioactive borosilicate glass scaffolds: improvement on the strength of glass-based scaffolds for tissue engineering, J. Mater. Sci. Mater. Med. 20 (2009) 365–72.

[89] X. Liu, W. Huang, H. Fu, A. Yao, D. Wang, H. Pan, et al., Bioactive borosilicate glass scaffolds: in vitro degradation and bioactivity behaviors, J. Mater. Sci. Mater. Med. 20 (2009) 1237–43.

[90] E. Munukka, O. Leppäranta, M. Korkeamäki, M. Vaahtio, T. Peltola, D. Zhang, et al., Bactericidal effects of bioactive glasses on clinically important aerobic bacteria, J. Mater. Sci. Mater. Med. 19 (2008) 27–32.

[91] Y. Gu, W. Huang, M.N. Rahaman, D.E. Day, Bone regeneration in rat calvarial defects implanted with fibrous scaffolds composed of a mixture of silicate and borate bioactive glasses, Acta Biomater. 9 (2013) 9126–36.

[92] V. Cannillo, A. Sola, Potassium-based composition for a bioactive glass, Ceram. Int. 35 (2009) 3389–3393.

[93] R.J. Cousins, A role of zinc in the regulation of gene expression, Proc Nutr Soc. 57 (1998) 307–311.

[94] N. Bobkova, S. Khot'ko, Structure of zinc-borate low-melting glasses derived from IR spectroscopy data, J. Appl. Spectrosc. 72 (2005) 853–857.

[95] A. Saranti, I. Koutselas, M.A. Karakassides, Bioactive glasses in the system CaO–B2O3–P2O5: Preparation, structural study and in vitro evaluation, J. Non. Cryst. Solids. 352 (2006) 390–398.

[96] D.E. Day, J.E. White, R.F. Brown, K.D. McMenamin, Transformation of borate glasses into biologically useful materials, Glas. Technol. - Eur. J. Glas. Sci. Technol. Part A. 44 (2003) 75–81.

[97] M.N. Rahaman, W. Liang, D.E. Day, N.W. Marion, G.C. Reilly, J.J. Mao, Preparation and bioactive characteristics of porous borate glass substrates, Ceram. Eng. Sci. Proc. 26 (2005) 3–10.

[98] F. Yang, J. Wang, J. Hou, H. Guo, C. Liu, Bone regeneration using cell-mediated responsive degradable PEG-based scaffolds incorporating with rhBMP-2, Biomaterials. 34 (2013) 1514–28.

[99] W. Holand, W. Vogel, Mechinable and phosphate glass-ceramics, An Introd. to Bioceram. (1993) 125–137.

[100] J.M. Oliveira, R.N. Correia, M.H. Fernandes, Effects of Si speciation on the in vitro bioactivity of glasses, Biomaterials. 23 (2002) 371–9.

[101] Y. Ebisawa, T. Kokubo, K. Ohura, T. Yamamuro, Bioactivity of CaO-SiO2-based glasses:in vitro evaluation, J. Mater. Sci. Mater. Med. 1 (1990) 239–244.

[102] J.. Oliveira, R.. Correia, M.. Fernandes, J. Rocha, Influence of the CaO/MgO ratio on the structure of phase-separated glasses: a solid state ^{29}Si and ^{31}P MAS NMR study, J. Non. Cryst. Solids. 265 (2000) 221–229.

[103] J.M. Oliveira, R.N. Correia, M.H. Fernandes, Surface modifications of a glass and a glass-ceramic of the MgO-3CaO.P2O5-SiO2 system in a simulated body fluid, Biomaterials. 16 (1995) 849–54.

[104] J. Burnie, T. Gilchrist, S. Duff, C. Dtake, N. Harding, A. Malcom, Controlled release glasses (C.R.G.) for biomedical uses, Biomaterials. 2 (1981) 244–246.

[105] I.D. Xynos, M.V.J. Hukkanen, J.J. Batten, L.D. Buttery, L.L. Hench, J.M. Polak, Bioglass (R)45S5 stimulates osteoblast turnover and enhances bone formation in vitro: implications and applications for bone tissue engineering, Calcif Tissue Int. 67 (2000) 321–329.

[106] G. Jell, M.M. Stevens, Gene activation by bioactive glasses, J. Mater. Sci. Mater. Med. 17 (2006) 997–1002.

[107] L.L. Hench, Bioceramics: From Concept to Clinic, J. Am. Ceram. Soc. 74 (1991) 1487–1510.

[108] S. Karatzas, A. Zavras, D. Greenspan, S. Amar, Histologic observations of periodontal wound healing after treatment with PerioGlas in nonhuman primates, Int. J. Periodontics Restorative Dent. 19 (1999) 489–99.

[109] M.G. Ulrich, M.-M. Christian, V. Christian, Ceravital® bioactive glass-ceramics. An Introduction to Bioceramics, World Scientific, 1993.

[110] D.G. Gillam, J.S. Bulman, M.A.J. Eijkman, H.N. Newman, Dentists' perceptions of dentine hypersensitivity and knowledge of its treatment, J. Oral Rehabil. 29 (2002) 219–225.

[111] O. Zinger, G. Zhao, Z. Schwartz, J. Simpson, M. Wieland, D. Landolt, et al., Differential regulation of osteoblasts by substrate microstructural features, Biomaterials. 26 (2005) 1837–1847.

[112] X. Zhu, J. Chen, L. Scheideler, T. Altebaeumer, J. Geis-Gerstorfer, D. Kern, Cellular reactions of osteoblasts to micron- and submicron-scale porous structures of titanium surfaces, Cells Tissues Organs. 178 (2004) 13–22.

[113] O. Zinger, G. Zhao, Z. Schwartz, J. Simpson, M. Wieland, D. Landolt, et al., Differential regulation of osteoblasts by substrate microstructural features, Biomaterials. 26 (2005) 1837–47.

[114] I.A. Silver, J. Deas, M. Erecińska, Interactions of bioactive glasses with osteoblasts in vitro: Effects of 45S5 Bioglass(®), and 58S and 77S bioactive glasses on metabolism, intracellular ion concentrations and cell viability, Biomaterials. 22 (2001) 175–185.

[115] I. Ochoa, J.A. Sanz-Herrera, J.M. García-Aznar, M. Doblaré, D.M. Yunos, A.R. Boccaccini, Permeability evaluation of 45S5 Bioglass-based scaffolds for bone tissue engineering., J. Biomech. 42 (2009) 257–260.

[116] G.E. Vargas, R.V. Mesones, O. Bretcanu, J.M.P. López, A.R. Boccaccini, A. Gorustovich, Biocompatibility and bone mineralization potential of 45S5 Bioglass-derived glass-ceramic scaffolds in chick embryos, Acta Biomater. 5 (2009) 374–80.

[117] O. Bretcanu, C. Samaille, A.R. Boccaccini, Simple methods to fabricate Bioglass®-derived glass–ceramic scaffolds exhibiting porosity gradient, J. Mater. Sci. 43 (2008) 4127–4134.

[118] Q.Z. Chen, I.D. Thompson, A.R. Boccaccini, 45S5 Bioglass®-derived glass–ceramic scaffolds for bone tissue engineering, Biomaterials. 27 (2006) 2414–2425.

[119] Q.-Z. Chen, K. Rezwan, V. Françon, D. Armitage, S.N. Nazhat, F.H. Jones, et al., Surface functionalization of Bioglass-derived porous scaffolds, Acta Biomater. 3 (2007) 551–62.

[120] Q. Fu, M.N. Rahaman, B.S. Bal, L.F. Bonewald, K. Kuroki, R.F. Brown, Silicate, borosilicate, and borate bioactive glass scaffolds with controllable degradation rate for bone tissue engineering applications. II. In vitro and in vivo biological evaluation, J Biomed Mater Res A. 95A (2010) 172–179.

[121] B.S. Miguel, R. Kriauciunas, S. Tosatti, M. Ehrbar, C. Ghayor, M. Textor, et al., Enhanced osteoblastic activity and bone regeneration using surface-modified porous bioactive glass scaffolds, J. Biomed. Mater. Res. Part A. 94A (2010) 1023–1033.

[122] L.-C. Gerhardt, A.R. Boccaccini, Bioactive Glass and Glass-Ceramic Scaffolds for Bone Tissue Engineering, Materials (Basel). 3 (2010) 3867–3910.

[123] M. Navarro, S. del Valle, S. Martínez, S. Zeppetelli, L. Ambrosio, J.A. Planell, et al., New macroporous calcium phosphate glass ceramic for guided bone regeneration, Biomaterials. 25 (2004) 4233–41.

[124] Q. Fu, E. Saiz, A.P. Tomsia, Bioinspired Strong and Highly Porous Glass Scaffolds., Adv. Funct. Mater. 21 (2011) 1058–1063.

[125] N. Li, Q. Jie, S. Zhu, R. Wang, Preparation and characterization of macroporous sol–gel bioglass, Ceram. Int. 31 (2005) 641–646.

[126] C. Wang, T. Kasuga, M. Nogami, Macroporous calcium phosphate glass-ceramic prepared by two-step pressing technique and using sucrose as a pore former, J. Mater. Sci. Mater. Med. 16 (2005) 739–44.

[127] S.K. Nandi, B. Kundu, S. Datta, D.K. De, D. Basu, The repair of segmental bone defects with porous bioglass: an experimental study in goat., Res. Vet. Sci. 86 (2009) 162–73.

[128] J.R. Jones, G. Poologasundarampillai, R.C. Atwood, D. Bernard, P.D. Lee, Non-destructive quantitative 3D analysis for the optimisation of tissue scaffolds, Biomaterials. 28 (2007) 1404–13.

[129] R.F. Brown, D.E. Day, T.E. Day, S. Jung, M.N. Rahaman, Q. Fu, Growth and differentiation of osteoblastic cells on 13-93 bioactive glass fibers and scaffolds, Acta Biomater. 4 (2008) 387–96.

[130] X. Liu, M.N. Rahaman, Q. Fu, Oriented bioactive glass (13-93) scaffolds with controllable pore size by unidirectional freezing of camphene-based suspensions: Microstructure and mechanical response, Acta Biomater. 7 (2011) 406–16.

[131] Q. Fu, M.N. Rahaman, B. Sonny Bal, R.F. Brown, D.E. Day, Mechanical and in vitro performance of 13–93 bioactive glass scaffolds prepared by a polymer foam replication technique, Acta Biomater. 4 (2008) 1854–1864.

[132] V. Aina, G. Malavasi, A. Fiorio Pla, L. Munaron, C. Morterra, Zinc-containing bioactive glasses: surface reactivity and behaviour towards endothelial cells, Acta Biomater. 5 (2009) 1211–22.

[133] C. Renghini, A. Giuliani, S. Mazzoni, F. Brun, E. Larsson, F. Baino, et al., Microstructural characterization and in vitro bioactivity of porous glass-ceramic scaffolds for bone regeneration by synchrotron radiation X-ray microtomography, J. Eur. Ceram. Soc. 33 (2013) 1553–1565.

[134] C. Vitale-Brovarone, F. Baino, M. Miola, R. Mortera, B. Onida, E. Verné, Glass-ceramic scaffolds containing silica mesophases for bone grafting and drug delivery., J. Mater. Sci. Mater. Med. 20 (2009) 809–20.

[135] C.V. Brovarone, E. Verné, P. Appendino, Macroporous bioactive glass-ceramic scaffolds for tissue engineering, J. Mater. Sci. Mater. Med. 17 (2006) 1069–1078.

[136] Q.Z. Chen, K. Rezwan, D. Armitage, S.N. Nazhat, A.R. Boccaccini, The surface functionalization of 45S5 Bioglass (R)-based glass-ceramic scaffolds and its impact on bioactivity, J Mater Sci-Mater Med. 11 (2006) 979 – 87.

[137] Q.Z. Chen, A. Efthymiou, V. Salih, A.R. Boccaccini, Bioglass-derived glass-ceramic scaffolds: study of cell proliferation and scaffold degradation in vitro, J. Biomed. Mater. Res. A. 84 (2008) 1049–60.

[138] C. Vitale-Brovarone, F. Baino, E. Verné, High strength bioactive glass-ceramic scaffolds for bone regeneration., J. Mater. Sci. Mater. Med. 20 (2009) 643–53.

[139] C. Renghini, V. Komlev, F. Fiori, E. Verné, F. Baino, C. Vitale-Brovarone, Micro-CT studies on 3-D bioactive glass-ceramic scaffolds for bone regeneration, Acta Biomater. 5 (2009) 1328–37.

[140] L. Moimas, M. Biasotto, R. Di Lenarda, A. Olivo, C. Schmid, Rabbit pilot study on the resorbability of three-dimensional bioactive glass fibre scaffolds, Acta Biomater. 2 (2006) 191–9.

[141] M.N. Rahaman, D.E. Day, R.F. Brown, F. Q., S.. Jung, Advances in Bioceramics and Porous Ceramics, John Wiley & Sons, Inc., Hoboken, NJ, USA, 2008.

[142] A. Yao, D. Wang, W. Huang, Q. Fu, M.N. Rahaman, D.E. Day, In vitro bioactive characteristics of borate-based glasses with controllable degradation behavior, J Am Ceram Soc. 90 (2007) 303–306.

[143] Q. Fu, M.N. Rahaman, B.S. Bal, R.F. Brown, Preparation and in vitro evaluation of bioactive glass (13-93) scaffolds with oriented microstructures for repair and regeneration of load-bearing bones., J. Biomed. Mater. Res. A. 93 (2010) 1380–90.

[144] S. Eqtesadi, A. Motealleh, A. Pajares, P. Miranda, Effect of milling media on processing and performance of 13-93 bioactive glass scaffolds fabricated by robocasting, Ceram. Int. 41 (2015) 1379–1389.

[145] S. Midha, T.B. Kim, W. van den Bergh, P.D. Lee, J.R. Jones, C.A. Mitchell, Preconditioned 70S30C bioactive glass foams promote osteogenesis in vivo, Acta Biomater. 9 (2013) 9169–82.

[146] T. Livingston, P. Ducheyne, J. Garino, In vivo evaluation of a bioactive scaffold for bone tissue engineering, J Biomed Mater Res. 62 (2002) 1–13.

[147] S. Deb, R. Mandegaran, L. Di Silvio, A porous scaffold for bone tissue engineering/45S5 Bioglass derived porous scaffolds for co-culturing osteoblasts and endothelial cells, J. Mater. Sci. Mater. Med. 21 (2010) 893–905.

[148] D. Bellucci, V. Cannillo, A. Sola, F. Chiellini, M. Gazzarri, C. Migone, Macroporous Bioglass®-derived scaffolds for bone tissue regeneration, Ceram. Int. 37 (2011) 1575–1585.

[149] S.-C. Wu, H.-C. Hsu, S.-H. Hsiao, W.-F. Ho, Preparation of porous 45S5 Bioglass-derived glass-ceramic scaffolds by using rice husk as a porogen additive, J. Mater. Sci. Mater. Med. 20 (2009) 1229–36.

[150] S.K. Ghosh, S.K. Nandi, B. Kundu, S. Datta, D.K. De, S.K. Roy, et al., In vivo response of porous hydroxyapatite and beta-tricalcium phosphate prepared by aqueous solution combustion method and comparison with bioglass scaffolds, J. Biomed. Mater. Res. B. Appl. Biomater. 86 (2008) 217–27.

[151] W. Liang, C. Rüssel, Resorbable, porous glass scaffolds by a salt sintering process, J. Mater. Sci. 41 (2006) 3787–3792.

[152] J. Vogel, W. Liang, C. Rüssel, Porous glasses by a salt sintering process, Porous Spec. Glas. 57 (1998) 105–111.

[153] T.S. Huang, M.N. Rahaman, N.D. Doiphode, M.C. Leu, B.S. Bal, D.E. Day, et al., Porous and strong bioactive glass (13–93) scaffolds fabricated by freeze extrusion technique, Mater. Sci. Eng. C. 31 (2011) 1482–1489.

[154] D.C. Clupper, J.E. Gough, P.M. Embanga, I. Notingher, L.L. Hench, Bioactive evaluation of 45S5 bioactive glass fibres and preliminary study of human osteoblast attachment. J. Mater. Sci. Mater. Med. (2004) 803–808.

[155] E. Pirhonen, L. Moimas, J. Haapanen, Porous Bioactive 3-D Glass Fiber Scaffolds for Tissue Engineering Applications Manufactured by Sintering Technique, Key Eng. Mater. 240-242 (2002) 237–240.

[156] P. Sepulveda, J.R. Jones, L.L. Hench, Bioactive sol-gel foams for tissue repair, J. Biomed. Mater. Res. 59 (2002) 340–8.

[157] H. Yuan, J.D. de Bruijn, X. Zhang, C.A. van Blitterswijk, K. de Groot, Bone induction by porous glass ceramic made from Bioglass (45S5), J. Biomed. Mater. Res. 58 (2001) 270–6.

[158] T. Qu, X. Liu, Nano-structured gelatin/bioactive glass hybrid scaffolds for the enhancement of odontogenic differentiation of human dental pulp stem cells, J. Mater. Chem. B. 1 (2013) 4764.

[159] C. Soundrapandian, A. Mahato, B. Kundu, S. Datta, B. Sa, D. Basu, Development and effect of different bioactive silicate glass scaffolds: In vitro evaluation for use as a bone drug delivery system, J. Mech. Behav. Biomed. Mater. 40C (2014) 1–12.

[160] E.A. Scott, M.D. Nichols, R. Kuntz-Willits, D.L. Elbert, Modular scaffolds assembled around living cells using poly(ethylene glycol) microspheres with macroporation via a non-cytotoxic porogen, Acta Biomater. 6 (2010) 29–38.

[161] M.M. Ristić, S.Đ. Milosević, Frenkel's theory of sintering, Sci. Sinter. 38 (2006) 7–11.

[162] J. Frenkel, Viscous flow of crystalline bodies under the action of surface tension, J. Phys. 9 (1945) 385–391.

[163] M.N. Rahaman, L.C. De Jonghe, G.W. Scherer, R.J. Brook, Creep and Densification During Sintering of Glass Powder Compacts, J. Am. Ceram. Soc. 70 (1987) 766–774.

[164] G.W. SCHERER, Sintering of Low-Density Glasses: I, Theory, J. Am. Ceram. Soc. 60 (1977) 236–239.

[165] J.K. Mackenzie, R. Shuttleworth, A Phenomenological Theory of Sintering, Proc. Phys. Soc. Sect. B. 62 (1949) 833–852.

[166] M.O. Prado, E.D. Zanotto, Glass sintering with concurrent crystallization, Comptes Rendus Chim. 5 (2002) 773–786.

[167] R.M. German, Fundamentals of sintering, ASM Int. Eng. Mater. Handb. 4 (1991) 260–269.

[168] D.A. Venkatu, D.L. Johnson, Analysis of Sintering Equations Pertaining to Constant Rates of Heating, J. Am. Ceram. Soc. 54 (1971) 641–641.

[169] E.M. Rabinovich, Preparation of glass by sintering, J. Mater. Sci. 20 (1985) 4259–4297.

[170] I.B. Cutler, R.E. Henrichsen, Effect of Particle Shape on the Kinetics of Sintering of Glass, J. Am. Ceram. Soc. 51 (1968) 604–604.

[171] P.M. Raj, A. Odulena, W.R. Cannon, Anisotropic shrinkage during sintering of particle-oriented systems—numerical simulation and experimental studies, Acta Mater. 50 (2002) 2559–2570.

[172] Z. Fu, A. Dellert, M. Lenhart, A. Roosen, Effect of pore orientation on anisotropic shrinkage in tape-cast products, J. Eur. Ceram. Soc. 34 (2014) 2483–2495.

[173] E.A. Giess, J.P. Fletcher, L.W. Herron, Isothermal sintering of cordierite-type glass powders, J. Am. Ceram. Soc. 67 (1984) 549–552.

[174] A.R. Boccaccini, G. Ondracek, Viscous sintering of non-spherical borosilicate-glass powder, Glas. Berichte. 65 (1992) 73–78.

[175] O. Guillon, S. Cao, J. Chang, L. Wondraczek, A.R. Boccaccini, Effect of uniaxial load on the sintering behaviour of 45S5 Bioglass® powder compacts, J. Eur. Ceram. Soc. 31 (2011) 999–1007.

[176] A.R. Boccaccini, E.A. Olevsky, Anisotropic shrinkage during sintering of glass-powder compacts under uniaxial stresses: Qualitative assessment of experimental evidence, Metall. Mater. Trans. A. 28 (1997) 2397–2404.

[177] H. Yuan, J.D. de Bruijn, X. Zhang, C.A. van Blitterswijk, K. de Groot, Bone induction by porous glass ceramic made from Bioglass® (45S5), J. Biomed. Mater. Res. 58 (2001) 270–276.

[178] O. Peitl, E. Dutra Zanotto, L.L. Hench, Highly bioactive P2O5–Na2O–CaO–SiO2 glass-ceramics, J. Non. Cryst. Solids. 292 (2001) 115–126.

[179] D.C. Clupper, L.L. Hench, Crystallization kinetics of tape cast bioactive glass 45S5, J. Non. Cryst. Solids. 318 (2003) 43–48.

[180] A.S. Rizkalla, D.W. Jones, D.B. Clarke, G.C. Hall, Crystallization of experimental bioactive glass compositions, J. Biomed. Mater. Res. 32 (1996) 119–24.

[181] A. Karamanov, M. Pelino, Sinter-crystallization in the diopside–albite system, J. Eur. Ceram. Soc. 26 (2006) 2519–2526.

[182] I.R. Oliveira, A.R. Studart, R.G. Pillegi, V.C. Pandolfelli, Dispersao e empacotamento de partículas: princípios e aplicaçoes em processamento cerâmico, Fazendo Arte, 2000.

[183] T. Yamamuro, K. Shimizu, Clinical application of AW glass ceramic prosthesis in spinal surgery, Nihon Seikeigeka Gakkai Zasshi. 68 (1994) 505–15.

[184] P.N. De Aza, A.H. De Aza, P. Pena, S. De Aza, Vidrios y Vitrocerámicos Bioactivos, Boletín La Soc. Española Cerámica Y Vidr. 46 (2011) 45–55.

[185] T. Kitsugi, T. Nakamura, T. Yamamura, T. Kokubu, T. Shibuya, M. Takagi, SEM-EPMA observation of three types of apatite-containing glass-ceramics implanted in bone: the variance of a Ca-P-rich layer, J. Biomed. Mater. Res. 21 (1987) 1255–71.

[186] D.C. Clupper, L.L. Hench, Crystallization kinetics of tape cast bioactive glass 45S5, J. Non. Cryst. Solids. 318 (2003) 43–48.

[187] J. Massera, S. Fagerlund, L. Hupa, M. Hupa, Crystallization Mechanism of the Bioactive Glasses, 45S5 and S53P4, J. Am. Ceram. Soc. 95 (2012) 607–613.

[188] P. Li, Q. Yang, F. Zhang, T. Kokubo, The effect of residual glassy phase in a bioactive glass-ceramic on the formation of its surface apatite layer in vitro, J Mater Sci Mater Med. 3 (1992) 452–456.

[189] O. Peitl Filho, G.P. LaTorre, L.L. Hench, Effect of crystallization on apatite-layer formation of bioactive glass 45S5, J. Biomed. Mater. Res. 30 (1996) 509–14.

[190] D.C. Clupper, J.J. Mecholsky, G.P. LaTorre, D.C. Greenspan, Bioactivity of tape cast and sintered bioactive glass-ceramic in simulated body fluid, Biomaterials. 23 (2002) 2599–606.

[191] D.C. Clupper, J.J. Mecholsky, G.P. LaTorre, D.C. Greenspan, Sintering temperature effects on the in vitro bioactive response of tape cast and sintered bioactive glass-ceramic in Tris buffer, J. Biomed. Mater. Res. 57 (2001) 532–40.

[192] K. Rezwan, Q.Z. Chen, J.J. Blaker, A.R. Boccaccini, Biodegradable and bioactive porous polymer/inorganic composite scaffolds for bone tissue engineering, Biomaterials. 27 (2006) 3413–3431.

[193] A.R. Boccaccini, Q. Chen, L. Lefebvre, L. Gremillard, J. Chevalier, Sintering, crystallisation and biodegradation behaviour of Bioglass®-derived glass–ceramics, Faraday Discuss. 136 (2007) 27.

[194] E. Vernè, S. Ferraris, C. Vitale-Brovarone, A. Cochis, L. Rimondini, Bioactive glass functionalized with alkaline phosphatase stimulates bone extracellular matrix deposition and calcification in vitro, Appl. Surf. Sci. 313 (2014) 372–381.

[195] H.F. Hildebrand, N. Blanchemain, G. Mayer, F. Chai, M. Lefebvre, F. Boschin, Surface coatings for biological activation and functionalization of medical devices, Surf. Coatings Technol. 200 (2006) 6318–6324.

[196] B. Arkles, Hydrophobicity Hydrophilicity and Silanes, Gelest Inc., Morrisville, PA. (2006).

[197] S. Joughehdoust, A. Behnamghader, M. Imani, M. Daliri, A.H. Doulabi, E. Jabbari, A novel foam-like silane modified alumina scaffold coated with nano-hydroxyapatite–poly(ε-caprolactone fumarate) composite layer, Ceram. Int. 39 (2013) 209–218.

[198] F. Avilés, C.A. Sierra-Chi, A. Nistal, A. May-Pat, F. Rubio, J. Rubio, Influence of silane concentration on the silanization of multiwall carbon nanotubes, Carbon N. Y. 57 (2013) 520–529.

[199] H.S. Mansur, R.L. Oréfice, W.L. Vasconcelos, Z.P. Lobato, L.J.C. Machado, Biomaterial with chemically engineered surface for protein immobilization, J. Mater. Sci. Mater. Med. 16 (2005) 333–40.

[200] A. Krishnan, Y.-H. Liu, P. Cha, R. Woodward, D. Allara, E.A. Vogler, An evaluation of methods for contact angle measurement, Colloids Surfaces B Biointerfaces. 43 (2005) 95–98.

[201] L.M. Alonso, J.Á.D. García-Menocal, M.T. Aymerich, J.Á.Á. Guichard, M. García-Vallés, S.M. Manent, et al., Calcium phosphate glasses: Silanation process and effect on the bioactivity behavior of glass-PMMA composites, J. Biomed. Mater. Res. B. Appl. Biomater. 102 (2013) 205–13.

[202] J.A. Howarter, J.P. Youngblood, Optimization of silica silanization by 3-aminopropyltriethoxysilane, Langmuir. 22 (2006) 11142–7.

[203] M. Zhu, M.Z. Lerum, W. Chen, How to prepare reproducible, homogeneous, and hydrolytically stable aminosilane-derived layers on silica, Langmuir. 28 (2012) 416–23.

[204] K. Sterzynska, J. Budna, E. Frydrych-Tomczak, G. Hreczycho, A. Malinska, H. Maciejewski, et al., Silane-modified surfaces in specific antibody-mediated cell recognition, Folia Histochem. Cytobiol. 52 (2014) 250–5.

[205] E. Verné, S. Ferraris, C. Vitale-Brovarone, S. Spriano, C.L. Bianchi, A. Naldoni, et al., Alkaline phosphatase grafting on bioactive glasses and glass ceramics, Acta Biomater. 6 (2010) 229–40.

[206] E. Verné, S. Ferraris, C. Vitale-Brovarone, S. Spriano, C.L. Bianchi, M. Morra, et al., Surface Functionalization of Biomaterials with Alkaline Phosphatase, in: Key Eng. Mater., 2008: pp. 593–596.

[207] E. Verné, C. Vitale-Brovarone, E. Bui, C.L. Bianchi, A.R. Boccaccini, Surface functionalization of bioactive glasses, J. Biomed. Mater. Res. A. 90 (2009) 981–92.

[208] Q.Z. Chen, K. Rezwan, D. Armitage, S.N. Nazhat, A.R. Boccaccini, The surface functionalization of 45S5 Bioglass-based glass-ceramic scaffolds and its impact on bioactivity, J. Mater. Sci. Mater. Med. 17 (2006) 979–87.

[209] R.F.S. Lenza, J.R. Jones, W.L. Vasconcelos, L.L. Hench, In vitro release kinetics of proteins from bioactive foams, J. Biomed. Mater. Res. A. 67 (2003) 121–9.

[210] M.R. Filgueiras, G. La Torre, L.L. Hench, Solution effects on the surface reactions of a bioactive glass, J. Biomed. Mater. Res. 27 (1993) 445–53.

[211] T. Kokubo, H. Kushitani, S. Sakka, T. Kitsugi, T. Yamamuro, Solutions able to reproduce in vivo surface-structure changes in bioactive glass-ceramic A-W3, J. Biomed. Mater. Res. 24 (1990) 721–734.

[212] D. Rohanová, A.R. Boccaccini, D.M. Yunos, D. Horkavcová, I. Březovská, A. Helebrant, TRIS buffer in simulated body fluid distorts the assessment of glass-ceramic scaffold bioactivity, Acta Biomater. 7 (2011) 2623–2330.

[213] T.R. Zeitler, A.N. Cormack, Interaction of water with bioactive glass surfaces, J. Cryst. Growth. 294 (2006) 96–102.

Chapter III

"Always do what you are afraid to do."

Ralph Waldo Emerson (1803-1882)

The present chapter deals with the experimental procedures and techniques used in the course of this work. Each of the following seven chapters has a section on "Materials and Methods", but due to constraints of article length, this section is short. A description of the experimental aspects from the production of the glasses, sample preparation and sample characterization is presented.

Chapter III

Materials and Methods

III.1. Materials

In this thesis four compositions of calcium phosphate glasses were produced which are presented in Table III.1.

Table III.1. Glass composition (mol. %).

mol. %	CaO	P_2O_5	SiO_2	MgO	Na_2O
G31N0	32.68	10.89	25.43	31.00	-
G29N2	32.68	10.89	25.43	29.45	1.55
G28N3	32.68	10.89	25.43	27.90	3.10
G25N6	32.68	10.89	25.43	24.80	6.20

The glasses were prepared by melting mixtures of carbonates and different oxides in platinum crucibles at temperatures between 1400 and 1550 °C using an electrically heated furnace. The melt was kept at this temperature, for 2 h, to ensure the attainment of high homogeneity.
All the reagents presented analytical purity and were not submitted to further purification Table III.2.

Table III.2. Reagents and purity.

Reagents	Suppliers	Purity
SiO_2	Fluka	99.9 %
MgO	Fluka	99.9%
$CaCO_2$	Fluka	99.9%
$Ca(H_2PO_4)_2.H_2O$	Fluka	≥99%
Na_2CO_3	Sigma	≥99.5%
NaCl	BDH	≥99%

A water soluble salt, sodium chloride, supplied by BDH, having a purity of 99 % was used as porogen for the production of scaffolds. The function of the salt is to act as an intermediary phase among the glass particles, being easily removed by dissolution after the thermal consolidation of the part.

III.2. Sample preparation

Glasses were prepared in both bulk and frit form.

III.2.1. Bulk samples

The bulks were obtained by pouring the melt into a stainless steel plate to obtain glass blocks followed by glass annealing at temperatures above Tg, for 30 minutes, and then slow cooled to room temperature. The dimensions of the blocks were approximately 40 × 30 × 7 mm^3. The annealed bulk glass samples were cut into slices (~4mm thickness) using a low speed (275 rpm) diamond saw (Buehler ISOMET 1000 Precision Saw). The slices were cleaned in an ultrasonic bath with alcohol for 15 minutes.

III.2.2. Glass powder

The glass powders were produced from glass frits, which were obtained by quenching the glass melts in cold water. The frits were dried in a heating chamber at 60 ° C, then milled for 20 to 30 min, depending on the composition and particle size distribution, in an agate mill, and sieved in order to obtain a fine powder with particle size ≤ 20 μm.

III.2.3. Glass powder compacts

Rectangular bars (5 x 5 x 10 cm^3) with a green density of 1.60 ± 0.01 (corresponding to 0.60 of relative density) were obtained by uniaxial pressing at 175 MPa, for 30 s, using a hydraulic press (CARVER Laboratory Press – Model C).

The samples were sintered up to 850 ºC, in non-isothermal conditions.

Some glass compact samples have been mounted in thermosetting resin (before and after sintering) and dried in air atmosphere. After mounting, the glass sintered compact samples were ground with abrasives in order to obtain the desired surface finishing. After that, a fine polishing was performed using 6, 3 and 1µm diamond pastes, for further microstructural studies.

III.2.4. Glass scaffolds

Glass-salt mixtures with NaCl average particle sizes in the range of 212-500 µm, and varying weight contents (0, 10, 30, 50, 60, 70, 90 and 100 wt. %) were mechanical mixed, during 15 min, in a turbula shaker-mixer, from Glen Mils, USA. The weight amount of the glass and salt powder in the mixture was estimated using the rule of the mixtures of binary composites.

Before sintering, the mixture powders were uniaxially pressed in a 10 mm diameter die. Cylindrical glass/salt compacts with an initial geometrical density of 1.60 ± 0.02 $g.cm^{-3}$ were obtained by uniaxially pressing at 175 MPa.

The best conditions for thermal cycling were established from the dilatometric curves.

After sintering, the salt crystals were leached using distilled stirring water at 30 ºC for 1 day to form the scaffold pores. The water was changed at intervals of 1 hour for the first 6 h and approximately 2 h for the remaining immersion time.

The pore size can be controlled by the size of the salt crystals, and the porosity by the glass/salt weight ratio. The samples weight was recorded after and before sintering, in order to control the salt losses and ensure that all the salt had been leached to avoid unexpected impact on cells in future studies.

III.2.5. Glass-ceramic bulk and scaffolds crystallization

Bulk and scaffolds glass-ceramics samples were prepared following a one-stage crystallisation process. The glass samples were heated at 5 ºC min^{-1} up to the optimum crystallisation temperature, as revealed by DTA studies, and held for the optimum crystallisation time. After heat treatment, the bulk samples were polished with diamond pastes of 15, 6, 3 and 1µm particle size.

III.3. Samples Characterization

III.3.1. Powders particle size distribution and specific surface area

In order to determine the morphological characteristics of the glass powders, powder particle size distributions were carried out by a laser particle size Coulter LS Particle Size Analyser 230, Fraunhofer optical model, Amherst, MA. The particle size distribution of the sodium chloride was carried out by sieving with cuts at 212 and 500 micrometres.

The specific surface area of the glass powders, salt and scaffolds were determined by physical adsorption of nitrogen gas, using the Brunauer, Emmett and Teller (BET) method. For those tests, a Quantachrome Quantasorb equipment, Germany, was used, and before determining the volume of adsorbed gas, samples were kept under vacuum at 200 °C, for 4 h.

III.3.2. Density

The real powder density of glass powders was determined by helium pycnometry (Accupyc 1330 pycnometer).

The density of the $CaO–P_2O_5–SiO_2–MgO$ glass system compacts, at given temperatures during sintering, was determined from the green density and the measured shrinkage using the relation, given by Eq. III.1,

$$\rho = \frac{\rho_0}{((1-\Delta a/a_0)^2\,(1-\Delta h/h_0))} \qquad \text{(Eq. III.1)}$$

where h and a are the length and width of the samples.

The final density of the sintered compacts was also determined by using the Archimedes principle.

The green density of the glass/salt mixtures was geometrically measured. The theoretic density of the glass/salt mixture was estimated using the rule of the mixtures, equation III.2,

$$\frac{1}{\rho_{t,m}} = \frac{f_{salt}}{\rho_{salt}} + \frac{f_{fr}}{\rho_{fr}} \qquad \text{(Eq. III.2)}$$

where $\rho_{t,m}$- theoretic mixture density, ρ_{salt} – salt density, ρ_{fr} - *glass density*, f_{fr} - glass powder volume fraction and f_{salt} - salt powder volume fraction.

The apparent scaffold density of the sintered scaffolds was determined geometrically.

III.3.3. Thermal analysis

Differential thermal analysis (DTA) of the glasses and of the salt was performed at a constant heating rate of 5 ºC min^{-1} in a SETARAM LABSYS equipment, in order to identify the nature of the reactions that occur during heating and the corresponding temperatures. For the glass system $CaO–P_2O_5–SiO_2–MgO$, this analysis was performed within a range of heating rates from 5 to 40 °C min^{-1} to study the crystallization mechanism and calculate the relevant parameters associated. The onset of crystallization peak temperature (Tc), the crystallization peak temperature (Tp) and the heating rate (β) were used to discern the crystallization behaviour of glasses in this system.

Dilatometry allows the in-situ monitoring of any sample dimensional changes with the temperature variation. It was performed on pressed glass, salt and glass/salt mixture powders. This characterization was done up to 1000 °C, at constant heating rate conditions in a horizontal Bahr Thermo Dilatometer DIL801L, Hüllhorst, Germany. For the glass system $CaO–P_2O_5–SiO_2–MgO$, this analysis was performed within a range of heating rates from 5 to 20 °C min^{-1} to study the crystallization mechanism and calculate relevant parameters associated.
The mean values and the standard deviations (SD) presented for the thermal expansion coefficient (CTE) determined for all glasses in the studied compositions, have been obtained from the characterization on each of three samples, using compact powders (10 mm diameter and 5 mm thick).

III.3.4. X-ray diffraction (XRD)

The crystallographic characterization was performed at room temperature in a Geigerflex powder diffractometer Rigaku D / Max SérieC equipped with a curved graphite monochromator using CuKα radiation (at 40 kV and 40 mA) and a scan speed of 0.02º s^{-1}. The X-ray diffraction (XRD) technique was used to evaluate the presence of crystalline phases in the powder compacts. The identification of crystalline phases was made using the base PDF (Powder Diffraction File) data provided by JCPDS / ICDD (Joint Committee on Powder Diffraction Standards / International Centre for Diffraction Data, Swarthmore, Pennsylvania, USA).

The amount of the crystalline phase (crystallized volume fraction) contained in the glass-ceramic bulk and scaffold samples was determined according to the procedure used by Krimm and Tobolsky [1]. The percent crystallinity, CI, was calculated by the ratio of the crystalline area, CA, present in the diffractogram of the glass-ceramics and the total area, TA (amorphous + crystalline), present in this diffractogram using Eq. III.3 [2]:

$$CI = (CA/TA) \times 100 \qquad \text{(Eq. III.3)}$$

III.3.5. High temperature X-ray diffraction (HT-XRD)

The formation of the crystalline phases within the glass powder was also followed by high temperature X-ray diffraction (HT-XRD) using a Philips X'Pert diffractometer, model MRD and also Cu-Ka radiation. Data were collected in a continuous scan type from 10º to 70º, with a step size of 0.02º and a counting time of 1 s per step. The in situ analysis was performed on glass powders each 10 ºC while being heated in air, from 770 to 900 ºC, using a heating rate of 10 ºC min^{-1} and a dwell time of 45 min per scan.

III.3.6. Infrared spectroscopy (FTIR)

Fourier Transform Infrared Spectroscopy provides information about the chemical bonding or molecular structure of materials. The spectra were collected using a FTIR, Brucker tensor 27. For this purpose, the glass powder and scaffolds (reduced to powder) samples were mixed with KBr (ratio 1:10) and pressed into a pellet using a hand press.

The FTIR spectra of the bulk samples was recorded using a Golden Gate single reflection diamond ATR system, with no need for sample preparation.

All spectra were collected over a region of 4000–400 cm^{-1} and are the average of two independent measurements with 256 scans at a resolution of 4 cm^{-1}.

III.3.7. Magic angle spinning-Nuclear magnetic resonance (MAS-NMR)

Glasses containing 6 and 0 % sodium oxide were investigated by ^{29}Si nuclear magnetic resonance (MAS-NMR) spectroscopy to determine the distributions of SiO_4 structural units, Q_n, where *n* is the number of bridging oxygen atoms bound to other Si atoms, as a function of composition. ^{29}Si MAS-NMR spectra were recorded on a Bruker ASX 400 spectrometer operating at 79.52 MHz (9.4 T) using a 7 mm probe at a spinning rate of 5 kHz. The pulse length was 2 μs and a 60s delay time was used. Kaolinite was used as the chemical shift reference.

III.3.8. Beam bending method - Viscosity

Viscosity, η, is probably one of the most important properties in glass making because it strongly influences the melting, fining and pouring conditions of the glass. During glass forming processes the viscosity must be tightly controlled to maintain a high product quality. A three point beam bending method was used to evaluate the viscosity. The measurements were performed in a Bahr Thermo analyse equipment (type 401), carried out under a stress of 0.45 MPa at 10 ºC min^{-1}, in the

glass transition range as described in ISO 7884-4 [3] and ASTM C1350 [4]. These analysis were performed in the Otto Schott Institute of Materials Research (OSIM) at the Friedrich Schiller University of Jena, Germany.

III.3.9. Scanning electron microscopy (SEM)

Scanning electron microscopy (SEM) was the technique utilized to perform the microstructural characterization of all samples. The SEM equipment used is a Hitachi, Model SU-70, with a maximum acceleration potential of 25 KeV and a resolution of 15Å, coupled with X-ray energy dispersive spectroscopy (EDS).

For glass powders observation, a drop of powder suspension in 2-propanol (0.1g/10ml) was deposited on aluminum sample holders further dried at 60 °C.

Sodium chloride powders were deposited on a double-sided carbon tape-adhesive.

The crystalline phases were observed by SEM using fracture surfaces of the compacts and scaffolds, under HCl acid attack for 3 seconds. All compact and bulk samples were fixed with glue carbon (Neubauer Chemikalien, Münster, Germany).

All samples were coated with a thin carbon film by deposition on Emitech K950 equipment. The elemental compositions of the samples were qualitatively identified by EDS in the SEM.

III.3.10. ImageJ analysis

ImageJ is a Java based image processing and analysis software developed by the U. S. National Institutes of Health, of public domain (available from http://imagej.nih.gov/). Parameters like grain size, median aspect ratio (defined as the major axis divided by the minor axis) and orientation distribution were determined through image analysis of SEM micrographs, using the ImageJ freeware, as detailed in Chapter IV. Editing functions used comprise contrast manipulation, sharpening, and edge detection. The calculation of area and pixel value statistics were performed using analysis functions.

To perform the image analysis, SEM micrographs were generally modified in the following way: contrast enhancement, median filtering and thresholding to obtain suitable binary images, Fig. III.1. The particles' sections were manually drawn and evaluated before and after thresholding to avoid errors in particles' area, Fig. III.1b. An elliptical shape was assumed for the quantitative analysis of grain shape and orientation, Fig. III.1c.

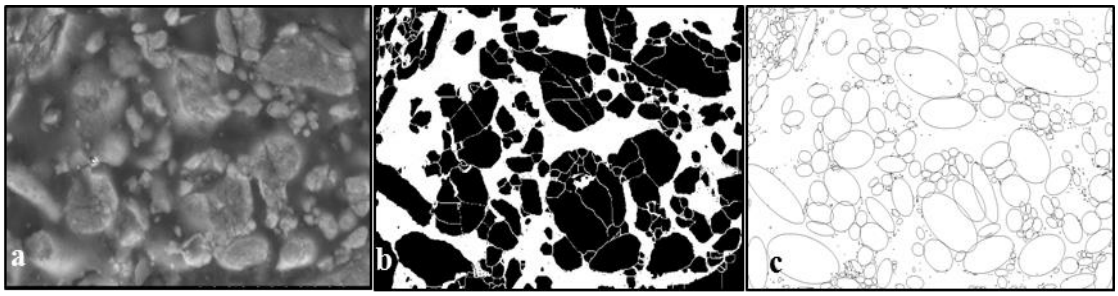

Fig. III.1. Image processing for microstructure characterization: (a) raw image, (b) after manual drawing of particles and binarization, (c) resulting ellipses.

An orientation factor was assumed to quantify the degree of shape anisotropy and orientation of the particles. Concerning particle orientation analysis, the direction perpendicular to the press conformation (x-plane direction) corresponds to 0° and the parallel direction to 90 º. This orientation factor is defined as the fraction of weighted cumulative lengths (sum of the length multiplied by the aspect ratio) of particles with orientation in the ranges 0°- 45° and 135º - 180º, as schematically represented in Fig. III.2.

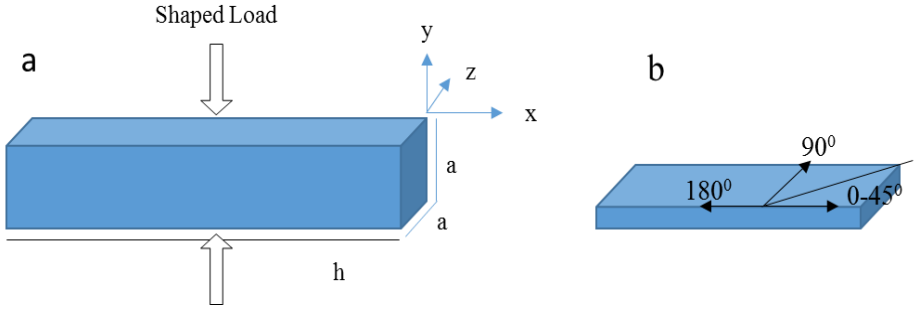

Fig. III.2. Illustration of the directions used for shrinkage quantification in the different planes (a) and scheme of the orientation range (0 º - 45 º and 135 º -180 º) considered in the orientation factor) (b).

Around 900 particles in 3 micrographs were considered for every sample. The error was determined by the standard deviation of the values obtained from the different images.

III.3.11. Static contact angle

In order to study the changes of the wettability of the glass-ceramic surfaces after surface modification treatments, static contact angle measurements were obtained by the sessile drop method [5] using a contact angle meter OCA15+ with high-performance image processing system from DataPhysics Instruments, Germany.

Ultrapure water (with a resistivity of 18.2 MU cm) obtained with a Milli-Q Ultrapure water purification system (Millipore, Bedford MA, USA) was added by a motor driven syringe, at room

temperature. Three measurements were taken in different regions and an averaged on each of five samples for each surface modification treatment, was considered.

III.3.12. Scaffold Porosity

The porosity of the scaffolds from each experimental group (n = 5 to 10 per group) was determined from the ratio of the measured apparent scaffold density and calculated theoretical scaffold density. Mercury intrusion porosimetry was also performed to characterize the macropores in the porous structure, based on the phenomenon of capillary rise of non-wetting liquid like mercury. Pressure is needed for the mercury to overcome the capillary force and intrude into the pores. To fill smaller pores, higher pressure is required. Therefore, the mercury volume intrusion into pores as a function of applied pressure reveals the information of the pore size distribution.

In principle, the mercury intrusion porosimeter can measure the pore size from 6 nm to 350 μm, which is determined by the highest pressure and lower pressure of 4.45 and 0.5 psia, respectively. However, there is always some inter-space between the sample and the wall of the chamber, where mercury cannot enter during the pre-filling. This makes the high-end measurement accuracy of large pores questionable. On the other hand, for the low end of the measurement, the high pressure might crack the fragile small pores walls, which could make the results inaccurate.

Overall, for our porous glass material, the practical range of this technique was from 100 nm to 300 μm. It was used an AutoPore IV 9500 V1.07 serial 734 porosimeter (Micromeritics) in Institute Pedro Nunes, Coimbra. A pressure of 0.5 psia (0.0034 MPa) was applied to pre-fill the chamber with mercury. The pressure then increases step-wisely for generating intrusion curve, which was used to calculate pore size distribution.

III.3.13. Scaffold water absorption

Water absorption measurements were performed on the sintered porous samples. The mass of leached samples was measured under various conditions: dry (w_d) and wet (w_w). The wet mass measurements were made after immersion in water, removing excess water from the sample surface with a plain paper, not very absorbent. The water absorption (WA) is given by equation III.4:

$$\%\, WA = \left[\frac{(w_w - w_d)}{w_d} \right] \times 100 \qquad \text{(Eq. III.4)}$$

All measurements were performed on 3 or more samples.

III.3.14. Scaffold Mechanical properties

The study of the mechanical properties of the produced bioactive glass scaffolds was focused on the mechanical response in compression loading only, giving values of the compressive strength and of the elastic modulus for the selected deformation rate. Six cylindrical leached samples, with 10 mm diameter and 10 mm thick were subjected to compression tests in a universal mechanical testing machine Zwick / Roell Z020, at 0.5 mm min^{-1} and a cell load of 20 KN. Prior to mechanical testing, the contact surfaces of each sample were ground to produce smooth parallel surfaces.

The elastic modulus from compression tests was determined from the initial linear region of the stress–stain curve and the average compressive strength, taken as the highest stress on the stress–strain curve, for six samples tested.

III.4. In vitro evaluation

III.4.1. Bioactivity studies

The definition of bioactive was given by Hench [6], who initiated this subject of research with his colleagues in the early 1970s, "a bioactive material is one that elicits a specific biological response at the interface of the material which results in the formation of a bond between the tissues and the material". The use of simulated body fluid (SBF) as first proposed by Kokubo et al. [7], allows to make an in vitro evaluation of the ability to precipitate calcium phosphates on its surface, the first indication of a potentially bioactive material.

III.4.1.1. Simulated body fluid (SBF)

Conventional simulated body fluid (1.0 SBF) was chosen as proposed by the Technical Committee ISO 23317 of International Organization for Standardization, in 2012, for in vitro evaluation for apatite-forming ability of implant materials [8]. The SBF was synthesised by adding the reagent-grade chemicals in the order listed in Table III.3 into distilled water, and buffered at pH 7.40 with trishydroxymethyl-aminomethane ($(CH_2OH)_3CNH_2$) and 1.0M hydrochloric acid at 36.5 ºC. This SBF is an aproteic and acellular solution with pH and composition simulating those of the human plasma (Table III.4). The SBF solution was prepared according to the formulation of Kokubo and Takadama [9].

Table III.3. Addition order of reactants used in SBF synthesis

Order	Reagents
1	NaCl
2	$NaHCO_3$
3	KCl
4	$K_2HPO_4.3H_2O$
5	HCl (1M)
6	$MgCl_2.6H_2O$
7	$CaCl_2.6H_2O$
8	Na_2SO_4
9	$NH_2C(CH_2OH)_3$

Table III.4. Ion concentrations (mM) of SBF solutions in comparison with those in human blood plasma

	Na^+	K^+	Ca^{2+}	Mg^{2+}	Cl^-	HCO^{3-}	HPO_4^{2-}	SO_4^{2-}
Plasma	142.0	5.0	2.5	1.5	103.0	27.0	1.0	0.5
SBF	142.0	5.0	2.5	1.5	147.8	4.2	1.0	0.5

The in vitro bioactivity was assessed by soaking the bulk and porous samples in SBF for periods from 1 h up to 28 days. To better understand the nature of the precipitated layer and also to obtain a sufficiently representative thickness layer, crystalline bulk samples were also analyzed for 10, 20, 30 days and 5 months. Subsequently, the samples were placed in polyethylene bottles containing SBF, and kept for various periods of time, without shaking, in an incubator at 37 ºC, in accordance with a protocol referred in literature [10–13]. Four samples were used for each immersion time, chapter VI to VIII. A constant specimen surface area to solution volume ratio of 0.1 cm^{-1} was used in the immersion tests, previously filtered through a Milipore 0.22 μm system. For the scaffolds it was considered the value of the surface area given by the BET method. After removal from the SBF, the samples were washed in distillated water and dried at 60 ºC.

III.4.1.2. Apatite layer characterization

After SBF immersion, the apatite layer deposited on the samples was detected by SEM/EDS. The microstructural observation of the samples' surface, before and after immersion in SBF, was carried out by SEM in the equipment referred in Section III.3.9.

Surface modifications of the materials after immersion were also studied by XRD, reducing the samples to powder.

The chemical structure of the glass and glass-ceramic surfaces, before and after SBF immersion, was analysed by Fourier transform attenuated total reflectance infrared spectroscopy (FTIR).

III.4.1.3. Inductively coupled plasma atomic emission spectrometry (ICP)

Elemental concentrations of the SBF before and after soaking of the glass and glass-ceramic samples (plates and scaffolds) were measured as a function of the immersion time [14], using inductively coupled plasma atomic emission spectrometry (Jobin Yvon 70 Plus, France), at the Laboratório Central de Análises from the University of Aveiro.

III.4.2. Biocompatibility studies

Biocompatible glasses and glass-ceramics are desired to generate the most appropriate beneficial cellular or tissue response in a specific situation. However, the definition does not explain what type of glass dissolution behaviour is desired in various applications. To understand the influence of the presence of biomaterials on cells, osteoblast cells have been used in different tests. Cell morphology, adhesion and proliferation were examined and then, cell activity was tested by measuring the amount of some specific enzymes produced, in this study, alkaline phosphatase.

III.4.2.1. Human bone marrow cells

In order to study the morphology, attachment and proliferation, Fig. III.3, of osteoblastic cell cultures over the glass bulk slices and scaffold surfaces, a human bone marrow (HBM) osteoblastic cell culture was used.

Human marrow cells, obtained from orthopaedic surgery procedures (after patient informed consent), was cultured, in α- Minimal Essential Medium (α-MEM) supplemented with 10 % Fetal Bovine Serum (FBS, Biochrome, Germany) and 100 $mg.ml^{-1}$ penicillin, 10 IU streptomycin and 2.5 $mg\ ml^{-1}$ fungizone, in controlled atmosphere conditions (37 ºC, 5 % CO_2, 100 % humidity). Detachment of confluent low passage cells was performed using 0.05 % tripsin and 0.25 % EDTA solution (Sigma, USA), for 10 min at 37 ºC. Subsequently, HBM cells were cultured over samples

in a concentration of 10^5 cell ml^{-1} and incubated in controlled atmosphere conditions for 24 h and 6 days (results in Chapter VII) and up to 21 days (chapter IX).

After each incubation period, samples were washed with Phosphate Buffer Saline (PBS, Sigma, USA) solution and fixed in Gluteraldehyde 2.5 % (V/V) for observation by means of CLSM, Leica SP2 AOBS. After fixation, samples were dehydrated in crescent ethanol concentrations (50 %, 70 %, 90 % and 100 %), air-dried and sputter-coated with gold.

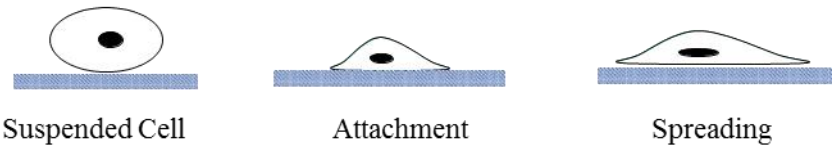

Fig. III.3. Cell attachment and spreading mechanism [15].

III.4.2.2. Cell viability/proliferation

Cellular cytotoxicity and viability/proliferation at each time period, was measured on triplicate samples by the MTT (3-(4,5-dimethylthiazol-2-yl)-2,5-diphenyltetrasodium bromide) colorimetric method, first developed by Mosmann [16].

This test is based on the capacity of viable cells to metabolize tetrazolium salt by forming purple formazan crystals, which can be dissolved and quantified by measuring the absorbance of the solution at 600 nm in an ELISA reader (Synergy HT; Biotek) and is commonly used for cell viability evaluation. Cells were then incubated for 3 h at 37 °C in a humidified atmosphere containing 5 % CO_2 with 0.5 $mg.ml^{-1}$ of MTT, followed by material samples wash with PBS for macroscopic surface area observation. Results were evidenced by the formation of a dark purple staining and expressed as $A.cm^{-2}$.

III.4.2.3. Alkaline phosphatase activity

The colonized materials were treated with 0.1 % triton in water (to lyse the cell layer) and the cell lysates were evaluated for alkaline phosphatase activity (ALP) and total protein content. ALP was assessed by the hydrolysis of p-nitrophenol phosphate in alkaline buffer solution, pH 10.3, for 30 min at 37 ºC. The resultant products are phosphate and p-nitrophenol. The last, turns the resultant solution into yellow, which can be measured by colorimetric determination at k = 405 nm. Results are expressed in nanomoles of p-nitrophenol produced per min per µg of protein (nmol min^{-1}/µg protein).

III.4.2.4. Statistical analysis

Statistical significance between groups was performed by one way analysis of variance (ANOVA) followed by Tukey multiple comparison test post-analysis to evaluate statistical differences among samples. All values are expressed as mean and SD. A p-value below 0.05 was considered significant.

References

[1] S. Krimm, A. V. Tobolsky, Quantitative x-ray studies of order in amorphous and crystalline polymers. Quantitative x-ray determination of crystallinity in polyethylene, J. Polym. Sci. 7 (1951) 57–76.

[2] J.K.M.F. Daguano, K. Strecker, E.C. Ziemath, S.O. Rogero, M.H. V Fernandes, C. Santos, Effect of partial crystallization on the mechanical properties and cytotoxicity of bioactive glass from the $3CaO.P_2O_5$-SiO_2-MgO system, J. Mech. Behav. Biomed. Mater. 14 (2012) 78–88.

[3] DIN ISO 7884-4:1998-02, Standard - Beuth.eu.

[4] ASTM C1350M - 96(2013) Standard Test Method for Measurement of Viscosity of Glass Between Softening Point and Annealing Range (Approximately 10^8 Pa·s to Approximately 10^{13} Pa·s) by Beam Bending (Metric).

[5] Y. Yuan, T.R. Lee, Surface Science Techniques, Springer Berlin Heidelberg, Berlin, Heidelberg, 2013.

[6] L.L. Hench, R.J. Splinter, W.C. Allen, T.K. Greenlee, Bonding mechanisms at the interface of ceramic prosthetic materials, J Biomed Mater Res. 2 (1971) 117–141.

[7] T. Kokubo, H. Kushitani, S. Sakka, T. Kitsugi, T. Yamamuro, Solutions able to reproduce in vivo surface-structure changes in bioactive glass-ceramic A-W3, J. Biomed. Mater. Res. 24 (1990) 721–734.

[8] BS ISO 23317:2012 - Implants for surgery. In vitro evaluation for apatite-forming ability of implant materials, 2012.

[9] T. Kokubo, H. Takadama, How useful is SBF in predicting in vivo bone bioactivity?, Biomaterials. 27 (2006) 2907–2915.

[10] D. Pereira, S. Cachinho, M.C. Ferro, M.H.V. Fernandes, Surface behaviour of high MgO-containing glasses of the Si–Ca–P–Mg system in a synthetic physiological fluid, J. Eur. Ceram. Soc. 24 (2004) 3693–3701.

[11] N.A.F. Almeida, M.H.F.V. Fernandes, Effect of Glass Ceramic Crystallinity on the Formation of Simulated Apatite Layers, Mater. Sci. Forum. 514-516 (2006) 1039–1043.

[12] C.M. Queiroz, J.R. Frade, M.H.F.V. Fernandes, SiO2- MgO-3CaO.P2O5- K2O Glasses and Glass-Ceramics: Effect of Crystallisation on the Adhesion of SBF Apatite Layers, Key Eng. Mater. 254-256 (2004) 155–160.

[13] C.A. Queiroz, S. Agathopoulos, J.R. Frade, M. Fernandes, Network connectivity and bio-mineralization of $0.45SiO_2$–-(0.45-x)MgO–-xK_2O–0.1($3CaO{\cdot}P_2O_5$) glasses | Queiroz - Academia.edu, Mater. Sci. Forum. (2004) 383–7.

[14] G.L. Moore, Introduction to Inductively Coupled Plasma Atomic Emission Spectrometry, Elsevier science B.V., 2012.

[15] S. Lavenus, G. Louarn, P. Layrolle, Nanotechnology and Dental Implants, Int. J. Biomater. 2010 (2010).

[16] T. Mosmann, Rapid colorimetric assay for cellular growth and survival: application to proliferation and cytotoxicity assays, J. Immunol. Methods. 65 (1983) 55–63.

Chapter IV

"The starting point of all achievement is desire"
(Napoleon Hill)

CHAPTER IV

EFFECT OF PARTICLE SIZE IN THE ANISOTROPIC SINTERING OF THE $3CAO.P_2O_5$-SIO_2-MGO GLASS POWDER

Abstract

Understanding the sintering behaviour and the interaction between the densification and crystallization processes of glass powders during sintering is essential for assessing the ideal sintering conditions for obtaining a glass scaffolds for tissue engineering applications. Our main goal was to carry out a comprehensive study of the bioactive glass sintering, identifying the powder and sintering variables effect on densification, for future design of sintered glassy materials with competent microstructures for functional applications in biological systems. This study was performed by dilatometric measurements, at different heating rates, using glass powders with different particle size distributions and detailed microstructural analysis with quantification of anisotropic parameters. The glass powder compacts could be densified at sintering temperature below 800 ºC through viscous sintering. The activation energy of sintering, Es, was evaluated by the application of Venkatu's equation for non-isothermal conditions and similar values were found for compacts with different particle size distributions.

When using the dilatometer, the load exerted on the sample by the dilatometer push-rod induced a significant increase of shrinkage anisotropy. The measured value of k for sintering under the dilatometric load and for the free sintering were always k>1, i.e., the samples shrank less in the direction of shaping pressing of green compacts. However, an interesting finding was that by a small adjustment of particle size distribution and decrease of the average powder particle size, from 6.8 to 3.5 μm, very different sintered microstructures could be obtained. Near full densification and negligible microstructural anisotropy was reached before crystallization in the finer glass compacts, whereas the coarser glass powder compact presents reduced final density and microstructural anisotropy.

IV.1. Introduction

Sintering of glass powder is a physical process that occurs by viscous flow [1]. It has the advantages of the attainment of different controllable porosities and complex forms, varying the format of the pressing mold, which cannot be acquired by the usual techniques of glass conformation. In scaffold fabrication to understand the sintering conditions of the base glass powders and the interaction between sintering and crystallization of the material is essential. By knowing the thermal behaviour and, consequently, the structural transformations of glasses, the process can be optimized to achieve the highest possible densification of the scaffold. Densification of the glass prior to crystallization is particularly important since the crystallization brings an accented reduction of densification for viscous flow: for about 10 % of the crystals formed, apparent viscosity increases about 100 times, implying an abrupt reduction of the viscous flow with shrinkage stopping that is observed in dilatometric curves [2]. If the crystallization stage begins before or during the sintering process, the resultant compact will have sufficiently porosity and heterogeneities due to the existence of crystalline phase in the glass matrix. In the glass sintering, if the interval between Tg and Tc (crystallization temperature) is too small, the glass will not have enough time for completely densification before crystallization. In the contraire, if the sintering stage finishes before the beginning of crystallization, a denser compact will be gotten with lower porosity [3].

The particle size is an important factor in the sintering of the glass [3–5]. Compact density increases with the biggest and smallest particle size ratio. Cutler and Henrichsen [6] had verified that glass particles with a varied distribution sizes and raised superficial area densified about five times more quickly than glasses with an equivalent average particle size but with a much uniform size distribution.

The ability to predict the final shrinkage of a sintering compact along its axes will enable to control the shape of the final product. Some equations, based on the Frenkel's model [7,8], had been proposed to describe the linear shrinkage in the initial stage of sintering and have been used in some crystalline or amorphous systems, namely in non-isothermal conditions, with constant heating rates. However, anisotropic sintering is often observed in porous glass systems and in this case the Frenkel´s model fails in the prediction of the overall shrinkage [9–11]. Anisotropic green microstructure can be formed during the shaping process as a result of many factors, the most frequent being non-equiaxed particle shape, particle alignment and non-uniform packing [11–13] which will give rise to anisotropic shrinkage behavior during sintering. Although an increased attention and relevant comprehensive studies have being done in anisotropic sintering of different systems, more research is yet missing for a full understanding of the factors governing the anisotropic densification.

In this work the anisotropic sintering of a Ca-P-Si-Mg glass powder with different particles size distributions was investigated. The effects of the particle size distribution on the particle alignment during shaping and of the packing characteristics together with the heating rate on the shrinkage behavior were investigated.

IV.2. Material and Methods

Reagent-grade powders of SiO_2, $CaCO_3$, $Ca(H_2PO_4)_2$ and MgO were mixed in the required proportions to obtain a glass with the nominal composition (wt. %) 54.89 % $3CaO.P_2O_5$ – 24.81 % SiO_2 – 20.30 % MgO. The raw materials were wet mixed in ethanol in an agate mill, for 45 min, and dried at 60 ºC. Batches of 80 g were melted in a platinum crucible at 1500 ºC, for 2h, in air, and then quenched into cold water. After quenching in water, a homogenous, transparent glass was obtained. The amorphous state of the glass was confirmed by XRD analysis of powdered samples, in a Rigaku Diffractometer Geigerflex Dmax-C, Japan, at room temperature with CuKα radiation at a scan speed of $0.02^o\ s^{-1}$. The XRD patterns were recorded in the 2θ range of 10–80 degree.

The glass was crushed in an agate ball mill for different periods of time and sieved to collect a fine fraction bellow 20 μm and an average particle size d50 of 3.5 and 6.8 μm using alcohol as solvent. The particle size measurements of the powdered glasses were carried out by a laser particle size Coulter LS Particle Size Analyser 230, Fraunhofer optical model, Amherst, MA.

DTA analysis of the glass particles was performed in order to assess the temperature range suitable for thermal treatments. The analysis was performed in a differential thermal analyzer Labsys Setaram TG-DTA/DSC, France, at a heating rate of 10 ºC min^{-1} from room temperature to 1000 ºC in air, using alumina (Al_2O_3) as a reference.

The density of the glass was determined as 2.65±0.05 g cm^{-3} at 25 ºC by helium pycnometry in a QuantaChrome equipment and further taken as theoretical density under the assumption that no closed porosity was present in the measured particles.

Rectangular bars (5 x 5 x 10 cm^3) with a green density of 1.60 ± 0.01 (corresponding to 0.60 of relative density) were obtained by uniaxial pressing at 175 MPa, for 30 sec, as represented in Fig. IV.1.

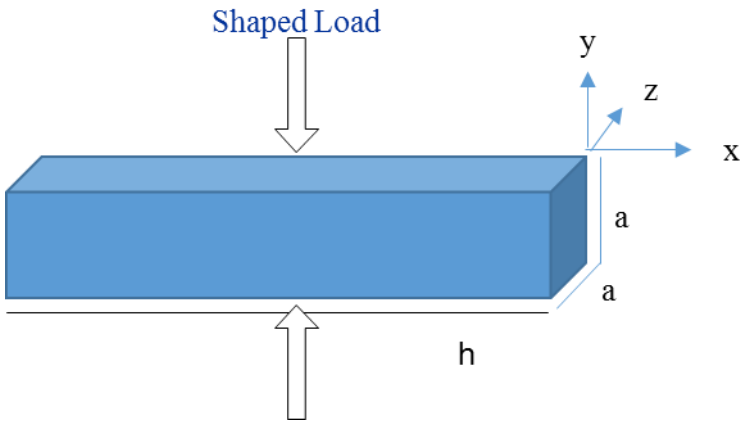

Fig. IV.1. Representation of the obtained glass powder compact samples. x-axis is perpendicular to the shaped load direction

The sintering behavior in non-isothermal conditions was investigated at constant heating rate dilatometry, using a Bahr Thermo Analyse DIL 801 L, Germany and heating rates from 5 to 20 ºC min^{-1} until a maximum temperature of 850 ºC.

The density of the compacts at given temperatures during sintering was determined from the green density and the measured shrinkage using the relation, given by Eq. IV.1,

$$\rho = \frac{\rho_0}{(1-\Delta a/a_0)^2\,(1-\Delta h/h_0)} \qquad \text{(Eq. IV.1)}$$

The final density of the sintered compacts was also determined by using the Archimedes principle. Average values of x- and y- shrinkage were calculated from 5 samples. With this data, the coefficient of shrinkage anisotropy, K, can be defined by the ratio between perpendicular and parallel strains, according to Eq. IV.2,

$$K = \frac{\varepsilon_y}{\varepsilon_x} = \frac{\ln(h/h_0)}{\ln(a/a_0))} \qquad \text{(Eq. IV.2)}$$

In order to characterize the particles orientation, the microstructure of the cross-sections in the y- and x- planes was analysed by scanning electron microscopy (SEM in a Hitachi, Model SU-70 equipment at an accelerating voltage of 25 KeV. Prior to SEM analysis, the planes of sintered specimen were finished with diamante slurry and sputtered with carbon.

From the original micrographs a binary image was created, with the grains in blank and the pores or resin in black, as exemplify in Fig. IV. 2. For the image analysis, the software ImageJ was used by defining a threshold value to convert the micrograph into binary pictures (Fig. IV. 2b). The shape of the particles was detected automatically and the desired information determined, not taken into account the particles located at the edge of the picture. To measure the degree of particle orientation and aspect ratio it was used the “best-fit ellipse method”, Fig. IV.2c.

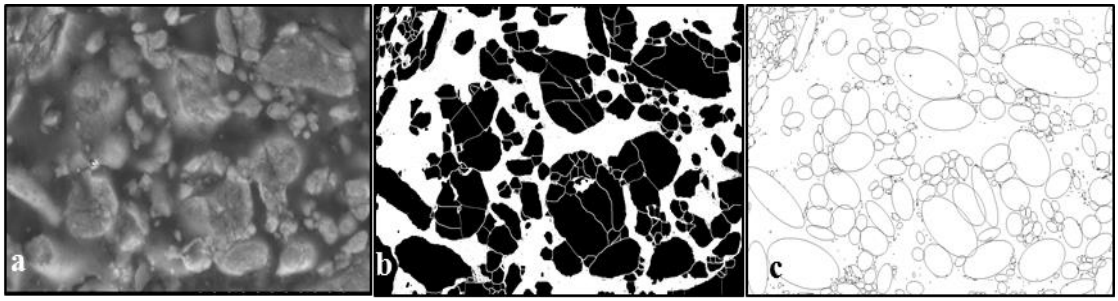

Fig. IV.2. Procedure of the software-assisted microstructure analysis

IV.3. Results and Discussion

The amorphous nature of the as quenched glasses was confirmed by XRD, curve not shown. The particle size distributions of the glass powders, after milling and sieving are represented in Fig. IV.3. It is possible to observe a particle size distribution varying between ~0.04 up to ~20 μm with an average particle size at 50 vol. % of 3.5 μm for G3 and a slight wider distribution for G6, with a larger fraction of coarser particles extending up to ~33 μm and an average size of 6.8 μm.

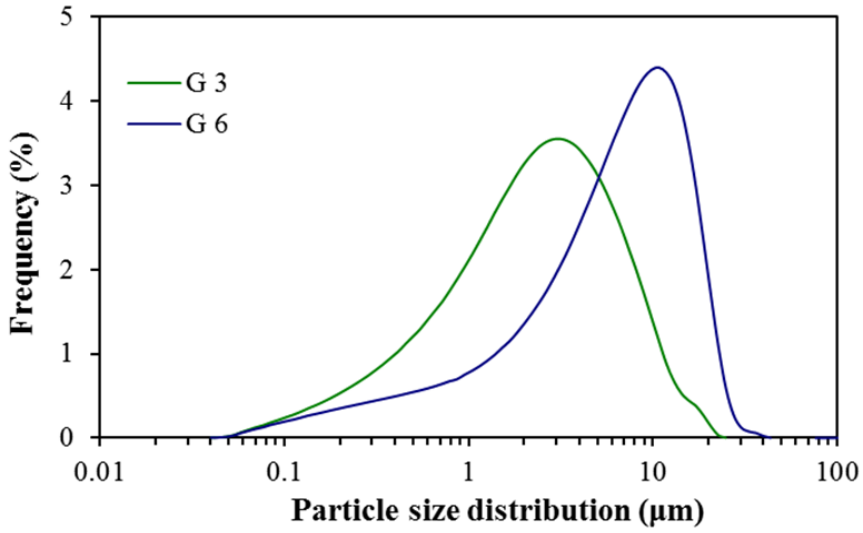

Fig. IV.3. Particle size distribution of the glass powders, after milling

The thermal behaviour of the glass powder G3 was characterized by DTA and dilatometry at 10 ºC min^{-1} and the respective curves are shown in Fig. IV.4. The beginning of sintering occurred at ~710 ºC, after the endothermic occurrence in DTA curve, which corresponds to the glass transition region in the range of 708–730 ºC.

It can be observed two regions of shrinkage in the dilatometric curve: the first one, region I, where the densification predominantly occurs (~14 % of shrinkage was attained) with the ending fairly close to the onset of the crystallization temperature (Tc), ~825 ºC. The second regimen, region II, occurred in competition with the devitrification process, presenting a slow densification process, leading to ~2 % of additional shrinkage.

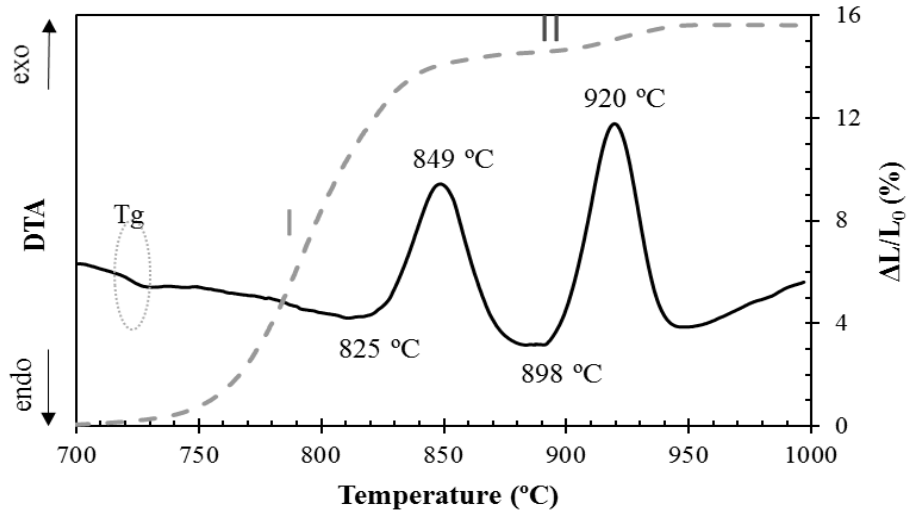

Fig. IV.4. DTA and dilatometric curves of the glass powder

IV.3.1. Shrinkage kinetic analysis

The shrinkage (y) and shrinkage rate (dy/dt) of the two powder compacts with varying heating rates are presented in Fig. IV.5. Shrinkage curves show a sigmoidal characteristic shape with temperature and shifted to higher temperatures with increasing heating rate [14,15].

The influence of the particle size distribution on the sintering rate was also clearly observed. A maximum shrinkage of 8 % was obtained for the coarser powder at 810 ºC (2 ºC min^{-1}), while 11.5 % densification was reached for the finer powder, at the same heating rate and temperature. This effect is correspondent to a higher shrinkage rate for the finer powder as can be observed in Fig. IV.4b. By comparing the maximum of the shrinkage rate at the same heating rate, it is very clear its increase with the decreasing of the average particle size, as expected from the sintering kinetic laws [5]. Above the maximum shrinkage rate, two processes occur in simultaneous competing between itself, namely the viscous flow and the nucleation and growth of crystalline phase. It seems that the higher the heating rate is, the higher the onset temperature for the crystallization, as already observed elsewhere [16,17].

Boccaccini et al. [16] fully densified glass particle compacts when heated at β = 15 °C min^{-1} to 1050 °C, however, the same powders densified to only 89 % at β = 1 ºC min^{-1}, thus confirming that high heating rates favored sintering in detriment to crystallization.

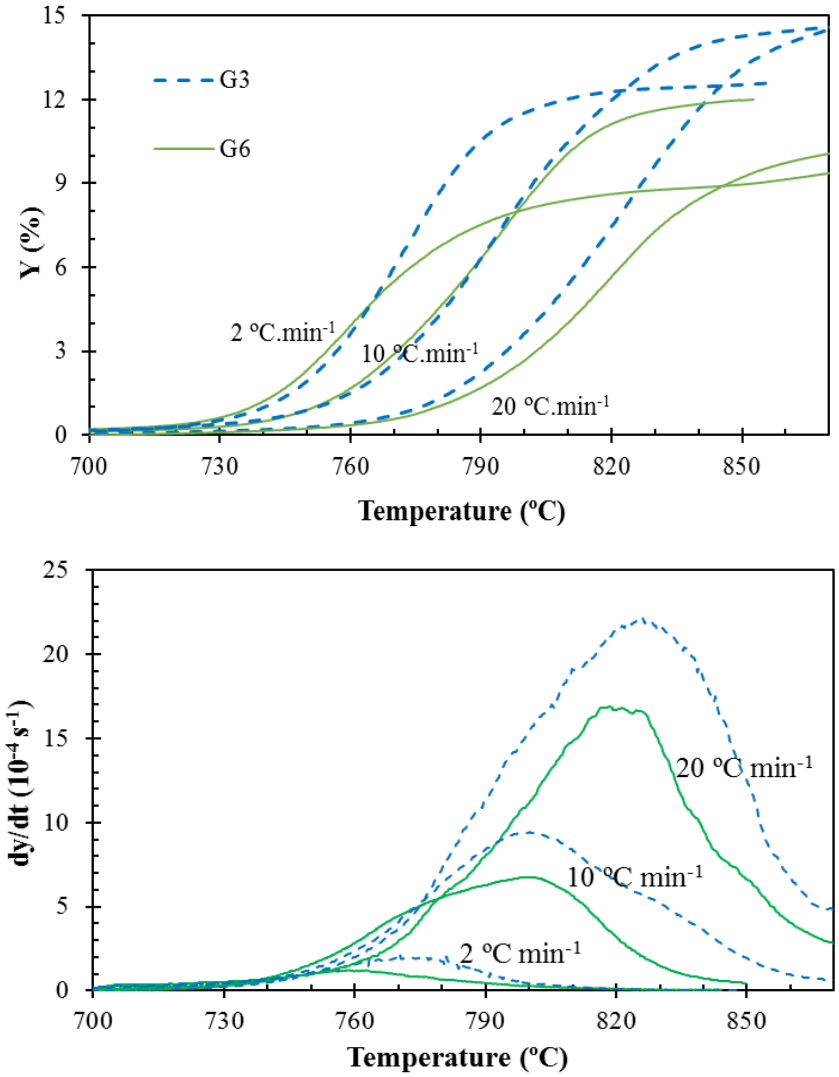

Fig. IV.5. Dilatometric sintering curves (a) and shrinkage rate (b) of the glass compacts with two particle sizes, at different heating rates, as a function of temperature

Using the data from the dilatometric experiments, it is possible to calculate the apparent activation energy and the kinetic exponent, characteristics of the densification mechanism involved in the sintering. The equation used, Eq. IV.3, for the calculation of the apparent activation energies and sintering exponent was proposed by Venkatu [18], valid for the initial sintering stage y ≤ 2 %:

$$y^p = \frac{A}{\beta}\exp\left[\frac{-(Q+Q')}{RT}\right] \qquad \text{(Eq. IV.3)}$$

where Q' is a constant with the value of 24.267 kJ mol^{-1}, for the viscous flow, A is a constant that only depends on the material and of the sintering mechanism and p it is the sintering exponent, which presents the values of p = 1 for viscous flow, p = 2 for volume diffusion and p = 3 for the diffusion mechanism by grain contour. The application of this equation is limited to a range of shrinkage (y ≤

2 %) into the initial stage. The determination of p is performed through a graph of ln y in function of ln β, for constant values of temperature, where the slope is equal to -1/p. The value gotten of p = 1.3 and 1.2, for G3 and G6, respectively, are approximately p ≈ 1, which corresponds to viscous flow. Equivalent average value for the viscosity activation energy, Es, of 521±6 kJ mol^{-1} and 511±24 kJ mol^{-1} were found for glass particle size of 3.5 μm and 6.8 μm respectively.

Table IV.1. Activation energies and kinetic exponents of the G3 and G6

Sample	p	Es (kJ mol^{-1})
G3	1.3	521 ± 6
G6	1.2	511 ± 24

IV.3.2. Effect of the heating rate and particle size on the final sintered density and anisotropy

The effect of the heating rate, β, and of the particle size on the final density, attained during sintering in the dilatometer up to 850 ºC, is shown in Fig. IV.6. The final density of the compacts was not significantly affected at the heating rates of 5 and 10 ºC min^{-1}, but at high heating rates, β >10 ºC min^{-1}, the density tends to decrease with increasing the heating rate, due to the reported shift of the shrinkage curves to higher temperatures, Fig. IV.5. For lower heating rates the shrinkage stops earlier do to the onset of crystallization. A densification of 97 % and 89 % was obtained for G3 and G6, respectively, for the compacts sintered at 10 ºC min^{-1}.

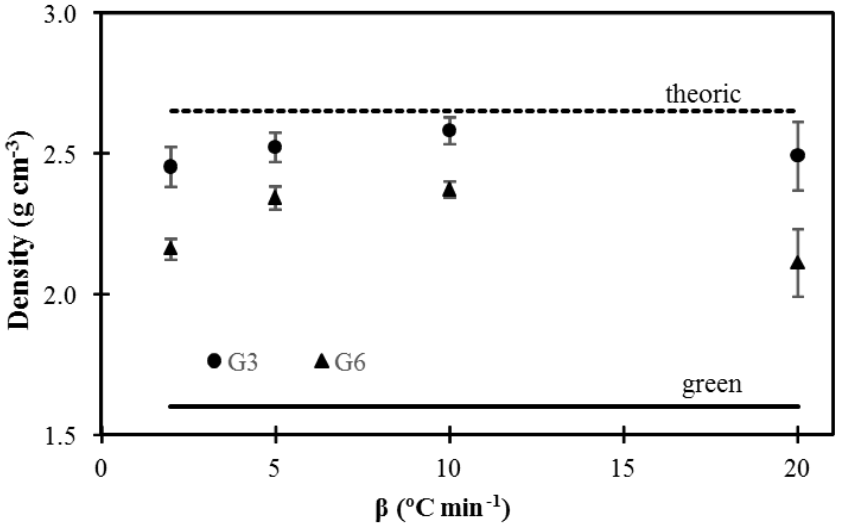

Fig. IV.6. Attained density values for the glass particle sizes, sintered in dilatometer up to 850 ºC

Shrinkage anisotropy can be quantified by the shrinkage anisotropy factor (k). Equation IV.2 describes a form to calculate the coefficient of anisotropy [11].

A value equal to 1 or near indicates isotropy. The more moved away from the coefficient value of 1, the biggest anisotropy will be.

As indicated by the K values, in Fig. IV.7, the shrinkage anisotropy increases with the heating rate, β, for both compacts and is higher for the coarser powder compacts, G6.

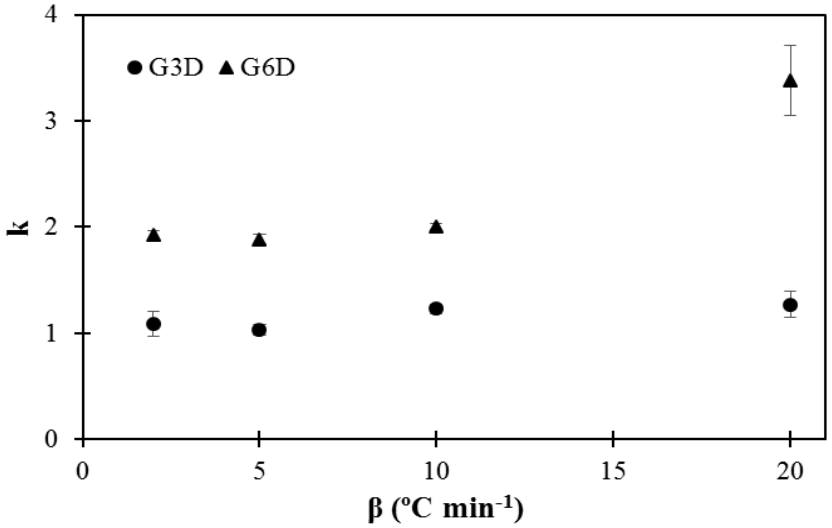

Fig. IV.7. Anisotropic factor as a function of heating rate for samples sintered in dilatometer up to 830 ºC

The variation of the shrinkage anisotropy factor (k) with the temperature performed at 10 ºC min^{-1} in the dilatometer is presented in Fig. IV.8, together with free sintered samples, without the dilatometric load. It was observed that x- shrinkage was always higher than the y- shrinkage.

In the dilatometer samples the k values for G3 compacts are lower than that for G6, and the shrinkage anisotropy factor decreases to a value near 1, i.e., the sintering becomes 'more isotropic' in nature, and therefore, the creep strain, according to Eq. IV.2, decreases. The shrinkage anisotropy factor decreases continuously during sintering and reaches a value close to 2.5 and 1.2 at 850 ºC for G6D and G3D respectively. In the early stages of sintering, the relative x-axes shrinkage was higher as much as three and two times that of y-axes shrinkage, for G6D and G3D respectively.

It is possible that with the sintering process, the neck length grows in the direction of the longer axis at a faster rate, resulting in the reduction of shrinkage in this direction and consequently of the anisotropy.

The shrinkage of the free sintered samples is nearly isotropic for G3, however, anisotropic shrinkage for G6 samples is observed (k~1.5). Without the applied load of the dilatometer, free sintering, the anisotropy factor k is smaller and seems to remain nearly constant throughout sintering, in agreement with the literature on glass compacts [13].

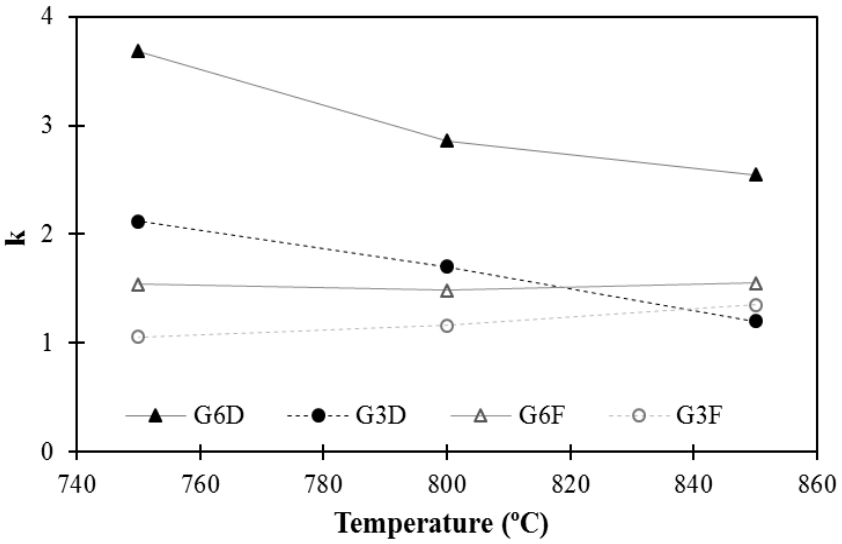

Fig. IV.8. Variation of the shrinkage anisotropy factor k as a function of dilatometric (D) or free sintering (F) at 10 ºC min^{-1}, for glass compacts with a green density of 1.6 g cm^{-3} at different particle sizes distributions (G3) and (G6)

These results are consistent with the literature result, elongated particles or pores lead to anisotropic shrinkage and the shrinkage is larger in the direction perpendicular to the shaping pressure. Anisotropic shrinkage is believed to come from green particle preferential orientation. The conditions for such can be found in uniaxial pressed compacts of irregular particles, which is here the case. If particles are oriented in the x- direction, the initial shrinkage rate will be higher in this direction because of the higher necks per unit length. However, as sintering progresses, the neck length grows at a faster rate. This results in the reduction of shrinkage in this direction and consequent reduction of shrinkage anisotropy as sintering progresses, because the rate of particle coalescence is a strong function of neck length. This can explain the reduction of shrinkage anisotropy in the final sintering stages, though the microstructure still has some anisotropy.

Considering that when applying a mechanical load, the degree of shrinkage anisotropy mentioned above was seen to increase, the main differences between G3 and G6 powder sintering may come from the particle size distribution, since other factors affecting shrinkage anisotropy, as pressing pressure, packing density, dilatometer stress and sintering cycles, are equivalent. It seems probable that finer particles can be packed with less preferential orientation, as shown for G3F and G6F samples.

When in presence of dilatometric load, Boccaccini and Olevsky [9], show that if the effective stress due to the dilatometer load is kept below 5 KPa, the shrinkage anisotropic factor will be nearly constant with the progress of sintering, confirming the free shrinkage results.

Anisotropy in densification occurs normally in uniaxial pressed samples, where a higher shrinkage in the radial direction (for cylindrical samples) is observed as in the case of cordierite type glass

powder [19] and on non-spherical [20] and spherical [21] borosilicate powder glass, although, on soda-lime glass [22] it was observed a higher contraction in the axial direction.

IV.3.3. Micrographs analysis of the anisotropy

To verify this matter and its relation to the compact densification, micrographs obtained from the compact impregnated with resin are present on Fig. IV.9. The x-plane (perpendicular the pressing direction) and y-plane (parallel to the pressing direction) were examined.

The particles, in the x- direction, in both systems, have their longer axes oriented, especially for the larger particle size system, as is revealed in the micrographs, Fig. IV.10. The shorter axes were observed in the y- direction.

Micrographs in Fig. IV. 10 revealed that the particles are of irregular shape and not equiaxed. When assimilated to two-dimensional (2D) ellipses, as present in Fig. IV.2, their median aspect ratio (defined as the major axis divided by the minor axis) was, for green samples, 1.63 and 1.67 for y- and 1.91 and 2.40 on x- direction, for G3 and G6 series respectively, table IV.1. This feature is important, as this intrinsic particle anisometry can lead to microstructural anisotropy in the sintered body if particles are aligned during the manufacturing process, which lead to the anisotropic shrinkage, evidenced by G6 experimental data in Fig. IV.10.

In the G3 particle distribution, with more isometric particles, no specific orientation was observed, the green glass powder was more uniform, leading finally, to a lower shrinkage anisotropy.

It can also be seen that the degree of particle orientation increased with temperature for both G3 and G6, probably due to the dilatometric process load, in the y- direction, that led to a significant increase of the necks per unit length in this direction and consequent coalescence of particles.

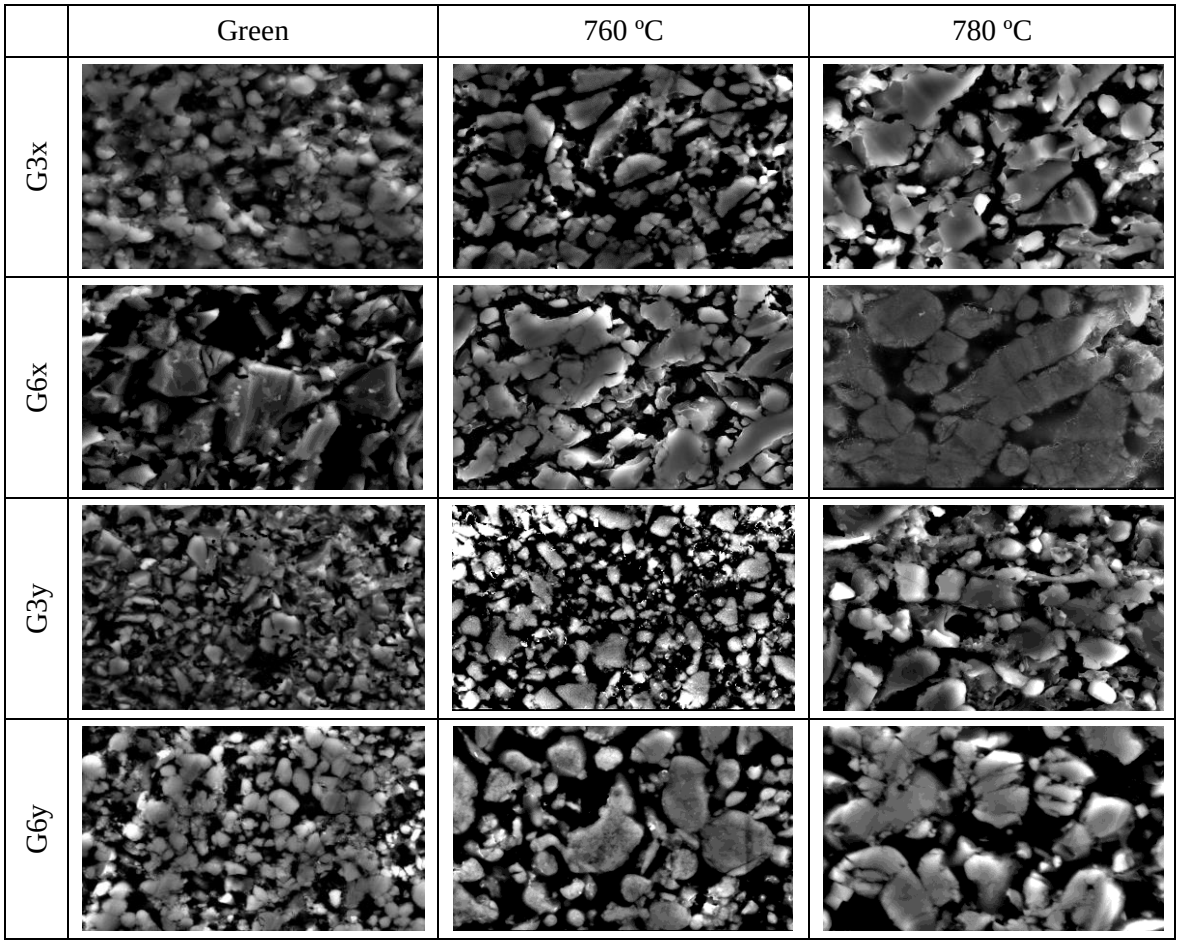

Fig. IV.9. SEM micrographs of polished sections of the samples during heat treatment at 10 ºC min^{-1} up to different temperatures

The densification using ImageJ was successfully correlated with the relative density of the samples using Eq, IV.1, confirming the suitability of the evaluated images as well as the reliability of the image analysis method used. Such output data can also be used to analyse particles or pore size, shape packing, and orientation within the sample. These results are summarised in Table IV.2. Around 900 particles in 3 micrographs were considered for every sample.

Table IV.2. Characteristics of densification evaluation

	Green				**760 ºC**				**780 ºC**			
Samples	G3		G6		G3		G6		G3		G6	
	x-	y-	x-	y-	x-	y-	x-	y-	x-	y-	x-	y-
Density (%)	57±0.5		58±0.8		59±0.4		61±0.6		70±0.5		67±0.4	
Image J density (%)	56±0.8		57±0.4		60±0.6		61±0.4		69±0.7		67±0.9	
Aspect ratio	1.91	1.61	2.40	1.67	2.09	1.74	2.59	1.75	2.23	1.75	2.65	1.85

In order to analyse the effect of particle size and the development of anisotropy during densification, we introduce the following particle orientation factor, which is defined as the fraction of weighted cumulative length (sum of the length multiplied by the aspect ratio) of particles with orientation in the ranges 0 - 45 ° and 135 - 180 º. If the particles are aligned in the x-axes direction the angle is 0º or 180º, an angle of 90º corresponds to the z- direction. In a randomly oriented isotropic material, a value of 0.5 would be expected [13].

In order to examine the correlation between particle alignment and shrinkage, the orientation of the particles with temperature was determined, Fig. IV.10. For both particle sizes distributions more than 50 % of the particles are oriented in the x- direction. That indicates that a preferred orientation exists. In the x-plane, G3 particles were more or less randomly distributed at the beginning but at the end they seem to be more aligned along the x-axis, which is the perpendicular to the load direction. In the G6 system, particles are mainly oriented along the x-axis. This result shows an important anisotropy in this plane, certainly induced by the manufacturing process. Fig. IV.10. A preferential orientation is induced, in lower degree in G3 system, leading to anisotropic viscous properties that should also affect the particle morphology during sintering.

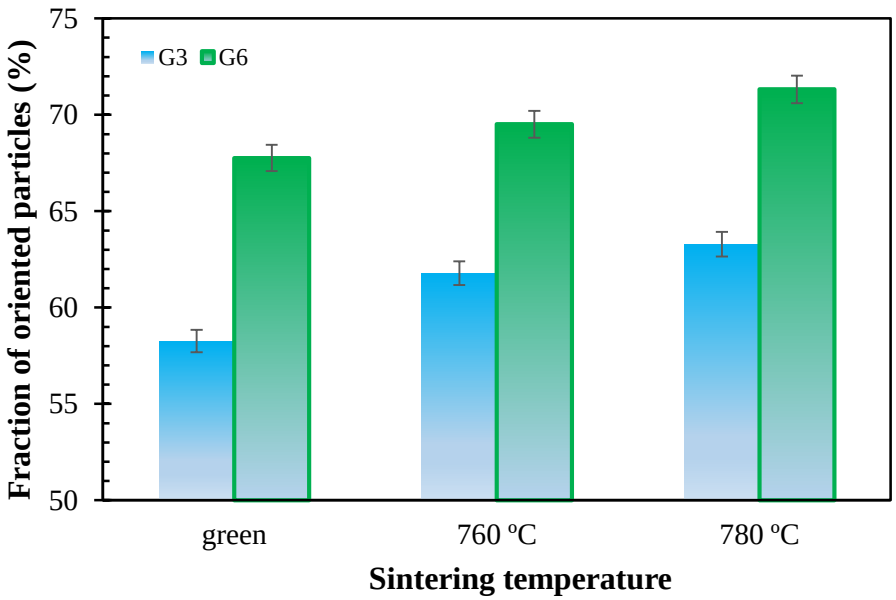

Fig. IV.10. Particle orientation distribution (cumulative lengths) for G3 and G6 particles system in the x - plane as a function of temperature

For the early stages of sintering, the shape of the particles and their nonhomogeneous spatial arrangement in the compact are the major variables affecting the shrinkage behaviour in the green body, as a result of the uniaxial pressure used, as seen in Fig. IV.1. The difference in the number of nearest-neighbour contact points along the x- versus y- planes, especially for G6, with a preferred spatial distribution, increases the area and number of particle's contacts site, consequently inducing an increase in shrinkage anisotropy.

The results clearly demonstrates the influence of the particle size distribution and, in addition, of the powder preparation and sintering on the degree of particle orientation and consequent densification of the final samples. The results suggested that changing the microstructure of the green body, by varying the morphology and size of the starting powders used, should lead to a change in the degree of shrinkage anisotropy, thus transforming the shrinkage behaviour from anisotropic to isotropic.

IV.4. Conclusion

The sintering behavior for $3CaO.P_2O_5$-MgO-SiO_2 system glass was investigated. The glass powder compacts can be densified at the sintering temperature below 800 ºC through viscous sintering, without the present of crystalline phases. Significant effect of the heating rate is observed on the relative rates of densification and crystallization. Increasing the heating rate leads to higher anisotropic shrinkage, for the same temperature, before the optimum temperature of sintering. Near full densification before crystallization was reached by a small decrease of the glass particle size from 6.8 μm to 3.5 μm. Comparing the effect of particle size in the particle orientation, a distinctive interrelation can be found between the degree of orientation and particle shape. Coarser powders compacts exhibited a higher degree of particle orientation, perpendicular to the shaping force direction, as those from finer powders.

References

[1] M.O. Prado, E.D. Zanotto, Glass sintering with concurrent crystallization, Comptes Rendus Chim. 5 (2002) 773–786.

[2] A. Karamanov, M. Pelino, Sinter-crystallization in the diopside–albite system, J. Eur. Ceram. Soc. 26 (2006) 2519–2526.

[3] C. Siligardi, M.C. D'Arrigo, C. Leonelli, Sintering behavior of glass-ceramic frits, Am. Ceram. Soc. Bull. 79 (2000) 88–92.

[4] C.J. Brinker, G.W. Scherer, Sol–Gel Science, Elsevier, 1990.

[5] S.-J.L. Kang, Sintering: Densification, Grain Growth and Microstructure, 2004.

[6] I.B. Cutler, R.E. Henrichsen, Effect of Particle Shape on the Kinetics of Sintering of Glass, J. Am. Ceram. Soc. 51 (1968) 604–604.

[7] M.M. Ristić, S.Đ. Milosević, Frenkel's theory of sintering, Sci. Sinter. 38 (2006) 7–11.

[8] J. Frenkel, Viscous flow of crystalline bodies under the action of surface tension, J. Phys. 9 (1945) 385–391.

[9] A.R. Boccaccini, E.A. Olevsky, Anisotropic shrinkage during sintering of glass-powder compacts under uniaxial stresses: Qualitative assessment of experimental evidence, Metall. Mater. Trans. A. 28 (1997) 2397–2404.

[10] P.M. Raj, A. Odulena, W.R. Cannon, Anisotropic shrinkage during sintering of particle-oriented systems—numerical simulation and experimental studies, Acta Mater. 50 (2002) 2559–2570.

[11] Z. Fu, A. Dellert, M. Lenhart, A. Roosen, Effect of pore orientation on anisotropic shrinkage in tape-cast products, J. Eur. Ceram. Soc. 34 (2014) 2483–2495.

[12] A.R. Boccaccini, Shrinkage anisotropy of glass powder compacts sintered in dilatometers, J. Mater. Res. 13 (2011) 1693–1697.

[13] O. Guillon, S. Cao, J. Chang, L. Wondraczek, A.R. Boccaccini, Effect of uniaxial load on the sintering behaviour of 45S5 Bioglass® powder compacts, J. Eur. Ceram. Soc. 31 (2011) 999–1007.

[14] H.E. Kissinger, Variation of peak temperature with heating rate in differential thermal analysis, J. Res. Natl. Bur. Stand. 57 (1956) 217–221.

[15] A.M.O.R. Senos, Cinética de sinterização nos estágios de porosidade aberta do óxido de zinco, Universidade de Aveiro, Thesis, 1993.

[16] A.R. Boccaccini, W. Stumpfe, D.M.R. Taplin, C.B. Ponton, Densification and crystallization of glass powder compacts during constant heating rate sintering, Mater. Sci. Eng. A. 219 (1996) 26–31.

[17] E.J.C. Davim, A.M.R. Senos, M.H.V. Fernandes, Non-isothermal crystallization kinetics of a Si-Ca-P-Mg bioactive glass, J. Therm. Anal. Calorim. 117 (2014) 643–651.

[18] D.A. Venkatu, D.L. Johnson, Analysis of Sintering Equations Pertaining to Constant Rates of Heating, J. Am. Ceram. Soc. 54 (1971) 641–641.

[19] E.A. Giess, J.P. Fletcher, L.W. Herron, Isothermal sintering of cordierite-type glass powders, J. Am. Ceram. Soc. 67 (1984) 549–552.

[20] A.R. Boccaccini, G. Ondracek, Viscous sintering of non-spherical borosilicate-glass powder, Glas. Berichte. 65 (1992) 73–78.

[21] M.N. Rahaman, L.C. Jonghe, Sintering of Spherical Glass Powder under a Uniaxial Stress, J. Am. Ceram. Soc. 73 (1990) 707–712.

[22] M.N. Rahaman, L.C. De Jonghe, G.W. Scherer, R.J. Brook, Creep and Densification During Sintering of Glass Powder Compacts, J. Am. Ceram. Soc. 70 (1987) 766–774.

Chapter V

"Glass and ceramic vessels are made with fire. If glass vessels break, they are redone, since they have been made through breath. But if ceramic vessels break, they are destroyed, since they have been made without breath."

Gospel of Philip

CHAPTER V

CRYSTALLIZATION KINETICS OF A SI-CA-P-MG BIOACTIVE GLASS BY NON-ISOTHERMAL METHODS

Abstract

In this work the crystallization process of a $3CaO.P_2O_5 – SiO_2 – MgO$ glass was studied by non-isothermal measurements using differential thermal analysis carried out at various heating rates. X-ray diffraction at room and high temperature was used to identify and follow the evolution of crystalline phases with temperature. The activation energy associated with glass transition, Eg, the activation energy for the crystallization of the primary crystalline phase (Ec) and the Avrami exponent (n), were determined under non-isothermal conditions using different equations, namely from Kissinger, Matusita & Sakka and Osawa.

A complex crystallization process was observed with associated activation energies reflecting the change of behaviour during in-situ crystal precipitation. It was found that the crystallization process was affected by the fraction of crystallization (x), giving rise to decreasing activation energy values, Ec(x), with the increase of x. Values ranging from about 580 kJ mol^{-1} for the lower crystallized volume fraction to about 480 kJ mol^{-1} for volume fractions higher than 80 % were found. The Avrami exponents, calculated for the crystallization process at a constant heating rate of 10 ^oC min^{-1}, increased with the crystallized fraction, from 1.6 to 2, indicating that the number of nucleant sites is temperature dependent and that crystals grow as near needle-like structures.

V - Crystallization kinetics of a Si-Ca-P-Mg bioactive glass by non-isothermal methods

These chapter is based on the following publication:

E.J.C. Davim, A.M.R. Senos, M.H.V. Fernandes, Non-isothermal crystallization kinetics of a Si-Ca-P-Mg bioactive glass, J. Therm. Anal. Calorim. 117 (2014) 643–651.

V.1. Introduction

The biocompatibility of many calcium-phosphate glasses and their controllable solubility in physiological fluids make them attractive candidates for biomedical applications [1–3]. A sensible way to control degradation of glasses is to promote the in-situ crystallization of adequate crystalline phases towards the production of a glass ceramic. The nature and relative amounts of crystalline phases and remaining glassy matrix determine the type of dissolution products and influence the response of these glasses when facing biological systems [4]. Crystallization of glasses depends on composition [5–14] but it is mostly affected by the time-temperature programs used in the development of the in-situ crystalline phases. Understanding the crystallization kinetics of bioactive glasses is thus of major importance because it will allow the optimization of the processing parameters and the tailoring of the microstructure that will provide the properties required for each specific application. A number of glasses from the $SiO_2 – 3CaO.P_2O_5 – MgO$ system has been studied by our group [15–17] with confirmed biocompatibility and in vitro bioactivity [16,17]. In some compositions the surface reactivity in a synthetic physiological fluid associated with the precipitation of an apatite-like layer becomes dramatically depressed when crystallizing the glass [18] and this may lead to distinct interfacial responses when in contact with living structures. The aim of this work is to study the crystallization process of the bioactive glass composition 25Si – 33Ca – 11P – 31Mg (mol. %) by determining relevant parameters, such as activation energy and Avrami exponent, through a non-isothermal method – differential thermal analysis (DTA). Kissinger [19], Matusita et al. [20], and Ozawa [21] equations were used to calculate the kinetic parameters and to examine its dependence on the fraction of crystallization [22]. The apparent activation energy associated with glass transition was also assessed from Kissinger and Ozawa methods [19,23,24].

V.2. Materials and Methods

A glass of molar composition 25Si – 33Ca – 11P – 31Mg was produced by the conventional melt quenching technique. A calcium to phosphorus molar ratio of 3:1, close to the equivalent ratio in the natural bone was used. The raw materials consisting of SiO_2 (99.9 %, Fluka), $CaCO_3$ (99.9 %, Fluka), $Ca(H_2PO_4)_2$ (85 %, Fluka) and MgO (99.9 %, Fluka); were ball-milled in an agate mill jar and melted in a platinum crucible at 1500 ºC, for 2 h in air, and poured into water to obtain a frit. The frit was dried, ball milled, and sieved to produce particle sizes ≤ 20 μm. Viscosity measurements were carried out in a beam bending viscometer Bahr Thermo analyse VIS 401) using 5 x 5 x 40 mm^3 samples and a heating rate of 10 ºC min^{-1}. For the crystallization kinetics studies and glass transition analysis,

differential thermal analysis (DTA) was performed in a L81Thermobalance-Linseis thermoanalyser, using 25 mg powdered samples with Al_2O_3 powder as reference material and employing heating rates of 2, 5, 10, 15, 20, 30 and 40 °C min^{-1} in open atmosphere. The instrument was calibrated for the temperature range of 30–1300 °C, using a sample of α-$A1_2O_3$ powder alone.

The crystalline phases, developed after 2 hours stages at the temperature peaks revealed by DTA, were identified by X-ray diffraction (XRD) analysis using a Rigaku "Geigerflex" D/Max- Series C diffractometer with CuKα radiation. The microstructure of the crystallized samples was observed by scanning electron microscopy (SEM), in a Hitachi, Model SU-70 equipment at an accelerating voltage of 25 KeV using fracture surfaces under HCl acid attack for 3 seconds, carbon coated before observation.

The formation of the crystalline phases within the glass was followed by high temperature X-ray diffraction (HT-XRD) using a Philips X'Pert diffractometer, model MRD and also Cu-Ka radiation. Data were collected in a continuous scan type from 10º to 70º, with a step size of 0.02º and a counting time of 1 s per step. The in-situ analysis was performed on glass powders while being heated in air, each 10 ºC from 770 to 900 ºC, using a heating rate of 10 ºC min^{-1} and a dwell time of 45 min per scan.

V.3. Results and Discussion

XRD to the obtained glass frit confirmed its amorphous state as shown in Fig. V.1.

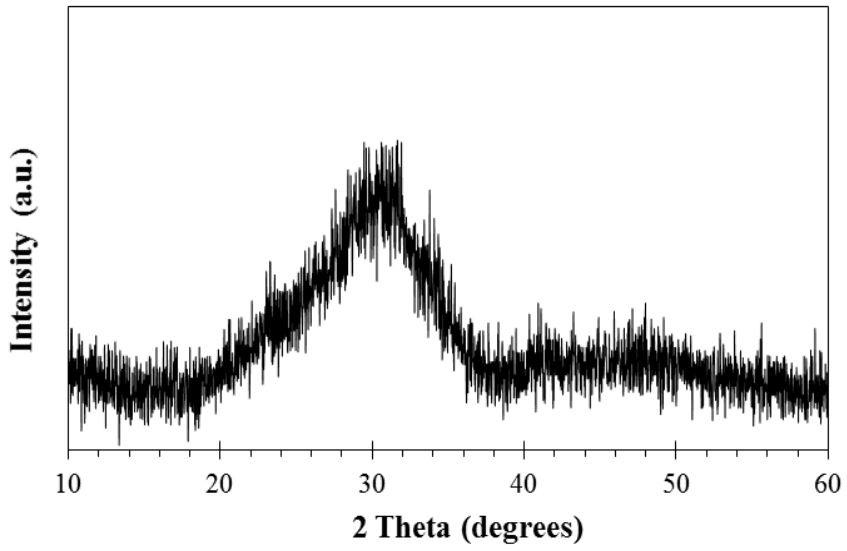

Fig. V.1. X-ray diffraction of the glass frit

DTA traces obtained at different heating rates from 2 to 40 ºC min^{-1} are represented in Fig. V.2. All curves exhibit an endothermic peak associated to a glass transition (not always obvious in the graphs but found with software help from the slope changing in the region 700 – 730 ºC) followed by two distinct exothermic crystallization peaks at higher temperatures strongly dependent on the heating rate. The relevant results concerning the thermal behavior of the glass are depicted in Table V.1. It is observed that the glass transition temperature increases with the increase in the heating rate, and the crystallization peak temperatures are also shifted towards higher values at faster heating rates [25]. It should be emphasized here that, although commonly designated by glass transition temperature or Tg, the heating rate dependent temperatures corresponding to the endothermic events in the DTA traces rather refer to fictive temperatures. Tg is defined on the basis of viscosity, i.e., Tg equals the temperature where viscosity is 10^{12} Pa.s, independently of the heating rate. To measure Tg from DSC or DTA, the respect of ASTM Standards is required, i.e., the heating rate of 10 ºC min^{-1}. This kind of analysis of the fictive temperature dependence on the heating rate, based on DTA traces, is commonly presented in the literature [26,27] because it can provide valuable insights into the understanding of structural relaxation phenomena near the glass transition temperature. In this study we will also adopt the designation Tg for the fictive temperatures associated with the different heating rates.

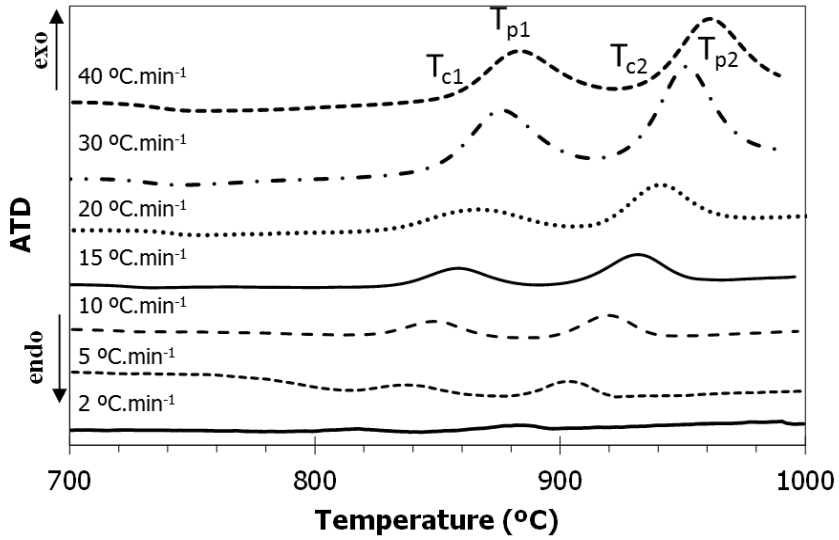

Fig. V.2. DTA traces for the glass powder at different heating rates

Table V. 1. Relevant temperatures obtained from DTA at different heating rates, β

β $^{o}C\ min^{-1}$	T_g (°C)	Tc_1 (°C)	Tp_1 (°C)	Tc_2 (°C)	Tp_2 (°C)
2	705	799	818	850	883
5	706	817	837	883	903
10	708	825	849	898	920
15	713	831	859	906	933
20	714	834	868	917	941
30	720	850	877	927	952
40	721	858	884	937	962

Tg - glass transition temperature, Tc - onset of crystallization temperature and Tp - peak crystallization temperature. 1 and 2 refer to the first and second crystallization peaks, respectively.

In order to identify the crystalline phases associated with the exothermic DTA peaks, powder compact samples were heated at 5 $^{o}C\ min^{-1}$ until 800, 820 and 920 ^{o}C and kept at those temperatures for 2 hours for subsequent XRD analysis at room temperature. The results revealed that no detectable crystallization was achieved before 800 ^{o}C as suggested by the DTA traces and the crystalline phase associated to the first peak corresponds to whitlockite, $CaMg(PO_4)_2$. The second peak is related to the formation of both forsterite and enstatite as minor Mg-silicate phases as shown in Fig. V.3 and Table V.2. The same crystalline phases were found when the powder compact samples were heat treated at 40 $^{o}C\ min^{-1}$ until 885 and 965 ^{o}C and kept at those temperatures for 2 hours, as shown in the XRD pattern, Fig. V.3b.

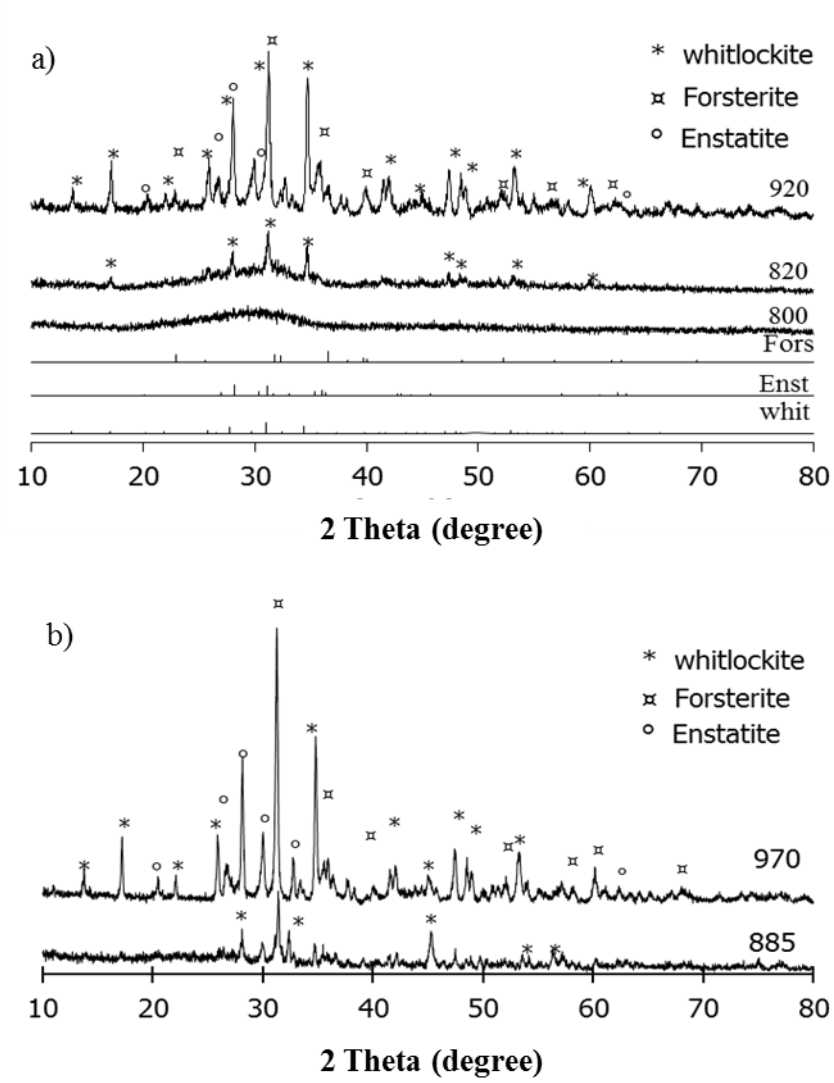

Fig. V.3. X-ray diffraction of glass-powder compacts heat treated at different temperatures with a holding time of 2h and heating rates of a) 5 ºC min^{-1} and b) 40 ºC min^{-1}

Table V. 2. Summary of the different crystalline phases found in the samples after heat treatment at 5 ºC min^{-1} with holding time of 2h at different temperatures

Temperature	Crystalline phases
820	Whitlockite [$(Ca_{2.589}MgO_{0.411})(PO_4)_2$]
840	Whitlockite [$(Ca_{2.589}MgO_{0.411})(PO_4)_2$]
910	Whitlockite [$(Ca_{2.589}MgO_{0.411})(PO_4)_2$]
920	Whitlockite [$(Ca_{2.589}MgO_{0.411})(PO_4)_2$] + Enstatite [$MgSiO_3$] + Forsterite [$Mg_2SiO_4$]

The cross sectional SEM micrographs represented in Fig. V.4 show the crystallization of a needle-like phase after heating up to 840 ºC (Fig. V.4a), probably corresponding to the whitlockite-type phosphate, together with a distinct phase, of polyhedral shape, detected after heat treating the glass at 1000 ºC (Fig. V.4.b), attributed to a magnesium silicate phase. A semi-quantitative elemental analyse by EDS in SEM was performed on the whitlockite and forsterite crystals. The determination of elements in the second phase was more difficult because of the surrounding signal of the primary phase, whitlockite. The two EDS traces are presented below the SEM images in Fig. V. 4, confirming the Ca/P ratio near 1.4 of whitlockite phase and Si/Mg ratio near 2 of the forsterite phase.

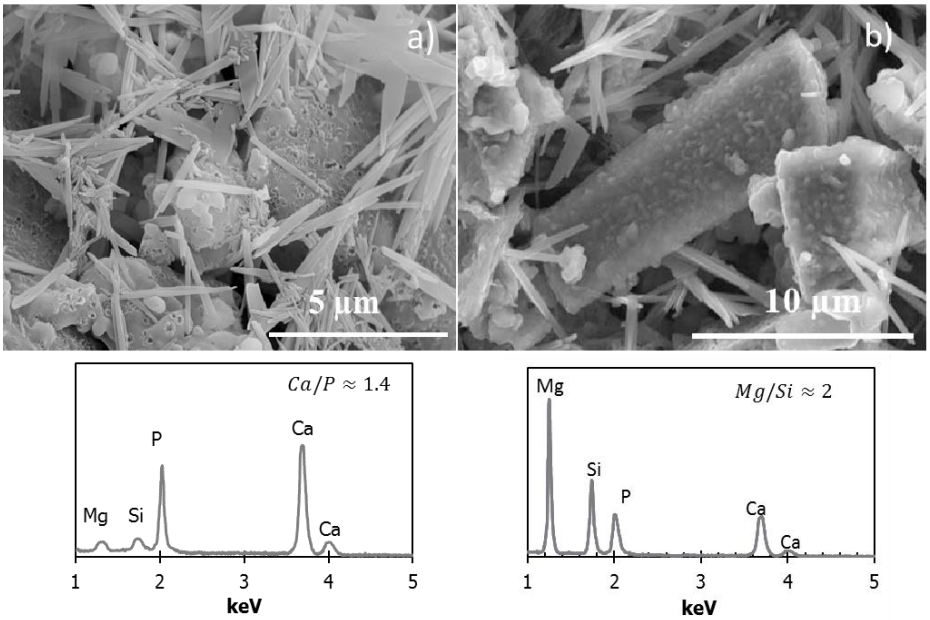

Fig. V.4. SEM micrographs and EDS of crystallized samples obtained by heating the glass-powder compact at 10 ºC min^{-1} up to a) 840 ºC, 2h and b) 1000 ºC, 2h. (Fracture surfaces under HCl acid attack for 3 seconds)

Crystallization was also followed by performing HT-XRD at the heating rate of 10 ºC min^{-1}. As shown in Fig. V.5, crystallization was detected earlier at 760 ºC being the primary crystalline phase the calcium phosphate phase, whitlockite. Forsterite started to precipitate at 900 ºC being more evident at 1000 ºC, associated with the presence of three peaks at 25.4º, 59.0º, and 66.9º. Comparing with the data from the XRD analysis at room temperature, it is shown that both techniques indicate the formation of the same crystalline phases, although at different temperatures. This discrepancy is a consequence of the different thermal cycles used in each analysis and different types of samples (loose powder for the HT-XRD analysis and broken samples previously heated at specific temperatures in the other case).

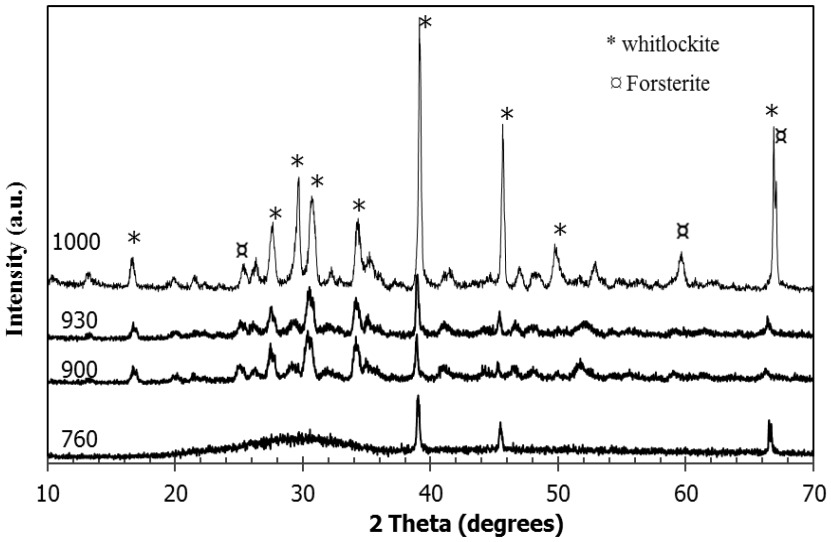

Fig. V.5. Phase evolution over increasing temperature of glass powder in the HT-XRD equipment

V.3.1. Glass transition kinetics

The study of the glass transition kinetics may be carried out through the analysis of activation energy values for thermal relaxation obtained from the variation of fictive temperatures (here generally designated by Tg) with the heating rate, β, using the Kissinger equation and the Moynihan model [24].

According to Kissinger equation, Eq. V.1, the apparent activation energy associated with the glass transition may be deduced from

$$\ln\left(\frac{\beta}{Tg^2}\right)=\left(\frac{-E_g}{RTg}\right)+const \qquad \text{(Eq. V.1)}$$

where E_g is the activation energy for glass transition and R is the ideal gas constant. A plot of $ln(\beta/T_g^2)$ versus 1/Tg should be a straight line, from the slope of which Eg can be determined, as represented in Fig. V.6. The value obtained for E_g is 1105 kJ mol^{-1}.

Another empirical method, suggested by Moynihan et al. [24], to calculate the activation energy for the glass transition, E_g, can be expressed according to the Ozawa method [23] by

$$\ln(\beta)=\left(\frac{-E_g}{RTg}\right)+const \qquad \text{(Eq. V.2)}$$

The difference between Eq.s V.1 and V.2 lies in the first member. Since Tg is β dependent the straight lines given by the plot of ln (β/Tg^2) versus 1/Tg (Eq. V.3) or by ln β against 1/Tg (Eq. V.2) may yield

different slopes thus giving different values for *Eg*. So, the use of Eq. V.2 requires that before submitting the glass to a heating process of rate β, it must be cooled to well below the glass transition region at a rate that should be similar to the heating rate. A plot of ln β against 1/Tg (Fig. V.6) yields an approximate straight line with a slope of –Eg/R, corresponding to an activation energy for the glass transition of 1128 kJ mol^{-1}.

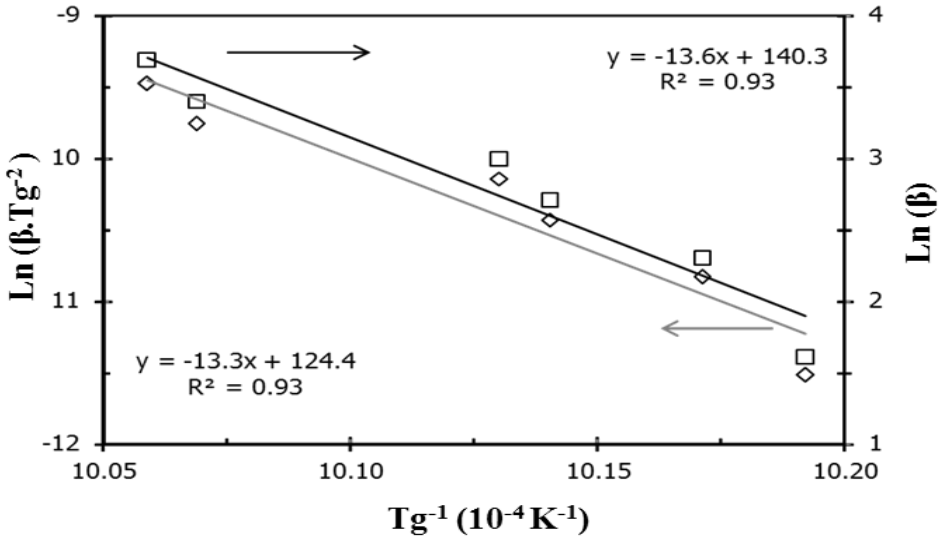

Fig. V.6. Plot of ln(β.Tg^{-2}) and ln β versus 1/Tg for the glass, according to the Kissinger and the Ozawa methods

Both methods give very close values for the activation energy associated with the glass transition, indicating that the thermal behaviour of the glass on heating was dependent on the heating rate but not significantly affected by the previous thermal history, i.e., by the rate at which the glass was cooled below the glass transition region.

V.3.2. Crystallization kinetics

DTA results were used to calculate relevant kinetic parameters of the glass-crystallization transformations, such as the overall crystallization activation energy (Ec) and the order of the reaction or Avrami exponent (*n*). The analysis was focused on the first exothermic peak. Three different equations were used, namely, Kissinger [19], Matusita et al. [28,29] and Ozawa [30]. In all of them, it is assumed that the variation of the peak crystallization temperature, *Tp*, is directly related to the heating rate, β, and that the glass composition does not change as crystallization takes place [14]. Although the first criterion seems to be not questionable, the second condition is difficult to fulfill since composition of the glassy matrix is changing as crystalline phases form. Despite these limitations the proposed analysis is usually accepted because it gives an important contribution for the understanding of crystal nucleation and growth in glass systems. From the Kissinger method, the

activation energy for crystallization, *Ec*, is determined using Eq. V.3 equivalent to Eq. V.1 for the glass transition activation energy, *Eg*

$$\ln\left(\frac{\beta}{Tp^2}\right) = -\frac{Ec}{RTp} + const \qquad \text{(Eq. V.3)}$$

where *Tp* is the crystallization peak temperature at the maximum of crystallization peak and β is the DTA heating rate. A plot of ln (β/Tp^2) vs. $1/Tp$ should be a straight line, from the slope of which *Ec* can be determined. This equation assumes that the crystal growth occurs on a fixed number of nuclei that does not change during heating in the DTA measurements. If the number of nuclei continuously varies while heating the samples, the obtained values for *Ec* may be incorrect. For this case a modified Kissinger equation has been proposed by Matusita et al. [29].

$$\ln\left(\frac{\beta^n}{Tp^2}\right) = -m\frac{Ec}{RTp} + const \qquad \text{(Eq. V.4)}$$

where *n* is the Avrami constant and m is a numerical factor related with the dimensionality of the crystal growth. The values of n and m for various crystallization mechanisms are shown in Table V.2. The value $m = 1$ is considered for one-dimensional growth of crystals or for surface crystallization and $m = 3$ for three-dimensional growth when the crystallization is predominantly bulk. When the number of nuclei is constant during DTA runs at different heating rates, $m = n$ but when nucleation occurs during DTA, $m = n - 1$, being the number of nuclei in the glass inversely proportional to β. In addition, $m = n = 1$ for the particular case of surface crystallization.

Table V. 3. Values of n and m for various crystallization mechanisms [31]

Crystallization mechanism	***n***	***m***
Bulk nucleation with varying number of nuclei [a]		
Three-dimensional growth (polyhedron)	4	3
Two-dimensional growth (plates)	3	2
One-dimensional growth (needles)	2	1
Bulk nucleation with constant number of nuclei [b]		
Three-dimensional growth	3	3
Two-dimensional growth	2	2
One-dimensional growth	1	1
Surface nucleation	1	1

a - The number of nuclei is inversely proportional to the heating rate

b - The number of nuclei does not change with the heating rate

Assuming a constant heating rate, β, the Avrami exponent, n, can be determined using the equation suggested by Matusita et al. [29] for non-isothermal crystallization:

$$\ln[-\ln(1-x)] = 1.052(n-1)\,Ec/RT \qquad \text{(Eq. V.5)}$$

where x is the fraction of crystallized glass, as given by the partial area of the crystallization peak, obtained at a fixed temperature from the DTA plot for the heating rate β. For the various heating rates (2, 5, 10, 15, 20, 30 and 40 ºC min^{-1}) typical sigmoidal curves are obtained (Fig. V. 7a) for the fraction of crystallization, x, versus temperature. At high temperatures, or in cases where crystallization fractions are large, a nonlinear behaviour is seen for all heating rates. This nonlinear character can be attributed to the saturation of nucleation sites in the final stages of crystallization [32,33].

According to Eq. V.5, the plot of ln[-ln(1-x)] versus 1/T for each heating rate should be a straight line [32] of slope $(n-1)Ec/R$. In Fig. V.7, the obtained trends are non-linear independently of the heating rates. This suggests that i) the crystallization mechanism changes with the heating rate (with the number of nuclei most probably varying during heating) and ii) during each DTA run performed at a given heating rate, the crystal growth mechanism depends on the volume fraction of crystallized glass (related with temperature as depicted in Fig. V.7 a. Under a practical point of view, this means that the activation energy, Ec, and the Avrami parameter, n, should vary during the non-isothermal crystallization process of the glass which is further investigated in this work.

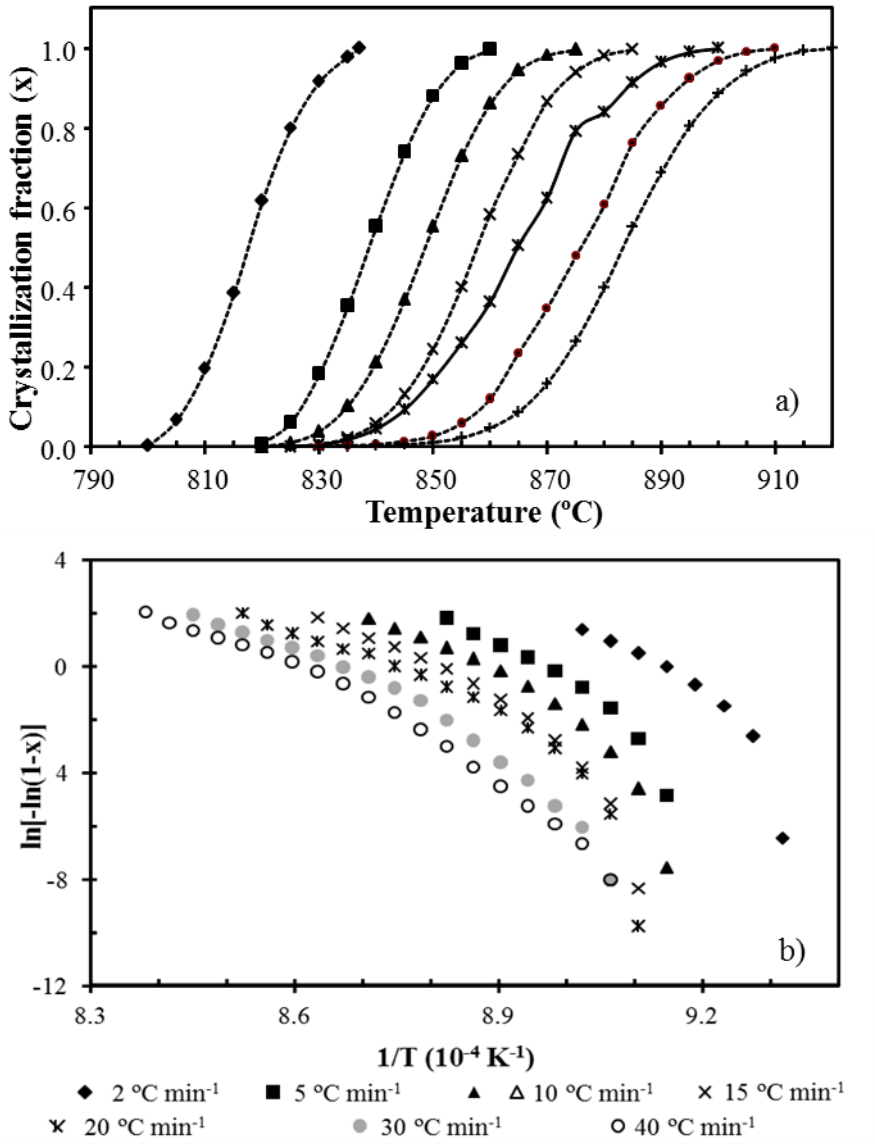

Fig. V.7. Curves for different heating rates of a) the evolution of crystallized volume fraction as a function of temperature and b) ln[-ln(1-*x*)] versus 1/T

V.3.3. Local activation energy

In the present case, as in few other glass systems, the activation energy for crystallization was seen to be dependent on the fraction of crystallization [34,35]. The value of the activation energy should thus reflect the variation of the crystal nucleation and growth mechanism with the volume fraction of crystallized glass. For these cases, the activation energy associated to a crystallization fraction *x*,

$Ec_{(x)}$, is referred as a local activation energy [36] and it can be obtained from the method introduced by Ozawa [23], which is based on Eq. V.2, now written as:

$$\ln \beta = \frac{-Ec_{(x)}}{RT_x} + const \qquad \text{(Eq. V.6)}$$

where T_x is the temperature corresponding to a fixed value of the crystallized fraction, x, at a given β. Using the data in Fig. V. 7 b, at a fixed value of the crystallized fraction, x, the value of $Ec_{(x)}$, can be deduced from the slope of ln (β) plotted against $1/T_x$ .This process can be repeated for various degrees of conversion, allowing to obtaining the $Ec_{(x)}$ values as a function of x. If the crystallization energy $Ec_{(x)}$ is not significantly different for various crystallized fractions x, the existence of a single-step reaction can be concluded. In contrast, different values of $Ec_{(x)}$ with x may indicate a complex non-isothermal crystallization process [34].

Fig. V. 8 represents the $Ec_{(x)}$ versus x dependence, showing that the crystallization fraction has a significant influence on $Ec_{(x)}$, decreasing as x increases. At the initial stages of crystallization of the glass, for example x = 0.1 Ec is 581 ± 10 kJ mol^{-1} and in the range of x = 0.2–0.7, $Ec_{(x)}$ decreases rapidly to about 495 ± 13 kJ mol^{-1}. Beyond this point, the decrease of $Ec_{(x)}$ is rather slow, reaching a quasi-constant value of 482 ± 14 kJ mol^{-1} for crystallization fractions higher than 0.8.

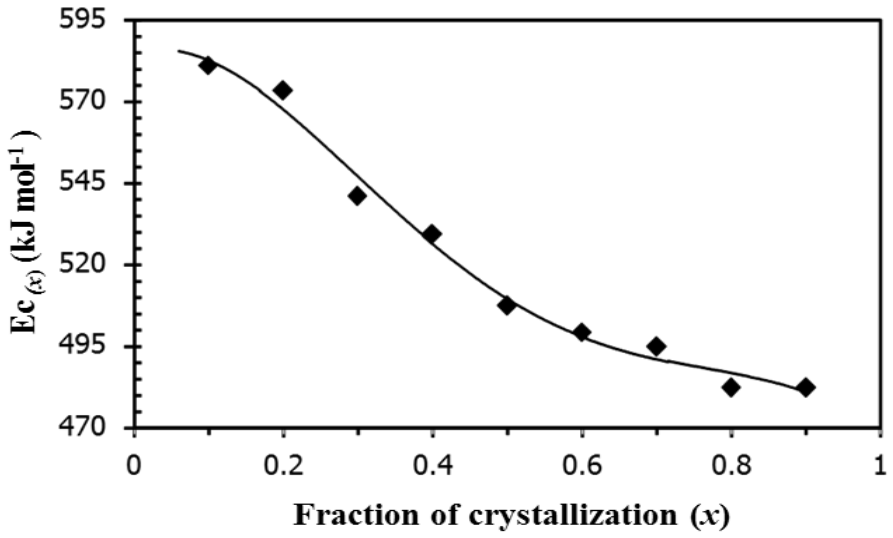

Fig. V.8. Dependence of Ec(x) on the crystallization fraction

The apparent activation energy values found in this work are in fact close to those obtained for other bioactive glasses [37, 38] from systems similar to the one studied in this work. A value of 447 kJ mol^{-1} was found by Yu et al. [39] for the crystallization activation energy in a 32CaO–18P_2O_5–35SiO_2–10MgO–5Al_2O_3 (wt. %) glass composition. For a AW glass-ceramic composition the

activation energy of apatite crystallization has been reported as 514 ± 57 and 482 ± 36 kJ mol^{-1}, for coarse and fine particles respectively [38]. In the commercial bioactive glass, 45S5, the crystallization of $Na_2CaSi_2O_6$, in fine or in coarse powder, was associated with activation energy values of 338 to 230 kJ mol^{-1}, respectively [37]. Although in most literature, activation energy for crystallization is usually compared to activation energy for viscous flow, Eη, there is no consensus in this matter [40,41]. As discussed by Fokin et al [42] the similarity between both values is just an indication that the thermal processes involved are associated with analogous molecular motions, even when considered in different temperature ranges. In fact, this was observed in some glass systems and compositions such as SiO_2–Li_2O [29] but for the 45S5 bioactive glass such similarity was not found [43,44].

For the present glass composition the dependence of viscosity from temperature in the range 710 – 750 ºC is described in Fig. V.10 by the Arrhenian dependence

$$log\eta = log\eta_0 + \frac{E\eta}{2.3RT} \qquad \text{(Eq. V.7)}$$

where η is the viscosity log η_0 is a constant, Eη the activation energy for viscous flow, R the gas constant, and T the absolute temperature.

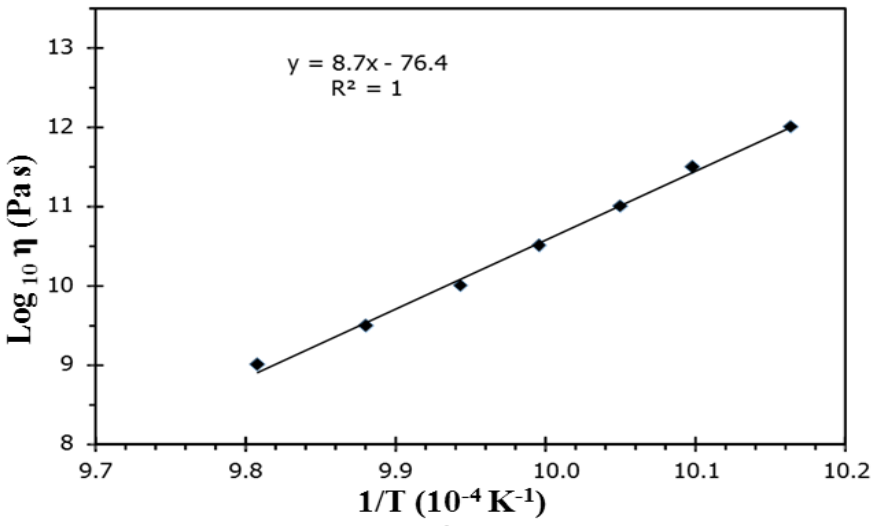

Fig. V.9. Temperature dependence of viscosity. The tests were carried out under stress of 0.45 MPa, at 10 ºC min^{-1}, in a beam bending viscometer

From the experimental viscosity data the glass transition temperature (corresponding to the viscosity of 10^{12} Pa s) is 710 ºC, which agrees with Tg value obtained from DTA trace as shown in Table V. 1.

Within that temperature range (710 – 750 ºC) the value obtained for Eη is around 1700 kJ mol^{-1} .This value is much higher than the apparent activations energies determined before for other temperature

intervals, emphasizing the idea that temperature and thus viscosity should be accounted for to understand molecular diffusion processes in glass systems [42], as discussed in the following paragraphs.

The viscosity data in Fig. 9 can be used for further calculations aiming to interpret the observed crystallization mechanism. The temperature dependence of η may be described by fitting the Vogel Fulcher Tammann (VFT) equation [45],

$$\log \eta = A + B/(T - T_0) \qquad \text{(Eq. V.8)}$$

where A, B and T_0 are constants that depend on the glass composition, and T is the temperature in degrees centigrade. Fitting the experimental data by the least squares method one obtains the values A = -11.85, B = 5902.29 and T_0 = 463.31 in the viscosity range between 10^9 and 10^{12}.

Figure 10 represents a tentative viscosity–temperature curve based on the VFT equation, Eq. V.8, described for the fitting parameters found. Together with the depicted experimental viscosity data, it is emphasized the region corresponding to the crystallization events, i.e., from 825 to 898 ºC as indicated in Table V.1, for the heating rate of 10 ºC min^{-1}.

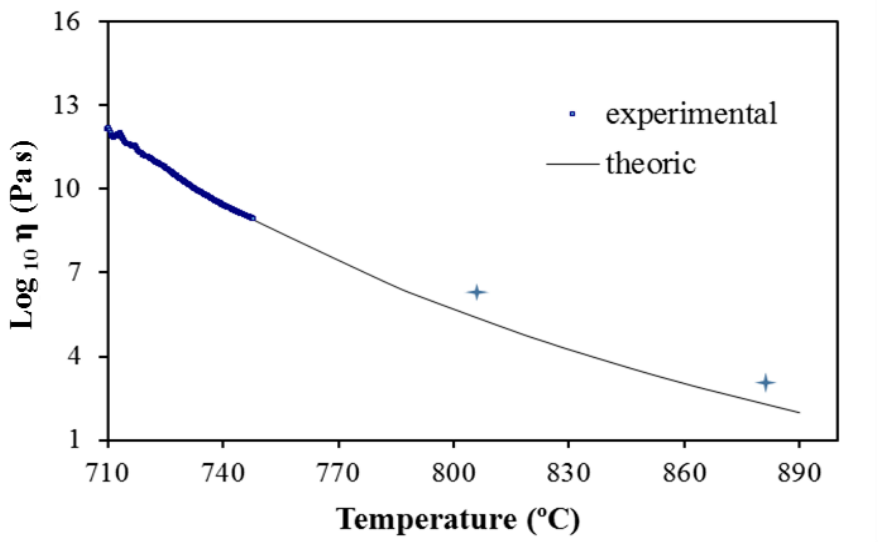

Fig. V.10. Theoretical viscosity-temperature curve based on the VFT equation in the range 10^{12} - 10^2 Pa.s. Depicted experimental data were obtained by a beam bending viscometer in the range of 10^{12} - 10^9 Pa.s. Crosses indicate the range of viscosity-temperature where crystallization takes place

A key question is to know which structural units control crystallization and viscous flow. Being both phenomena controlled by diffusion it should be relevant to have a clear indication on 1) the size and nature of the diffusing building species and 2) the diffusion coefficients of those species in the glass-forming liquid [41]. In a Si–Ca–P–Mg glass, any of the cations and the anion O^{2-} may behave as migrating species. Diameters of all these species are well documented, but diffusion data are scarcely

found in the literature. In the particular case of Ca^{2+} and Mg^{2+}, it is generally accepted that these ions diffuse faster than Si^{4+} and O^{2-}, but this conclusion is inferred by analogy among silicate glasses. In our study, the activation energy for viscous flow Eη in the range 10^9–10^{12} Pa.s (i.e., 710 – 750 ºC) is 1700 kJ mol^{-1} and the apparent activation energy for crystallizations lies in the range 480 – 580 kJ mol^{-1} depending on the crystallized volume fraction. This difference indicates that it is likely that the migrating species at the temperatures at which the viscosity data was collected are not the same that diffuse in the range of temperatures at which crystallization takes place. In fact, larger structural units such as $(SiO_4)_4$ – tetrahedral in different bridging coordination may control viscous flow, and their higher diameter could explain the higher viscosity data measured. Information on the ionic bond strenghts of cation-oxygen pairs in the glass structure may as well give an additional contribution for the understanding of the crystall precipitation within the Si –Ca–P–Mg system [6]. Based on the ionic bond strenghts of P – O and Si – O which are 465 – 368 and 443 kJ mol^{-1} respectively [31,44,46,47], the apparent activation energy values obtained in this work suggest that during crystallization a significant amount of the P – O and Si – O bonds are being restored towards the formation of whitlockite, $CaMg(PO_4)_2$, forsterite, Mg_2SiO_4 and Enstatite, $MgSiO_3$.

V.3.4. Avrami exponent

Taking into account the calculated local activation energy, the Avrami exponents at a heating rate of 10 ºC min^{-1} were determined using Eq. V.9, [35]

$$n_{(x)} = \frac{-R\partial \ln\left[-\ln(1-x)\right]}{Ec_x \partial \ln\left(1/T_x\right)} \qquad \text{(Eq. V.9)}$$

where $n_{(x)}$ is the local Avrami exponent. In Fig. V. 11 the variation of Avrami exponent, $n_{(x)}$, with the fraction of crystallization, *x*, is represented, being clear that it increases from 1.6 ± 0.1 for low *x* to 2.0 ± 0.1 for high *x*. The results indicate that as crystallization proceeds, and thus the crystallized fraction increases, the Avrami exponent increased, corresponding to a crystallization with one-dimensional growth associated to a bulk nucleation with varying number of nuclei, as suggested by the values depicted in Table V.3. In fact, observation of SEM micrographs in Fig. V. 4 suggests that crystals of the primary precipitated phase, whitlockite, appear as long needles in agreement with a preferential one-dimensional growth.

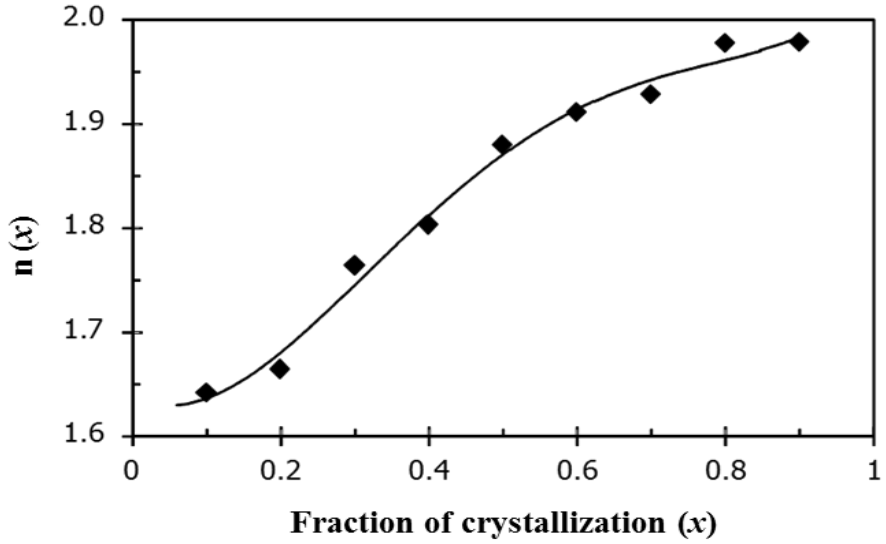

Fig. V.11. Avrami exponent (n) as a function of crystallized fraction (x) at 10 ºC min^{-1}

V.4. Conclusions

The crystallization of a $3CaO.P_2O_5$–MgO–SiO_2 glass was followed by DTA performed at various heating rates. Whitlockite, forsterite and enstatite were the crystalline phases forming on heat treating the glass. The crystallization of the Si–Ca–P–Mg glass starts with the whitlockite phase, and this process was found to be dependent on the amount of the crystallized fraction. The local activation energy values showed to decrease with the increase of the crystallized fraction, from 580 kJ mol^{-1}, for low volume fractions, to about 480 kJ mol^{-1} for volume fractions higher than 80 %. The Avrami parameter increased with increasing crystallized fraction, from 1.6 to 2, indicating that crystallization is mostly in volume and occurs with one-dimensional growth, as confirmed by SEM, from a number of nucleant sites that probably varies during the thermal treatment.

Acknowledgments

This work was financed by FEDER funds through the Operational Programme COMPETE and by FCT - Foundation for Science and Technology funds under the grant SFRH / BD / 48357 / 2008. We also acknowledge the program financing CICECO, Pest-C/CTM/LA0011/2011.

References

[1] E. Dietrich, H. Oudadesse, A. Lucas-Girot, M. Mami, In vitro bioactivity of melt-derived glass 46S6 doped with magnesium., J. Biomed. Mater. Res. A. 88 (2009) 1087–96.

[2] J. Ma, C.Z. Chen, D.G. Wang, J.H. Hu, Synthesis, characterization and in vitro bioactivity of magnesium-doped sol–gel glass and glass-ceramics, Ceram. Int. 37 (2011) 1637–1644.

[3] L. Radev, V. Hristov, I. Michailova, H.M. V. Fernandes, M.I.M. Salvado, In vitro bioactivity of biphasic calcium phosphate silicate glass-ceramic in CaO-SiO2-P2O5 system, Process. Appl. Ceram. 4 (2010) 15–24.

[4] A.C.M. Renno, P.S. Bossini, M.C. Crovace, A.C.M. Rodrigues, E.D. Zanotto, N.A. Parizotto, Characterization and in vivo biological performance of biosilicate, Biomed Res. Int. 2013 (2013) 141427.

[5] M. Sitarz, K. Bulat, M. Szumera, Aluminium influence on the crystallization and bioactivity of silico-phosphate glasses from NaCaPO4–SiO2 system, J. Non. Cryst. Solids. 356 (2010) 224–231.

[6] M. Szumera, I. Wacławska, Effect of molybdenum addition on the thermal properties of silicate–phosphate glasses, J. Therm. Anal. Calorim. 109 (2012) 649–655.

[7] M. Sitarz, K. Bulat, A. Wajda, M. Szumera, Direct crystallization of silicate–phosphate glasses of NaCaPO4–SiO2 system, J. Therm. Anal. Calorim. 113 (2013) 1363–1368.

[8] M. Szumera, I. Wacławska, Spectroscopic and thermal studies of silicate-phosphate glass, J. Therm. Anal. Calorim. 88 (2007) 151–156.

[9] M. Szumera, I. Wacławska, Z. Olejniczak, Influence of B2O3 on the structure and crystallization of soil active glasses, J. Therm. Anal. Calorim. 99 (2009) 879–886.

[10] M. Sitarz, K. Bulat, M. Szumera, Influence of modifiers and glass-forming ions on the crystallization of glasses of the NaCaPO4–SiO2 system, J. Therm. Anal. Calorim. 109 (2012) 577–584.

[11] H. Arstila, E. Vedel, L. Hupa, M. Hupa, Factors affecting crystallization of bioactive glasses, J. Eur. Ceram. Soc. 27 (2007) 1543–1546.

[12] P.F. James, W. Shi, Crystal nucleation kinetics in a 40CaO-40P2O5-20B2O3 glass - a study of heterogeneously catalysed crystallization, J. Mater. Sci. 28 (1993) 2260–2266.

[13] I.M. Reaney, P.F. James, W.E. Lee, Effect of Nucleating Agents on the Crystallization of Calcium Phosphate Glasses, J. Am. Ceram. Soc. 79 (1996) 1934–1944.

[14] A. Clifford, R. Hill, A. Rafferty, P. Mooney, D. Wood, B. Samuneva, et al., The influence of calcium to phosphate ratio on the nucleation and crystallization of apatite glass-ceramics, J. Mater. Sci. Mater. Med. 12 (2001) 461–469.

[15] E. Davim, M.H.F.V. Fernandes, A.M.R. Senos, Preparation of Porous Glass Scaffolds by Salt Sintering Technique, Mater. Sci. Forum. 587-588 (2008) 52–56.

[16] P. Lopes, M. Corbellini, B.L. Ferreira, N. Almeida, M. Fredel, M.H. Fernandes, et al., New PMMA-co-EHA glass-filled composites for biomedical applications: Mechanical properties and bioactivity, Acta Biomater. 5 (2009) 356–62.

[17] J.K.M.F. Daguano, K. Strecker, E.C. Ziemath, S.O. Rogero, M.H. V Fernandes, C. Santos, Effect of partial crystallization on the mechanical properties and cytotoxicity of bioactive

glass from the 3CaO.P(2)O(5)-SiO(2)-MgO system., J. Mech. Behav. Biomed. Mater. 14 (2012) 78–88.

[18] N.A.F. Almeida, M.H.F.V. Fernandes, Effect of Glass Ceramic Crystallinity on the Formation of Simulated Apatite Layers, Mater. Sci. Forum. 514-516 (2006) 1039–1043.

[19] H.E. Kissinger, Variation of peak temperature with heating rate in differential thermal analysis, J. Res. Natl. Bur. Stand. (1934). 57 (1956) 217–221.

[20] K. Matusita, T. Komatsu, R. Yokota, Kinetics of non-isothermal crystallization process and activation energy for crystal growth in amorphous materials, J. Mater. Sci. 19 (1984) 291–296.

[21] T. Ozawa, Applicability of friedman plot, J. Therm. Anal. 31 (1986) 547–551.

[22] M. Fatmi, B. Ghebouli, M.A. Ghebouli, T. Chihi, M. Abdul Hafiz, The kinetics of precipitation in Al-2.4 wt% Cu alloy by Kissinger, Ozawa, Bosswel and Matusita methods, Phys. B Condens. Matter. 406 (2011) 2277–2280.

[23] T. OZAWA, Estimation of activation energy by isoconversion methods, Thermochim. Acta. 203 (1992) 159–165.

[24] C.T. Moynihan, A.J. Easteal, J. Wilder, J. Tucker, Dependence of glass-transition temperature on heating and cooling rate, J. Phys. Chem. 78 (1974) 2673–2677.

[25] A. Marotta, A. Buri, F. Branda, Surface and bulk crystallization in non-isotherml devitrification of glasses, Thermochim. Acta. 40 (1980) 397–403.

[26] K. Majhi, K.B.R. Varma, Crystallization kinetic studies of CaBi2B2O7 glasses by non-isothermal methods, J. Mater. Sci. 44 (2008) 385–391.

[27] K. Majhi, K.B.R. Varma, Crystallization kinetics of SrBi2B2O7 glasses by non-isothermal methods, J. Therm. Anal. Calorim. 98 (2009) 731–736.

[28] K. Matusita, S. Sakka, Y. Matsui, Determination of activation-energy for crystal-growth by differential thermal-analysis, J. Mater. Sci. 10 (1975) 961–966.

[29] K. Matusita, T. Komatsu, R. Yokota, Kinetics of non-isothermal crystallization process and activation-energy for crystal-growth in amorphous materials, J. Mater. Sci. 19 (1984) 291–296.

[30] T. Ozawa, Kinetic analysis of derivative curves in thermal analysis , J. Therm. Anal. Calorim. 2 (1970) 301–324.

[31] M. Erol, S. Küçükbayrak, A. Ersoy-Meriçboyu, The application of differential thermal analysis to the study of isothermal and non-isothermal crystallization kinetics of coal fly ash based glasses, J. Non. Cryst. Solids. 355 (2009) 569–576.

[32] B.K. Money, K. Hariharan, Crystallization kinetics and phase transformation in superionic lithium metaphosphate (Li2O-P2O5) glass system, J. Physics-Condensed Matter. 21 (2009) 1–10.

[33] M.M.A. Imran, N.S. Saxena, D. Bhandari, M. Husain, Glass transition phenomena, crystallization kinetics and enthalpy released in binary Se100-xInx (x=2, 4 and 10) semiconducting glasses, Phys. Status Solidi a-Applied Res. 181 (2000) 357–368.

[34] C. Păcurariu, R.I. Lazău, I. Lazău, D. Tiţa, Kinetics of non-isothermal crystallization of some glass-ceramics based on basalt, J. Therm. Anal. Calorim. 88 (2007) 647–652.

[35] W. Lu, B. Yan, W. Huang, Complex primary crystallization kinetics of amorphous Finemet alloy, J. Non. Cryst. Solids. 351 (2005) 3320–3324.

[36] F. Sun, T. Gloriant, Primary crystallization process of amorphous Al88Ni6Sm6 alloy investigated by differential scanning calorimetry and by electrical resistivity, J. Alloys Compd. 477 (2009) 133–138.

[37] J. Massera, S. Fagerlund, L. Hupa, M. Hupa, Crystallization Mechanism of the Bioactive Glasses, 45S5 and S53P4, J. Am. Ceram. Soc. 95 (2012) 607–613.

[38] S. Likitvanichkul, W.C. Lacourse, Apatite–wollastonite glass-ceramics part I Crystallization kinetics by differential thermal analysis, J. Mater. Sci. 33 (1998) 5901–5904.

[39] B. Yu, K. Liang, A. Hu, S. Gu, Influence of different TiO2 content on crystallization of CaO–MgO–P2O5–SiO2 system glasses, Mater. Lett. 56 (2002) 539 – 542.

[40] A.L. Oliveira, J.M. Oliveira, R.N. Correia, M.H. V. Fernandes, J.R. Frade, Crystallization of Whitlockite from a Glass in the System CaOP 2 O 5 SiO 2 MgO, J. Am. Ceram. Soc. 81 (1998) 3270–3276.

[41] M.L.F. Nascimento, E.B. Ferreira, E.D. Zanotto, Kinetics and mechanisms of crystal growth and diffusion in a glass-forming liquid., J. Chem. Phys. 121 (2004) 8924–8.

[42] V.M. Fokin, M.L.F. Nascimento, E.D. Zanotto, Correlation between maximum crystal growth rate and glass transition temperature of silicate glasses, J. Non. Cryst. Solids. 351 (2005) 789–794.

[43] L. Lefebvre, J. Chevalier, L. Gremillard, R. Zenati, G. Thollet, D. Bernache-Assolant, et al., Structural transformations of bioactive glass 45S5 with thermal treatments, Acta Mater. 55 (2007) 3305–3313.

[44] D.C. Clupper, L.L. Hench, Crystallization kinetics of tape cast bioactive glass 45S5, J. Non. Cryst. Solids. 318 (2003) 43–48.

[45] G. Adam, J.H. Gibbs, On the Temperature Dependence of Cooperative Relaxation Properties in Glass-Forming Liquids, J. Chem. Phys. 43 (1965) 139.

[46] J.M.F. Navarro, El vidrio: Constitución, fabricación, propiedades, 2nd ed., Consejo Superior de Investigaciones Científicas, Sociedad Española de Cerámica y Vidrio, Madrid, 1991.

[47] Y.M. Sung, Nonisothermal phase formation kinetics in sol-gel-derived strontium bismuth tantalate., J. Mater. Res. 16 (2001) 2039–2044.

Chapter VI

"A pessimist sees the difficulty in every opportunity; an optimist sees the opportunity in every difficulty".

Winston Churchill (1874 – 1965)

Chapter VI

INCREASED SURFACE AREA DURING SINTERING OF CALCIUM PHOSPHATE GLASS AND SODIUM CHLORIDE MIXTURES

Abstract

Glass scaffolds were obtained by the salt sintering method, using mixtures of calcium phosphate glass, 25.42 % SiO_2 – 10.89 % P_2O_5 – 32.68 % CaO – 31 % MgO (mol. %), and salt, NaCl, pressed and sintered bellow the salt melting point, followed by leaching of the salt in water. The sintering behaviour of glass/salt powder mixtures was followed by dilatometry, BET and SEM. It was found that the specific surface area (SSA) of supports sintered between 700 – 750 ºC and leached, can be 15 – 50 times higher than that of the glass precursor powder, a very surprising behaviour because it presents the opposite tendency of a typical sintering process. Dilatometric curves showed an unusual expansion from ~450 ºC until ~700 ºC, followed by shrinkage at higher temperatures. This expansion accompanies the observed increase of SSA and the microstructures showed a clear effect of reaction between the glass and the salt with remarkable wrinkling of the glass particle surfaces. This phenomenon was further investigated by using DTA, XRD and FTIR.

*These chapter is based on the following publication:

Davim EJC, Fernandes MHV, Senos AMR. Increased surface area during sintering of calcium phosphate glass and sodium chloride mixtures. J Eur Ceram Soc 2015;35:329–36.

VI.1. Introduction

The use of scaffolds plays a key role in the process of regeneration in tissue engineering [1,2]. The scaffold has to meet certain criteria related to the internal porosity architecture, available surface and mechanical properties. For bone related purposes the scaffold material should also have a suitable rate of degradation and biocompatibility with the bone to be replaced [1–4]. Materials such as metals, polymers, ceramics and composites are commonly used in the manufacture of scaffolds, each one with their advantages and disadvantages [3]. The use of phosphate glasses as scaffolds can be viable, once they have already been used as bioabsorbable implants. A major advantage is their easily adjustable solubility, predictable degradation structure and similar mineral composition to bone tissue [5]. Bioactive glasses are very interesting as they possess both osseointegration and osteoconductive properties although their intrinsic mechanical weakness may represent a serious disadvantage. This critical point can be optimized by microstructural design using the sintering variables [6,7]. Despite the large potential of glass or glass-ceramic scaffolds for bone regeneration applications, the research in those materials is yet incipient [8–10], limiting their application, in contrast with the widespread use of ceramic scaffolds, such as hydroxyapatite (HA) [11–13] and related calcium phosphates (CaP) (e.g., β-tricalcium phosphate) [14–16].

Various methods are commonly used for the preparation of scaffolds with suitable porosity for applications as tissue engineering templates [17,18], such as foam replica technique [10,12,19–21], incorporation of volatile organic particles [22], sol-gel [23], gel-casting techniques [24,25], and salt sintering [26], among others. In all the methods to produce 3D structures from glass particles it is necessary a sintering step to consolidate the scaffold [8,9,26]. As a result of the relatively high temperatures required for sintering [19], the achievement of porous supports with adequate mechanical resistance and keeping the former glass structure is a challenging task. More and deeper research on the processing understanding and control is clearly missing.

Among the several available methods, the salt sintering process appears as very attractive due to its versatility and simplicity. The method consists of mixing glass particles with a certain proportion of soluble salt particles which serves as porogen, such as NaCl, $MgSO_4$ and K_2SO_4 [27,28]. This mixture is then compressed and sintered. After sintering, the salt particles are dissolved in water, leaving interconnected pores in the structure. This technique, initially used in the manufacture of glass membranes for microfiltration, to remove contaminants from agro-industry, showed the ability to be further applied in the production of materials for various areas of biotechnology and medicine. Depending on the ratio glass/salt and particle size distribution, the salt sintering technique allows the preparation of porous materials with large amount of interconnected macroporosity, up to 75 vol. % [27,28]. The selected salt must have a suitable particle size, a

melting temperature higher than the temperature needed for the scaffold consolidation and a high solubility in a solvent in which the glass is insoluble. The pore size distribution will be dependent on the size distribution of the salt particles. In this work, the sintering of calcium phosphate glass and sodium chloride powder mixtures to obtain porous glass scaffolds was investigated by following the salt sintering method.

VI.2. Material and methods

A 32.68 % CaO – 10.89 % P_2O_5 – 25.43 % SiO_2 – 31 % MgO (mol. %) glass was produced via the conventional melt quenching technique. The raw materials were ball-milled in agate mill jars and melted in a platinum crucible at 1500 ºC, for 2 h, in air, and poured into water to obtain a frit. The frit was ball milled, and sieved to produce a glass powder with particle size below 20 µm. Sodium chloride was used as porogen, supplied by BDH, Middle East LLC, with a purity of 99 %.

The evaluation of the particle size distribution of the glass was made by laser diffraction in a Coulter LS 230 Particle Size Analyser, Fraunhofer optical model, Amherst, MA. The specific surface areas of the glass powder and salt were determined by physical adsorption of nitrogen gas, using the Brunauer, Emmett and Teller (BET) method. For those tests, a Quantachrome Quantasorb equipment, Germany, was used, and before determining the volume of adsorbed gas, powders were kept under vacuum at 200 °C, for 4 h. The real density of the glass powder was evaluated by a helium pycnometer model Accupyc 1330-Micrometrics.USA.

The microstructures of the glass and salt powders were characterized by scanning electron microscopy (SEM), in Hitachi, Model SU-70, Germany. For the observation of glass powders, a powder suspension (0.1g/10ml 2-propanol) was prepared and deposited on an aluminium sample holder. For the observation of powdered sodium chloride, the salt was deposited in a double-adhesive tape face of carbon. All samples were coated with a carbon thin film by deposition in an EMITECH K950 device.

Mixtures of glass and salt in varied proportions, from 10 up to 90 wt. % NaCl, were prepared by mechanical mixing, during 15 min, in a turbula shaker-mixer, from Glen Mils, USA. The mixtures were designated in accordance to the amount of salt, as presented in Table V.1. The theoretical density of the glass: salt mixtures was calculated by the mixture rule, taking into account the determined real density of the glass powder, and the sodium chloride density indicated by the supplier. Differential thermal analysis (DTA) of the glass, salt and mixtures were performed in a Labsys Setaram TG-DTA, France, using 25 mg powdered samples, Al_2O_3 powder as a reference material, and a heating rate of 5 ºC min^{-1}, from 25 to 900 ºC. Cylindrical green bodies (10 mm diameter and 10 mm thick) of the glass/salt mixtures were shaped by uniaxial pressing at 175 MPa,

for 30 sec. The green density for the GS50 compacts was geometrically determined to be 1.64 g cm^{-3}.

Table VI. 1. Samples designation and amount of salt.

Samples name	wt. % salt
G	0
GS10	10
GS30	30
GS50	50
GS60	60
GS70	70
GS90	90
S	100

The sintering behaviour of the compacts was investigated by dilatometry, using a Bahr DIL801L dilatometer, Hüllhorst, Germany, at a constant heating rate of 5 ºC min^{-1}, until a maximum temperature of 800 ºC, in air. The sintered samples were leached in a water bath, at 30 ºC, for 3 days, to remove the salt fraction and produce a structure with interconnected pores. The microstructure of the obtained scaffolds was observed by SEM and the specific surface area was determined by BET with the above refereed equipment.

The apparent density of scaffolds with high enough consolidation to maintain the structural integrity after immersion in water was calculated by the geometric measurement of the apparent volume. The correspondent porosity was calculated considering the measured value of 2.65 g cm^{-3} for the glass real density. The Fourier-transform infrared spectroscopy (FTIR) spectra were collected using a Bruker IFS 28 EQuinox spectrometer, Germany, in transmittance mode in the mid-IR region (4000 – 650 cm^{-1}). Room temperature XRD analysis (Rigaku D/Max-B, Cu Kα, Japan) was also conducted to investigate the possible crystallinity of the fabricated glass powder and scaffolds.

VI.3. Results and Discussion

VI.3.1. Characterization of the glass and salt powders

The glass powders, after crushing and sieving, Fig. VI.1a, are predominantly composed of angular particles with irregular shape. The glass particles have a wide size distribution, ranging from ~0.04 to 20 μm and average particle size, D_{50} = 6.8 μm, as determined by laser diffraction. A value of 0.8 $m^2.g^{-1}$ was found for the specific surface area, Table VI.2.

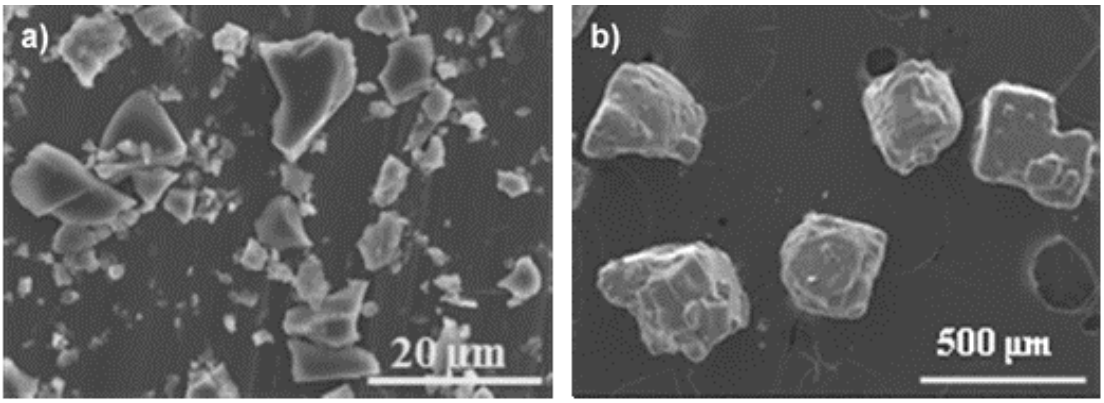

Fig. VI.1. SEM micrographs of the glass (a) and salt particles (b)

Fig. VI.2 shows the DTA curve for the glass powder obtained at a heating rate of 5 ºC min^{-1}. It can be observed in Fig. VI.2a, for the glass powder, an endothermic deflection in the temperature range of 706 – 726 ºC, which corresponds to the glass transition region, with an average value at 716 ºC. Later, an exothermic phenomena starting near 817 ºC is observed, with two peaks at 837 and 903 °C in the curve of Fig. VI.2a. These exothermic peaks are associated with the complex crystallization phenomena of this glass, occurring in two stages, as reported in another study [29]. Those and other characteristics of the glass powder are summarized in Table VI.2.

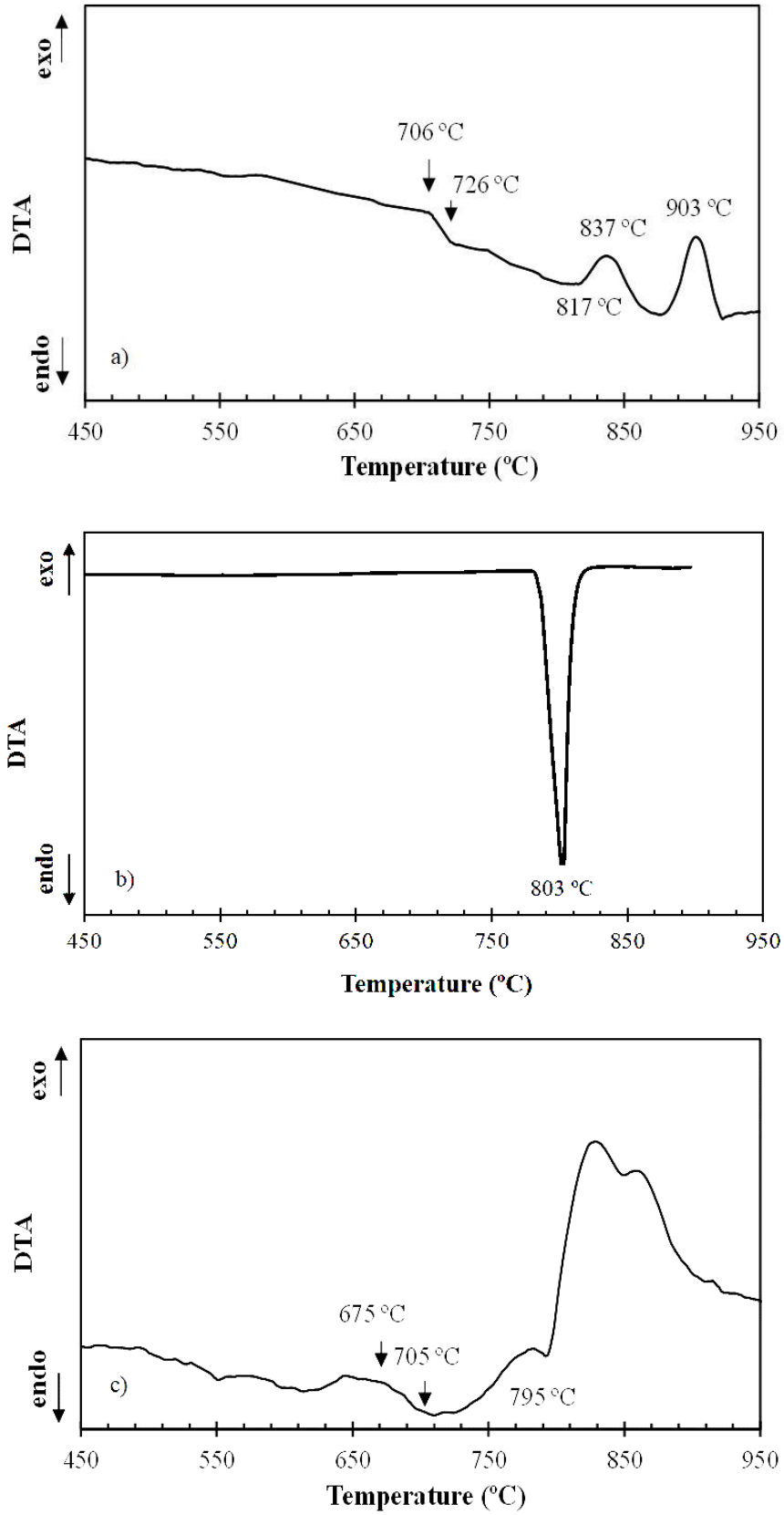

Fig. VI.2. DTA curves of the glass (a) salt (b), and of the mixture GS50 (c), using a constant heating rate of 5 ºC min^{-1}

The SEM micrograph of the salt particles, after sieving, Fig. VI.1b, shows that they have a polyhedral shape with dimensions varying between 220 and 500 μm and are aggregates of smaller crystals. Fig. VI.2b presents the DTA curve of the salt with a well-defined endothermic peak near 800 ºC, corresponding to the salt melting. Other physical characteristics of the salt powders are also summarized in Table VI. 2.

Table VI. 2. Characterization of the glass, salt and GS50 powders.

	ρ **(g cm^{-3})**	**SSA** **(m^2 g^{-1})**	**D** **(μm)**	**Tg (ºC)** **DTA**	**Tc$_1$ (ºC)** **DTA**	**Tm (ºC)** **DTA**	**α $_{100-400}$** **(10^{-6} ºC^{-1})**
Glass	2.65	0.8	6.8**	~ 706	817	-	8
Salt	2.16*	-	220–500***	-	-	800*	43
GS50	2.38	-	-	~ 675	795	-	29

ρ – true density; SSA – specific surface area; D - average particle size; Tg - glass transition temperature; Tc$_1$- onset of crystallization temperature; Tm- melting temperature, α - linear thermal expansion coefficient; *commercial information, ** D_{50}, Coulter, and *** SEM

VI.3.2. Thermal Behaviour of the Glass and Salt Mixtures

It can be observed in Fig. VI.2c, that the endothermic deflection, corresponding to the glass transition region, shifts to a lower temperature range, 675-705 ºC, average 690 ºC in Table VI.2. The onset temperature of crystallization, ~795 ºC occurred also at lower temperatures when compared with the glass curve in Fig. VI.2a and the respective temperature in Table VI.2. The anticipation of both phenomena, glass transition and crystallization, suggests that the glass structure is probably affected by the presence of the salt.

The hastening of the glass crystallization in the presence of salt was confirmed by the XRD spectra of a mixture GS50, after sintering at 5 ºC min^{-1} up to 760 ºC and 800 ºC and leaching, when compared with the XRD of the glass powders submitted to sintering up to 800 ºC, in Fig. VI.3. It can be observed that the glass presents an amorphous structure up to 800 ºC, whereas the peaks corresponding to the calcium phosphate crystallization, although incipient at 760 ºC become defined at 800 ºC in the spectrum of the glass after heated with the salt.

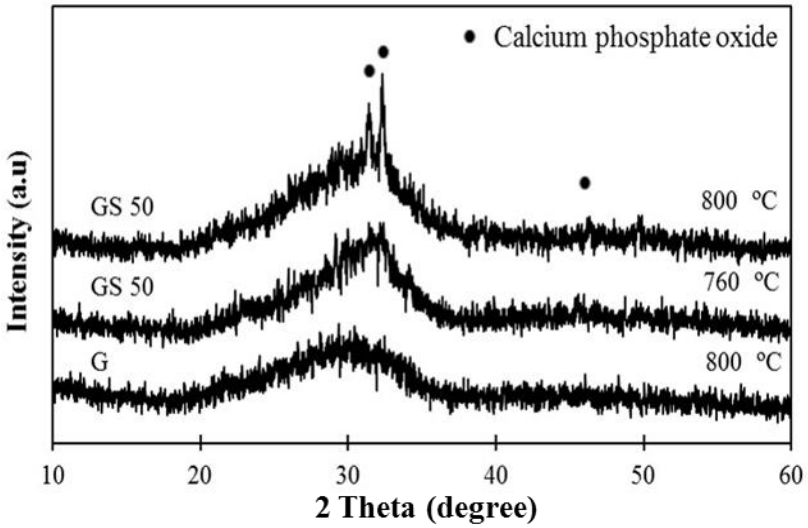

Fig. VI.3. Diffractogram of the glass, G, after heating until 800 ºC and of the mixture GS50 after sintering up to 760 and 800 ºC and leaching

Fig. VI.4 shows the dilatometric curves of glass-salt pressed compacts with different salt contents, from 10 until 90 wt. %, heated at 5 °C.min^{-1} to a maximum temperature of 800 °C. For comparison, it is also shown in Fig. VI.4a, the dilatometric curves of a glass compact, G, to a maximum temperature of 900 ºC and another of a salt compact, S. It is observed in Fig. VI.4 that the addition of salt increases the thermal expansion of the compacts, as expected by the effect of the higher thermal expansion coefficient of the salt, when compared with that of the glass: a linear thermal expansion coefficient of 8 x 10^{-6} °C^{-1} was determined for the glass in the range of 100 – 400 °C, whereas a value of 43 x 10^{-6} ºC^{-1} (~5 times higher) could be calculated for the salt particles compact (S) and an intermediate value of 29 x 10^{-6} °C^{-1}, Table VI.2, was found for GS50 in Fig. VI.4.

In addition, for compacts with salt contents from 30 to 70 wt. % and temperatures in the range of ~ 450 to 720 °C, the dilatometric curves present a sharp expansion at those temperatures, losing the quasi-linear behaviour of the characteristic curves for salt or glass compacts. This expansion is not reported in literature and will be further analysed ahead. It is also observed that the total shrinkage is progressively decreasing when increasing the level of added salt, suggesting that the salt particles act as rigid inclusions hindering the glass viscous flow and, consequently, the densification of the compact. The glass compact shrinks up to ~ 850 ºC with a total amount of shrinkage ~ 14.5 %, whereas the glass/salt compacts densify until ~ 780 ºC and exhibit much lower shrinkage values: for 30 wt. % salt the shrinkage percentage is ~ 4.7 % and above this percentage, from 50 to 70 wt. % salt, the compacts exhibit even lower shrinkage values of ~ 2 % (the shrinkage values were calculated considering the difference between the length of the sample at the maximum expansion

and the length at the maximum shrinkage in the dilatometric curves, normalized for the initial length).

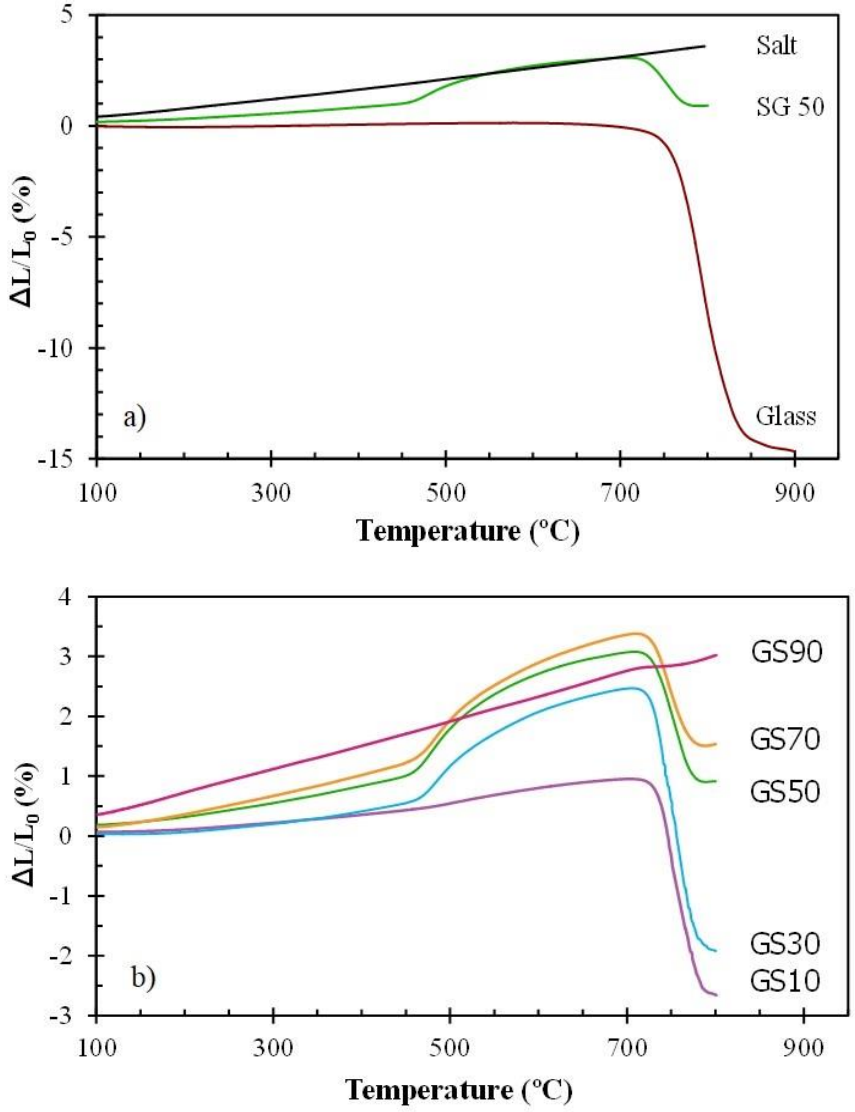

Fig. VI.4. Dilatometric analysis of samples with a) 0, 50 and 100 % salt and b), different percentages of salt at a heating rate of 5 °C min^{-1}

Another interesting observation is that the shrinkage of the glass in Fig. VI.4a significantly decelerates at temperatures of 820 – 830 ºC, a behaviour which, in viscous sintering, is normally associated to the sudden decrease of mobility within the glass due to the beginning of the glass crystallization [30,31]. With the introduction of salt, shrinkage decelerates earlier, at ~ 790 ºC. This behaviour is in accordance with the observed hastening of the onset of crystallization shown in the DTA and XRD results, and is associated to reaction effects between the glass and the salt during

the heating stage. Dilatometric analysis is a good tool to detect many thermal reactions upon heating [32,33]and the above reported expansion can be related to those reaction effects, as well.

Further investigation of the expansion phenomena during the sintering of the glass-salt mixtures was performed on the GS50 mixture. Table VI.3 shows the linear expansion, $\Delta l/l_0$, and the corresponding specific surface area, SSA, and porosity of the leached porous structures sintered at different temperatures and holding times. Values for SSA of known glassy porous structures from other works are not greater than 1.6 $m^2\ g^{-1}$ after sintering, typically an order of magnitude below the values here reported [34]. The obtained values of SSA are significantly increased up to 700 - 740 ºC, Table VI.3 and Fig. VI.5. Above 740 ºC, the reduction of the specific surface area indicates that the effect of sintering in decreasing the surface area overlaps the effect produced by the presence of salt during heating. Accordingly, the reduction of SSA is accompanied by shrinkage of the sample, Fig. VI.5, and correspondent decrease of porosity, Table VI.3. Despite the limited pore removal during sintering of the glass/salt mixtures, well consolidated glass scaffolds can be reached by sintering at temperatures in the range 700 – 760 ºC, as shown in Fig. VI.6, with reported mechanical resistance compatible with its application in bone tissue engineering [7].

Table VI. 3. Shrinkage and specific surface area of supports from mixtures with 50 wt. % salt, after leaching, for varied sintering conditions

T (ºC)	Sintering time (min)	$\Delta l/l_0$ (%)	Specific surface area ($m^2\ g^{-1}$)	Porosity (%)
100	0	0	1.8 ± 0.1	N.A
300	0	0.09 ± 0.1	5.2 ± 0.2	N.A
450	0	1.0 ± 0.1	10.3 ± 0.9	N.A
550	0	2.1 ± 0.1	15.7 ± 0.2	N.A
650	0	3.2 ± 0.1	40.6 ± 0.1	74.1 ± 0.5
700	0	3.5 ± 0.3	45.0 ± 0.2	75.5 ± 0.3
740	0	3.7 ± 0.2	47.3 ± 1.6	75.2 ± 0.2
750	0	3.2 ± 0.3	37.5 ± 2.0	64.9 ± 0.1
	5	2.9 ± 0.3	20.1 ± 0.2	65.1 ± 0.2
	10	1.7 ± 0.4	12.2 ± 0.1	64.3 ± 0.3
800	0	0.9 ± 0.1	9.0 ± 0.4	64.0 ± 0.3

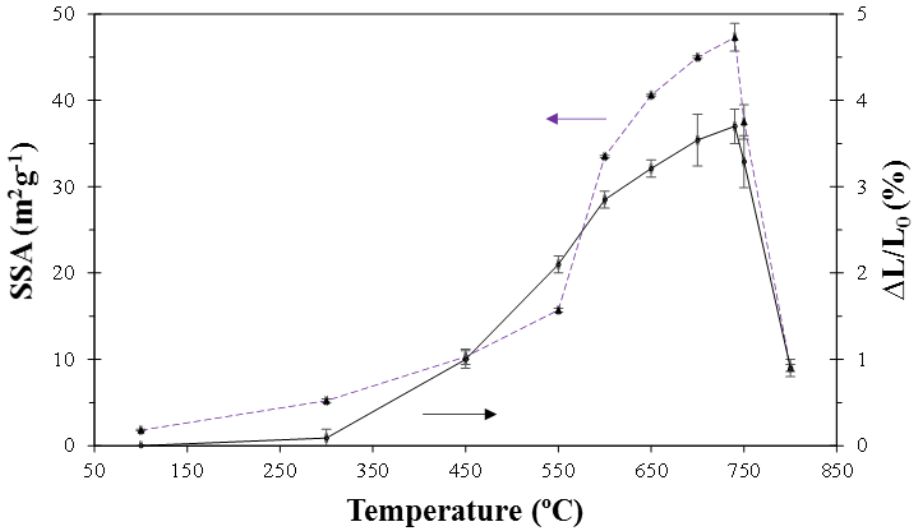

Fig. VI.5. Shrinkage and specific surface area of supports, after leaching, in function of the sintering temperature (heating rate of 5 ºC min^{-1}) from mixtures with 50 wt. % salt

SEM observation of the fracture surfaces of GS50 compacts sintered at 750 ºC, for 10 min, after salt leaching, was performed and representative images are shown in Fig. VI.6a-c. In Fig. VI.6a it can be observed, the general microstructure of the scaffold presenting a consolidated porous glass structure with large pores up 500 μm. These large pores were created by the salt leaching after sintering. By inspecting the pores surfaces in Fig. VI.6 b and c it can be observed that they present high roughness, suggesting again that during the thermal treatment the sodium chloride reacted with the glass surface, promoting the wrinkling of the surface with the consequent increase of the respective area. For comparison, the microstructure of a glass compact, G, also sintered at 750 ºC is presented in Fig. VI.6d and, in this case, a high dense microstructure with particles of irregular shape but a smooth surface are observed.

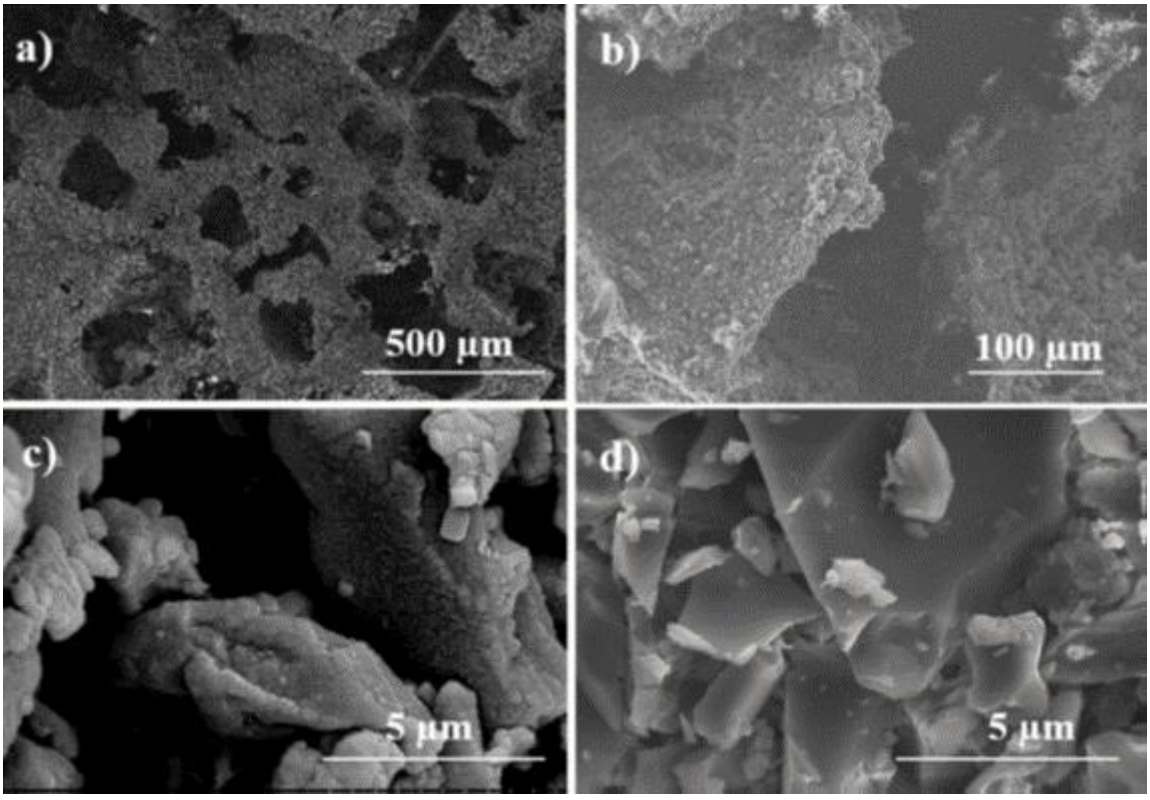

Fig. VI.6. SEM micrographs of the GS50 ((a)–(c)) and G (d) powder compacts sintered at 750 ºC, for 10 min

VI.3.3. Glass/salt reaction

To study the glass/salt reaction, porous structures GS50 were sintered (i) at 450 ºC, where the abnormal expansion phenomenon becomes significant in Fig. VI.4, and (ii) after the maximum of expansion effects, at 760 ºC. After leaching, all samples were analysed by FTIR. For comparison, it was also analysed the parent glass powder, G, without heat treatment and sintered at 760 ºC, respectively. The spectra of all the samples are presented in Fig. VI.7 and Table VI.4 summarizes the main bands found in those spectra.

In the glass without heat-treatment, G, and glass sintered at 760 ºC, the main absorption band at 1000 – 1200 cm^{-1} corresponds to Si – O – Si stretching vibration [35,36]. The bands from 940 to 925 cm^{-1} are assigned to the Si – O symmetric stretch (non-bridging oxygen, NBO) with one non-bridging oxygen per SiO_4 tetrahedron (Q^3 groups) [37–39]. The band, centred at 551 cm^{-1} can be assigned to the presence of bending modes of PO_4 amorphous phosphate. For the glass sintered at 760 ºC, there's also the band centred at 603 cm^{-1}, attributed to the presence of PO_4 groups. The band seen at 1370 cm^{-1} in G is attributed to $(CO_3)^{2-}$ groups present due to the superficial carbonation of calcium in atmospheric CO_2. By comparing the two spectra of the glass without and with heat-treatment at 760 ºC, it can be concluded that they are similar and at this temperature the

glass is essentially amorphous, in agreement with the DTA results, Fig. VI.2a, where the crystallization process was identified to start at ~825 ºC and the XRD results, in Fig. VI.3, showing that the glass doesn't present phase crystallization up to 800 ºC.

When the glass was sintered in the presence of salt, GS50, at 450 ºC, the bands are essentially the same as observed for the glass, G, before and after sintered, although some peaks at 558 and 605 cm^{-1} start to form and are attributed to the formation of an amorphous phosphate phase. However, it is for the glass sintered in the presence of salt at 760 ºC, that a well differentiated spectrum is observed, clearly distinct from the one of the glass, G, and also from that of the GS50 at 450 ºC. First of all, all the bands are sharper than in the other spectra, indicating a higher degree of structural organization, the beginning of crystallization suggested in Fig. VI.3. Additionally, the peaks attributed to the phosphate phase, at 560 and 606 cm^{-1}, are now well defined and a shoulder appears at 571 cm^{-1} which is associated with the asymmetric stretching vibrational mode of phosphate groups (P – O – P) related to the presence of crystalline phosphates in the glasses, in agreement with the expected first crystallization of a phosphate-based at temperatures close to 760 ºC (DTA and XRD results, Figs. 2 and 3). Furthermore, Si – O bands, from 750 – 1100 cm^{-1} are now clearly splitted into sharper bands with peaks in the range 850 – 950 cm^{-1} corresponded to Si – O – 2NBO (non-bridging oxygen) vibrational modes associated with alkali ions in the glass network and two well-defined bands at 1050 and 1090 cm^{-1}, attributed to the symmetric stretching mode Si – O^- and to the asymmetric stretching mode Si – O – Si, respectively, which are indicative of disintegration of the glass structure surface in contact with the salt.

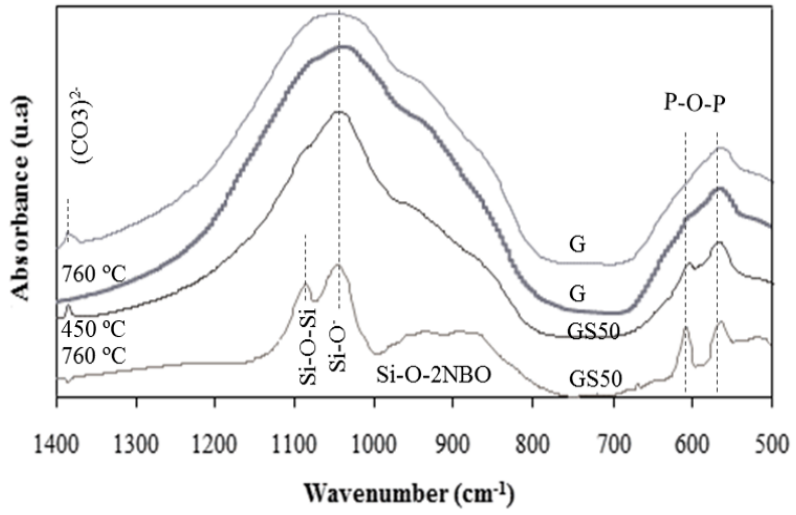

Fig. VI.7. FTIR spectra of the parent glass powder, G, and glass powder compact sintered at 760 ºC, G760, and of the porous structures sintered at 450 and 760 ºC, GS450 and GS760, respectively

Table VI. 4. IR Absorptions main peaks of spectra in Fig. VI.8 [26,36,40,41]

Wavenumber (cm^{-1})	**Assignment**
500 - 560	Bending mode P – O – P
560 - 615	Asymmetric stretching mode P – O – P
720 - 840	Si – O – Si (Tetrahedral)
725 - 770	Symmetric stretching mode P – O – P
860 - 970	stretching mode Si – O
1000	Symmetric stretching $(PO_3)^{2-}$
1045 - 1060	Symmetric stretching mode Si – O^-
1085 - 1100	Asymmetric stretching mode Si – O – Si
1100	Asymmetric stretching mode $(PO_2)^-$
1370	$(CO_3)^{2-}$ groups

These results clearly show that relevant physical and chemical reactions have occurred during the thermal processing of the glass/ salt mixture in the regions of contact between the salt particles and the glass, as already confirmed by the DTA and XRD, together with the dilatometric curves and SEM analysis presented before.

The calcium phosphate crystalline phase is formed from the glass structure but it is likely that the sodium chloride react with the glass surface, inducing the occurrence of surface crystallization. The detection by FTIR of organized phosphate ions and the formation of non-bridging oxygen, incipient after sintering at 450 ºC but well defined at 760° C, and the earlier glass crystallization in the XRD spectrum, together with the effect of expansion in dilatometric curves are strongly indicative of a disruption of the glass structure surface in contact with the salt. The chemical composition of the glass and porogen used favour the occurrence of a reaction between the glass and the salt, which extent will be dependent on the salt fraction in the mixture and other processing variables, namely temperature and time of heat treatment. This reaction is responsible for the unusual surface modifications of the glass particles that gives rise to the exceptional specific surface area of the obtained porous structures. This is a unique feature, since it was obtained during the sintering heat treatment, which commonly occurs with reduction of SSA and not with the significant increase of

that parameter, as here observed. The increase of the SSA was physically correspondent to an unusual wrinkling of the inner walls of the macropores, as observed in Fig. VI.6.

Based on the reported results, a reaction involving the vitreous network and the alkaline salt (alkaline reaction) is proposed which is schematically represented by, Eq. VI.1.

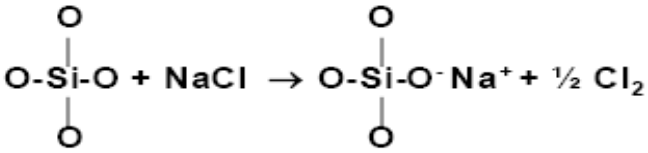

(Eq. VI.1)

This reaction will produce the disruption of the glass structure at the particles surfaces and the formation of chlorine gas causing the expansion phenomenon observed in the dilatometric curves, Fig. VI.4, and the wrinkling of the surfaces. Additionally, these changes in the glass structure promote the decrease of the glass transition temperature, Tg, and the anticipation of the organization of the amorphous structure towards a crystallized one at lower temperatures.

This phenomenon of glass-salt reaction is of high technological interest for the production of glass and glass-ceramic supports for different applications, namely for bone tissue engineering purposes. The exceptional surface area available after sintering provides a higher contact with the surrounding physiological fluids and cells, creating the required conditions for a sustainable formation of new bone. Increasing the specific surface area and pore volume of bioactive glass scaffolds greatly contributes for the acceleration of mineralization and therefore enhances its bioactive behaviour [42]. Studies in this area are a vast field of research to be explored in the future.

VI.4. Conclusion

Glass scaffolds were produced by the salt sintering method, using a mixture of calcium phosphate glass, 25.42 % SiO_2 – 10.89 % P_2O_5 – 32.68 % CaO – 31 % MgO (mol. %), and NaCl as porogen, in proportions varying from 10 up to 90 wt. %. The porous supports were obtained by pressing and sintering the mixture bellow the salt melting point, followed by the leaching of the salt particles in water.

The sintering behaviour of the glass: salt mixtures was investigated by dilatometric analysis and showed an unusual expansion from ~450 ºC until ~760 ºC in the mixtures of glass and salt, followed by shrinkage at higher temperatures where sintering is prevalent. This expansion is accompanied by an increase of the scaffolds specific surface area, SSA, during heating up to ~760 ºC, and it was found that the SSA values for the supports made from mixtures with 50 wt. % of salt,

after sintering at temperatures between 700 – 750 ºC and leaching, are 15 – 50 times higher than the corresponding to the glass precursor powder, a very surprising behaviour because it presents the opposite tendency of a typical sintering process. The microstructural analysis of these supports by SEM also showed a remarkable wrinkling of the glass particle surfaces. Additionally, results of differential thermal analysis, DTA, of the mixtures and X-ray diffraction, XRD, Fourier-transform infrared spectroscopy, FTIR, of supports sintered at different temperatures showed net alterations of the glass structure during heating in the presence of salt, with lowering of the glass transition temperature, Tg, and anticipation of the glass crystallization phenomena. Based on the reported results, a reaction involving the glass network and the alkaline salt is proposed, in which, a structural disruption of the glass surfaces takes place, with formation of chlorine gas that causes the expansion phenomenon observed in the dilatometric curves. That reaction would be also responsible for the increase of the SSA by the wrinkling of the surfaces and for the creation of preferential crystallization sites at the surface. This phenomenon of salt–glass reaction is of high technological interest for the production of glass based scaffolds for many purposes including bone related biomedical applications where the exceptional surface area available after sintering can provide a high contact surface with the surrounding biological system, promoting the sound integration of the newly formed bone.

Acknowledgments

This work was financed by FEDER funds through the Operational Programme COMPETE and by FCT - Foundation for Science and Technology funds under the project CICECO - FCOMP-01-0124-FEDER-037271 (Refª. FCT PEstC/CTM/LA0011/2013) and the grant SFRH/BD/48357/2008.

References

[1] O. F., Biomaterials and scaffolds for tissue engineering, Mater. Today. 14 (2011) 88–95.

[2] A. Kramschuster, L.-S. Turng, 17 - Fabrication of Tissue Engineering Scaffolds, in: Handb. Biopolym. Biodegrad. Plast., William Andrew Publishing, Boston, 2013: pp. 427–446.

[3] Q. Chen, C. Zhu, G. Thouas, Progress and challenges in biomaterials used for bone tissue engineering: bioactive glasses and elastomeric composites, Prog. Biomater. 1 (2012) 2.

[4] Y. Chen, S. Zhou, Q. Li, Microstructure design of biodegradable scaffold and its effect on tissue regeneration, Biomaterials. 32 (2011) 5003–5014.

[5] J.R. Jones, Review of bioactive glass: From Hench to hybrids, Acta Biomater. 9 (2013) 4457–4486.

[6] E. Davim, M.H.F.V. Fernandes, A.M.R. Senos, Preparation of Porous Glass Scaffolds by Salt Sintering Technique, Mater. Sci. Forum. 587-588 (2008) 52–56.

[7] E.J.C.R. Davim, Suportes porosos vítreos do sistema Si-Ca-P-Mg para aplicações biomédicas, Universidade de Aveiro, 2008 (MSc Thesis).

[8] X. Yan, X. Huang, C. Yu, H. Deng, Y. Wang, Z. Zhang, et al., The in-vitro bioactivity of mesoporous bioactive glasses., Biomaterials. 27 (2006) 3396–403.

[9] X. Yan, C. Yu, X. Zhou, J. Tang, D. Zhao, Highly ordered mesoporous bioactive glasses with superior in vitro bone-forming bioactivities., Angew. Chem. Int. Ed. Engl. 43 (2004) 5980–4.

[10] C. Wu, Y. Zhou, W. Fan, P. Han, J. Chang, J. Yuen, et al., Hypoxia-mimicking mesoporous bioactive glass scaffolds with controllable cobalt ion release for bone tissue engineering, Biomaterials. 33 (2012) 2076–85.

[11] S. Callcut, J.C. Knowles, Correlation between structure and compressive strength in a reticulated glass-reinforced hydroxyapatite foam, J. Mater. Sci. Mater. Med. 13 (2002) 485–489.

[12] J. Dong, H. Kojima, T. Uemura, M. Kikuchi, T. Tateishi, J. Tanaka, In vivo evaluation of a novel porous hydroxyapatite to sustain osteogenesis of transplanted bone marrow-derived osteoblastic cells, J. Biomed. Mater. Res. 57 (2001) 208–16.

[13] H.-W. Kim, J.C. Knowles, H.-E. Kim, Hydroxyapatite porous scaffold engineered with biological polymer hybrid coating for antibiotic Vancomycin release, J. Mater. Sci. Mater. Med. 16 (2005) 189–195.

[14] H. Hattori, K. Masuoka, M. Sato, M. Ishihara, T. Asazuma, B. Takase, et al., Bone formation using human adipose tissue-derived stromal cells and a biodegradable scaffold, J. Biomed. Mater. Res. B. Appl. Biomater. 76 (2006) 230–9.

[15] M. Mastrogiacomo, S. Scaglione, R. Martinetti, L. Dolcini, F. Beltrame, R. Cancedda, et al., Role of scaffold internal structure on in vivo bone formation in macroporous calcium phosphate bioceramics, Biomaterials. 27 (2006) 3230–7.

[16] G. Liu, L. Zhao, W. Zhang, L. Cui, W. Liu, Y. Cao, Repair of goat tibial defects with bone marrow stromal cells and beta-tricalcium phosphate, J. Mater. Sci. Mater. Med. 19 (2008) 2367–76.

[17] Q. Fu, E. Saiz, M.N. Rahaman, A.P. Tomsia, Bioactive glass scaffolds for bone tissue engineering: state of the art and future perspectives, Mater. Sci. Eng. C. 31 (2011) 1245–1256.

[18] C. Vitale-Brovarone, M. Miola, C. Balagna, E. Verné, 3D-glass–ceramic scaffolds with antibacterial properties for bone grafting, Chem. Eng. J. 137 (2008) 129–136.

[19] Q.Z. Chen, I.D. Thompson, A.R. Boccaccini, 45S5 Bioglass®-derived glass–ceramic scaffolds for bone tissue engineering, Biomaterials. 27 (2006) 2414–2425.

[20] H.S. Costa, M.F. Rocha, G.I. Andrade, E.F. Barbosa-Stancioli, M.M. Pereira, R.L. Orefice, et al., Sol–gel derived composite from bioactive glass–polyvinyl alcohol, J. Mater. Sci. 43 (2007) 494–502.

[21] A. Rainer, S.M. Giannitelli, F. Abbruzzese, E. Traversa, S. Licoccia, M. Trombetta, Fabrication of bioactive glass-ceramic foams mimicking human bone portions for regenerative medicine, Acta Biomater. 4 (2008) 362–369.

[22] D. Bellucci, V. Cannillo, A. Sola, F. Chiellini, M. Gazzarri, C. Migone, Macroporous Bioglass®-derived scaffolds for bone tissue regeneration, Ceram. Int. 37 (2011) 1575–1585.

[23] Z. Zhou, J. Ruan, J. Zou, Z. Zhou, Preparation and bioactivity of sol-gel macroporous bioactive glass, J. Univ. Sci. Technol. Beijing, Miner. Metall. Mater. 15 (2008) 290–296.

[24] H. Yun, S. Kim, Y. Hyun, S. Heo, J. Shin, Hierarchically mesoporous-macroporous bioactive glasses scaffolds for bone tissue regeneration, J. Biomed. Mater. Res. B. Appl. Biomater. 87 (2008) 374–380.

[25] O. Peitl, E. Dutra Zanotto, L.L. Hench, Highly bioactive P_2O_5–Na_2O–CaO–SiO_2 glass-ceramics, J. Non. Cryst. Solids. 292 (2001) 115–126.

[26] J. Vogel, W. Liang, C. Rüssel, Porous glasses by a salt sintering process, Porous Spec. Glas. 57 (1998) 105–111.

[27] W. Liang, C. Rüssel, Resorbable, porous glass scaffolds by a salt sintering process, J. Mater. Sci. 41 (2006) 3787–3792.

[28] D.C. Vieira, O.B.G. Assis, XRD investigation of phases induced by additions of NaCl and MgCO3 during open-pore glass processing, J. Mater. Sci. Lett. 19 (2000) 1975–1977.

[29] E.J.C. Davim, A.M.R. Senos, M.H.V. Fernandes, Non-isothermal crystallization kinetics of a Si-Ca-P-Mg bioactive glass, J. Therm. Anal. Calorim. 117 (2014) 643–651.

[30] A. Karamanov, B. Dzhantov, M. Paganelli, D. Sighinolfi, Glass transition temperature and activation energy of sintering by optical dilatometry, Thermochim. Acta. 553 (2013) 1–7.

[31] L. Lefebvre, L. Gremillard, J. Chevalier, R. Zenati, D. Bernache-Assolant, Sintering behaviour of 45S5 bioactive glass, Acta Biomater. 4 (2008) 1894–903.

[32] Y.X. Huang, A.M.R. Senos, J.L. Baptista, Preparation of an aluminium titanate-25 vol% mullite composite by sintering of gel-coated powders, J. Eur. Ceram. Soc. 17 (1997) 1239–1246.

[33] Y.X. Huang, A.M.R. Senos, Effect of the powder precursor characteristics in the reaction sintering of aluminum titanate, Mater. Res. Bull. 37 (2002) 99–111.

[34] D. Rohanová, A.R. Boccaccini, D.M. Yunos, D. Horkavcová, I. Březovská, A. Helebrant, TRIS buffer in simulated body fluid distorts the assessment of glass-ceramic scaffold bioactivity, Acta Biomater. 7 (2011) 2623–2330.

[35] S.R. Federman, V.C. Costa, D.C.L. Vasconcelos, W.L. Vasconcelos, Sol-Gel SiO_2-CaO-P_2O_5 biofilm with surface engineered for medical application, Mater. Res. 10 (2007) 177–181.

[36] G. Orcel, J. Phalippou, L.L. Hench, Structural changes of silica xerogels during low temperature dehydration, J. Non. Cryst. Solids. 88 (1986) 114–130.

[37] A.R. Boccaccini, Q. Chen, L. Lefebvre, L. Gremillard, J. Chevalier, Sintering, crystallisation and biodegradation behaviour of Bioglass®-derived glass–ceramics, Faraday Discuss. 136 (2007) 27.

[38] N. Patel, S.M. Best, W. Bonfield, I.R. Gibson, K.A. Hing, E. Damien, et al., A comparative study on the in vivo behavior of hydroxyapatite and silicon substituted hydroxyapatite granules, J. Mater. Sci. Mater. Med. 13 (2002) 1199–206.

[39] M. Cerruti, D. Greenspan, K. Powers, Effect of pH and ionic strength on the reactivity of Bioglass 45S5, Biomaterials. 26 (2005) 1665–74.

[40] A. Balamurugan, G. Balossier, D. Laurent-Maquin, S. Pina, A.H.S. Rebelo, J. Faure, et al., An in vitro biological and anti-bacterial study on a sol-gel derived silver-incorporated bioglass system, Dent. Mater. 24 (2008) 1343–51.

[41] B. Stuart, D.J. Ando, Modern infrared spectroscopy, Published on behalf of ACOL (University of Greenwich) by Wiley, 1996.

[42] M. Vallet-Regí, C.V. Ragel, A.J. Salinas, Glasses with Medical Applications, Eur. J. Inorg. Chem. 2003 (2003) 1029–1042.

Chapter VII

"When one puts up a building one makes an elaborate scaffold to get everything into its proper place. But when one takes the scaffold down, the building must stand by itself with no trace of the means by which it was erected…"

Andres Segovia (1893 – 1987)

CHAPTER VII

EFFECT OF GLASS COMPOSITION ON THE PROCESSING AND PROPERTIES OF CA-P-MG-SI SCAFFOLDS

Abstract

Glass scaffolds in the system $CaO – P_2O_5 – SiO_2 – MgO – Na_2O$, with an open interconnected porosity, favourable for bone tissue ingrowth, were produced by a salt sintering process. The effect of Na_2O additions to 3Ca.P – Si – Mg glasses, from which scaffolds were produced, have been investigated with regard to sintering behaviour, densification and compressive mechanical properties.

The introduction of Na_2O by substitution of MgO in the glass composition, decreased the glass transition (Tg) and the onset of crystallisation (Tc) temperatures of the glass/salt mixtures. The addition of sodium has enabled the scaffolds (glass/salt mixture) to be treated at a lower temperature. An assessment of their sintering window indicate an improvements in the densification of the glass scaffold struts leading to favourable mechanical properties, important for further applications, namely for tissue engineering.

VII.1. Introduction

The challenge of manufacturing scaffolds from glass particles, is to obtain a good compromise between densification, pore size and interconnectivity and mechanical properties [1–4]. It is important to be able to adjust and to control the sintering working range of the glass, to ensure easy manufacturing. As a bioactive glass scaffold, its increased specific surface area and pore volume may greatly accelerate the kinetics of the deposition process of hydroxyapatite and, therefore, enhance the bone-forming activity of these glasses [5,6]. There is no agreement as to the ideal specification for the pore network of the scaffolds [7,8]. It is widely accepted that the optimal pore size for bone in-growth within a biomaterial scaffold is 200–400 μm [9] with a minimum pore diameter of at least 100 μm, interconnected, important for allowing migration and proliferation of osteoblasts and mesenchyme cells and ultimately tissue formation [10], whereas microporosity (<10 μm pores) allows body fluid circulation.

The salt sintering process method is a common and simple way to produce glass scaffolds [11–13]. This method implies a heat treatment that can induce a devitrification of the glass, namely in some compositions of the $3CaO.P_2O_5 – SiO_2 – MgO$ system [13]. In the salt sintering process one should sinter the salt/glass mixture at a relatively low temperature, bellow salt particles fusion and glass crystallisation onset. However, sufficient densification by sintering at low temperatures is difficult and therefore very fragile scaffolds are produced [11].

The addition of alkali metal oxides, can be used to sinter at low temperatures yet getting extensive densification of the struts and mechanically competent scaffolds [14–16].

In this work, we investigate the influence of adding Na_2O to the glass composition on the sintering behaviour of glass/salt mixtures, thermal properties, microstructures and mechanical properties of the scaffolds. The relationships between the sintering temperatures, porosity and mechanical behaviour evolution of the glass scaffolds with various Na_2O contents are also discussed.

VII.2. Material and methods

VII.2.1. Glass preparation

From a base composition 32.68% CaO – 10.89% P_2O_5 – 25.43% SiO_2 – 31% MgO (mol. %) three other compositions were investigated with a constant Ca/P molar ratio of 3 and the substitution of MgO content by Na_2O up to 20 %. This was the highest percentage possible, without phase separation.

These compositions, presented in Table VII.1, were designated hereafter as G31N0, G29N2, G28N3 or G25N6 where the number after G means the molar % of MgO and the digit after N refers to the mol. % of Na_2O. The criterion for the choice of these values was the substitution of the initial MgO molar percentage, by 5, 10 and 20 % of sodium oxide.

Table VII.1. Compositions of the glasses (mol. %).

	G31N0	G29N2	G28N3	G25N6
CaO	32.68	32.68	32.68	32.68
P_2O_5	10.89	10.89	10.89	10.89
SiO_2	25.43	25.43	25.43	25.43
MgO	31.00	29.45	27.90	24.80
Na_2O	-	1.55	3.10	6.20

Glasses were obtained by a melt-quenching route. The chemicals used for the preparation of the glasses were reagent-grade $CaCO_3$, Na_2CO_3, SiO_2 and $Ca(H_2PO_4)_2 \cdot H_2O$. The mixed powders were melted for 2 h in a Pt crucible at temperatures in the range of 1550 to 1450 ºC (depending on the sodium content in the composition). Glasses were quenched in water to obtain frits. Then the glass frits were dried and milled in an agate mill and sieved to obtain a glass powder with a particle size smaller than 20 μm and a mean size of 3.5 μm, as determined by the light scattering technique (Coulter LS 230, Fraunhofer optical model, Amherst, MA).

VII.2.2. Glass powder characterization

X-ray diffraction (XRD) analysis of the glass powders was performed using a Rigaku Diffractometer Geigerflex Dmax-C at room temperature with CuKα radiation (at 40 kV and 40 mA) and a scan speed of $0.02^o\ s^{-1}$. The XRD patterns were recorded in the 2θ range of 10-60 degree to evaluate the amorphous nature of the as-prepared glasses (Fig. not shown).

The true density was measured by helium pycnometry in a model Accupyc 1330-Micrometrics, USA, equipment. The specific surface area was determined by physical adsorption of nitrogen gas, using the Brunauer, Emmettand Teller (BET) method. For these tests, a Quantachrome Quantasorb equipment, Germany, was used and powders were previously kept under vacuum, at 200 ºC, for 4 h. Differential thermal analysis (DTA) of the glasses was performed in a Labsys Setaram, France, using 25 mg powdered samples, at a heating rate of 5 °C min^{-1}, from 25 to 1000 °C, using Al_2O_3 powder

as a reference material, to obtain the glass transition temperature, Tg, and the onset of crystallization temperature, Tc, of the glasses.

The thermal expansion coefficient (TEC) of the powder compact glasses and mixtures was measured by dilatometry in a Bahr Thermo Analyse DIL 801 L, Germany at 5 ºC min^{-1}, using (10 mm diameter x 10 mm thick) cylindrical samples.

VII.2.3. Structural characterization of the glass powders

Fourier-Transform Infrared Spectroscopy spectra were collected using a FTIR, Brucker tensor 27. For this purpose, the glass samples were mixed with KBr (ratio 1:10) and pressed into a pellet using a hand press. All spectra were collected over a region of 4000–400 cm^{-1}, with 256 scans and resolution of 4 cm^{-1}.

29Si MAS-NMR spectra were recorded on a MSL400P Avance Bruker spectrometer, 9.4 T, wide-bore, Germany, operating at 79.49 MHz, using 7 mm zirconia rotors at a spinning rate of 5 kHz at room temperature, with powdered glass samples. The pulse length was 2 μs and a 60 s delay time was used in order to prevent the different relaxation times between glasses. Kaolinite was used as the chemical shift reference.

VII.2.4. Glass scaffold preparation

Following the salt sintering method, [13,17], the glass powders with a mean particle size of 3.5 μm were mixed with NaCl salt, with particle sizes between 212-500 μm, supplied by BDH, Middle East LLC, with a purity of 99 %. Mixtures of glass and salt with 50 wt. % NaCl**,** were prepared by mechanical mixing, during 15 min, in a turbula shaker-mixer, from Glen Mils, USA**.** Cylindrical green bodies (10 mm diameter and 10 mm thick) of the glass/salt mixtures were shaped by uniaxial pressing with a geometrically initial density of 1.62 ± 0.02 $g.cm^{-3}$. The thermal expansion coefficient (TEC) of the glass-salt mixtures was measured by dilatometry at 5 ºC min^{-1}, using a Bahr DIL801L dilatometer, Hüllhorst, Germany. The dilatometry was performed from 25 to 800 ºC, to evaluate the effect of glass composition on the shrinkage of the mixtures. The optimal sintering temperature was determined from the derivative of the dilatometric curve of the glass/salt compacts, when viscous flow sintering dominates and no undesired structural changes, due to crystallization, is detected.

The samples were heated up to the optimal sintering temperature, at 5º C min^{-1} and held during 10 min at these temperatures and then left to cool inside the furnace. The salt was used as a porogen, remaining unaltered during the entire sintering process, being easily removed by leaching after the heat treatment. Leaching was performed by immersing the salt glass mixture samples during one day in water at 30 ºC and 175 rpm. This operation was followed by one day drying in a furnace at 100

ºC, giving rise to a scaffold. These scaffolds, obtained from the mixture of each glass composition with the salt porogen, were designated hereafter as GS31N0, GS29N2, GS28N3 or GS25N6 based on the names of the respective glasses. These designation is also used for the glass/salt mixtures.

VII.2.5. Glass scaffolds characterization

X-ray diffraction (XRD) analysis of the crushed scaffolds were performed to confirm the amorphous nature of the scaffolds.

The total porosity was calculated from Eq. VII.1. The apparent density of the scaffolds (ρ scaffolds) was determined from the apparent volume and mass measurements taken on 6 samples and the density of the glass. The porosity P was then calculated by

$$P = 1 - \frac{\rho_{scaffold}}{\rho_{glass}} = 1 - \rho_{relative} \qquad \text{(Eq. VII. 1)}$$

Mechanical properties at compression were studied in a Bose/Electro Force 3400 testing machine. Six cylindrical scaffolds per composition were compressed at a speed of 0.5 mm min^{-1}. Prior to mechanical testing, the contact surfaces of each sample were ground to produce smooth parallel surfaces. The elastic modulus from compression tests was determined from the initial linear region of the stress–stain curve and the average compressive strength, taken as the highest stress on the stress–strain curve, for six samples tested.

VII.3. Results and Discussion

VII.3.1. Glass / salt sintering behaviour

Fig. VII.1 shows the linear shrinkage vs. temperature of the 50 wt. % glass/salt mixtures for a heating rate of 5 ºC min^{-1}. For the GS25N6, GS28N3, and GS29N2 and GS31N0 the shrinkage starts at temperatures ~ 630, 648, 652 and 700 ºC respectively, as shown in Table VII.2, designated as Ts. Glass scaffold GS31N0 exhibits the lower densification, while the highest is shown by GS25N6.

The thermal expansion coefficients (TEC) of the mixture compacts with 50 wt. % salt, were calculated between 100 – 400 ºC and are summarized in Table VII.2. It is observed that the addition of the salt as porogen increases the thermal expansion of the compacts, when compared to the dilatometric behaviour of the base glasses alone, as expected by the effect of the higher thermal expansion coefficient of the salt, 43 x 10^{-6} $°C^{-1}$, near 6 times larger than that of the base glasses, as already discussed elsewhere [11]. This effect is higher for the GS31N0 composition and decreases

with the increase of sodium content in the glass composition. This will be discussed, further, in the structural section.

Table VII.2. Thermal behaviour of the 50% glass salt mixtures and glass powders

	GS31N0	GS29N2	GS28N3	GS25N6
Ts_i (ºC)	700	652	648	630
Ts_f	755	711	721	722
ΔTs (ºC)	55	59	73	92
ΔT (ºC)	111	92	90	89
TEC mixture (x 10^{-6} °C^{-1})	31.0 ± 0.8	38.4 ± 0.5	32.3 ± 0.5	26.2 ± 0.6
TEC glass (x 10^{-6} °C^{-1})	7.1±0.2	8.8±0.2	9.0±0.2	9.4±0.3

Ts_i - onset of sintering temperature of mixture, Ts_f - final sintering temperature before the onset crystallization temperature of the mixture. ΔTs – Sintering window, without undesired structural changes of the glass structure in the mixture. ΔT – working window for glasses (from DTA).

The dilatometric results of the mixtures also show that the introduction of sodium into the composition of the glasses, also promotes an earlier onset of crystallization, of the glass/salt mixture compacts Table II, as expected by the thermal analysis of the base glasses. The introduction of Na_2O to the composition of the glasses decreased the Tg and the Tc, Fig. VII.3, and increased the TEC of the glass compact powders.

The derivative of the dilatometric curve, Fig. VII.2, of the GS25N6 shows that the shrinkage starts near 630 ºC. The shrinkage rate then increases rapidly and steadily up to 712 ºC, and then more slowly up to 722 ºC, when it starts to decrease significantly due to the increase of viscosity and structural changes due to the onset of crystallization. Dilatometry shrinkage rate results, confirmed that the optimum sintering temperature for GS25N6 compacts lies in the interval 712–722 ºC. The optimal sintering temperature was chosen at 720 ºC. The same procedure was performed for all compositions.

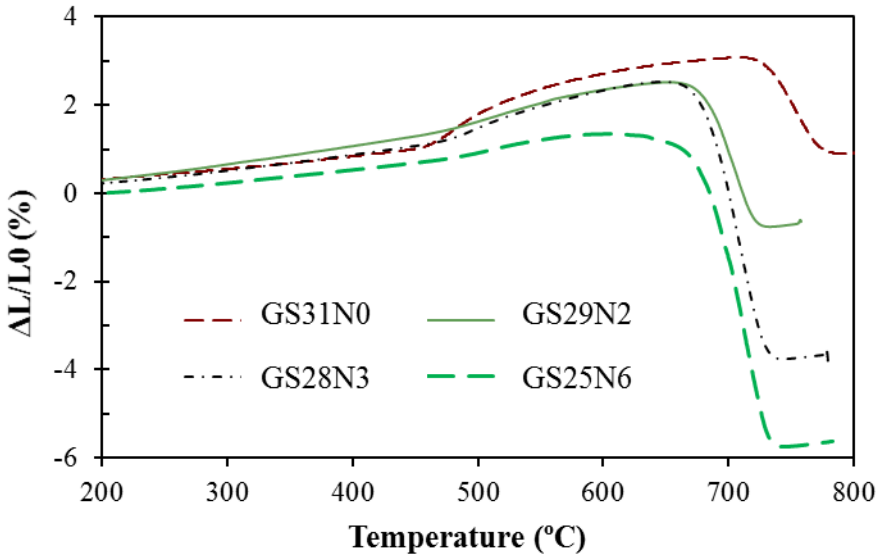

Fig.VII. 1. Dilatometric curves obtained from the 50 wt. % salt mixtures compacts, with different glass compositions at a heating rate of 5 ºC min^{-1}

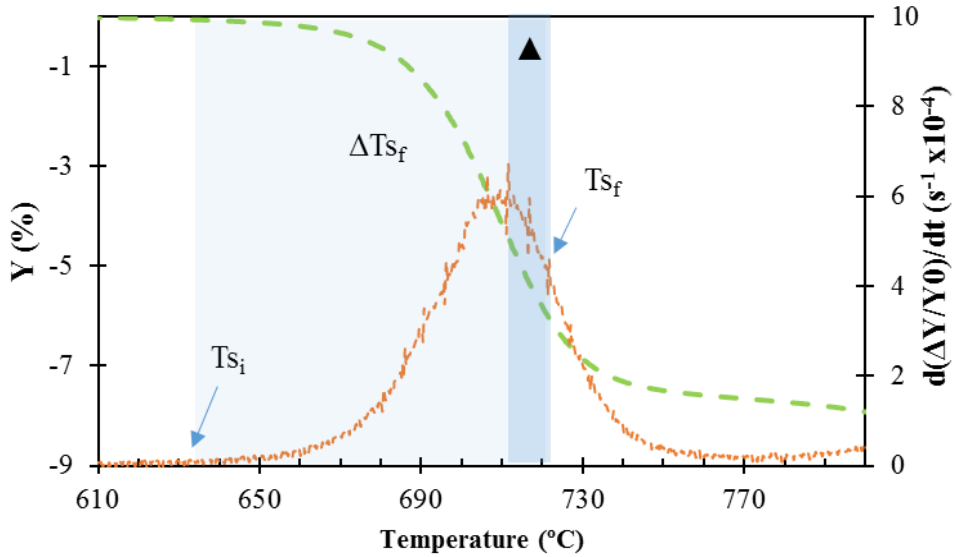

Fig.VII. 2. Dilatometric derivate curve obtained from the 50 wt. % salt mixtures compacts, with 6 % Na_2O (GS25N6) at a heating rate of 5 ºC min^{-1}, ▲- optimum sintering range

The sintering window, defined as the temperature interval where the viscosity allows sintering without undesired structural changes [18], of the mixture compacts increased by the addition of sodium to the composition of the glass, Fig. VII.1 and Table VII.2. In the absence of the porogen, DTA analyses of the glass powders, Fig. VII. 3 show that the Tg of the glasses, decrease from 706 to 635 ºC for G31N0 and G25N6 respectively, and the onset of crystallization temperature also decreases from 817 to 724 ºC. Consequently, the glass working windows ($\Delta T = T_c - T_g$) decrease from 111 ºC to 89 ºC for glasses G31N0 and G25N6 respectively, Table VII.2. As shown in literature,

devitrification can be avoided and thus the working window enlarged by decreasing the amount of alkali, or by increasing the amount of alkaline earths [15].

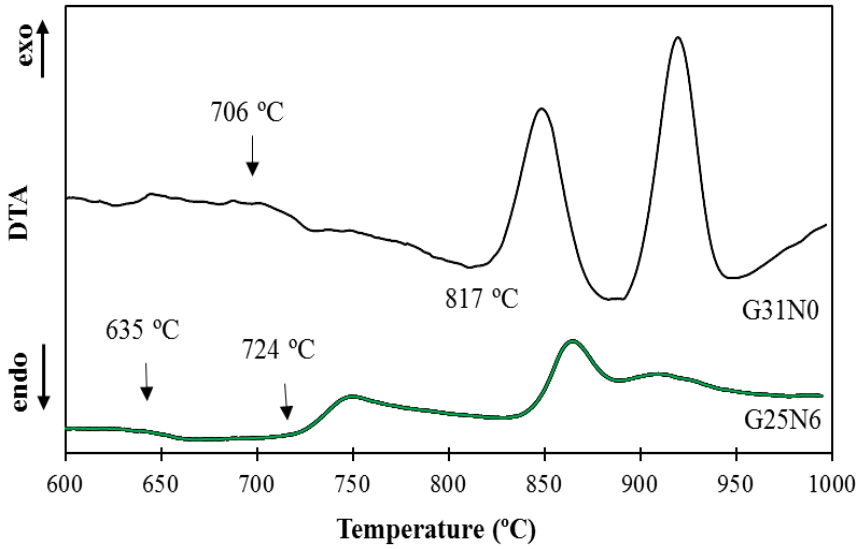

Fig.VII. 3. DTA curves of the base composition G31N0 and G25N6, at 5 ºC min^{-1}

It should be emphasised that the main goal of this work is to increase the sintering window of the glass scaffolds. The salt porogen fusion starts near 795 ºC and promotes an earlier crystallization of the GS31N0 glass structure, detected at 760 ºC as reported in a previous work [13]. In the presence of the salt porogen, the sintering window decrease from 111 ºC, as shown by DTA analysis to ~ 55 ºC, as confirmed by the dilatometry of the scaffold, Fig. VII.1, the lowest sintering window of all mixtures, as resumed in Table VII.2.

Results showed that the addition of Na_2O was beneficial to the densification of the glass/salt mixture compacts, due to the decrease of the onset of densification and increase of sintering window, without the presence of crystallization.

VII.3.2. Glass scaffolds characterization

Cylindrical scaffolds were obtained by the salt sintering process and lixiviation of the salt porogen. Sintering of the 50 wt. % salt mixtures was performed near the maximum shrinkage temperature at a velocity of 5 ºC min^{-1}. As the densification of the compacts with time occurs especially in the first minutes, with a drastic decrease of specific surface area values, as studied before [13], samples were held for 10 min at the maximum selected temperature. The sintering conditions are presented in table VII.3.

From Table VII.3 it is observed that with the addition of sodium oxide, to the base glass composition, and a reduction of 50 ºC (GS29N2) to 30 ºC (GS28N3 or GS25N6) from the initial sintering treatment,

(750 ºC for GS31N0), the porosity of the scaffolds decreased from 65.5 % for GS31N0 to 60.8 % GS25N6.

The compressive strength increased from 1.3 (GS31N0) to 1.4, 1.7 and 1.8MPa for the GS29N2, GS28N3 and GS25N6 scaffolds respectively, as summarized in table VII.3.

Table VII.3. Properties of the glass scaffolds obtained by heat treating the glass-salt mixtures at 5 ºC min^{-1}, at different temperatures in air during 10 min

Scaffold	Sintering conditions	Porosity (%)	Compressive strength (MPa)	Elastic modulus (GPa)
GS31N0	750 ºC for 10 min	65.5 ± 0.4	1.3 ± 0.2	0.010 ± 0.001
GS29N2	700 ºC for 10 min	63.0 ± 0.2	1.4 ± 0.2	0.040 ± 0.003
GS28N3	720 ºC for 10 min	60.5 ± 0.4	1.7 ± 0.2	0.040 ± 0.003
GS25N6	720 ºC for 10 min	60.8 ± 0.4	1.8 ± 0.2	0.040 ± 0.003
Trabecular bone [19]		85-98	1.9-12	0.05-0.5

The addition of sodium, a glass network modifier, has enabled the scaffolds (glass/salt mixture) to be treated at a lower temperature, comparing with the sodium-free composition GS31N0, increasing at the same time the sintering interval of the compacts (Table VII.2), and the densification and consequently the mechanical behaviour of the scaffolds, important for further applications, namely for tissue engineering.

Since the porogen (NaCl) is responsible for the macroporosity, and given that the salt content is the same in all compacts, the observed higher densification is probably due to the diminishing of micropores percentage occurring during the sintering process.

Fig. VII. 4 compares the effect of sodium addition on the specific surface area of the as-prepared glass powders, without the porogen presence, and of the corresponding scaffolds, sintered at the conditions presented in table VII.3. As the content of sodium in the glass composition increases, the surface area of the correspondent scaffolds decrease.

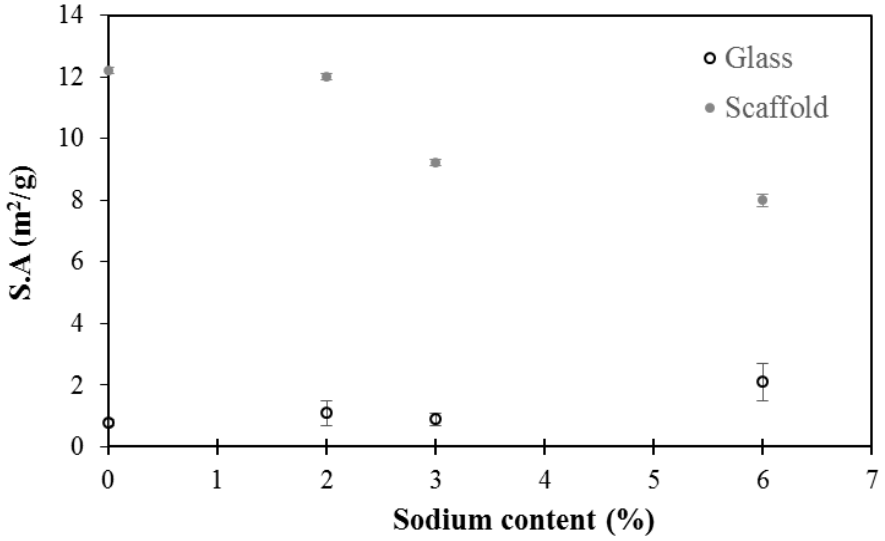

Fig.VII. 4. Effect of sodium content on the S.S.A of the glass powder (before sintering) and corresponding scaffolds obtained at the optimum sintering temperature during 10 min at a heating rate of 5 ºC min^{-1}

As discussed in a previous work [13], the porogen favour the occurrence of an alkaline reaction between the glass surface particles of G31N0 and the salt, producing the expansion phenomenon observed in the dilatometric curves, Fig. VII.1 and the increase of the specific surface area of the obtained porous structures, Fig. VII.4. These results show that the effect of sodium porogen on the glass surface becomes less evident with the increase of sodium content in the glass.

To understand this observation, transmittance FTIR spectroscopy was performed on the as-prepared G31N0 and G25N6 glasses, and corresponding glass scaffolds, being the obtained spectra shown in Fig. VII.5. FTIR spectra of both glasses, reveals a main absorption band at 1000 – 1200 cm^{-1} corresponding to Si – O – Si stretching vibration and a shoulder at 890-960 cm^{-1} assigned to Si – O symmetric stretch (non-bridging oxygen, NBO). Another peak was observed at 455 – 476 cm^{-1} which is due to Si – O – Si bending vibration. The peaks at 560 cm^{-1} in the P – O – P bending mode, suggest the presence of an amorphous calcium phosphate phase, confirmed by XRD (Fig. not shown) [20–23].

After the contact with the salt, the peak attributed to the phosphate phase, split in two, at 557 and 600 cm^{-1}, for both compositions, due to the formation of a phosphate phase, still amorphous. The GS31N0 spectra is more affected, in the presence of salt, Fig. VII.5b. To the shoulder associated to Si – O stretch, with one non-bridging oxygen (Si – O – NBO), a new is added, near 850 cm^{-1} assigned to the Si – O(s) with two non-bridging oxygen per SiO_4 tetrahedron (Si – O – 2NBO), also called Q^2 groups associated with alkali ions in the glass network, which are indicative of disintegration of the glass structure in contact with the salt [24,25].

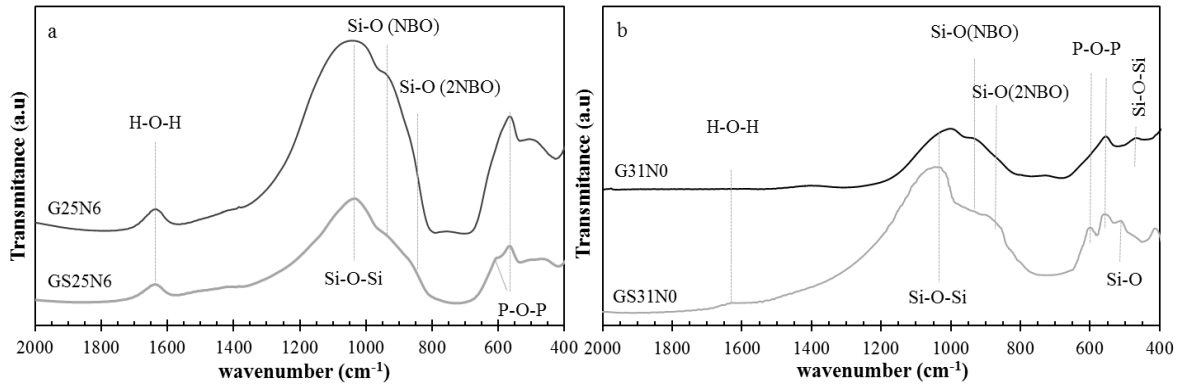

Fig.VII. 5. FTIR data of the as-prepared glasses and corresponding scaffolds a) G25N6 and GS25N6 and b) G31N0 and GS31N0.

MAS-NMR results of the ^{29}Si spectra are presented in Fig. VII. 6. The centre of Q^2 peak shifted from -80.9 ppm for the base glass to -82.1 ppm for the glass with 6 % Na_2O, thus suggesting a slight decrease polymerization of the silicate glass network. The addition of alkali oxides to the base glass composition, G31N0, modified the network structure by replacing bonding oxygen's (BO) by non-bridging oxygen (NBO), thus opening the glass structure.

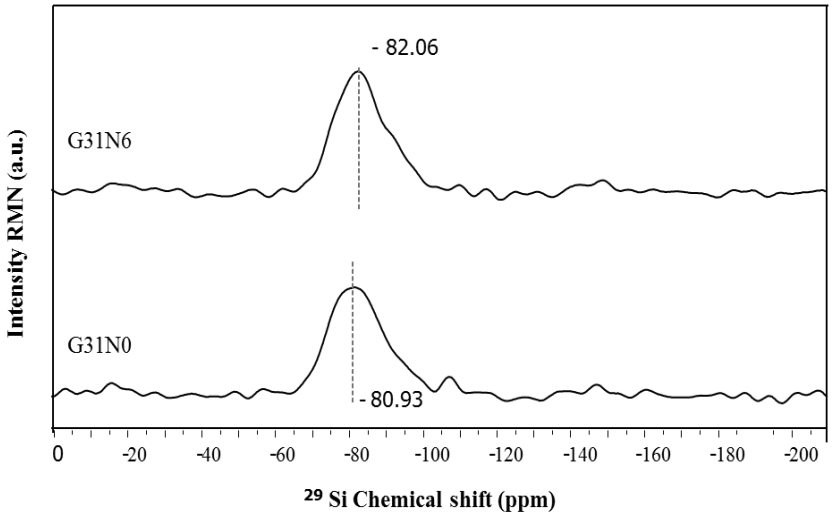

Fig.VII. 6. ^{29}Si MAS NMR spectra of some investigated glasses.

These results confirm that the salt porogen attack, to the glass structure of the particles surfaces during sintering, is more effective when there is no sodium in the glass composition. It is possible that the presence of sodium in the composition creates the higher allowable amount of non-bridging oxygens in the glass structure thus reducing the possibility of the porogen NaCl to react with the glass surface by a salt-glass alkali reaction, as suggested in a previous work [13].

VII.4. Conclusion

Five scaffolds with different chemical compositions, in the $3CaO.P_2O_5 – SiO_2 – MgO – Na_2O$, have been successfully prepared by the salt sintering method, with 60 to 66 % porosity. The scaffolds with higher sodium content showed a compressive strength near 2 MPa, close to the minimum value for natural trabecular bone.

The addition of Na_2O to the glass composition increased the sintering ability of the glass scaffolds which led to denser struts with higher mechanical strength. The sintering window for the processing of the new glass scaffolds, when compared to sodium-free glass scaffolds, increased by 4 ºC, 18 °C and 37 °C with 5, 10 and 20 mol. % MgO substitution by Na_2O, respectively.

Therefore, the produced scaffolds can be proposed as effective candidates in the field of bone tissue regeneration due to their mechanical strength, porosity, SSA and easy tailoring.

References

[1] O. Bretcanu, C. Samaille, A.R. Boccaccini, Simple methods to fabricate Bioglass®-derived glass–ceramic scaffolds exhibiting porosity gradient, J. Mater. Sci. 43 (2008) 4127–4134.

[2] A.M. Deliormanlı, In vitro assessment of degradation and bioactivity of robocast bioactive glass scaffolds in simulated body fluid, Ceram. Int. 38 (2012) 6435–6444.

[3] H. Fu, Q. Fu, N. Zhou, W. Huang, M.N. Rahaman, D. Wang, et al., In vitro evaluation of borate-based bioactive glass scaffolds prepared by a polymer foam replication method, Mater. Sci. Eng. C. 29 (2009) 2275–2281.

[4] M.N. Rahaman, D.E. Day, B.S. Bal, Q. Fu, S.B. Jung, L.F. Bonewald, et al., Bioactive glass in tissue engineering, Acta Biomater. 7 (2011) 2355–2373.

[5] X. Liu, W. Huang, H. Fu, A. Yao, D. Wang, H. Pan, et al., Bioactive borosilicate glass scaffolds: in vitro degradation and bioactivity behaviors, J. Mater. Sci. Mater. Med. 20 (2009) 1237–43.

[6] Q. Fu, E. Saiz, M.N. Rahaman, A.P. Tomsia, Bioactive glass scaffolds for bone tissue engineering: state of the art and future perspectives, Mater. Sci. Eng. C. 31 (2011) 1245–1256.

[7] Y. Gu, W. Huang, M.N. Rahaman, D.E. Day, Bone regeneration in rat calvarial defects implanted with fibrous scaffolds composed of a mixture of silicate and borate bioactive glasses, Acta Biomater. 9 (2013) 9126–36.

[8] A. El-Ghannam, P. Ducheyne, I.M. Shapiro, Bioactive material template for in vitro synthesis of bone, J. Biomed. Mater. Res. 29 (1995) 359–370.

[9] M. Liu, X. Yu, F. Huang, S. Cen, G. Zhong, Z. Xiang, Tissue Engineering Stratified Scaffolds for Articular Cartilage and Subchondral Bone Defects Repair | Orthopedics, Orthopedics. 36 (2013) 868–73.

[10] S.K. Nandi, S. Roy, P. Mukherjee, B. Kundu, D.K. De, D. Basu, Orthopaedic applications of bone graft & graft substitutes: a review, Indian J. Med. Res. 132 (2010) 15–30.

[11] W. Liang, C. Rüssel, Resorbable, porous glass scaffolds by a salt sintering process, J. Mater. Sci. 41 (2006) 3787–3792.

[12] E. Davim, M.H.F.V. Fernandes, A.M.R. Senos, Preparation of Porous Glass Scaffolds by Salt Sintering Technique, Mater. Sci. Forum. 587-588 (2008) 52–56.

[13] E.J.C. Davim, M.H.V. Fernandes, A.M.R. Senos, Increased surface area during sintering of calcium phosphate glass and sodium chloride mixtures, J. Eur. Ceram. Soc. 35 (2015) 329–336.

[14] N. Sharmin, M.S. Hasan, A.J. Parsons, D. Furniss, C.A. Scotchford, I. Ahmed, et al., Effect of boron addition on the thermal, degradation, and cytocompatibility properties of phosphate-based glasses, Biomed Res. Int. 2013 (2013) 902427.

[15] M. Brink, The influence of alkali and alkaline earths on the working range for bioactive glasses, J. Biomed. Mater. Res. 36 (1997) 109–17.

[16] M. Brink, T. Turunen, R.P. Happonen, A. Yli-Urpo, Compositional dependence of bioactivity of glasses in the system Na2O-K2O-MgO-CaO-B2O3-P2O5-SiO2, J. Biomed. Mater. Res. 37 (1997) 114–21.

[17] J. Vogel, W. Liang, C. Rüssel, Porous glasses by a salt sintering process, Porous Spec. Glas. 57 (1998) 105–111.

[18] R. Comesaña, F. Lusquiños, J. Del Val, M. López-Álvarez, F. Quintero, A. Riveiro, et al., Three-dimensional bioactive glass implants fabricated by rapid prototyping based on CO(2) laser cladding, Acta Biomater. 7 (2011) 3476–87.

[19] C.B. Carter, M.G. Norton, Ceramic Materials: Science and Engineering, 2 nd Editi, Springer New York, 2007.

[20] D.C. Clupper, J.J. Mecholsky, G.P. LaTorre, D.C. Greenspan, Sintering temperature effects on the in vitro bioactive response of tape cast and sintered bioactive glass-ceramic in Tris buffer, J. Biomed. Mater. Res. 57 (2001) 532–40.

[21] Q. Fu, E. Saiz, A.P. Tomsia, Bioinspired Strong and Highly Porous Glass Scaffolds, Adv. Funct. Mater. 21 (2011) 1058–1063.

[22] O. Bretcanu, X. Chatzistavrou, K. Paraskevopoulos, R. Conradt, I. Thompson, A.R. Boccaccini, Sintering and crystallisation of 45S5 Bioglass® powder, J. Eur. Ceram. Soc. 29 (2009) 3299–3306.

[23] M. Cerruti, D. Greenspan, K. Powers, Effect of pH and ionic strength on the reactivity of Bioglass 45S5, Biomaterials. 26 (2005) 1665–74.

[24] L.K. Jones, Development of a Sol-gel-based Thin-layer Chromatography Stationary Phase for In-situ Infrared Analysis, ProQuest, 2008.

[25] H. Aguiar, E.L. Solla, J. Serra, P. González, B. León, N. Almeida, et al., Orthophosphate nanostructures in SiO2–P2O5–CaO–Na2O–MgO bioactive glasses, J. Non. Cryst. Solids. 354 (2008) 4075–4080.

Chapter VIII

"…we need to remember that only 35 years ago the concept of a material that would not be rejected by living tissues also seemed unimaginable. Bioglass® provides a starting point."

L.L. Hench. The story of Bioglass® (2006)

CHAPTER VIII

EFFECT OF GLASS COMPOSITION ON THE IN VITRO BIOACTIVITY AND BIOCOMPATIBILITY OF CA-P-MG-SI-NA SCAFFOLDS

Abstract

Porous glass structures with an open interconnected porosity favourable for tissue ingrowth were produced by a salt sintering process and characterized in terms of their in vitro behaviour both in acellular and in cellular media. The in vitro bioactivity of the scaffolds was tested by soaking them in a simulated body fluid (SBF) and by subsequent characterization of the materials surface by SEM, EDS, and X-ray diffraction and of the immersion fluid by ICP. The replacement of 6 % MgO by Na_2O in the glass network allowed to tailor the dissolution rate and bioactivity of the glass scaffolds and to obtain significant improvements in the mechanical properties of the scaffolds.

Regarding the biological assessment, the incorporation of sodium to the composition resulted in a poor cell response for small periods. Nevertheless, it was demonstrated that for 21 days the cells on the glass containing sodium surface recovered, are in a similar number and differentiated stage compared to those growing over non-sodium glass. This shows that the cells exhibit full functionality after adaptation to the scaffold containing sodium, which takes a few days. This scaffold does not negatively affect osteoblasts proliferation rate as shown by the increasing ALP activity and presence of mineralized deposits.

The results showed that scaffolds with different bioactivity and degradation rates can be achieved by replacing 6 % of MgO in silicate phosphate bioactive glass with Na_2O.

VIII.1 Introduction

There has been an increasing interest in the development of porous structures for bone tissue engineering applications that allow cells to attach, proliferate, differentiate and organize into healthy bone tissue as the scaffold degrades [1–4]. Great attention has been paid to bioactive glasses, because they have the ability to build a strong interface between the material surface and bone tissue, through the formation of a carbonated hydroxyapatite layer on their surface [5]. The bioactivity and biocompatibility of these bioactive glasses are strongly affected by their degradation rate and associated ion release [6–8]. Therefore, it is expected that the chemical durability and the dissolution rates can be tailored by adjusting for example, the oxide composition of the glasses, to suit with their end application [9–14]. Several studies showed that addition of B_2O_3 to phosphate glasses improved there chemical durability [14,15]. Incorporation of boron by replacing Na_2O into the P_2O_5–CaO–Na_2O–MgO–B_2O_3 glass system showed favourable effects on the cell metabolic activity, proliferation, and morphology. The ALP activity improved for glasses containing 0 – 5 % B_2O_3 [14]. Substituting Na_2O with CaO yielded less degradable glass in the (40-x)Na_2O–xCaO–60P_2O_5 systems [16]. An increase of the cross-linkage or the introduction of highly insoluble ions, makes the glass structure less susceptible to solution attack. Reducing the degradation rate, concomitant with the reduction in the release rate of certain ions, has led to better biocompatibility [17].

In the previous chapter it was reported the effect of Na_2O addition on the processing, structure and some properties of glasses within the Ca–P–Mg–Si–Na system. Although the incorporation of Na_2O in the CaO–P_2O_5–SiO_2–MgO glass composition was advantageous for the scaffolds production, one of the main problems associated with high alkali content is its high dissolution rate, when exposed to a biological fluid and consequent rapid release of soluble ionic species that regulate the cells response [18]. This rapid lixiviation can cause faster bone resorption that may negatively affect the balance of natural bone regeneration. Thus compromising the usefulness of the glass behaviour in vivo [18,19].

The aim of this study is focused on the influence of 6 mol. % MgO substitution by Na_2O, on the surface reactivity, and biocompatibility of similar scaffolds produced by the salt sintering process from glasses of the Si–Ca–P–Mg–Na system.

VIII.2 Materials and method

VIII.2.1. Glass scaffold preparation

Glass scaffolds designated by GS31N0 and GS25N6 were prepared via salt sintering process, as previously described [20]. Cylindrical green bodies (10 x 10 mm^2) of mixtures consisting of glass particles (average size 3.5 μm) and 50 wt. % salt particles (212–500 μm) were shaped by uniaxial pressing with an initial density of 1.60±0.02 $g.cm^{-3}$.

The compositions of the glasses are presented in Table VIII.I.

Table VIII.1. Nominal composition of the glasses (mol. %)

mol. % / Sample	CaO	P_2O_5	SiO_2	MgO	Na_2O
G31N0	32.68	10.89	25.43	31.00	-
G25N6	32.68	10.89	25.43	24.80	6.20

The cylindrical glass/salt powder compacts were heated in an electric furnace up to 750 ºC and 710 ºC for GS31N0 and GS25N6 respectively, at a heating rate of 5 ºC min^{-1} and held during 10 min at these temperatures. Samples were left to cool inside the furnace until room temperature. The salt was removed by leaching in water bath at 30 ºC and 175 rpm, followed by one day drying in a furnace at 100 ºC, giving rise to the scaffolds.

VIII.2.2. Glass scaffold characterization

The amorphous nature of the glass particles for the scaffolds was confirmed by X-ray diffraction (XRD) analysis using a Rigaku Diffractometer Geigerflex Dmax-C at room temperature with CuKα radiation (at 40 kV and 40 mA) and a scan speed of 0.02º s^{-1}. The XRD patterns were recorded in the 2θ range of 10–60 degree.

The specific surface area of the scaffolds was determined by physical adsorption of nitrogen gas, using the Brunauer, Emmettand Teller (BET) method. For those tests, a Quantachrome Quantasorb equipment, Germany was used, small pieces of broken scaffolds were previously kept under vacuum, at 200 ºC, for 4 h.

Fourier-Transform Infrared Spectroscopy spectra were collected using a Bruker IFS 28 EQuinox spectrometer, Germany. For this purpose, the glass samples were mixed with KBr (ratio 1:10) and

pressed into a pellet using a hand press. Transmission spectra of the KBr pellets were collected over a region of 4000 – 400 cm^{-1}, with 256 scans and resolution of 4 cm^{-1}.
Porosities of the scaffolds were measured by Mercury Intrusion Porosimetry, using an AutoPore IV 9500V1.07 serial 734 Penetrometer. Sample weight varied from 0.25 to 0.3 g.

Mechanical properties of the scaffolds at compression were studied in a Bose/Electro Force 3400 testing machine. Six cylindrical samples (10 x 10 mm^2) were compressed at a speed of 0.5 mm min^{-1}. Prior to mechanical testing, the contact surfaces of each sample were ground to produce smooth parallel surfaces. The elastic modulus was determined from the linear region of the stress vs. strain response.

VIII.2.3. Bioactivity in SBF

The preparation of the SBF was carried out following the procedure proposed by Kokubo [21,22]. In vitro tests were performed under static conditions soaking the glass scaffolds samples in sealed polyethylene bottles with SBF solution at 37 ºC, with a constant specimen surface area to solution volume ratio of 0.1 cm^{-1}, considering the value of the surface area given by the BET method. The samples were kept immersed for different periods of time between 1 hour and 21 days at 37 ºC. After each time point, the solution was filtered through a Milipore 0.22 μm system. The samples were studied by XRD, FTIR spectroscopy and SEM. A scanning electron microscope attached with an energy dispersive electron probe X-ray analyser (SEM-EDS, Hitachi Su-70, Germany system) was used to analyse both microstructure of scaffolds before and after immersion into SBF. All samples were coated with carbon using an EMITECH K950 device coater, prior to observation.
The changes in the concentration of Ca, Si, P and Mg ions in SBF solution were determined by Inductively Coupled Plasma spectroscopy (ICP, Jobin Yvon, JY70 Plus) at different soaking times.

VIII.2.4. Biocompatibility studies

Human bone marrow, obtained from orthopaedic surgery procedures (after patient informed consent), were cultured in in α-Minimal Essential Medium (α-MEM) supplemented with 10% fetal bovine serum, 100 mg ml^{-1} penicillin, 10 IU streptomycin, 2.5 mg ml^{-1} fungizone, at 37 ºC in a humidified atmosphere of 5 % CO2 in air. For subculture, phosphate-buffered saline (SBF) was used to wash, twice, the cell monolayer and then incubated with a trypsin–EDTA solution (0.05 % trypsin, 0.25 % EDTA) for 10 min at 37 ºC to detach the cells. Material samples were sterilized by autoclaving at 120 ºC and the cells were re-suspended in culture medium and seeded (10^5 cells cm^{-2}) over the materials surface for up to 6 days in the experimental conditions described above.

Colonized materials were evaluated at days 7, 14 and 21 for cellular viability/proliferation and observed by confocal laser scanning microscopy (CLSM; Leica SP2 AOBS), to evaluate throughout the culture time the cell morphology, cell viability/proliferation, alkaline phosphatase (ALP) activity and ability to form calcium phosphate deposits. Control cultures and seeded material samples were cultured for 7 and 21 days in the presence of 50 μg ml^{-1} ascorbic acid, 10mM β-glycerophosphate and 10 nM dexamethasone. This experimental conditions reported to allow the osteoblast differentiation in this culture system [23]. All the experiments were performed in the first subculture, since the sequential passage of bone marrow cells results in a progressive loss of the osteoblastic phenotype [24].

ALP results are expressed in nanomoles of p-nitrophenol produced per min per lg of protein (nmol min^{-1}/lg protein). Values are expressed as mean ± standard deviation (SD) of three replicates and were compared using the student's t-test, with a significance level of $p < 0.05$.

VIII.3 Results and Discussion

VIII.3.1 Scaffold characterization

SEM micrographs of the scaffolds GS31N0 and GS25N6, Fig. VIII.1, clearly show an interconnected macroporosity with smaller pores distributed throughout the structure within larger pores. The two samples are quite similar from a macroscopic point of view, as expected, since the size of the macropores is controlled by the NaCl particle sizes (250-350 μm). The macropores with size ranging from 60 to 500 μm, were 3 dimensionally opened and continuously connected.

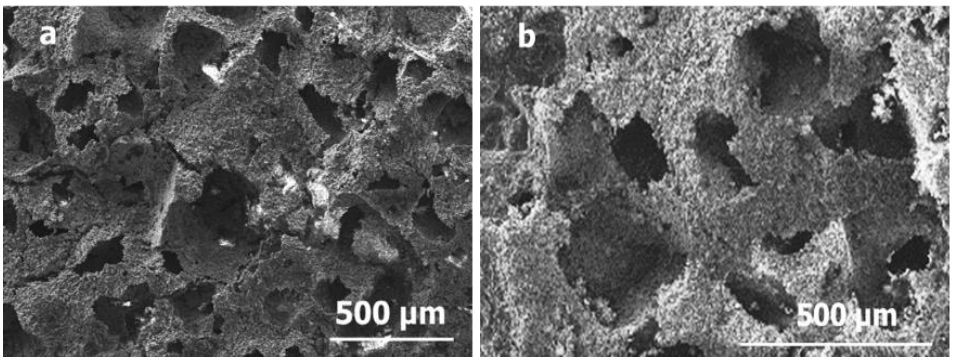

Fig.VIII.1. Representative SEM micrographs of the glass scaffolds samples showing large pores (larger than 400 μm) for a) GS31N0 and b) GS25N6

To assess the microstructural pore features of the GS31N0 and GS25N6 porous glass samples mercury porosimetry was performed, providing the total pore volume and the pore size characterization as summarized in Table VIII.2. The pore size smaller than 10 μm correspond to the

micropores resulting from the sintering process, increasing the interconnectivity of the porous structure.

Macroporosity volume of the two scaffolds was identical, as expected, since it is a result of the same salt content present in the mixture. The larger pores were distributed between 60 and 350 μm. This pore size was well below the observed in SEM, Fig. VIII.1. The discrepancy between the observed values by microscopy and porosimetry is well known, and is attributed to the fact that porosimetry technique measures the size of the constrictions of the pores, resulting in an underestimate pore size. The median pore diameter ~ 90 μm of the constrictions is near 100 μm. The diameter of interconnecting pores seems to dictate the quality of tissue growing into the pores. Although there are different views, literature compromise seems to be that the optimal pore size for mineralized bone ingrowth varies between 100 and 400 μm.

The resulting porous glass cylinders also showed an open porosity of about 63 % for both GS31N0 and GS25N6, with about 12 % porosity caused by micropores (< 10 μm). The porosity of the scaffolds is higher than the theoretical one (45 percent of the pore-foaming agent), which indicated that sintering procedure promotes the appearance of some microporosity as shown in the SEM and mercury porosimetry. The microporosity < 10 μm with a median pore ~2 μm is also important since scaffolds involving both micro and macro porosities can perform better than only macro porous scaffolds [25].

Table VIII.2. Structural parameters of the different scaffolds obtained by mercury porosimetry

Composition	Open Porosity (%)	Total Pore Area m^2/g	Median pore diameter (vol.) 60-350 μm	Porosity (%) < 10 μm	Median pore diameter (vol.) < 10 μm
GS31N0	63.2	0.54	88	13	1.9
GS25N6	63.2	0.53	89	12	1.7

For bone tissue engineering applications, the diameter of the interconnecting pore structures is one of the most important parameters. It should be greater than 100 μm to allow bone tissue ingrowth and eventually vascularisation. In this study a median pore diameter near 90 μm was obtained.

The main goal of this work was to prepare two similar scaffolds with different composition. By decreasing the sintering temperature of 750 ºC for the GS31N0 in 40 ºC for the GS25N6, it was possible to produce scaffolds with similar porosity. Nevertheless, the resulting scaffolds presented, a higher strength and elastic modulus for GS25N6, as resumed in Table VIII.3. The compressive strength is inside the range of trabecular bone, 0.1–16MPa [26] and near the Young's modulus 0.05–0.5GPa [27].

Table VIII.3. Scaffolds sintering conditions and characterization

Scaffold	Sintering conditions	strength (MPa)	Elastic modulus (GPa)
GS31N0	750 ºC for 10 min	1.3 ± 0.2	0.010 ± 0.001
GS25N6	710 ºC for 10 min	1.6 ± 0.2	0.030 ± 0.003

VIII.3.2 In vitro bioactivity studies in SBF

The in vitro tests in SBF were performed on both glass scaffolds, to evaluate the composition effect on bioactivity, in acellular media. The FTIR absorbance spectra for the glass scaffolds, before and after immersion into SBF are shown in Fig. VIII.2, for 3 and 7 days immersion.

Before soaking, both scaffolds showed intense silicate group absorption bands. The intense bands at ~1020 and ~920 cm^{-1} are assigned to the Si – O – Si asymmetric stretch and Si – O (NBO) symmetric stretch respectively. The peaks at ~ 594, 552 and 600 cm^{-1}, correspondent to the P – O bending, were present in both samples. GS25N6 also presented an additional peak at ~459 cm^{-1} correspondent to the Si – O – Si bending.

The FTIR spectra of the GS31N0, after 3 days of immersion in SBF, showed a decrease in transmittance intensity and a split into a weak twin band around 570 and 600 cm^{-1} which corresponds to the bending mode of P – O bonds in the amorphous calcium phosphate [28,29]. After 7 days, another set of peaks formed at 1460, 1420 and 870 cm^{-1}, was attributed to the formation of C – O bonds [30].

In the GS25N6, a behaviour similar to that of GS31N0 was observed at 3 days immersion. After 7 days immersion, the peaks related with the presence of calcium phosphate phase 602 and 506 cm^{-1}, became sharper which is related to the presence of apatite crystalline phase [31] as a consequence of the reaction with the SBF. CO_2 is incorporated from the solution, producing a broad peak near 870 cm^{-1}. The C – O bonds (at 1460 and, 1420 cm^{-1}) have undergone peak splitting.

The presence of P – O and C – O bonds suggests the formation of apatite and indicates the in vitro SBF bioactivity of the scaffolds [32]. All glasses exhibited the splitter band at 1412 and 1460 cm^{-1} and the band at 875 cm^{-1} which indicate the presence of CO_3 groups whereas the bands observed at 1040 – 1050, 602 and 563 cm^{-1} were assigned to PO_4/HPO_4 groups (crystalline HCA). The P – O bending peak pronunciation indicates the growth of the hydroxyapatite-like layer [33].

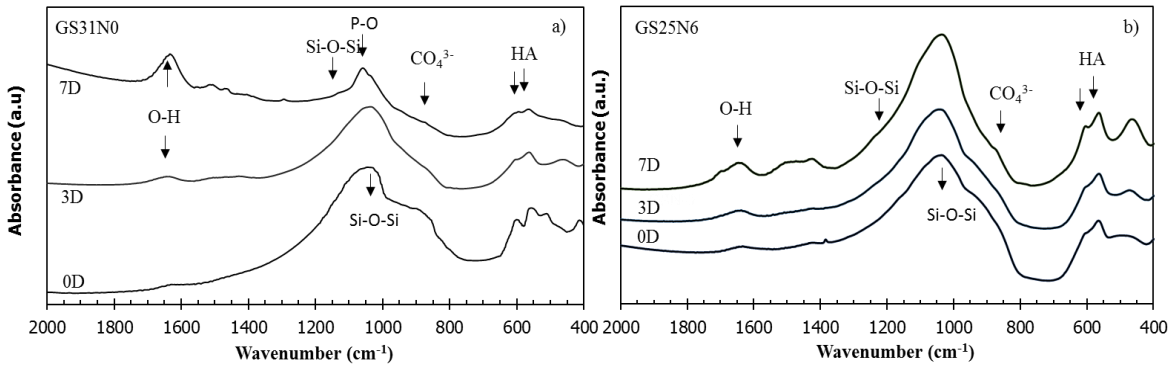

Fig.VIII.2. FTIR data after immersion of the prepared glass scaffolds in SBF for 3 and 7 days; a) GS31N0 and b) GS25N6

The X-Ray diffractographs of the scaffolds after 1 hour, 3, 7 and 14 days immersion in SBF are presented in Fig. VIII. 3. After 1 hour immersion, both scaffolds are essentially amorphous, with some insipient apatitic peaks, observed especially on GS31N0.

After 3 days soaking the diffraction planes (2 1 3), (2 1 1), and (0 0 2), of GS31N0 and GS25N6, corresponding to the peaks at 49º, 32º, and 26º respectively, indicate that small apatitic crystals precipitate after immersion, $Ca_5(PO_4)_3(OH)$ according to the card No. 01-086-0740, the X'Pert HighScore database, confirming the previous FTIR results. Also incipient peaks of whitlockite ($Ca_{2.859}Mg_{0.411}(PO_4)_2$) appear in the GS31N0, at (2 1 4), (0 2 10), (1 2 8) and (2 1 10) corresponding to the peaks 28º, 31º, 33º and 36º, according to the card No. 01-087-1582.

After 14 days immersion, both scaffolds presented, together with the apatite phase diffraction planes, new diffraction peaks for 13.7º, 17º and 58º assigned to the reflection (1 0 4), (1 1 0) and (3 3 9) of whitlockite. It is possible that magnesium is incorporated into the atomic structure of HA and that HA phase cohabites with whitlockite. The precipitation of these two phases (apatite and whitlockite), was also observed in the literature, on the surface of glasses containing Mg when exposed to SBF [34–36]. The increased intensity of the hydroxyapatite peaks with soaking time is indicative of the growth of an apatite layer of enhanced crystallinity.

By 14 days, in GS25N6, it was no longer possible to observe the amorphous halo, in the range of 20-30 degrees, promoted by the presence of an amorphous phase on the sample probably due to the completely covered of the surfaces by the HA layer. The mechanisms of the interaction between both glass scaffolds compositions and the SBF seem basically the same. In the first 3 days the presence of HA was higher on GS31N0, although the development of hydroxyapatite seems to slow down on GS31N0, for longer immersion times. The presence of the amorphous halo is particularly evident even after 14 days of immersion on the GS31N0 while on GS25N6 it disappears, been covered by the crystalline phases present.

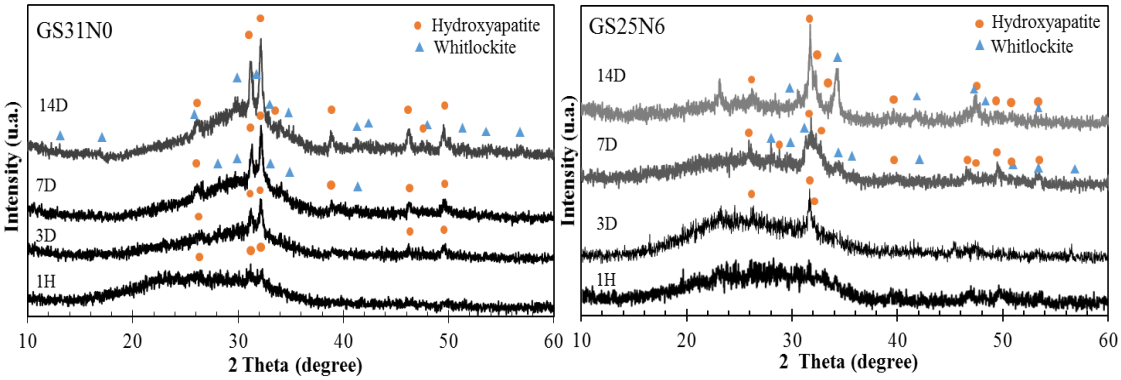

Fig.VIII.3. XRD of the scaffolds after immersion in SBF, for 7 and 14 days for a) GS31N0 and b) GS25N6 samples

The surface modifications observed after immersion of the scaffolds in SBF were accompanied with microstructural observation. Fig. VIII.4 shows the SEM micrographs of the surface of the scaffolds GS31N0 and GS25N6, after soaking in SBF for 3, 7 and 21 days. The macroporous structure for all scaffolds was intact after soaking, although the surfaces of these scaffolds have presented important changes. Soon after 3 days, some agglomerates formed on the surface of the scaffolds and after 7 days a dense layer was found on both surfaces. Needle-shaped crystallites fully covering the surfaces can be observed after 21 days. The morphology of the precipitated layer on GS31N0 is somehow different from that on GS25N6, probably due to the different degrees of crystallinity of the calcium phosphates formed on the scaffolds, slightly higher on GS31N0, as suggested by the XRD patterns, Fig. VIII.3.

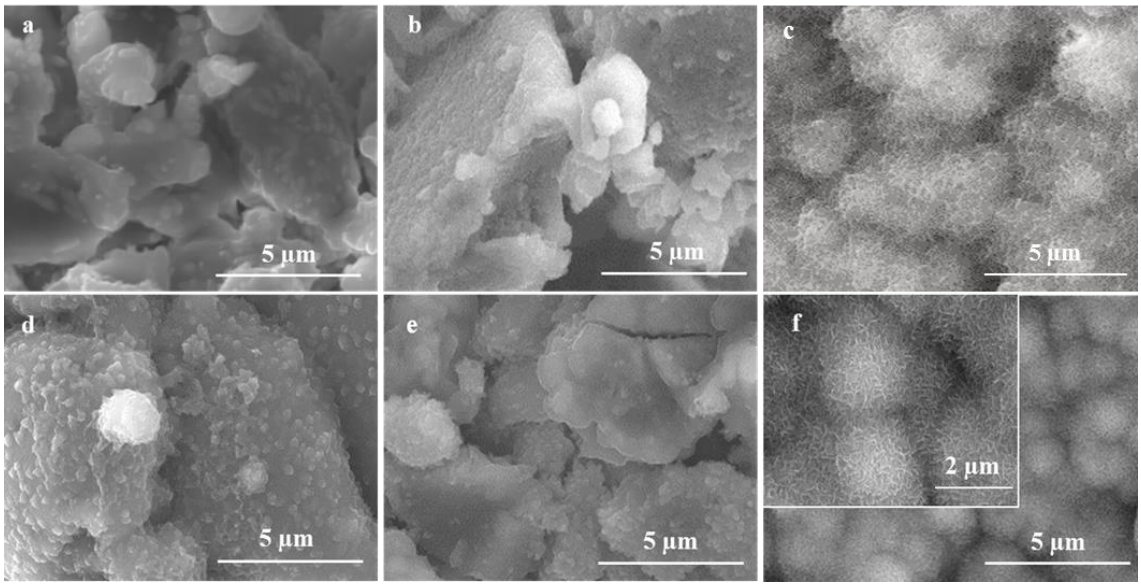

Fig.VIII.4. SEM micrographs of the scaffolds after immersion in SBF during 3, 7 and 21 days, for GS31N0 (a, b and c) and GS25N20 (d, e and f) respectively

EDS analysis to the precipitated layers confirmed that their chemical compositions can be assigned to a hydroxyl apatite phase. Fig. VIII. 5, shows for 14 days soaking a Ca/P ratio of 1.6 and 1.7 for GS31N0 and GS25N6 respectively, while in the stoichiometric HA $Ca_{10}(PO_4)_6(OH)_2$ is 1.67.

The above results indicate that these scaffolds can induce the formation with different rates, of a HCA layer on their surface in SBF, confirming the bioactivity of the scaffolds and their capacity as a material for bone tissue engineering.

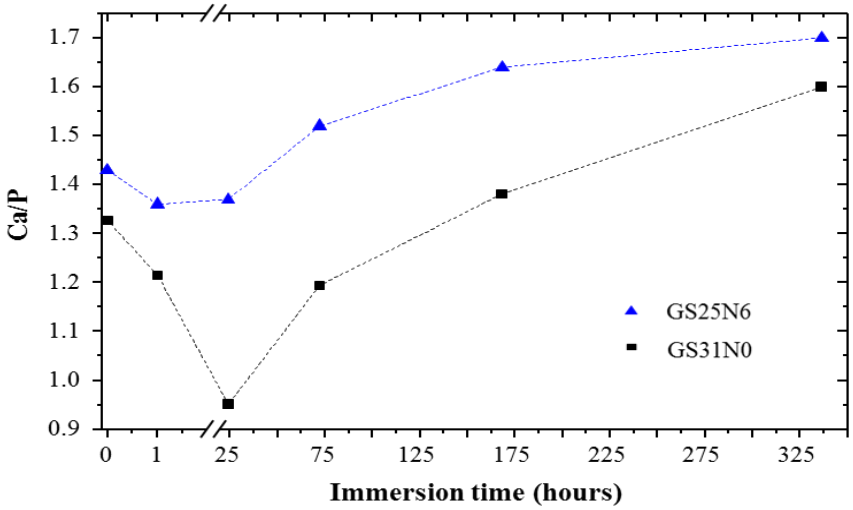

Fig.VIII.5. Variation of Ca/P ratio with soaking time, up to 14 days, for GS31N0 and GS25N6 determined by EDS. Lines are to guide the eye

The ion release profile of the glass scaffolds in SBF provides an outline of the degradation behaviour of all ions of the glass, Fig. VIII.6.

After the initial short period, in which phosphorus ions dissolution occurs, it is observed for GS25N6 a decrease of P ion concentration in solution, together with the drop of Ca^{2+} concentration, soon after 1 day, Fig. VIII.6a.

In the base glass scaffold, GS31N0, it was found that the concentration of calcium increased up 7 days followed by a gradually decrease. After 1 hour immersion, phosphate ions remain almost constant up to 7 days followed also by a decreased.

The GS25N6 release the greatest amount of Si in the first hour and Mg in the first day, Fig. VIII.6b. After the first hour, Si dissolution profile was similar for both scaffolds. Si concentration increased during the first 7 days immersion, and then no significant changes took place, Fig. VIII.6b. The Mg concentration release on GS25N6 was lower than that observed for GS31N0 as a consequence of the lower content of MgO in the composition of the G25N6 glasses. The decrease in Mg^{2+} concentrations in the SBF after reaching maximum can also indicates that such ions could be incorporated in the HA layer formed on the surface of the glasses, as confirmed by XRD presence of apatite and whitlockite phases, for 14 days immersion.

The pH variation with time, Fig. VIII.6c, strongly increased during the first 72 h for GS25N6, reaching a value of 8.2 after 14 days. The increase of pH on GS31N0 was slower, increasing up to 8.2 after 7 days immersion and then no significant change took place. This increase probably results from the reduction in the concentration of H^+ ions due to their exchange with the cations in the glasses (Ca^{2+}, Mg^{2+} and also Na^+ in the GS25N6). The stabilization of the Ca^{2+} concentration in SBF can be explained by considering two opposite processes. In one hand, the release of Ca^{2+} from the glass, and in the other hand, the consumption of these ions due to the formation of the apatite-type layer, as confirmed by SEM images in Fig. VIII.5. Together with this process the increase of hydroxyl concentration in the solution contributes for the attack of the silica glass network, resulting in the breaking of Si – O – Si bonds and consequent formation of Si – OH (silanols) on the glass/solution interface (FTIR results, Fig. VIII.2b. The condensation and re-polymerisation of a SiO_2-rich layer on the surface of the scaffolds may explain the stabilization of Si and pH, Fig. VIII.6c, in the solution.

The formation of apatite due to the crystallization of the amorphous calcium phosphate by incorporation of OH and CO_3^{2-} anions from the solution, is confirmed by FTIR, XRD and EDS.

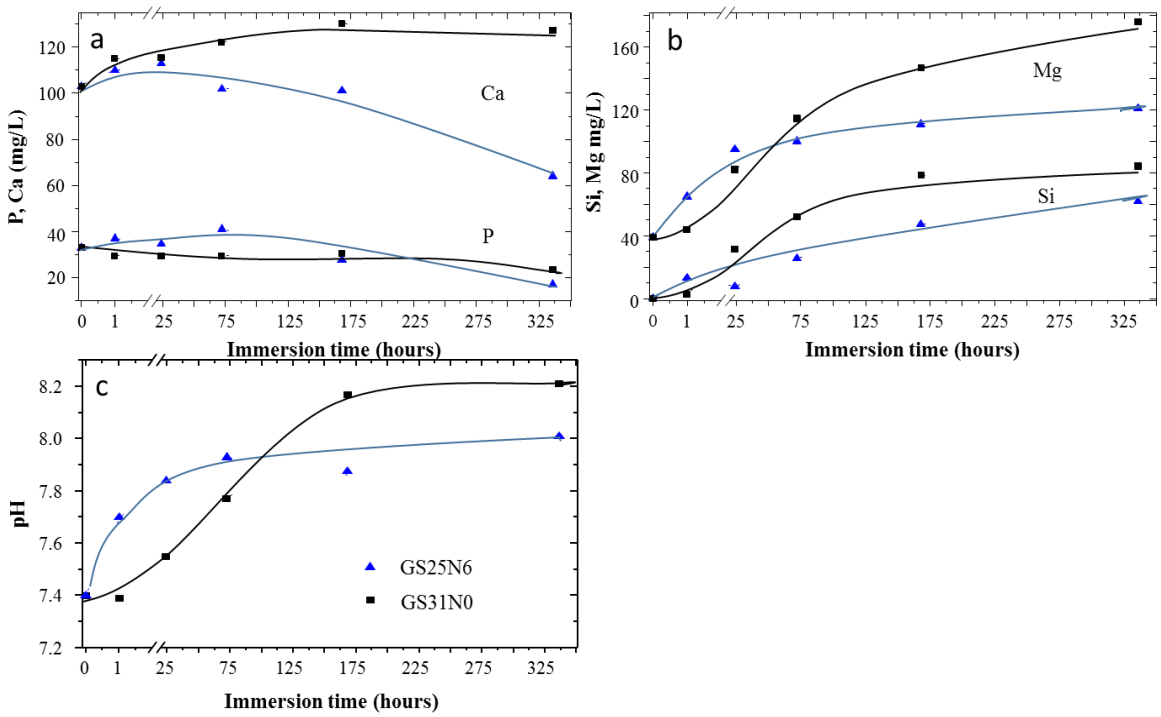

Fig.VIII.6. Variations, after soaking the scaffolds GS31N0 and GS25N6 in SBF of (a) phosphorus and calcium content and (b) silica and magnesium content and (c) pH values. Lines are to guide the eye

With the introduction of sodium in the glass composition to produce the GS25N6 scaffold, the network connectivity reduces and the glass solubility tends to increase. In fact substituting MgO with Na_2O usually produces more degradable glasses, since Na^+ ions have less stronger

field strengths than Mg^{2+} ions [37]. This seems to facilitate the higher concentration of Mg and Si in the first hours and consequent higher pH, in the first 72 hours.

The lower rate of the calcium phosphate layer formation, due to the presence of Mg observed in the GS31N0 composition in the first hours, is also reported in literature [34], with glasses containing MgO above 7 mol. %. The role of Mg^{2+} is interpreted as an inhibitor in the formation of the silica gel [38], due to the suppressing effect on the calcium dissolution. Marie Vallet-Regí et al [34] also reported a whitlockite-like phase together with the apatite-like phase and an increase in thickness of the formed HA layer with the height content of MgO.

VIII.3.3 Biocompatibility studies

Human bone marrow cells, cultured in experimental conditions that favour the osteoblastic differentiation [23,24] were seeded over the glass scaffold (GS31N0 and GS25N6) samples up to 21 days. Fig. VIII.7 shows the results for viability/proliferation and the ALP activity observed over the materials. Cell viability/proliferation increased throughout the 21 days culture time on both scaffolds. At day 7, values observed on GS25N6 were significantly lower indicating the presence of a lower number of cells, compared to that on GS31N0. This observation suggests some deleterious effects in the adhesion of the cells on GS25N6 and on the subsequent proliferation during the first days of culture. This is most probably due to the high dynamics of the interactions between this scaffold and the medium observed during the first days, as described above, leading to a surface instability which hinders cell adhesion. However, after that period, cells proliferated with a high growth rate and, at day 21, values were only slightly lower than those observed on GS31N0. The progressive establishment of a more stable surface environment on GS25N6, with time, created favourable conditions for cell proliferation.

ALP activity also increased with culture time in both scaffolds, suggesting the on-going of differentiation osteogenic pathway. ALP is an early marker of osteoblast lineage cells, and is known to have a determinant role in the mineralization of the extracellular collagenous matrix, by providing phosphate ions that, with calcium ions are used in the formation of the cell-mediated mineralized matrix [39]. Compared to GS31N0, ALP activity was significantly lower on GS25N6 at days 7 and 14. However, at day 21, the enzyme activity was only slightly lower. These results suggest that, after the initial delay, cultures recovered tending to behave similarly to that observed on GS31N0.

Colonized scaffolds were observed by SEM up to day 21. At day 7, both scaffolds presented well spread cells, adapting to the irregular underlying topography, and evidence of cell growth inside the pores. GS25N6 presented lower number of attached cells. At day 21, a more abundant and organized cell layer was noticed on both scaffolds and, in close association, the presence of mineralized deposits was observed (slightly lower in GS25N6).

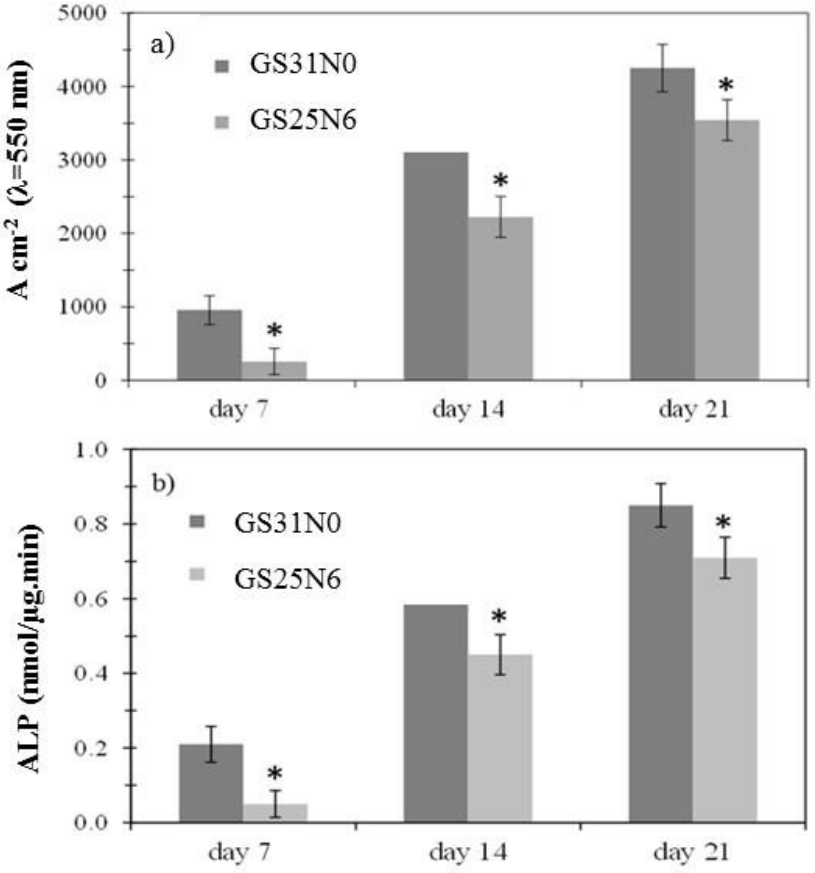

Fig.VIII.7. Cell viability/proliferation (a) and alkaline phosphatase activity (b) of human osteoblastic bone marrow cells cultured on the glass scaffolds GS31N0 and GS25N6 up to 21 days.*Significantly different from GS31N0

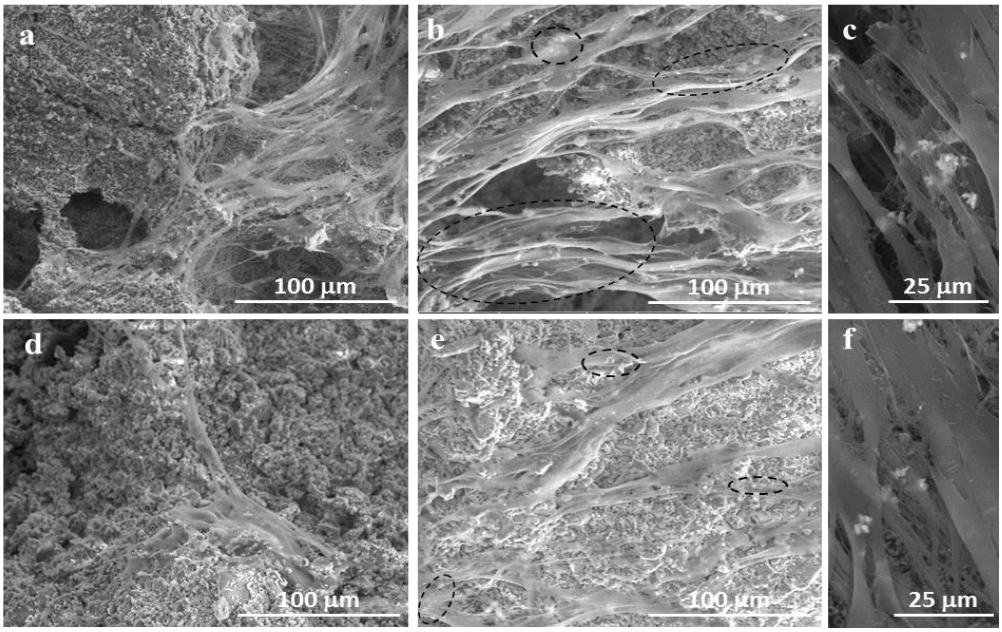

Fig.VIII.8. SEM observation of human osteoblastic bone marrow cells cultured on the glass scaffolds GS31 (a, b and c) and GS25N6 (d, e and f) for 7 days (a, d) and 21 days (b, c, e and f) with two different magnifications

Biocompatibility observations are in line with those reported in the bioactivity studies performed in SBF (Figs. VIII.4 and 5). Both glass scaffolds compositions GS31N0 and GS25N6 were able to support the formation of cells mediated mineralized deposits. The globular structures associated with the cell layer, seen at day 21 (Fig. VIII.8 (c and f)), contain Ca and P peaks. The observed rough surface, due to the sintering with salt, is a key factor in the attachment and proliferation of bone cells, increasing the surface area of the scaffold.

The higher concentration of magnesium present in the ICP measurements in the first days due to the faster degradation on the glass scaffolds containing sodium, may result in a negative effect on adhesion and initial cell proliferation.

From the results above, it is indicated that the composition modification of the scaffolds had a deleterious effect on the attachment and proliferation of HBMC's during the first days. As referred above, the faster degradation originates highly dynamic ion exchange reactions, which is deleterious for cell attachment, as the ionic environment influences the interaction of cells and materials. However, the progressive stabilization of the cell surface allowed a fast recovery of the osteoblastic proliferation and differentiation. In vivo, it is believed that this initial effect might be greatly attenuated, due to the continuous circulation of the body fluids, improving cell response [5,18].

VIII.4 Conclusions

Two similar glass scaffolds with different chemical compositions in the system $3CaO.P_2O_5$- SiO_2-MgO-Na_2O have been successfully prepared by the salt sintering method. The scaffolds exhibited *in vitro* bioactive behaviour, as a hydroxyapatite layer was formed on samples surface after soaking in simulated body fluids.

Cell culture studies of the glass scaffolds using HBM cells showed that both scaffolds possessed good cellular response in terms of cell viability, proliferation, and differentiation.

Substitution of MgO by Na_2O in the base glass network, lowered the scaffolds chemical durability, which explains the faster degradation rate and formation of surface HA. The faster degradation originates highly dynamic ion exchange reactions, with deleterious effect on the attachment and proliferation of HBMC's during the first days. A rapid recover of the Na containing scaffold promote similar results for longer times. Therefore, the produced scaffolds can be proposed as effective candidates in the field of bone tissue replacement due to their easy tailoring, bioactivity and biocompatibility.

Acknowledgments

I would like to express my thanks to Professor Maria Helena Raposo Fernandes and her group - School of Dental Medicine, University of Porto – for their collaboration in studies of in vitro biocompatibility.

References

[1] I.A. Aksay, S. Weiner, Biomaterials - is this really a field of research?, Curr Opin Solid State Mater Sci. 3 (1998) 219–220.

[2] D.W. Hutmacher, Scaffolds in tissue engineering bone and cartilage, Biomaterials. 21 (2000) 2529–2543.

[3] Q.Z. Chen, D. Mohn, W.J. Stark, Optimization of bioglass (R) scaffold fabrication process, J Am Ceram Soc. 94 (2011) 4184–4190.

[4] S. Shruti, A.J. Salinas, G. Lusvardi, G. Malavasi, L. Menabue, M. Vallet-Regi, Mesoporous bioactive scaffolds prepared with cerium-, gallium- and zinc-containing glasses, Acta Biomater. 9 (2013) 4836–4844.

[5] F. Barrère, C.A. van Blitterswijk, K. de Groot, Bone regeneration: molecular and cellular interactions with calcium phosphate ceramics, Int. J. Nanomedicine. 1 (2006) 317–32.

[6] Q. Fu, M.N. Rahaman, H. Fu, X. Liu, Silicate, borosilicate, and borate bioactive glass scaffolds with controllable degradation rate for bone tissue engineering applications. I. Preparation and in vitro degradation, J. Biomed. Mater. Res. - Part A. 95 (2010) 164–171.

[7] J.R. Jones, L.M. Ehrenfried, P. Saravanapavan, L.L. Hench, Controlling ion release from bioactive glass foam scaffolds with antibacterial properties, in: J. Mater. Sci. Mater. Med., 2006: pp. 989–996.

[8] S. Haimi, G. Gorianc, L. Moimas, B. Lindroos, H. Huhtala, S. Räty, et al., Characterization of zinc-releasing three-dimensional bioactive glass scaffolds and their effect on human adipose stem cell proliferation and osteogenic differentiation, Acta Biomater. 5 (2009) 3122–31.

[9] A.S.K.H.T.S.P.S.R.P. Vikash Kumar Vyas, Effect Of Cr2O3 Addition on their Bioactivity and Physico-Mechanical Properties of 45S5 Bioactive Glass and Glass-Ceramic, Vol. 3 - I (2014).

[10] I. Ahmed, M. Lewis, I. Olsen, J.C. Knowles, Phosphate glasses for tissue engineering: Part 1. Processing and characterisation of a ternary-based P2O5–CaO–Na2O glass system, Biomaterials. 25 (2004) 491–499.

[11] A.A. El-Kheshen, F.A. Khaliafa, E.A. Saad, R.L. Elwan, Effect of Al2O3 addition on bioactivity, thermal and mechanical properties of some bioactive glasses, Ceram. Int. 34 (2008) 1667–1673.

[12] M. Kamitakahara, C. Ohtsuki, H. Inada, M. Tanihara, T. Miyazaki, Effect of ZnO addition on bioactive CaO-SiO2-P2O5-CaF2 glass-ceramics containing apatite and wollastonite, Acta Biomater. 2 (2006) 467–471.

[13] I. Ahmed, A. Parsons, A. Jones, G. Walker, C. Scotchford, C. Rudd, Cytocompatibility and effect of increasing MgO content in a range of quaternary invert phosphate-based glasses, J. Biomater. Appl. 24 (2010) 555–75.

[14] N. Sharmin, M.S. Hasan, A.J. Parsons, D. Furniss, C.A. Scotchford, I. Ahmed, et al., Effect of boron addition on the thermal, degradation, and cytocompatibility properties of phosphate-based glasses, Biomed Res. Int. 2013 (2013) 902427.

[15] J. Massera, C. Claireaux, T. Lehtonen, J. Tuominen, L. Hupa, M. Hupa, Control of the thermal properties of slow bioresorbable glasses by boron addition, J. Non. Cryst. Solids. 357 (2011) 3623–3630.

[16] H. Gao, T. Tan, D. Wang, Effect of composition on the release kinetics of phosphate controlled release glasses in aqueous medium, J. Control. Release. 96 (2004) 21–8.

[17] E.A. Abou Neel, W. Chrzanowski, S.P. Valappil, L.A. O'Dell, D.M. Pickup, M.E. Smith, et al., Doping of a high calcium oxide metaphosphate glass with titanium dioxide, J. Non. Cryst. Solids. 355 (2009) 991–1000.

[18] M.N. Rahaman, D.E. Day, B.S. Bal, Q. Fu, S.B. Jung, L.F. Bonewald, et al., Bioactive glass in tissue engineering., Acta Biomater. 7 (2011) 2355–2373.

[19] Q. Fu, E. Saiz, A.P. Tomsia, Bioinspired Strong and Highly Porous Glass Scaffolds., Adv. Funct. Mater. 21 (2011) 1058–1063.

[20] E.J.C. Davim, M.H.V. Fernandes, A.M.R. Senos, Increased surface area during sintering of calcium phosphate glass and sodium chloride mixtures, J. Eur. Ceram. Soc. 35 (2015) 329–336.

[21] T. Kokubo, H. Kushitani, S. Sakka, T. Kitsugi, T. Yamamuro, Solutions able to reproduce in vivo surface-structure changes in bioactive glass-ceramic A-W3, J. Biomed. Mater. Res. 24 (1990) 721–734.

[22] T. Kokubo, H. Takadama, How useful is SBF in predicting in vivo bone bioactivity?, Biomaterials. 27 (2006) 2907–2915.

[23] M.. Coelho, M.. Fernandes, Human bone cell cultures in biocompatibility testing. Part II: effect of ascorbic acid, β-glycerophosphate and dexamethasone on osteoblastic differentiation, Biomaterials. 21 (2000) 1095–1102.

[24] M.J. Coelho, A.T. Cabral, M.H. Fernande, Human bone cell cultures in biocompatibility testing. Part I: osteoblastic differentiation of serially passaged human bone marrow cells cultured in alpha-MEM and in DMEM., Biomaterials. 21 (2000) 1087–94.

[25] S.S. Banerjee, S. Tarafder, N.M. Davies, A. Bandyopadhyay, S. Bose, Understanding the influence of MgO and SrO binary doping on the mechanical and biological properties of beta-TCP ceramics, Acta Biomater. 6 (2010) 4167–74.

[26] T.M. Keaveny, E.F. Morgan, G.L. Niebur, O.C. Yeh, Biomechanics of trabecular bone, Annu. Rev. Biomed. Eng. 3 (2001) 307–33.

[27] K. Rezwan, Q.Z. Chen, J.J. Blaker, A.R. Boccaccini, Biodegradable and bioactive porous polymer/inorganic composite scaffolds for bone tissue engineering, Biomaterials. 27 (2006) 3413–3431.

[28] A. Saboori, M. Rabiee, F. Moztarzadeh, M. Sheikhi, M. Tahriri, M. Karimi, Synthesis, characterization and in vitro bioactivity of sol-gel-derived SiO2–CaO–P2O5–MgO bioglass, Mater. Sci. Eng. C. 29 (2009) 335–340.

[29] J.P. Fan, P. Kalia, L. Di Silvio, J. Huang, In vitro response of human osteoblasts to multi-step sol-gel derived bioactive glass nanoparticles for bone tissue engineering, Mater. Sci. Eng. C. Mater. Biol. Appl. 36 (2014) 206–14.

[30] P. Sepulveda, J.R. Jones, L.L. Hench, In vitro dissolution of melt-derived 45S5 and sol-gel derived 58S bioactive glasses, J. Biomed. Mater. Res. 61 (2002) 301–11.

[31] A.J. Salinas, S. Shruti, G. Malavasi, L. Menabue, M. Vallet-Regí, Substitutions of cerium, gallium and zinc in ordered mesoporous bioactive glasses, Acta Biomater. 7 (2011) 3452–8.

[32] P. Saravanapavan, L. L. Hench, Mesoporous calcium silicate glasses. II. Textural characterisation, J. Non. Cryst. Solids. 318 (2003) 14–26.

[33] L.M. Mukundan, R. Nirmal, D. Vaikkath, P.D. Nair, A new synthesis route to high surface area sol gel bioactive glass through alcohol washing: a preliminary study, Biomatter. 3 (2013) 1–10.

[34] M. Vallet-Regí, A.J. Salinas, J. Román, M. Gil, Effect of magnesium content on the in vitro bioactivity of CaO-MgO-SiO2-P2O5 sol-gel glasses, J. Mater. Chem. 9 (1999) 515–518.

[35] P.P. Lopes, B.J.M.L. Ferreira, P.S. Gomes, R.N. Correia, M.H. Fernandes, M.H. V Fernandes, Silicate and borate glasses as composite fillers: a bioactivity and biocompatibility study, J. Mater. Sci. Mater. Med. 22 (2011) 1501–10.

[36] J. Pérez-Pariente, F. Balas, J. Román, A.J. Salinas, M. Vallet-Regí, Influence of composition and surface characteristics on the in vitro bioactivity of SiO(2)-CaO-P(2)O(5)-MgO sol-gel glasses, J. Biomed. Mater. Res. 47 (1999) 170–5.

[37] J.M.F. Navarro, El vidrio: Constitución, fabricación, propiedades, 2nd ed., Consejo Superior de Investigaciones Científicas, Sociedad Española de Cerámica y Vidrio, Madrid, 1991.

[38] Y. Ebisawa, T. Kokubo, K. Ohura, T. Yamamuro, Bioactivity of CaO-SiO2-based glasses:in vitro evaluation, J. Mater. Sci. Mater. Med. 1 (1990) 239–244.

[39] H. Orimo, The mechanism of mineralization and the role of alkaline phosphatase in health and disease, J. Nippon Med. Sch. 77 (2010) 4–12.

Chapter IX

"Science never solves a problem without creating ten more."

George Bernard Shaw (1856 – 1950)

CHAPTER IX

CRYSTALLIZATION EFFECT IN THE IN VITRO BIOACTIVITY AND BIOCOMPATIBILITY OF A CALCIUM-PHOSPHATE-BASED GLASS BULK AND SCAFFOLD

Abstract

The mineralization of glasses and glass-ceramics in an acellular medium is related with the ability to form an apatite layer on their surfaces. Glass-ceramics and glasses have significant differences in the formation of this layer due to distinct surface reactivities. The surface reactivity is related with the rate of glass dissolution and with the nature and amount of crystalline phases in the glass-ceramics. The *in vitro* behaviour of the $3CaO.P_2O_5$–SiO_2–MgO glass and glass-ceramics bulks and their corresponding scaffolds, were studied in this work. FTIR, XRD, SEM and EDS analysis of the samples after immersion in simulated body fluid showed the presence of an apatite layer on their surfaces, which formed faster on the glass than on the glass-ceramics. In addition, biocompatibility studies were investigated by *in vitro* cell culture with human bone marrow cells. The cells showed a normal morphology and high growth rate in the glass when compared to standard culture plates. Contrarily, lower cell proliferation occurred in the glass-ceramics, especially on the bulk probably due to high Mg ionic concentration in the cell culture medium as a consequence of the degradation of the amorphous phase. Therefore, the goal of an ideal scaffold that provides good mechanical support temporarily while maintaining a tailorable bioactivity and biocompatibility can be achieved with the development of glass-ceramic scaffolds.

IX.1. Introduction

Since the development by Hench et al. [1,2], of the designated 45S5 Bioglass, with a composition of 45% SiO_2, 24.5% Na_2O, 24.4% CaO and 6% P_2O_5 in wt. %, many different compositions have been explored over the years for bone repair applications. Bioactive glasses constitute an interesting group of inorganic materials to be used as bone repair scaffolds, due to their high bioactivity, biocompatibility, osteoconductive and osteoproductive properties [3,4]. These materials are able to bind with bone and soft tissues through their unique ability to form a hydroxyl carbonate apatite (HCA) layer on the surface as a result of their chemical reactivity in physiological media. The release of ionic species from bioactive glasses, due to dissolution, is the first step of a sequence of events that lead to the precipitation of HCA on the glass surface *in vitro* [5,6] and in vivo [7,8], creating a favourable environment for osteoblast proliferation and differentiation thus stimulating new bone formation. This sequence of events, reactions on the material surface, are explained in detail by Hench [2,9,10]. The degradation kinetics of the glasses should match the regeneration kinetics of new bone *in vitro* and/or *in vivo*. A further requirement, particularly in bone engineering, for a scaffold, is a controllable interconnected porosity that can provide greater surface area for vascularization, and bone in-growth [11,12].

Developing biocompatible glass and glass scaffolds with adequate degradability and appropriate mechanical properties for tissue engineering applications remains a challenge for biomedical engineers [13–15]. Controllable dissolution rates and suitable strength can be achieved by the production of glass-ceramics through controlled glass crystallization [16].

Chen et al [17] have successfully synthesized highly porous, mechanically competent, bioactive and biodegradable 45S5 Bioglass-derived glass–ceramic scaffolds for bone engineering, with fine crystals of $Na_2Ca_2Si_3O_9$. After immersion in simulated body fluid for 28 days, this crystalline phase was transformed into an amorphous calcium phosphate phase. By controlling the crystallinity fraction, authors found that the biodegradable rate could be tailored since the degradation rate and conversion to an HA-like material of 45S5 glass-ceramics become very slow with crystallization increase [18].

Previous work on the crystallization process of a $3CaO.P_2O_5$–SiO_2–MgO glass has shown that the crystallization of this glass starts with the whitlockite phase (in fact magnesium whitlockite – $(Ca_{2.589}MgO_{0.411})(PO_4)_2$), also known as β-TCMP [19].

It has been reported [20] that the presence of magnesium in β-TCP, significantly decreases the solubility due to the partially replacement of Ca^{2+} by Mg^{2+}, a smaller cation that promotes increased

bonding and consequent stability. Recently, the Mg-containing β-TCP [21,22] has been gain much attention, improving bone metabolism and biocompatibility [23,24] when compared to β-TCP.
The aim of this work was to modulate the glass surface reactivity through carefully controlled thermal treatments obtaining a glass-ceramic, with only one crystalline phase, whitlockite. The effect of crystallinity degree on the *in vitro* behaviour was attested in simulated body fluid SBF and through human osteoblast cells response. The effect of microstructural characteristics on the bioactivity of the glass–ceramics (bulk and porous scaffolds) was also discussed.

IX.2. Materials and Methods

IX.2.1. Glass and glass-ceramic bulks

Glass with molar composition 32.7 % CaO, 10.9 % P_2O_5, 25.4 % SiO_2 and 31 % MgO (mol. %) was produced by conventional melt quenching technique, mixing the required amounts of analytical grade SiO_2, $Ca(H_2PO_4)_2.H_2O$, MgO and $CaCO_3$ and melting at 1500 ºC in Pt crucible for 2 h in air.
The glass was cast in a stainless steel mould and annealed for 30 minutes at 740 ºC. The bulk glass samples were prepared with dimensions of 1 x 1 x 0.5 cm^3, polished with sandpaper grain size successively thinner and finished with diamond paste of 15, 6, 3 and 1 µm particle size. The polished samples were cleaned in ultrasonic bath, first with alcohol and then with ultrapure water.
The samples were further treated, based on DTA data obtain in previous work [19], at 840 and 910 ºC for 2 hours at a heating rate of 5 ºC min^{-1} in order to crystallize the glass samples. The amorphous bulk specimens were designated G31 and the glass-ceramics were denominated G31C-84 and G31C-91 in accordance with their respective heat treatment, at 840 and 910 ºC, respectively. After heat treatment the samples were polished with diamond paste of 15, 6, 3 and 1µm particle size.

IX.2.2. Scaffolds

Glasses were also prepared in frit form for scaffolds production using the salt sintering technique [25]. The frit was dried and then milled and sieved to obtain glass powders with mean particle size of 3.5 µm, as determined by the light scattering technique (Coulter LS 230, Fraunhofer optical model, MA). A mixture of glass particles and 50 wt. % NaCl (212-500 µm) was prepared. The mixture was pressed and sintered at 750 ºC for 10 min. After sintering, the incorporated porogen was removed through aqueous washing, thus resulting a porous glass scaffold, denominated GS31, with ~ 65 % porosity, containing macropores with diameters between 150 and 500 µm and micropores with diameter < 60 µm.

Crystallization of the glass scaffolds was performed by heating the samples in an electric furnace up to 900 ºC, at a heating rate 5 ºC min^{-1}, and maintained at this temperature for 30 min, in order to crystallize the glass scaffolds. These heat-treatments were chosen based on dilatometric and DTA analysis of the glass/salt mixture, as studied before [25]. These glass-ceramic scaffolds were denominated GS31C-90.

Mechanical properties of the scaffolds at compression were studied in a Bose/Electro Force 3400 testing machine. Six cylindrical samples (10 x 10 mm^2) were compressed at a speed of 0.5 mm min^{-1}. Prior to mechanical testing, the contact surfaces of each sample were ground to produce smooth parallel surfaces.

Mercury Intrusion Porosimetry, was used to measure both porosity and pore sizes using an AutoPore IV 9500V1.07 serial 734 Penetrometer. Sample weight varied from 0.25 to 0.3 g. Given that the porosimeter measurement determines the intruded volume of mercury per gram sample, it is assumed that this value gives the open porosity i.e., is equal to the porous volume (V) per gram sample.

IX.2.3. Phase analysis

X-ray diffraction (XRD) analysis was performed in all samples using a Rigaku Diffractometer Geigerflex Dmax-C at room temperature with CuKα radiation (at 40 kV and 40 mA) and a scan speed of 0.02^o s^{-1}. Data was obtained in the 2θ range of 10-80 degree to investigate the characteristic phases and crystallinity amount of the fabricated samples. For XRD measurements, the samples were ground and measured in powder form.

The amount of the crystalline phase (crystallized volume fraction) contained in the glass-ceramic, bulk and scaffolds, was determined according to the procedure used by Krimm and Tobolsky [26] and recently by Daguano et al [27]. The percent crystallinity, CF, was calculated by the ratio of the crystalline area, CA, present in the diffractogram of the glass-ceramics and the total area, TA (amorphous + crystalline), present in this diffractogram using the following equation [28]:

$$CF = (CA/TA) \times 100 \qquad \text{(Eq. IX.1)}$$

The crystallized phases were observed by scanning electron microscopy (SEM) using a Hitachi Su-70, Japan system. Back-scattered electron (BSE) images were also used on bulk glass-ceramics.

IX.2.4. In vitro bioactivity

The *in vitro* behaviour was assessed by soaking glass and glass-ceramic bulk and porous samples in simulated body fluid (SBF) for periods from 1 hour up to 14 days. The SBF solution was prepared according to the formulation of Kokubo and Takadama [29]. A constant specimen surface area to

solution volume ratio of 0.1 cm^{-1} was used, considering the value of the surface area given by the BET method. Glass-ceramic bulk samples were also analyzed for longer times, 10, 20, 30 days and 5 months. Subsequently the samples were placed in a polyethylene bottle containing SBF solution, and kept for various periods of time, without shaking, in an incubator at 37 ºC, in accordance with a protocol referred to in literature [30–32]. Four samples were used for each immersion time. After removal from the SBF, samples were dried at 60 ºC. The assessment of the samples dissolution profile, ionic concentration changes in SBF, was based on data from inductively coupling plasma spectrometry (ICP) testing using a Jobin-Yvon JY70 Plus, France. The pH changes were evaluated at the different soaking times.

SEM and XRD were used as described previously. Energy dispersive X-ray spectroscopy (EDS) was applied to analyze the elemental composition of the surface of the samples immersed in SBF at different time intervals. For EDS analysis the samples were carbon sputtered under high vacuum (6.7 x 10^{-3} Pa).

FTIR analysis, were also used to characterize the HA-like layer formed on all samples after immersion in SBF. Bulk samples were recorded in a Brucker tensor 27 spectrometer, using a Golden Gate single reflection diamond ATR system, with no need for sample preparation. Scaffolds were reduced to powder and mixed with KBr (ratio 1:10) and pressed into a pellet using a hand press. All spectra were collected over a region of 4000 – 400 cm^{-1} and taken as the average of two independent measurements with 256 scans at a resolution of 4 cm^{-1}. For comparison purposes samples without immersion were analysed as well.

IX.2.5. Osteoblastic cytocompatibility

IX.2.5.1. Human bone marrow cell cultures

Human bone marrow, obtained from orthopaedic surgery procedures (after patient informed consent), was cultured in α-Minimal Essential Medium (α-MEM) supplemented with 10 % fetal bovine serum, 100 mg/ml penicillin, 10 IU streptomycin, 2.5 mg ml^{-1} fungizone, at 37 ºC in a humidified atmosphere of 5 % CO_2 in air. For subculture, the cell monolayer was incubated with a trypsin–EDTA solution (0.05 % trypsin, 0.25 % EDTA) for 10 min at 37 ºC to detach the cells. Cells were re-suspended in culture medium and seeded (5 x 10^4 cells cm^{-2}) over the material samples (previously sterilized by autoclaving at 120 ºC). Seeded material samples were cultured for 21 days in the presence of 50 μg ml^{-1} ascorbic acid, 10 mM β-glycerophosphate and 10 nM dexamethasone. This experimental conditions are reported to allow the osteoblast differentiation in this culture system [33]. All the experiments were performed in the first subculture, since the sequential passage of bone marrow cells results in a progressive loss of the osteoblastic phenotype

[34]. Colonized materials were evaluated for cell morphology, cell viability/proliferation, alkaline phosphatase (ALP) activity and ability to form calcium phosphate deposits.

IX.2.5.2. Cell viability/proliferation

Cell viability/proliferation was evaluated by the Resazurin assay. Resazurin (7-Hydroxy-3*H*-phenoxazin-3-one 10-oxide), a non-fluorescent blue component is reduced in the mitochondria of the living cells to the pink fluorescent component resorufin. This is a non-destructive assay, alloying the same samples to be followed throughout the culture time. At each time-point, culture medium was removed, and fresh medium with 10 % (v/v) of resazurin was added to the cells. Cultures were incubated at 37 ºC in a humidified atmosphere of 95 % air and 5 % CO_2 for 3 h. Then, 100 µL of the culture medium were transferred to a 96-well plate and the fluorescence intensity was measured in a microplate reader (Synergy HT, BioTek, USA) at 535 nm excitation wavelength and 590 nm emission wavelength. The results were expressed in relative fluorescence units.

For celular observation, samples were fixed (1.5 % glutaraldehyde in 0.14 *M* sodium cacodylate buffer, pH = 7.3, 10 min), dehydrated in graded alcohols, critical-point dried, sputter-coated with a Au/Pd thin film (SPI Module Sputter Coater equipment), and observed in a High resolution (Schottky) Environmental Scanning Electron Microscope (Quanta 400 FEG ESEM) with a X-ray energy dispersive spectroscopy (EDS) microanalysis capability.

IX.2.5.3. Alkaline phosphatase activity

ALP activity was evaluated in cell lysates (0.1 % Triton X-100, 5 min) by the hydrolysis of *p*-nitrophenyl phosphate in alkaline buffer solution (pH ~10.3; 30 min, 37 ºC) and colorimetric determination of the product (*p*-nitrophenol) at 400 nm in an ELISA plate reader (Synergy HT, Biotek). ALP activity was normalized to total protein content (quantified by Bradford's method) and was expressed as nmol/min.µg protein^{-1}.

IX.2.5.4. Statistical analysis

Values are expressed as mean ± standard deviation (SD) of three replicates and were compared using the student's t-test, with a significance level of $p < 0.05$.

IX.3. Results and discussion

IX. 3.1. Bulk and scaffolds characterization

The XRD patterns of all the samples, glass and glass-ceramics bulk and scaffolds are shown in Fig. IX.1a and 1b, respectively. All glass-ceramics studied in this work presented a whitlockite phase with Ca substituting Mg, $(Ca,Mg)O{\cdot}P_2O_5$ solid solution or β-TCMP, according to the card No. 01-087-1582 in the X'Pert HighScore database. As can be observed in Fig. IX. 1, a higher degree of crystallization was obtained in the glass-ceramics bulk by increasing the temperature from 840 to 910 ºC, with a holding time of 2 hours. The XRD pattern of the glass-ceramic scaffold, GS31C-91, after heat treatment at 910 ºC, 30 min, were also shown in Fig. IX.1.

Glass-ceramic G31C-84 presents an amount of 39 % crystal phase, calculated according to Eq. IX.1. The crystallinity (CF) increased considerably to 82 % with the treatment at 910 ºC, G31C-91. Glass-ceramic scaffolds presented an amount of 76 % crystal phase. As observed in previous work [25] the salt sintering method promote an earlier crystallization of the glass scaffolds when compared to the glass heat treatment without salt. In this case, it is possible to obtain the same crystalline phase with a treatment 10 ºC lower and a holding time 90 min shorter. Although the goal of the work was to prepare a glass-ceramic bulk and scaffold with the same crystalline fraction, due to experimental difficulties (presence of a second crystalline phase on the scaffold) we choose to work with a difference of 6 % crystalline fraction between the G31C-91 and the GS31C-90.

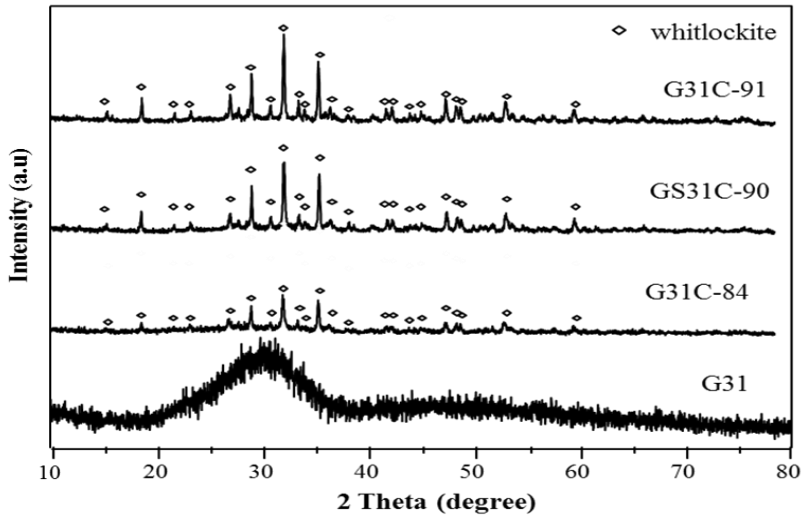

Fig.IX.1. XRD pattern of the base glass G31 and after heat treatment for 2 hours at 840 ºC, G31C-84, and at 910 ºC, G31C-91, and of the corresponding scaffold heat treated at 900 ºC for 30 min, GS31C-90

The development of a crystalline phase in the bulk samples with increasing temperature could be also observed on the micrographs obtained by SEM, Fig. IX. 2.

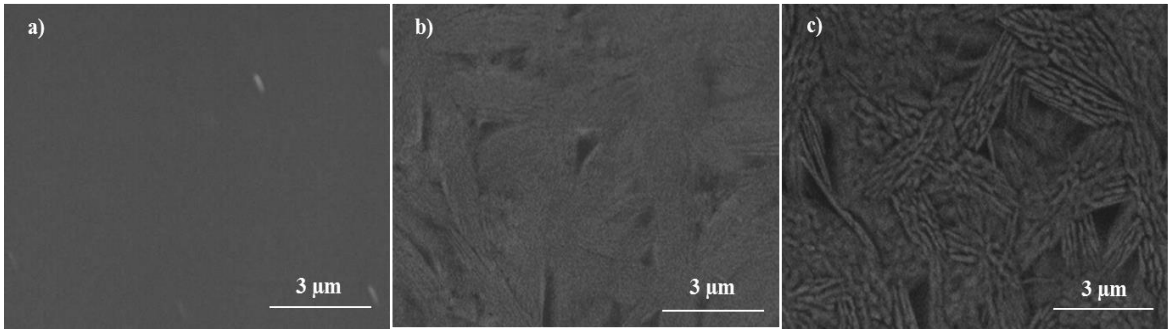

Fig.IX.2. Microstructure of the bulk base glass, G31 (a) and correspondent glass-ceramic after heat treatment at 5 ºC min^{-1}, for 2 hours at b) 840 ºC, G31C-84 and c) 910 ºC, G31C-91

Glass and glass-ceramic scaffolds present a similar microstructure, namely porosity with interconnected pores in the range of 100 – 500 µm, Fig. IX. 3a) and b).

These results were confirmed by the intrusion data determined by mercury porosimetry, Table IX.1. The glass and glass-ceramic scaffold present a porosity of 63 % and 68 % respectively (pores < 400 µm), with similar microporosity (13 % < 10 um).

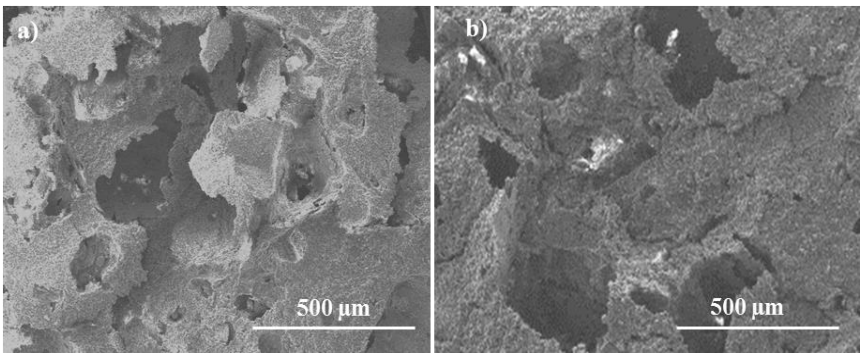

Fig.IX.3. Microstructure of the glass scaffold, GS31 (a) and of the glass-ceramic scaffold after heat treatment at 5 ºC min^{-1}, for 30 min at 900 ºC, GS31C-90 (b)

The obtained glass-ceramic scaffold presented an increase on the compression strength compared with the untreated glass scaffolds, from 1.3±0.2 to 5.9±0.1 MPa. Since the porosity of the glass and glass-ceramics are similar, the significant increase mechanical behaviour was provided by the presence of the crystalline phase on the scaffold.

Table IX. 1. Structural parameters of the glass and glass-ceramic scaffolds obtained by mercury porosimetry and correspondent compression mechanical behaviour

Scaffold	Open Porosity (%)		Total Pore Area (m^2/g)	Median pore Diameter µm		Compressive strength (MPa)
	total	<10 µm		60-350	<10 µm	
GS31	63.2	13	0.54	88	1.9	1.3±0.2
GS31C-90	67.7	13	0.71	91	2.0	5.9±0.1

IX. 3.2. In vitro bioactivity

IX.3.2.1. In vitro bioactivity of bulk samples

During the first SBF soaking hour it was observed mainly the dissolution of the glass bulk, G31, Fig. IX.4a and 4b. With one day immersion, Fig. IX.4c, it was already observed a completely formed layer. Finally, for 5 and 7 days immersion the precipitated layer takes a form of plates with reasonable dimensions, Fig. IX.4d, weakly adherent to the glass surface (without effort the layer stands out).

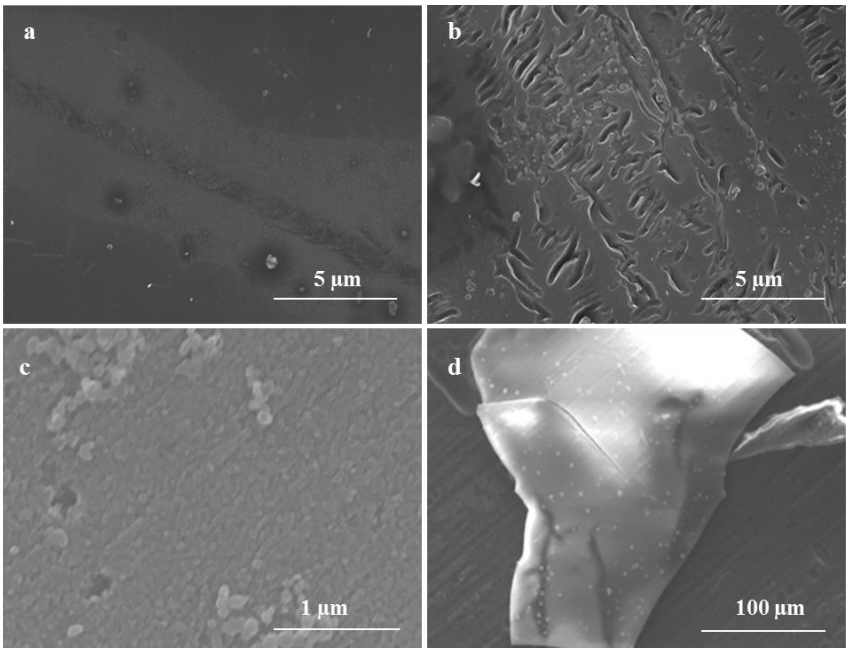

Fig.IX.4. SEM micrographs of the G31 glass surface for a) 1h, b) 2h, c) 1day and d) 7 days soaking times in SBF

IX.3.2.2. In vitro bioactivity of the bulk glass-ceramic

In the first soaking hours of the glass-ceramic samples, G31C-84 and -91, it was observed the dissolution of sample. G31C-84 dissolution occurs primarily between crystals of calcium phosphate, as can be seen in Fig. IX.5a and 5b. With the immersion time, the amount of small deposits considerably increases. With 30 days immersion, Fig. IX.5c, it was clearly seen the formation of

precipitates on the surface, with approximately 8 μm wide. To better understand the nature of the precipitated layer and also to obtain a sufficiently representative thickness layer, a 5 months immersion was performed, wherein the SBF was replaced monthly. A large precipitate amount was observed on the surface of the glass-ceramics, Fig. IX.5e, where a part of the glass-ceramic was partially covered by a fissured layer, apparently with no separation from the substrate.

The G31C-91 with an IC of 82 % had a slower dissolution. During the thirty days of immersion in SBF it wasn't detected any formation of precipitates, Fig. IX.5d, in G31C-91 while on the surface of G31C-84, Fig. IX.5c, globular structures and cracks are noticed.

The same results are observed only after 5 months, for the G31C-91 in Fig. IX.5f. During immersion in SBF, the onset time of the precipitate layer formation changed from 1 day, for the original bulk glass, to 5 months for the 82 % crystallized sample. The reaction rate was reduced with increase crystallization degree.

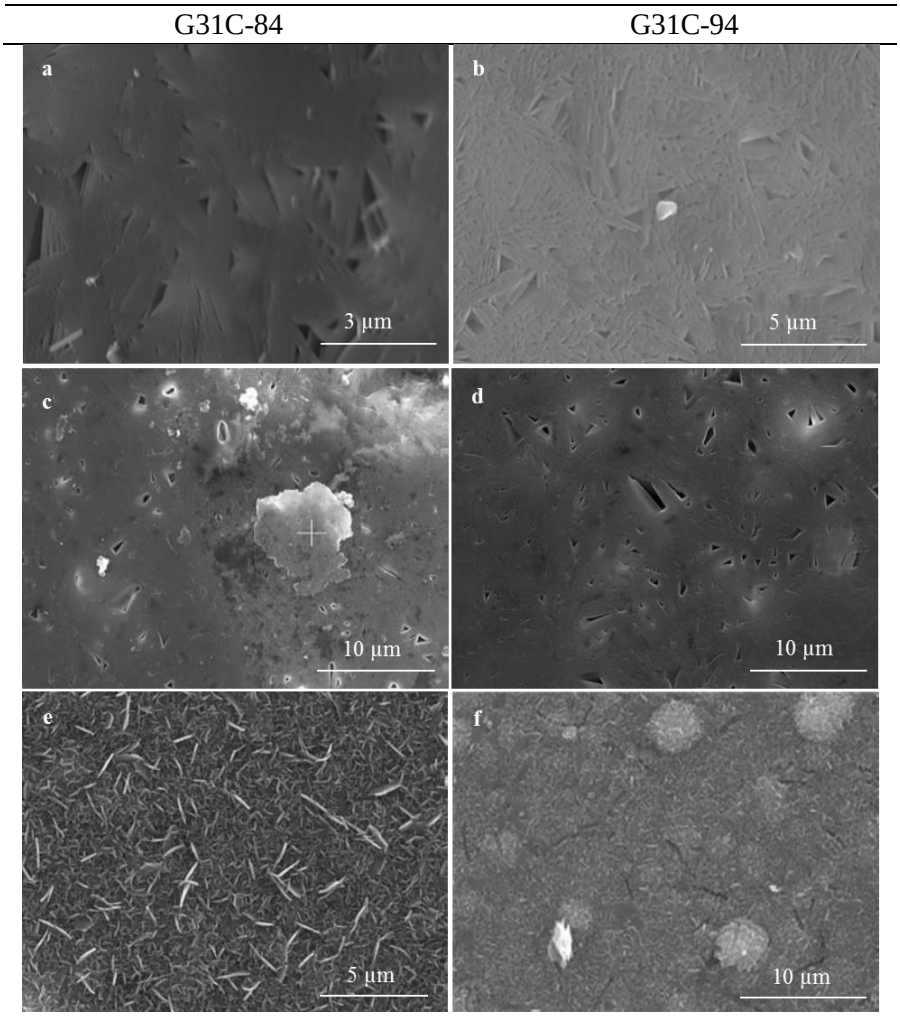

Fig.IX.5. SEM micrographs of the surfaces of G31C-84 and G31C-91 for different soaking times in SBF; a, b) 1day, c, d) 30 days and e, f) 5 months

IX.3.2.3. In vitro bioactivity of the scaffolds

SEM micrographs of the glass scaffolds exhibited, soon after 3 days in the SBF solution, Fig. IX.6a, a detectable surface precipitate. After 7 days immersion, Fig. IX. 6c), it was observed a complete coverage of the surface of the porous structure. Glass-ceramic scaffolds also present spherical particles aggregates that for 7 days almost fully cover the surface. For soaking times below 7 days there was no clear difference on the surfaces of the glass and glass-ceramic scaffold, i.e., there are no obvious effect of crystallinity on the precipitated structures of the scaffolds.

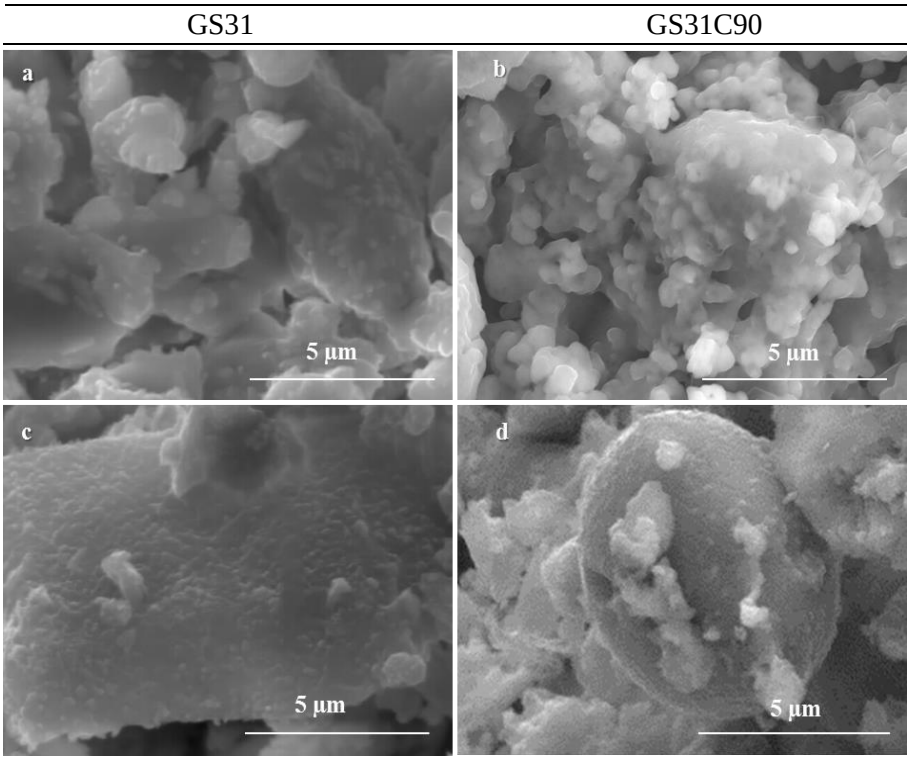

Fig.IX.6. SEM micrographs illustrate the growth of the Ca-P layer on the glass and glass-ceramic scaffolds with immersion time, a, b) 3 days and c, d) 7 days immersion

IX.3.2.4. Analysis of the precipitated layer

The XRD analysis, Fig. IX.7, presented on the glass bulk samples after 7 days immersion and on glass-ceramics after 5 months immersion, the diffraction peaks characteristic of hydroxyapatite at 2θ= 25.9º, 31.6º, 32.7º, 34º, 50º and 53º attributed to reflections (0 0 2), (1 2 1), (3 0 0), (2 0 2), (2 1 3) and (0 0 4) respectively accordingly to the card No. 01-073-2567.

After 5 months immersion in SBF, both glass-ceramic bulks presented in addition to the growing peaks of hydroxyapatite-like phase, the decrease crystallinity of the whitlockite phase. The sharp diffraction peaks of the whitlockite phase, observed in Fig. IX.1, disappeared from the XRD

spectrum of the G31C-84 leaving a typical broad halo (produced by an amorphous phase) overlapped by the sharp diffraction peaks of the HA phase. This indicates that under the detection limits of XRD, the G31C-84 was mainly composed of an amorphous phase and crystalline apatite.

In the glass scaffold, Fig. IX.7b, after 3 day immersion it was detected the characteristic peaks of crystalline hydroxyapatite. After 14 days immersion, the scaffold GS31 present increased intensity of the characteristic peaks of hydroxyapatite, $2\theta = 25.9º, 31.6º, 32.7º, 34º, 50º$ card No.01-073-2567. Also incipient peaks of whitlockite ($Ca_{2.859}Mg_{0.411}(PO_4)_2$) appear in the GS31 at the peaks 28º, 31º, and 36º, corresponding to the planes (2 1 4), (0 2 10) and (2 1 10) according to the card No. 01-087-1582.

The difference between G31 and GS31 bioactivity are more evident in XRD. For 7 days immersion the apatite layer on the G31 was more crystalline than that on GS31.

The glass-ceramic scaffold presented after 3 days, a decrease intensity of the whitlockite peaks, but no detectable apatite phase peaks. After 7 days immersion, the whitlockite was still present with lower intensity and the diffraction peaks characteristic of hydroxyapatite emerge with increase intensity after 14 days immersion. The peaks characteristic of whitlockite phase almost disappears after 14 days immersion.

The transformation of a crystalline phase to a degradable amorphous phase prior to CHA layer deposition, observed in this work for all glass-ceramics, was also observed in the literature on 45S5 glass-ceramics [35], HA and related calcium phosphates ceramics in an *in vivo* environment [23].

As the crystallization fraction increase the time required for HA layer formation on the material surface was higher. The glass-ceramic scaffold high surface area increased the kinetic of this transformation, lowering the onset of HA formation when compared to the bulk glass-ceramics.

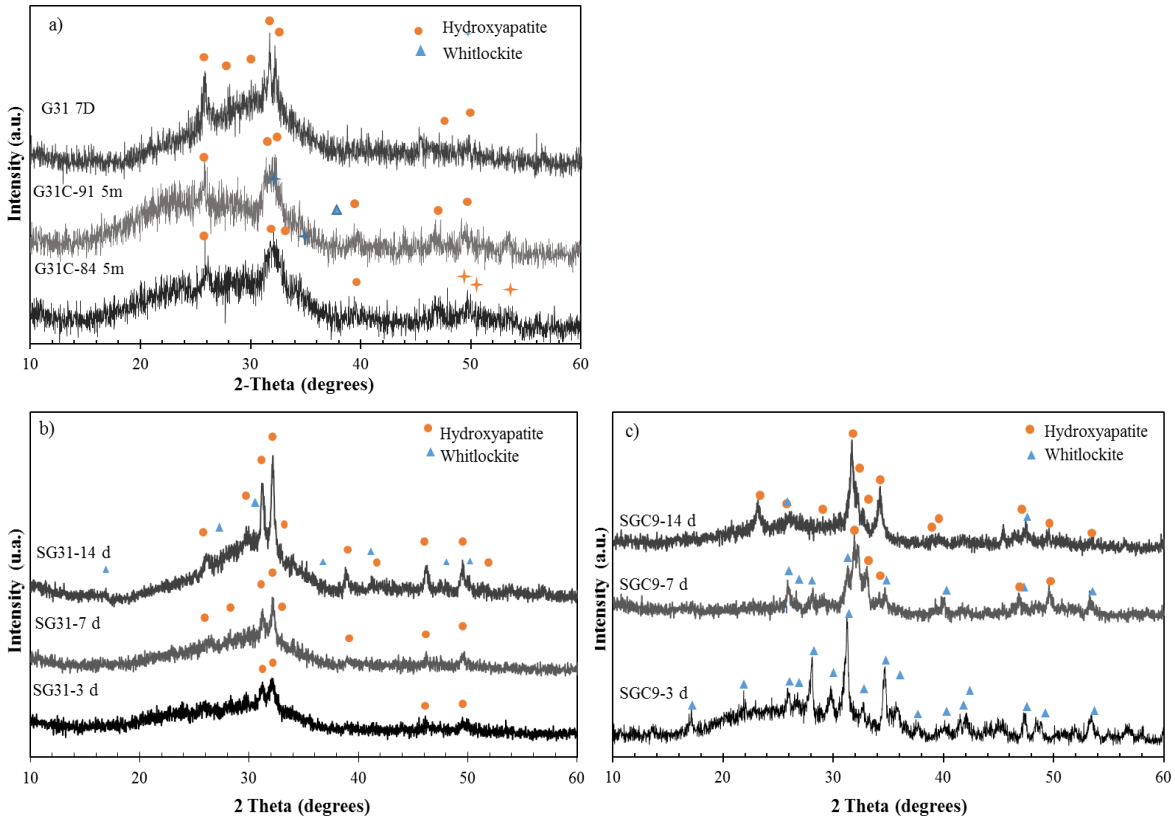

Fig.IX.7. XRD pattern of the samples after immersion in SBF; a) G31 for 7 days immersion and respective glass-ceramics with 5 months immersion, b) glass scaffold GS31 and c) glass-ceramic scaffold, GS31C-90, after immersion in SBF

The FTIR spectra of the bulks before SBF immersion, G31, G31C-84 and G31C-91, are shown in Fig. IX. 8a, 8c and 8d respectively and the glass-ceramic scaffolds spectra, before and after immersion, in Fig. IX.8b.

The control spectra of the G31, Fig. IX.8a, contained wide vibrational bands assigned to the Si – O – Si stretching and P – O bending at ~1000 and 554 cm^{-1}, respectively. The broad resonance in the range 850–950 cm^{-1} correspondent to the Si – O – NBO (non-bridging oxygen) vibrational mode was associated with the Ca ions in the glass network.

The bulk glass-ceramics before immersion presented a peak at 1060 cm^{-1} and a double peak at 565 and 603 cm^{-1}, attributed to the P – O bending vibrations due to the presence of whitlockite phase [36].

In the glass bulk, Fig. IX.8a, after 7 days, the appearance of the double peak from P – O bending bonds at 565 and 605 cm^{-1} revealed the presence of HA. The C – O stretching band at 800–890 cm^{-1} and P – O stretching at 910–1040 cm^{-1} are due the crystalline nature of HCA layer [37].

The increased definition of the peaks related to PO vibrations, P – O bend (at 565, 603 [1] and 1050 cm^{-}) and the apperence of a P – O stretch (at 1120 and 945 cm^{-1}) is indicative of an increase in the crystallinity of the precipitated HCA layer [37], on the glass-ceramic scaffold, after 7 days immersion.

In the G31C-84 spectrum, Fig. IX.8c, as the crystalline Ca-P layer grows, the double peaks correspondent to P – O bend (at 565, 605 and 1050 cm^{-1}) become sharp and dominate the FTIR spectra after 5 months immersion, indicating the growth of crystalline apatite *in vitro*.

The G31C-91, Fig. IX.8d, samples does not show modification of the structure after 7 days. Well established hydroxyapatite were present at 5 months, as evidenced by the pronounced dual P – O peaks near 602 and 575 cm^{-1} in the glass-ceramic and the presence of the peaks at 1450 and 1410 cm^{-1} and a third at 870 cm^{-1}, due to the presence of CO vibration.

These results suggest that the apatite formed on the surface of all bulk samples, after 7 days and 5 months immersion in SBF, for glass and glass-ceramic bulks respectively, was carbonated apatite, which is similar in composition and structure to bone apatite. Glass-ceramic scaffolds results after 7 days immersion were similar to the glass bulk.

The characteristic bands of the hydroxyl carbonate apatite layer (HCA) after 5 months immersion completely overlays the peaks related to Si – O bonds.

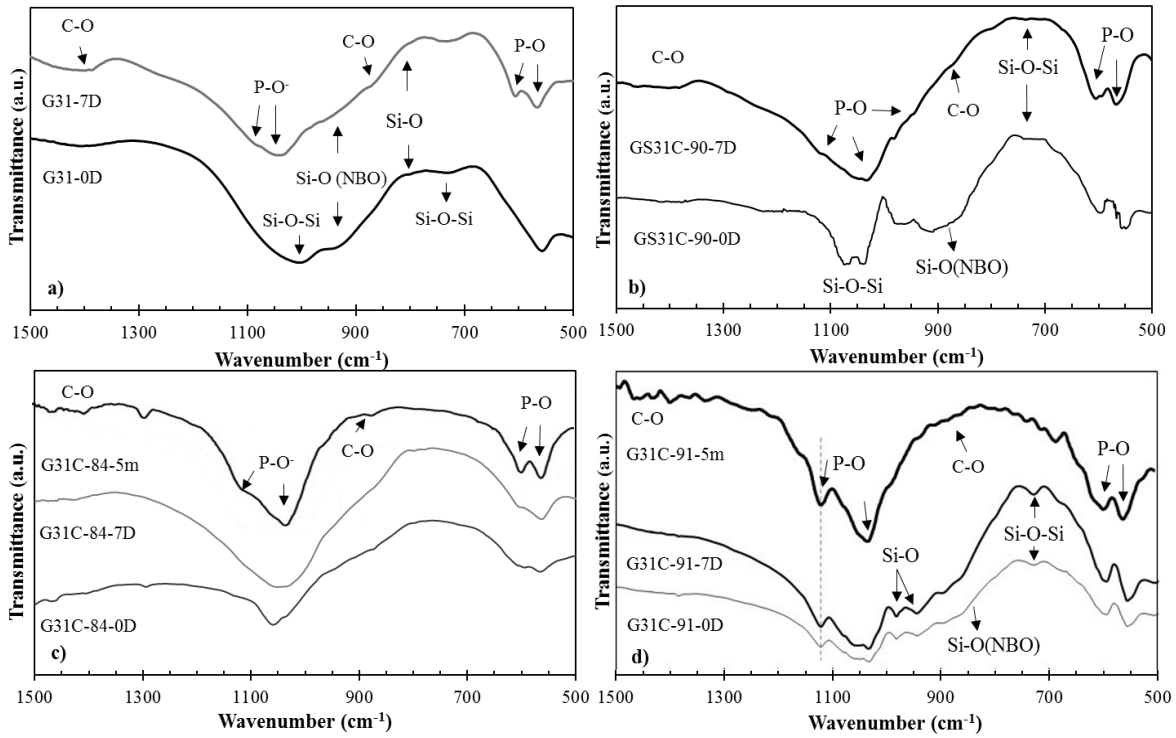

Fig.IX.8. FTIR reflection spectra of the a) parent bulk glass (G31), b) glass–ceramic G31C-84 and c) G31C-91 before and up to 7 days immersion in SBF. The glass-ceramic bulk spectrums after 5 months soaking are also presented.

The EDS pattern for the bulk glass, G31, Fig. IX.9, reveals that after 5 days immersed in SBF (value not shown) the precipitated layer observed on Fig. IX.3c, has a Ca/P ratio of 1.30 near an octacalcium phosphate OCP (Ca/P = 1.33) that gradually changes to hydroxyapatite (Ca/P = 1.66) between 14

and 21 days immersion. This value is very similar to the Ca/P molar ratio characteristic of stoichiometric HA - 1.67.

For the glass-ceramic bulk, G31C-84, the OCP layer was only observed at 7 days immersion where a Ca/P ratio of 1.32 was detected on the precipitates observed at Fig. IX.3c. Up to 21 days, the precipitated layer exhibit a pronounced increase in the Ca and P signal, with a Ca/P ratio of 1.60.

In the G31C-91, the kinetic deposition rate decreased, since the analysis of the precipitated layer on the surface of the glass-ceramic, for 5 months immersion, only detected the presence of a Ca/P ratio of 1.57. The presence of higher crystalline phase has a slowdown effect on the *in vitro* behaviour of the glass-ceramics.

Glass scaffold, after 1 day immersion, present a Ca/P ratio near 1, due to the presence of brushite. Between 14 and 21 days the Ca/P ratio increased from 1.62 to 1.67. In the glass-ceramic scaffolds, it was detected a Ca/P ratio of 1.54, after 14 days immersion. After 21 days a Ca/P of 1.63 was detected. The high surface area of the glass-ceramic scaffolds make possible that the transformation of whitlockite into the amorphous phase of calcium phosphate occurs at a reasonably faster rate than that on bulk glass-ceramics, since in fact the bioactive reactions only occur at the surface of the bulk solid glass-ceramics. For the same reasons, the glass scaffold present higher dissolution rate than the bulk glass. For 14 days immersion there is no difference between G31 and GS31 samples, both present a Ca/P ~ 1.6.

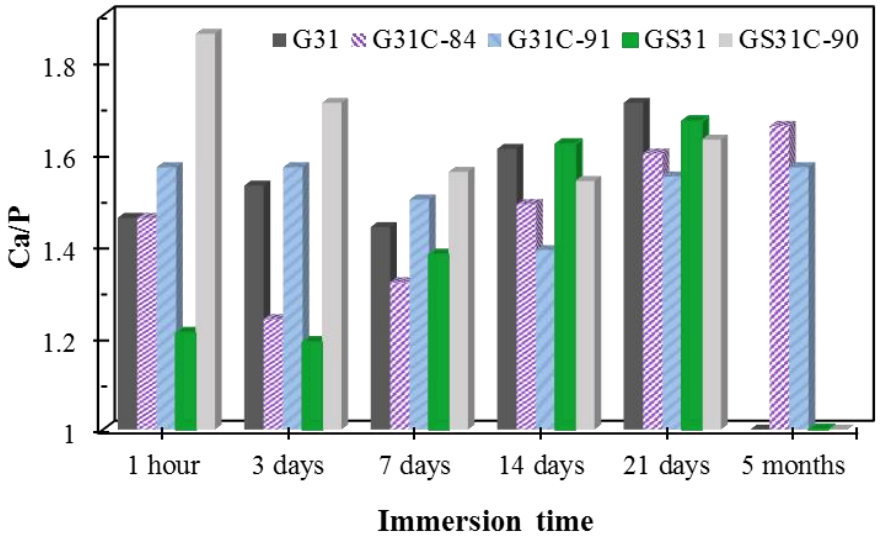

Fig.IX.9. EDS profiles of the glass and glass-ceramic bulk and scaffolds. For each measurement a standard deviation of approximately 0.2 was determined

IX.3.2.5. Dissolution in SBF of the studied materials

Fig. IX. 10 shows the concentrations of Ca, Mg, P and Si ions from the studied glass and glass-ceramics, bulk and scaffolds samples, after being soaked in SBF for different times.

The bulk glass-ceramics G31C-84 and -91, exhibit similar dissolution profiles between them. When compared with the bulk glass, G31, calcium and phosphorous ions are released faster from the glass bulk, reaching a maximum after 24 hours and then decreases with the development of a Ca-P rich layer as confirmed by SEM/EDS and DRX results. On both glass-ceramic bulks Ca ions continue to increase in the solution as the other ions.

The higher dissolution rate of Si and Mg from glass scaffold, compared to G31 can be explained by the increase of the surface area.

The glass-ceramic scaffolds dissolution profile shows no release of phosphorous species from the scaffolds, on the contrary, after 14 days immersion, most of the phosphorous was removed from the SBF. The same behaviour was observed for the Ca ion except in the first hour. The decrease concentration of calcium species, after 1 hour immersion, from 110 to 50 $mg.l^{-1}$ after 14 days, implies that calcium ions deposited on the glass-ceramic surface after 1 h immersion.

The higher magnesium dissolution observed in Fig. IX. 10, for both glass-ceramic bulk and glass scaffold when compared with bulk glass may retard the crystallization of hydroxyapatite by replacing calcium in the structure.

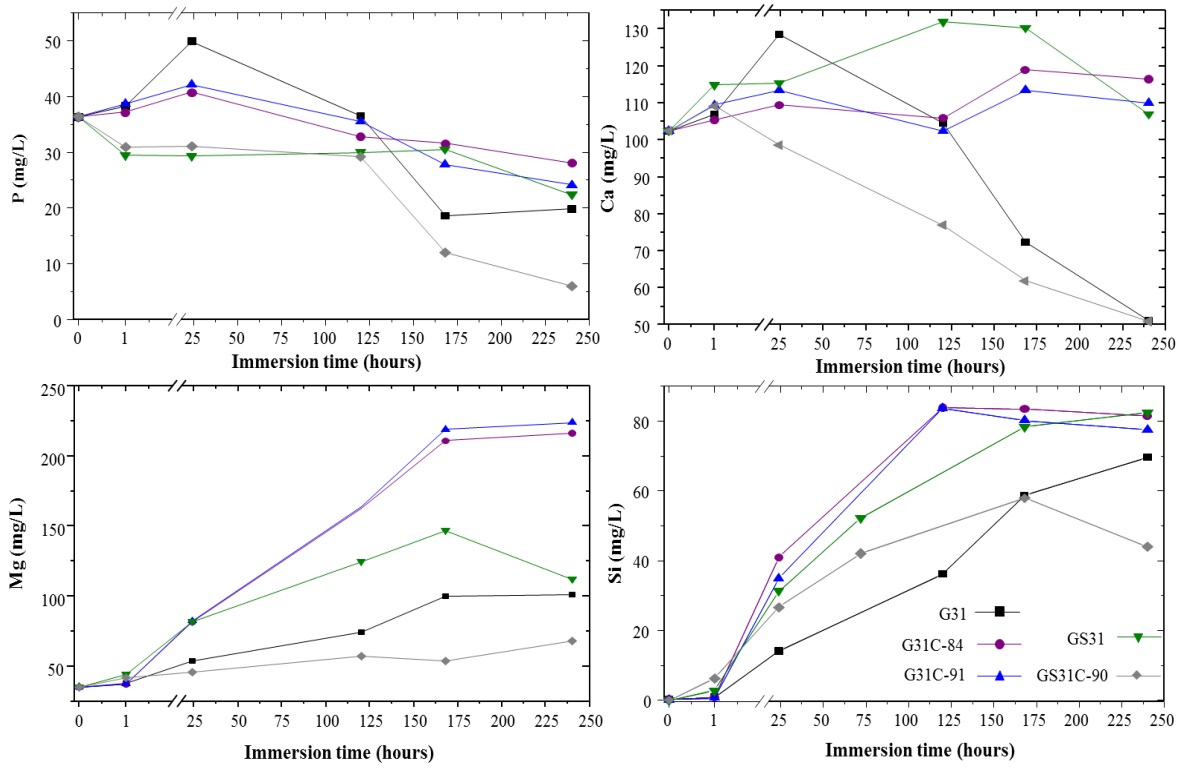

Fig.IX.10. Variation of ionic concentration in SBF due to immersion of the parent glass and correspondent glass-ceramics bulk and scaffolds. Lines are to guide the eye.

Fig. IX. 11 represents the variation of pH with soaking time for the glass and glass-ceramic bulk and scaffold samples. All testing solutions with exception to the glass-ceramic scaffold GS31C-90, showed a decrease in pH after 1 hour immersion. The bulk glass-ceramic G31C-84 showed the largest

decrease achieving the pH of 7.3. After that, for all samples, the pH increased rapidly during the first 125 h of immersion, slowed up and reached a nearly constant, limiting value above 10 days immersion. The glass scaffold showed the same trend, stabilizing earlier, after 7 days immersion, with a final pH of 8.2. Subsequently, the pH remained constant over the remaining weeks of immersion, reaching a saturated state. The lowest change in the pH-value was observed for the solution containing the GS31C-90 increased from the initial value 7.4 to 7.8 at the end of incubation period. The highest change was observed for bulk glass-ceramic G31C-91.

During soaking in SBF, Mg and Ca cations are leached from the sample surface in exchange for H^+ ions from the solution (from dissociation of water into H^+ and OH^-) resulting in an increase of the pH-value. The phosphate ions can be exchanged against OH^- ions, removing hydroxyl ions from solution and providing phosphate ions which buffer the effect of alkali ion release.

Hence, the higher phosphate concentration in the first hour of G31C-91 immersion results in a decrease of pH-value. In the case of GS31C-90 the high calcium and phosphate release promote a much lower increase of the pH-value. The similar dissolution profile of Ca and P ions dissolution in the bulk G31 promote the slowest increase of the pH value.

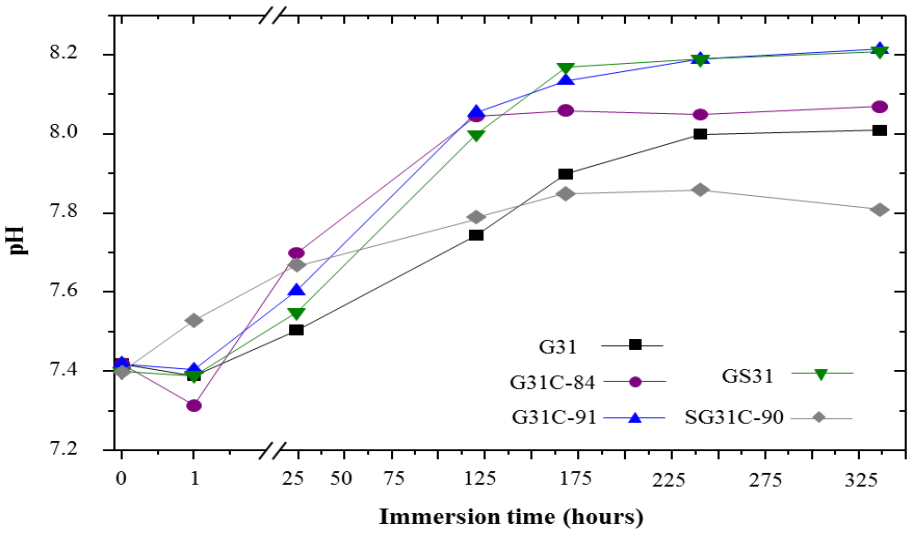

Fig.IX.11. Change of pH value of SBF solution with increasing soaking period for glass G31 and glass-ceramics G31C-84 and G31C-91 and the scaffolds GS31 and GS31C-90. Lines are to guide the eye

Taken together, SEM/EDS and XRD analyses indicate that the glass G31 precipitate HCA after 7 days immersion. Evaluating the sequence of reactions observed during the formation of the HCA layer, it can be noted that the time required for the glass-ceramics bulk G31C-84 was higher than the glass bulk and, occurs only after 5 months immersion for G31C-91.

In comparison with the G31C-84, there was a decrease in the amount of precipitate layer on the G31C-91, which can be connected to the decrease in the amount of amorphous phase still present in

the material. The inhibitory effect of crystallization on the *in vitro* bioactivity of these kind of materials, was also observed in other systems [35]. This can be linked to the large amount of Mg released from the glass to the solution [38–40]. However, in the current work, it was observed that the formation of HCA was delayed, but not hindered. The ability to control the degradability of these glasses, by crystallization, makes them potentially clinically helpful for tissue engineering,

IX.3.2.6. Biocompatibility studies

Human bone marrow cells, cultured in experimental conditions that favour the osteoblastic differentiation [33,34] were seeded over the glass and glass-ceramics bulk (G31, G31C-84 and G31C-91) and scaffold (GS31 and GS31C-90) samples for 21 days.

Fig. IX.12 shows the results for viability/proliferation (a) and the ALP activity (b) observed over the materials. For the bulk glass and glass-ceramics, results were compared to those on the standard tissue culture plate, and were normalized to the surface area. Compared to the polystyrene culture plate, the G31 glass and the glass-ceramic G31C-84 presented higher viability/proliferation values, with a statistical significance at days 14 and 21. However, the glass-ceramic G31C-91 showed lower values throughout the culture time. Among the bulk samples, values were similar for G31 and G31C-84 samples, and were significantly higher than those on G31C-91.

ALP activity was low at day 7 for all samples. At day 14, compared to the polystyrene surface, values were significantly higher on G31 and G31C-84 and lower on G31C-91, particularly at day 14. At day 21, values were similar in the culture surface, G31 and G31C-84, but they were slightly lower on G31C-91.

Regarding the two tested scaffolds, cell viability/proliferation and ALP activity increased throughout the culture time, and the pattern of behavior was similar to that seen on the corresponding bulk samples, i.e., values were significantly higher on GS31 compared to that on GS31C-90. Differences were higher at day 14 compared to that observed at day 21. ALP is an early osteoblastic marker and has a key role in the mineralization of the extracellular matrix, by providing phosphate ions for the formation of the calcium phosphate deposits [41].

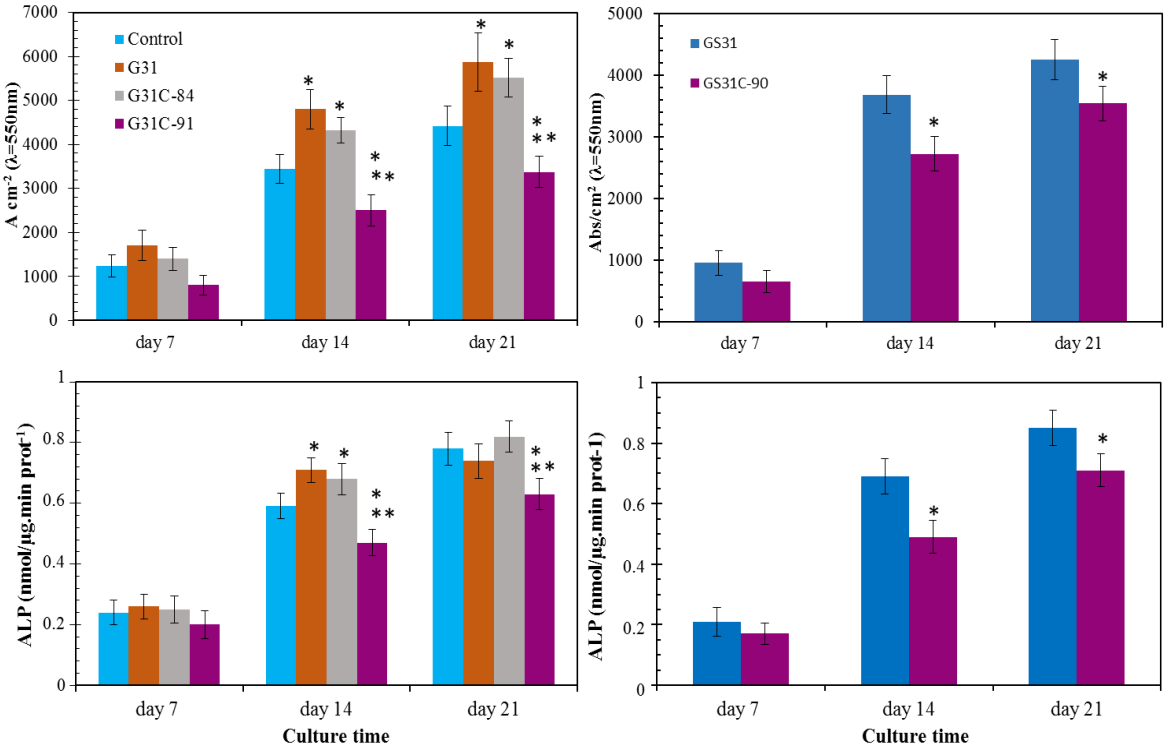

Fig.IX.12. Cell viability/proliferation (a) and alkaline phosphatase activity (b) of human osteoblastic bone marrow cells cultured over the bulk and scaffold glass (G31 and GS31, respectively) and the glass-ceramics bulk (G31C-84 and G31C-91) and the glass-ceramic scaffold GS31C-90), for 21 days.*Significantly different from control

Samples were observed by SEM at day 21. Fig. IX.13 shows the appearance of the bulk glass and glass-ceramics. The surface of the three bulk materials was covered by a cell layer, which was clearly thicker on G31 and G31C-84, compared to that on G31C-91. On high magnification images, the three bulk surfaces showed elongated cells and a well-organized fibrillar matrix with associated calcium phosphate mineral deposits, as shown on the EDS spectrum Fig. IX.13.g and 13.h.

The matrix mineralization was much lower on the G31C-91 glass-ceramic, compared to that on G31 and G31C-84.

Regarding the scaffold samples, cell growth was also observed on GS31 and GS31C-90, although, similar to that observed on the bulk samples, GS31C-90 presented lower cellular proliferation. However, on both scaffolds, there was evidence of cell growth inside the pores and the cell layer was able to successful adapt to the underlying surface. In addition, the presence of calcium phosphate deposits closely associated with the cell layer was observed on both scaffolds, Fig. IX.13.i, although with higher abundance on GS31.

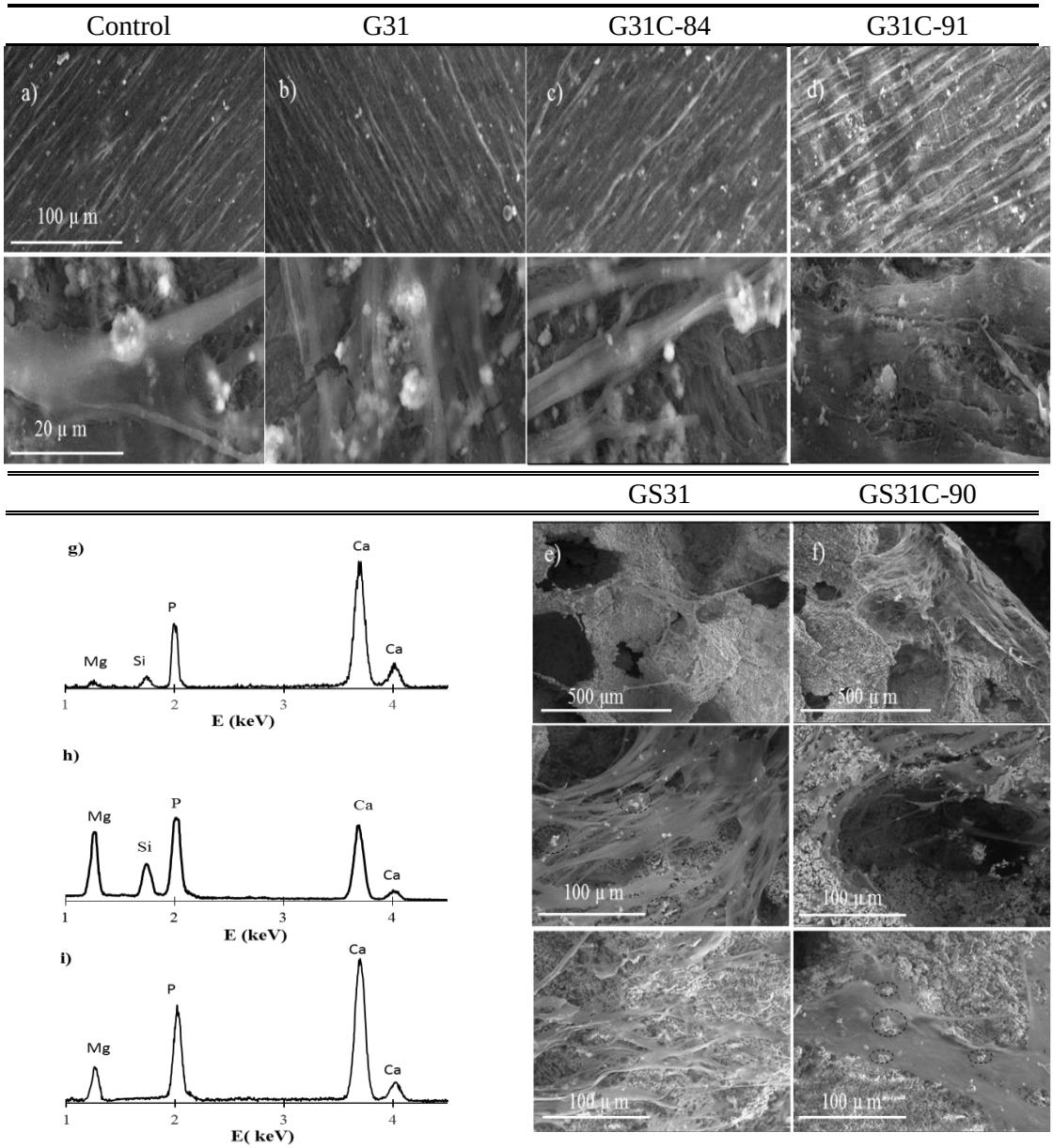

Fig.IX.13. SEM observation of glass and glass-ceramics in bulk and scaffolds samples colonized with human osteoblastic bone marrow cells, at 21 days. The presence of cells was evident on all the bulk samples (b, c, d), and scaffolds (e, f). EDS spectrum of the mineralized samples G31 (g), G31C-91 (h) and GS31 (i)

The higher concentration of magnesium present in the ICP measurements of the G31C-91 due to the degradation, may result in a negative effect on cell proliferation. However, literature have shown that cytotoxicity *in vitro*, is not always observed in vivo, since, the effects of ion release under static conditions is different from the dynamic body fluid system in which the continuous circulation attenuate the local chemical changes, preventing the excessive level of ions at the interface cell/material [21,42].

The level of hydroxyapatite crystallisation (surface reactivity), the HCA rate formation and the surface characteristics could influence cell adhesion and the subsequent proliferation and differentiation events. Also Ca, P and Si ionic concentration during sample incubation with cells, could influence osteoblastic differentiation [43].

The scaffold topography property plays a crucial role not only on the reactivity of the material, but also on the ability to trap the new array and facilitate the migration of osteogenic cells and anchoring to the surface of the material [5]. When this migration occurs the temporary fibrin matrix will suffer contraction and consequently will detach from the surface if it is not well secured to the surface [6], as observed in the bulk glass sample G31 and G31C-84. Other studies have shown [6, 7] that ‘‘rougher’’ surface will be able to imprison the fibrin matrix, better than a smoother one, and hence facilitating the migration of osteogenic cells to the materials surface. The bulk and scaffold glass-ceramics were proven non-cytotoxic and have good cytocompatibility *in vitro*. The mineralised nodule formation is basically considered to be the final result of differentiation and function of the osteoblasts. It is interesting that the final ALP activity were equivalent, bearing in mind the differences in cell number and proliferation observed for each sample at day 14. This may be due to the cellular reaching maximum levels on all surfaces due to overgrowth of cells in each culture prior to day 21 of analysis. The formation of this HCA layer was related to the amount of existing residual glassy phase since it is a source of ions through the dissolution of this phase.

IX.4. Conclusion

The studied glass and glass-ceramic samples presented the ability to induce the precipitation of calcium phosphate compounds on its surface, when immersed in synthetic physiological fluids, indicating that all are potentially bioactive. Bulk glass samples exhibited, after 7 days, a significant precipitate formation on the surface rich in Ca and P, as confirmed by FTIR, SEM-EDS and XRD, although, the corresponding glass-ceramics G31C-84 only formed an equivalent layer after 21 days incubation.

The kinetics transition of the whitlockite phase to amorphous in the glass-ceramic scaffold seems to be sufficiently fast for application of the material in bone engineering and can be controlled by factors such as initial crystallinity and porosity.

Mg ions concentration in SBF have slow down the formation of amorphous calcium phosphate phase and retarded the crystallisation of HCA on the glass surface.

The comparative study of glass and glass-ceramics bulk and scaffolds showed that all presented good performance regarding bioactivity and osteoblastic cytocompatibility. The higher surface area of the scaffolds attenuated the effect of crystallization observed for bulk glass-ceramics. The cell layer

growing on the materials exhibited high ALP activity and a well-organized mineralized matrix, suggesting that these glass and glass-ceramic may have a stimulatory effect on bone formation in vivo. These considerations, suggest the possibility of performing heat treatments, in order to obtain scaffolds with slower degradation. It is possible to control and tune the bioactivity and biocompatability by means of a controlled crystallization according to the requirements of the application.

Acknowledgments

I would like to express my thanks to Professor Maria Helena Raposo Fernandes and her group - School of Dental Medicine, University of Porto – for their collaboration in studies of *in vitro* biocompatibility.

References

[1] L.L. Hench, The story of Bioglass, J. Mater. Sci. Mater. Med. 17 (2006) 967–78.

[2] J.R. Jones, Review of bioactive glass: From Hench to hybrids, Acta Biomater. 9 (2013) 4457–4486.

[3] L.-C. Gerhardt, A.R. Boccaccini, Bioactive Glass and Glass-Ceramic Scaffolds for Bone Tissue Engineering, Materials (Basel). 3 (2010) 3867–3910.

[4] I.D. Xynos, A.J. Edgar, L.D.K. Buttery, L.L. Hench, J.M. Polak, Gene-expression profiling of human osteoblasts following treatment with the ionic products of Bioglass(R) 45S5 dissolution, J Biomed Mater Res. 55 (2001) 151–157.

[5] I.D. Xynos, M. V Hukkanen, J.J. Batten, L.D. Buttery, L.L. Hench, J.M. Polak, Bioglass 45S5 stimulates osteoblast turnover and enhances bone formation In vitro: implications and applications for bone tissue engineering, Calcif. Tissue Int. 67 (2000) 321–9.

[6] S.B. Jung, D.E. Day, Conversion kinetics of silicate, borosilicate, and borate bioactive glasses to hydroxyapatite, Phys. Chem. Glas. - Eur. J. Glas. Sci. Technol. Part B. 50 (2009) 85–88.

[7] A.C.M. Renno, P.S. Bossini, M.C. Crovace, A.C.M. Rodrigues, E.D. Zanotto, N.A. Parizotto, Characterization and in vivo biological performance of biosilicate, Biomed Res. Int. 2013 (2013) 141427.

[8] L.L. Hench, Genetic design of bioactive glass, J. Eur. Ceram. Soc. 29 (2009) 1257–1265.

[9] L.L. Hench, T. Kokubo, Properties of bioactive glasses and glass-ceramics, Handb. Biomater. Prop. (1998) 355–363.

[10] L.L. Hench, J. Wilson, An Introduction to bioceramics, World Scientific, 1993.

[11] Q. Chen, C. Zhu, G. Thouas, Progress and challenges in biomaterials used for bone tissue engineering: bioactive glasses and elastomeric composites, Prog. Biomater. 1 (2012) 2.

[12] I. Marcos-Campos, D. Marolt, P. Petridis, S. Bhumiratana, D. Schmidt, G. Vunjak-Novakovic, Bone scaffold architecture modulates the development of mineralized bone matrix by human embryonic stem cells, Biomaterials. 33 (2012) 8329–8342.

[13] E. El-Meliegy, R. van Noort, Glasses and Glass Ceramics for Medical Applications (Google eBook), Springer, 2011.

[14] M. Edirisinghe, S.M. Best, A.E. Porter, E.S. Thian, J. Huang, Bioceramics: Past, present and for the future, J. Eur. Ceram. Soc. 28 (2008) 1319–1327.

[15] M. Vallet-Regí, Evolution of bioceramics within the field of biomaterials, Comptes Rendus Chim. 13 (2010) 174–185.

[16] A. Hoppe, N.S. Güldal, A.R. Boccaccini, A review of the biological response to ionic dissolution products from bioactive glasses and glass-ceramics, Biomaterials. 32 (2011) 2757–2774.

[17] Q.Z. Chen, I.D. Thompson, A.R. Boccaccini, 45S5 Bioglass®-derived glass–ceramic scaffolds for bone tissue engineering, Biomaterials. 27 (2006) 2414–2425.

[18] M. Hamadouche, A. Meunier, D.C. Greenspan, C. Blanchat, J.P. Zhong, G.P. La Torre, et al., Long-term in vivo bioactivity and degradability of bulk sol-gel bioactive glasses, J. Biomed. Mater. Res. 54 (2001) 560–6.

[19] E.J.C. Davim, A.M.R. Senos, M.H.V. Fernandes, Non-isothermal crystallization kinetics of a Si-Ca-P-Mg bioactive glass, J. Therm. Anal. Calorim. 117 (2014) 643–651.

[20] X. Li, A. Ito, Y. Sogo, X. Wang, R.Z. LeGeros, Solubility of Mg-containing beta-tricalcium phosphate at 25 degrees C, Acta Biomater. 5 (2009) 508–17.

[21] L.M. Ryan, H. S. Cheung, R. Z. LeGeros, I. V. Kurup, J. Toth, P.R. Westfall, G.M. McCarthy, Cellular Responses to Whitlockite, Calcif. Tissue Int. 65 (1999) 374–377.

[22] R. Lagier, C.A. Baud, Magnesium whitlockite, a calcium phosphate crystal of special interest in pathology, Pathol. Res. Pract. 199 (2003) 329–35.

[23] H.-S. Ryu, K.S. Hong, J.-K. Lee, D.J. Kim, J.H. Lee, B.-S. Chang, et al., Magnesia-doped HA/β-TCP ceramics and evaluation of their biocompatibility, Biomaterials. 25 (2004) 393–401.

[24] M.S. Sader, R.Z. Legeros, G.A. Soares, Human osteoblasts adhesion and proliferation on magnesium-substituted tricalcium phosphate dense tablets, J. Mater. Sci. Mater. Med. 20 (2009) 521–7.

[25] E.J.C. Davim, M.H.V. Fernandes, A.M.R. Senos, Increased surface area during sintering of calcium phosphate glass and sodium chloride mixtures, J. Eur. Ceram. Soc. 35 (2015) 329–336.

[26] S. Krimm, A. V. Tobolsky, Quantitative x-ray studies of order in amorphous and crystalline polymers. Quantitative x-ray determination of crystallinity in polyethylene, J. Polym. Sci. 7 (1951) 57–76.

[27] J.K.M.F. Daguano, P.A. Suzuki, K. Strecker, J.M.M. Oliveira, M.H.F. Fernandes, C. Santos, Development and characterization of 3CaO·P2O5-SiO2-MgO glass-ceramics with different crystallization degree, J. Adv. Ceram. 2 (2013) 378–388.

[28] J.K.M.F. Daguano, K. Strecker, E.C. Ziemath, S.O. Rogero, M.H. V Fernandes, C. Santos, Effect of partial crystallization on the mechanical properties and cytotoxicity of bioactive glass from the 3CaO.P(2)O(5)-SiO(2)-MgO system, J. Mech. Behav. Biomed. Mater. 14 (2012) 78–88.

[29] T. Kokubo, H. Takadama, How useful is SBF in predicting in vivo bone bioactivity?, Biomaterials. 27 (2006) 2907–2915.

[30] D. Pereira, S. Cachinho, M.C. Ferro, M.H.V. Fernandes, Surface behaviour of high MgO-containing glasses of the Si–Ca–P–Mg system in a synthetic physiological fluid, J. Eur. Ceram. Soc. 24 (2004) 3693–3701.

[31] N.A.F. Almeida, M.H.F.V. Fernandes, Effect of Glass Ceramic Crystallinity on the Formation of Simulated Apatite Layers, Mater. Sci. Forum. 514-516 (2006) 1039–1043.

[32] C.M. Queiroz, J.R. Frade, M.H.F.V. Fernandes, SiO2- MgO-3CaO.P2O5- K2O Glasses and Glass-Ceramics: Effect of Crystallisation on the Adhesion of SBF Apatite Layers, Key Eng. Mater. 254-256 (2004) 155–160.

[33] M.. Coelho, M.. Fernandes, Human bone cell cultures in biocompatibility testing. Part II: effect of ascorbic acid, β-glycerophosphate and dexamethasone on osteoblastic differentiation, Biomaterials. 21 (2000) 1095–1102.

[34] M.J. Coelho, A.T. Cabral, M.H. Fernande, Human bone cell cultures in biocompatibility testing. Part I: osteoblastic differentiation of serially passaged human bone marrow cells cultured in alpha-MEM and in DMEM., Biomaterials. 21 (2000) 1087–94.

[35] O. Peitl Filho, G.P. LaTorre, L.L. Hench, Effect of crystallization on apatite-layer formation of bioactive glass 45S5, J. Biomed. Mater. Res. 30 (1996) 509–14.

[36] J. Peña, Hydroxyapatite, tricalcium phosphate and biphasic materials prepared by a liquid mix technique, J. Eur. Ceram. Soc. 23 (2003) 1687–1696.

[37] O. Peitl, E. Dutra Zanotto, L.L. Hench, Highly bioactive P2O5–Na2O–CaO–SiO2 glass-ceramics, J. Non. Cryst. Solids. 292 (2001) 115–126.

[38] Y. Zhang, J. Santos, Microstructural characterization and in vitro apatite formation in CaO–P2O5–TiO2–MgO–Na2O glass-ceramics, J. Eur. Ceram. Soc. 21 (2001) 169–175.

[39] E. Jallot, Role of magnesium during spontaneous formation of a calcium phosphate layer at the periphery of a bioactive glass coating doped with MgO, Appl. Surf. Sci. 211 (2003) 89–95.

[40] A. Bigi, G. Falini, E. Foresti, A. Ripamonti, M. Gazzano, N. Roveri, Magnesium influence on hydroxyapatite crystallization, J. Inorg. Biochem. 49 (1993) 69–78.

[41] C.G. Bellows, J.E. Aubin, J.N. Heersche, Initiation and progression of mineralization of bone nodules formed in vitro: the role of alkaline phosphatase and organic phosphate, Bone Miner. 14 (1991) 27–40.

[42] Q. Fu, M.N. Rahaman, H. Fu, X. Liu, Silicate, borosilicate, and borate bioactive glass scaffolds with controllable degradation rate for bone tissue engineering applications. I. Preparation and in vitro degradation, J Biomed Mater Res A. 95A (2010) 164–171.

[43] P.E. Keeting, M.J. Oursler, K.E. Wiegand, S.K. Bonde, T.C. Spelsberg, B.L. Riggs, Zeolite A increases proliferation, differentiation, and transforming growth factor beta production in normal adult human osteoblast-like cells in vitro, J. Bone Miner. Res. 7 (1992) 1281–9.

Chapter X

"Everything is theoretically impossible, until it is done".

Robert A. Heinlein (1907-1988)

CHAPTER X

SURFACE MODIFICATION OF SI-CA-P-MG GLASS-CERAMIC: A BIOACTIVITY STUDY

Abstract

When the surface properties required for a glass-ceramic are different from those which are intrinsic of the material these can be modified. Indeed, the variation in chemical functional groups is known to affect hydrophobicity, which in turn affects protein adsorption and conformation, subsequently affecting various cellular responses. Different activation methods have been applied to a glass-ceramic G31C-91, where whitlockite was the crystalline phase detected, with a crystallinity percent of 82 %, in order to expose hydroxyl groups. The formation of silanols on the surface of the activated glass-ceramic, with acid, basic or neutral aqueous media, was investigated. The cleaned glass-ceramics were then functionalized using 3-aminopropyl-triethoxysilane (APTES).

The acetone pre-treated (G31C-91-1) and further silanized (G31C-91-1S) glass-ceramic surfaces presented the highest contact angle indicating that the acetone pre-treated glass-ceramic surface was more hydrophobic and that APTES immobilization was successful. The recover bioactivity of the acetone treatment before and after silanization, compared with the "as-prepared" glass-ceramic bioactivity, was investigated using simulated body fluid (SBF) tests up to 21 days. The post-soaking samples were characterized by scanning electron microscopy (SEM), energy dispersive spectroscopy (EDS) and FTIR. Both glass-ceramic surfaces exhibited an accelerated crystalline hydroxyapatite layer formation upon immersion in SBF after 21 days while the "as-prepared" glass-ceramic G31C-91 had no detected formation of calcium phosphate up to 5 months.

X.1. Introduction

Bioactive glasses have the characteristic of bonding to bone provided by the formation of a biologically active apatite layer due to the rapid rate of surface reactions. In the last decades, increasing effort has been directed toward potential applications of glass-ceramics and to understand if this is a common characteristic to bioactive glasses and glass-ceramics [1–4]. It was demonstrated in a previous work [5] that when the bioactive glass (mol. %) 32.7% CaO, 10.9% P_2O_5, 25.4% SiO_2 and 31% MgO was transformed into a glass-ceramic, the formation of the surface apatite layer depended on the relative amount of residual glassy phase in the glass-ceramic. The glass-ceramic with 18 % of residual glassy phase exhibited no formation of a surface HCA layer, when exposed to SBF solutions, during thirty days. Only after 5 months immersion it was formed a large plate of calcium phosphate. It was observed that the high concentration of Mg ions in SBF, slow down the formation of amorphous calcium phosphate phase (β-CaP) and greatly retarded the crystallisation of HCA on the glass surface, as also observed in literature [6,7]. Although some authors underline the inhibitory effect on bioactivity due to crystallization [1], most of the findings agree that crystal phase slightly decreases the kinetics of HCA layer formation on the implant surface [8], but there is no loss in bioactivity, even with crystallinity up to 100 % [9]. The reaction rate observed in the 45S5 glass-ceramic was found to be up to seven times faster than that reported for A/W glass-ceramics with respect to the formation of crystalline HCA [9]. Even if the kinetics of apatite formation is slower, the preserved bioactivity of the derived glass-ceramics offers new interesting opportunities, since crystallized systems are mechanically more reliable than the original parent glass [10]. Moreover, the reaction rate of the biomedical device can be adjusted by surface modification [11,12].

For the aforementioned reasons, it is important to investigate the proper cleaning methods for the activation of a bioactive surface on the G31C-91 glass-ceramic before silanization.

Glass-ceramic surfaces can then be silanized, as they contain hydroxyl groups which attack and displace the alkoxy groups on the silane thus forming a covalent Si – O – Si bond [13]. Silanization through 3-Aminopropyltriethoxysilane (APTES) has been used as a process for modification of the surface, by forming a monolayer of aminosilane for further bio-functionalization [2]. The active amino groups ($–NH_2$) facilitate the further functionalization and can covalently bond with other active groups, such as the carboxyl (–COOH) that can conveniently conjugate with enzyme.

X.2. Materials and methods

X.2.1. Glass fabrication

Glass with molar composition 32.7 % CaO, 10.9 % P_2O_5, 25.4 % SiO_2 and 31 % MgO (mol. %) was produced by conventional melt quenching technique, as reported elsewhere [14–16]. The obtained bulk was annealed for 30 minutes at 740 ºC. Slices samples were prepared with dimensions of 1 x 1 x 0.5 cm^3 polished with sandpaper grain size successively thinner, finished with diamond pastes of 15, 6, 3 and 1µm particle size.

The samples were further heat treated to obtain glass ceramics with 82 % crystallized fraction. Glass-ceramic samples were denominated G31C-91 or "as-prepared" glass-ceramics. After heat treatment the samples were polished with diamond pastes of 15, 6, 3 and 1µm particle size.

X.2.2. Glass-ceramic surface hydroxyls exposition

The first step of functionalization process is a cleaning treatment able to promote both the surface removal of contaminants and the exposition of reactive hydroxyls. The polished slices have been cleaned by the following three different methods:

1) Sonification for 5 min in a solution of acetone in H_2O (95 vol. %) in order to remove surface contaminants and subsequently 3 times for 5 min in distilled water in order to expose reactive groups. The samples subjected to this treatment were designated G31C-91-1.

2) The same procedure as in point 1, followed by further soaking for 1 min in acid solution H_2SO_4 at pH = 4 followed by rinsing in distilled water (three times for 5 min each in ultrasonication apparatus). These samples were designated G31C-91-2.

3) The same procedure as in point 1, followed by further soaking for 3 min in basic solution NaOH 0.1M followed by rinsing in distilled water (three times for 5 min each in ultrasonication apparatus). These samples were designated G31C-91-3.

The three methods have been adapted from those described in the literature [17–19] and have been compared with each other to assess their efficiency in the activation of bioactive glass-ceramic surfaces.

X.2.3. Surface silanization

After cleaning, all samples (G31C-91-1, -2 and -3) have been silanized with APTES following two protocols reported in the literature, depending on the previous cleaning method.

1S) After cleaning with acetone, the slices were soaked for 6 h in an ethanol solution (95 vol. %) containing 35 µL of APTES. After soaking, samples was rinsed in ethanol, thermally treated at 100 ºC for 1 h, to consolidate the bonding between the silane and the glass surface, and stored in a dry box. (G31C-91-1S)

2S) After cleaning with H_2SO_4 or NaOH, the silanization was carried out by soaking the samples for 3 min in 102 mL of ethanol solution containing 3 mL of APTES. After soaking, each sample was rinsed in ethanol, thermally treated at 100 ºC for 1 h, and stored in a dry box. The samples were designated G31C-91-2S and G31C-91-3S, for glass-ceramic surfaces pre-cleaned with H_2SO_4 and NaOH, respectively.

X.2.4. Characterization of surface modification

The activated and functionalized glass-ceramic surfaces were investigated using Attenuated Total Reflection (ATR) spectroscopy on a Brucker tensor 27 spectrometer, using a Golden Gate single reflection diamond ATR system, with no need for sample preparation. All spectra were collected over a region of 4000–400 cm^{-1} with 256 scans at a resolution of 4 cm^{-1}.

The influence of surface modification and functionalization on the hydrophilic/hydrophobic behaviour of glass slice was estimated via static contact angle measurements with distilled water at room temperature using the sessile drop method, where the angle was determined from the tangent made to the drop curvature at the base, through image analysis of the drop profile. All the measurements have been performed on the mirror polished glass-ceramic slice surfaces, before and after each cleaning step, and after silanization. The instrument, using a charge coupled device (CCD) camera and an image analysis software, was purchased from DataPhysics OCA - Series. The distilled water (Milli-Q, Integral; Millipore, USA) droplet volume was 1 µL, and the contact angle was measured 5 s after the drop deposition on the sample surface. The measures were performed on each glass-ceramics samples in triplicates always using fresh surfaces. For each slice sample, the reported value is the average of the results obtained on three droplets.

X.2.5. In vitro bioactivity

The in vitro bioactivity was assessed by soaking all samples in a solution of simulated body fluid (SBF) for periods from 1 day up to 21 days prepared according to the formulation of Kokubo and Takadama [17]. It was used a constant specimen surface area to solution volume ratio of 0.1 cm^{-1}, previously filtered through a Milipore 0.22 μm system. The samples were placed in a polyethylene bottle containing SBF solution, and kept in an incubator at 37 ºC, without shaking, in accordance to a protocol referred in the literature [18–21]. Four samples were used for each immersion time. After removal from the SBF, the samples were dried at 60 ºC. SEM and XRD were used to analyze the structure of the reacted samples, using the conditions described previously. Energy dispersive X-ray spectroscopy (EDS) was utilized to analyze the elemental composition of the converted layer on the surface of the samples immersed in SBF at different time intervals. X-ray diffraction (XRD) analysis was performed using a Rigaku Diffractometer Geigerflex Dmax-C at room temperature with CuKα radiation (at 40 kV and 40 mA) and a scan speed of 0.02º s^{-1}. Data was obtained in the 2θ range of 10-60 degree to investigate the crystalline phases of the grinded samples.

X.3. Results and Discussion

The name and characterization of surface pre-treatment processes are summarize in Table X.1.

Table X.1. Names and characteristics of treated glass-ceramic surfaces

Sample name	Treatment
G31C-91	"As-prepared" glass-ceramic
G31C-91-1	Glass-ceramic acetone cleaning
G31C-91-2	Glass-ceramic acetone cleaning + H_2SO_4
G31C-91-3	Glass-ceramic acetone cleaning + NaOH
G31C-91-1S	Glass-ceramic acetone cleaning + silanization
G31C-91-2S	Glass-ceramic acetone cleaning + H_2SO_4 + silanization
G31C-91-3S	Glass-ceramic acetone cleaning + NaOH + silanization

X.3.1. Surface characterization-FTIR spectroscopy

Fig. X.1 shows the FTIR spectra of glass-ceramic slices G31C-91, before and after cleaning with acetone, basic and acid solutions and the corresponding silane-modified glass-ceramic surfaces. The

range between 4000 – 1400 cm^{-1} was chosen because it contains most important peaks of –CH stretching and functional groups without overlapping with glass characteristic peaks Si – O – Si.

The FTIR spectra of the "as prepared" glass-ceramic G31C-91 reveals at around 3500 cm^{-1}, the absorption band of the –OH bonds and the combination of the Si – O – Si stretch (asymmetric) at 1200–970 cm^{-1} band, Si – O stretch band at 940–860 cm^{-1} and the bending Si – O – Si at 500 – 400 cm^{-1} [20]. The FTIR also show the additional bands at wavenumbers 560 and 601 cm^{-1} a peak at 1060 cm^{-1} correspondent to the P–O bending and symmetric stretch vibrations, respectively, due to the presence of whitlockite [21].

With cleaning treatments the bands assigned to P – O stretching asymmetric decrease intensity. The new Si – O band at ~ 930 cm^{-1} (with two non-bridging oxygen) was detected in the samples G31C-91-1 and -2.

The cleaned samples G31C-91-1 and G31C-91-2 showed increased transmittance bands of the vibrational modes due to Si – O stretch, showing an enrichment in Si – OH bonds, as proposed.

Table X.2. FTIR band assignment, a- asymmetric, s- symmetric [20–24]

Wavenumber (cm^{-1})	Vibration mode	Wavenumber (cm^{-1})	Vibration mode
3500	Si – OH	1120, 1040, 1025	P – O stretch (a)
3451	–NH stretch	1060, 460	P – O bend
3360, 3280	$–NH_2$	1020-1010	Si – O (NBO) stretch
2930	$–CH_2$ (a)	974, 945	P – O stretch (s)
2860-2870	$–CH_2$ (s)	975 – 900	Si – O (2NBO) stretch
1635	$–NH_3^+$ (a)	878 – 870	C – O stretch
1570	$–NH_2$ scissor	840	Si – O (2NBO) stretch
1484	$–NH_3^+$ (s)	830 – 795	Si – O – Si bend
1460 – 1410	C – O stretch	720	Si – O – Si, CH_2 rocking
1260-1200	Si – O – Si stretch (a) LO	606 – 600, 594, 571, 552	P – O bend (a)
1200-1000	Si – O – Si stretch (a) TO	476 – 455	Si – O – Si bend

For silane-modified glass-ceramic surfaces Fig. X.1b, in the FTIR range between 4000 – 1400 cm^{-1}, no differences were found in the G31C-91-2S and -3S samples. In the same range, APTES gave to G31C-91-1 new peaks at ~ 3451 cm^{-1} due to –NH stretching [24,25]. It can also be observed the presence of the antisymmetric and symmetric $–CH_2$ stretching vibration bands 2930 and 2860 cm^{-1}, respectively, mainly related to the presence of propyl chain added with APTES on the glass-ceramic

surfaces [26,27]. The vibration at 1484 and 1635 cm^{-1} correspond to the symmetric and asymmetric $–NH_3^+$ deformation modes, indicative of amine group protonation when the samples were exposed to air. In addition to these modes, NH_2 scissor vibration found at 1570 cm^{-1} confirms the presence of the terminal groups of the APTES molecules after grafting [26]. Remain spectra, between 1400 and 400 cm^{-1}, Fig. X.1b, include a positive contribution in the spectral range at 1008–1070 cm^{-1} due to extra Si – O – Si modes correspondent to the presence of siloxane on the surface of G31C-91-1. These stretching modes confirm the adsorption of the silane on the modified acetone surface G31C-91-1.

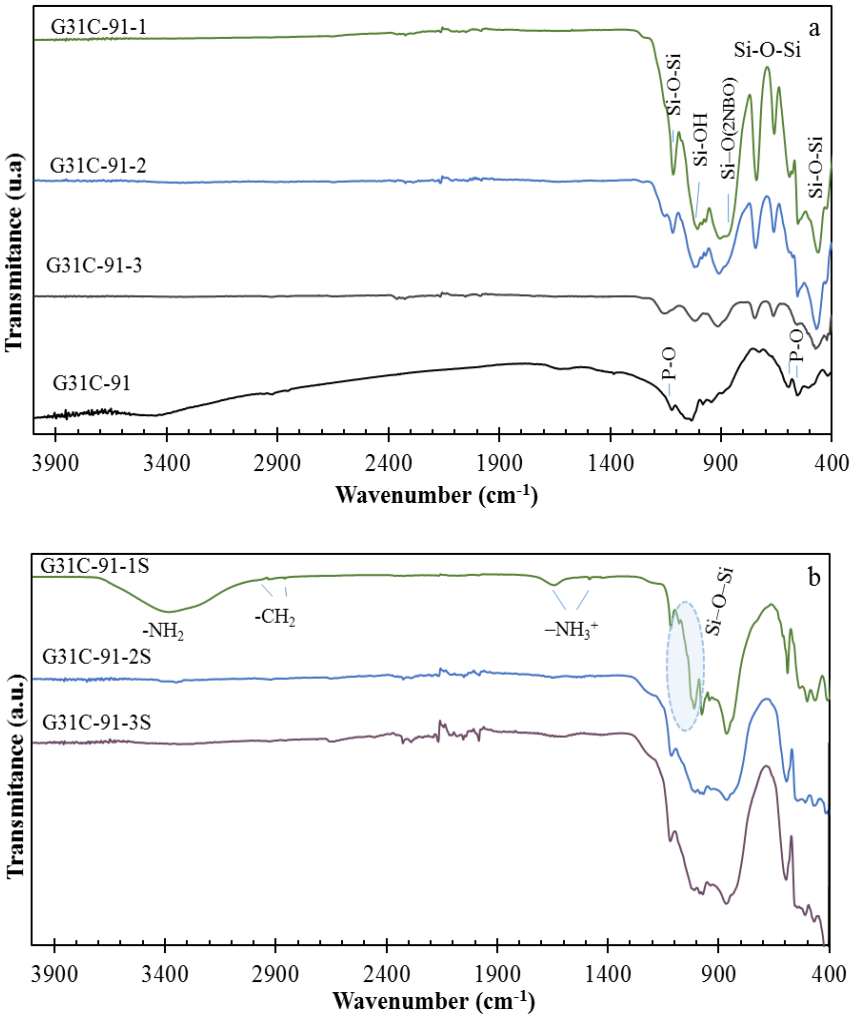

Fig. X.1. FTIR spectra of the glass-ceramic surfaces, before and after pre-treatments (a) and functionalization of the correspondent pre-treated samples (b)

The micrographs of the glass-ceramics before and after the different modifications treatments are present in Fig. X.2. With the cleaning treatment, it is observed that the glass matrix dissolves leaving the crystalline particles exposed on the surface, as seen in Figs. X.2b, 2c and 2d. The treatments with acidic or basic solutions caused a very strong dissolution of the glass matrix.

The silanization performed on the three different glass surfaces previously cleaned did not modify significantly the surface of the glass.

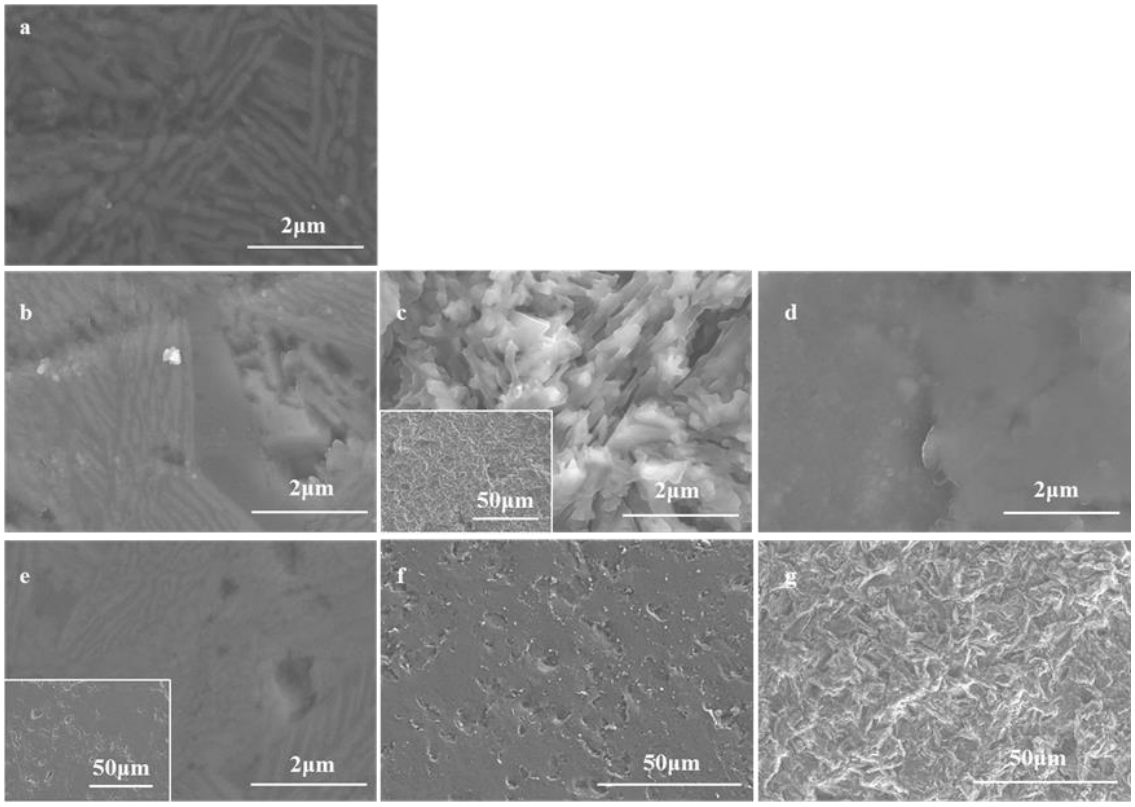

Fig. X.2. Microstructure of the as prepared glass-ceramic surface (a), after pre-treatment with acetone (b), acid (c) and base (d), and of the correspondent functionalization with APTES (e, f and g)

X.3.2. Surface characterization-contact angle analysis

The contact angle characterization has been used for accessing the presence of –OH on the glass-ceramic surfaces as a result of their chemical modifications, Fig. X.3.

The contact angle measurements results as a function of the chemical groups added to the surfaces are summarized in Table X.3. All washing treatments produced a decrease of the contact angle when compared with the as-prepared glass-ceramic slices. The first method (acetone) was more effective than the others with a contact angle bellow 8º, a significant difference when compared with the reference "as-prepared G31C-91". As expected, the washing step induced a higher hydrophilicity of the glass-ceramic surface, with respect to the as-prepared one, because of the –OH groups presence, whereas silanization enhances its hydrophobicity, due to the configuration of the silane at the surface which is assumed to bend and orient its polar NH_2 head toward the surface, driven by the formation of strong hydrogen bonds with the glass hydroxyl groups. This configuration leaves the ethylene

sequences exposed at the surface, thus providing the assessed hydrophobic character, coherent with the literature dealing with alkyl silane modifiers for glass and glass-ceramic surfaces [28–31].

Table X.3. Contact angle after different pre-treatment methods and correspondent functionalization treatment

Methods	As-prepared	Acetone/H_2O	H_2SO_4	NaOH
Cleaning	49.1±1.4	< 8 º	20.1±0.2	28.8±0.4
Cleaning + APTES	–	76.1±0.4	54.2±0.2	50.8±0.3

Based on the results, the relative hydrophobicity increased in the following sequence of chemical groups: hydroxyls < "as-prepared G31C-91" < amines. Surface activation and contamination removal by acetone pre-treatment method revealed the best results, where surfaces were free of hydrophobic contaminants with low contact angles ranging from 4° to 8°, producing a very hydrophilic surface with low water contact angles, prone to silanization. The surface of silanized glass should be much more hydrophobic than that of the pre-treated glass. In the present study, the acetone pre-treated silanized glass surface presented the highest contact angle indicating that silanized glass was more hydrophobic and that APTES immobilization on the silanized glass was successful. Glass surfaces cleaned using H_2SO_4 and NaOH method, had a mean contact angle value after silanization significantly lower than those from acetone method, indicating poor silanization, confirming the FTIR results.

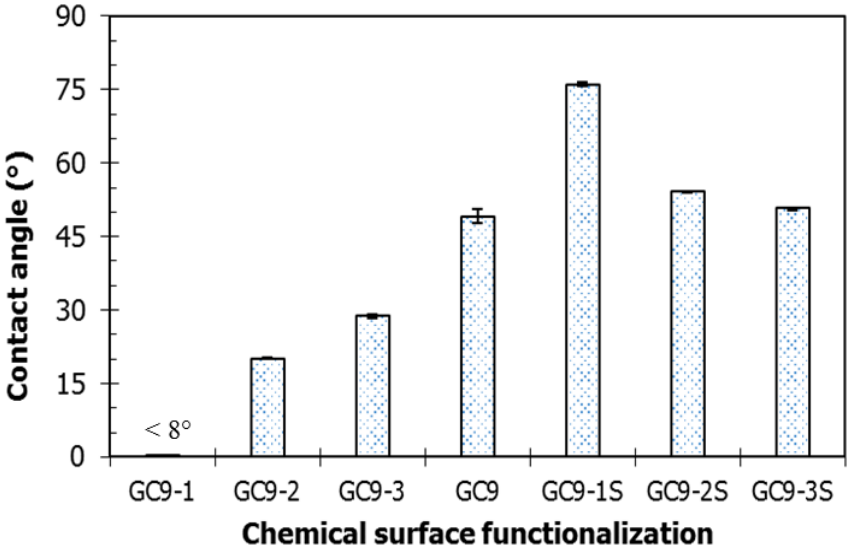

Fig. X.3. Evolution of contact angle measurements before and after glass-ceramic modified surfaces

The role of the different cleaning media on the surface modification of the glasses can be understood by the capability of the glass to be leached when in contact with an aqueous medium, by the breaking of an oxygen bridge and the forming of two terminal –OH.

The first washing method should be able to activate hydroxyls on the glass-ceramic surface. An acid environment (method 2) can be more effective on the ion exchange step. A basic environment (method 3) could promote the hydroxylation of the glasses through the catalytic effect of – OH ions in the solution. This action probably induced poor hydroxyls exposition reducing silanization as observed in Fig. X.1.

The silane attachment on glass-ceramic surfaces requires the presence of hydroxyl groups for attachment of the molecules. The –OH on the surface can react with APTES as the process shown in Fig. X.4b. The silane molecule was first hydrolysed to form reactive silanol groups that further condense with surface hydroxyl groups to form Si – O – Si bonds or with other hydrolysed silane molecule to form Si – O – Si cross-linking.

The three hydrolysable ethoxy groups of the APTES, allows for multiple points of surface attachment and polymerization with APTES molecules in both horizontal and vertical directions.

The pre-cleaning with acetone surface produces significant improvements in the APTES coating. It has been reported that the thicker the water layer at silicon oxide surfaces, the more significant the growth of silane at the surface and also the most stable the silane layer can be [27].

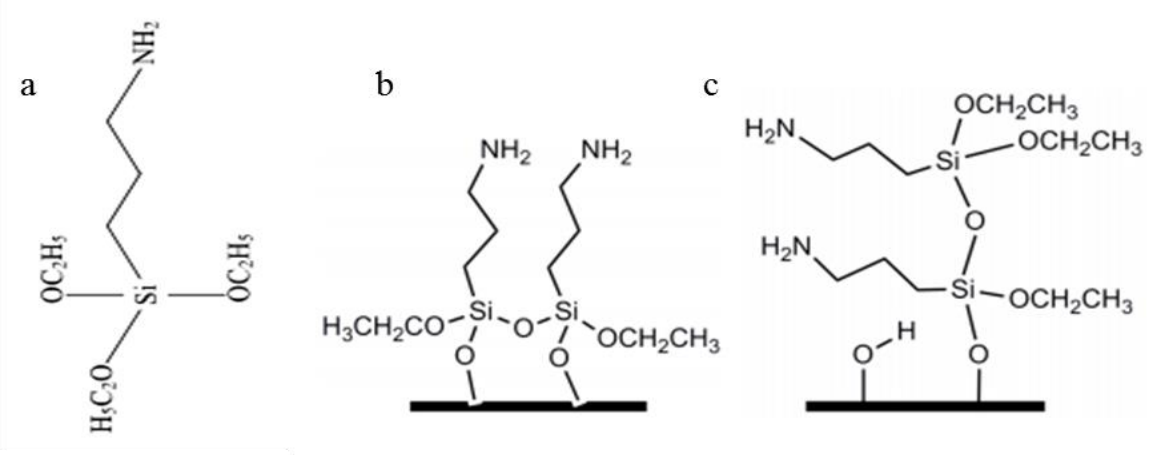

Fig. X.4. APTES molecular structure (a) horizontal (b) vertical and (c) polymerization of APTES on a silica substrate [32]

The acetone treatment G31C-9-1 seems to be the best treatment for surface functionalization and further bioactivity evaluation. The stability and structural alteration of the APTES upon exposure to SBF was monitored using FTIR, since other studies shown that the silane layer was not stable in buffered solutions [35].

X.3.3. Bioactivity studies

The samples submitted to acetone and the correspondent silanization were used for further bioactivity and stability studies following the protocol reported by Kokubo [33].

After 1 day immersion in SBF, the FTIR analysis, Fig. X.5, shows the decrease of the intensity vibration bands of Si – O – Si (stretch and bending),when compared with the G31C-91-1 in Fig. X.1. The vibration peaks of the P – O stretch at 1030 and P–O bend mode at 560 and 600 cm^{-1} increased intensity. The bands at 1090 cm^{-1} assigned to the Si–O–Si asymmetric stretching mode and the band at 476 cm^{-1} assigned to the Si – O – Si symmetric bending mode tends to decrease it's intensity with HCA phase formation.

For 14 days soaking, the peaks correspondent to the Si – O groups, present in the G31C-91-1.1D, disappeared with the repolymerization process. Two peaks at 1450 and 1410 cm^{-1} and a third at 870 cm^{-1} increased intensity, due to the incorporation of CO_2 from the solution, during the crystallization of HCA.

The increased definition of the peaks related to PO vibrations, P – O bend (560 and 602 cm^{-1}) and the apperence of a P – O stretch (1050 cm^{-1}) and of a P – O bending peak at 460 cm^{-1} was indicative of an increase in the crystallinity of the precipitated HCA layer [34] for 14 days immersion while in the as-prepared glass-ceramic HCA was only detected after 30 days [5].

Therefore, it can be stated that the developed procedure for altering the surface properties based on chemically changing the surface of glass-ceramic G31C-91 was effective.

The vibration modes related with absorbed silane molecules like CH_3, CH_2 and NH_2 were barely observed at the first 24 hours but increased intensity after 14 days. The peak at 730 cm^{-1} could be assigned to –NH vibration. The corresponding stretching mode of NH at ~3400 cm^{-1} was too weak to be discernible in the spectra. The stability of aminosilane layer in SBF was observed.

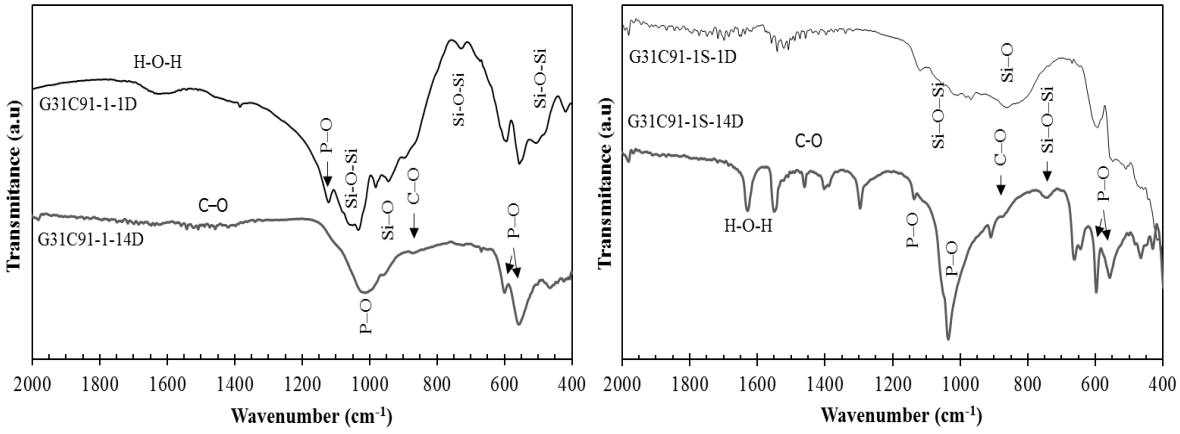

Fig. X.5. FTIR spectra, after 3 and 14 days immersion in SBF, of the glass–ceramic surface pre-treated in acetone (a) and after silanization (b)

The XRD spectra for all investigated samples are shown in Fig. X.6. The ‘‘as-prepared’’ spectra represent the results for crystalline sample. Before immersion in SBF, all samples (with and without surface modification) exhibited sharp diffraction peaks, which were identified as diffractions of the whitlockite phase ($(Ca_{2.859}Mg_{0.411}(PO_4)_2$ according to the card No. 01-087-1582 in the X’Pert HighScore database).

After 7 days immersion in SBF, the as prepared G31C-91 with an IC of 82 % had no detected formation of calcium phosphate (Fig. X.6a) showing only a reduction in crystallinity. After 30 days in SBF, the sharp diffraction peaks of whitlockite crystalline phase are overlapped by a broad halo, consequence of the presence of an amorphous phase, and some incipient peaks of HA were detected. The same process was observed in the surface modified samples with a remarkably faster process (Fig. X.6b and 6c) than in the as-prepared samples (Fig. X.6a). XRD analysis confirmed that the overlapped of the whitlockite by an amorphous phase was accelerated to 3 days (in surface-modified samples), and that after 3 weeks, HA peaks are identified in the surface modified samples. The XRD spectra suggest that hydroxyapatite did not detach from the glass-ceramic surfaces after prolonged soaking times. The surface treatment played a critical role in the acceleration of the reaction.

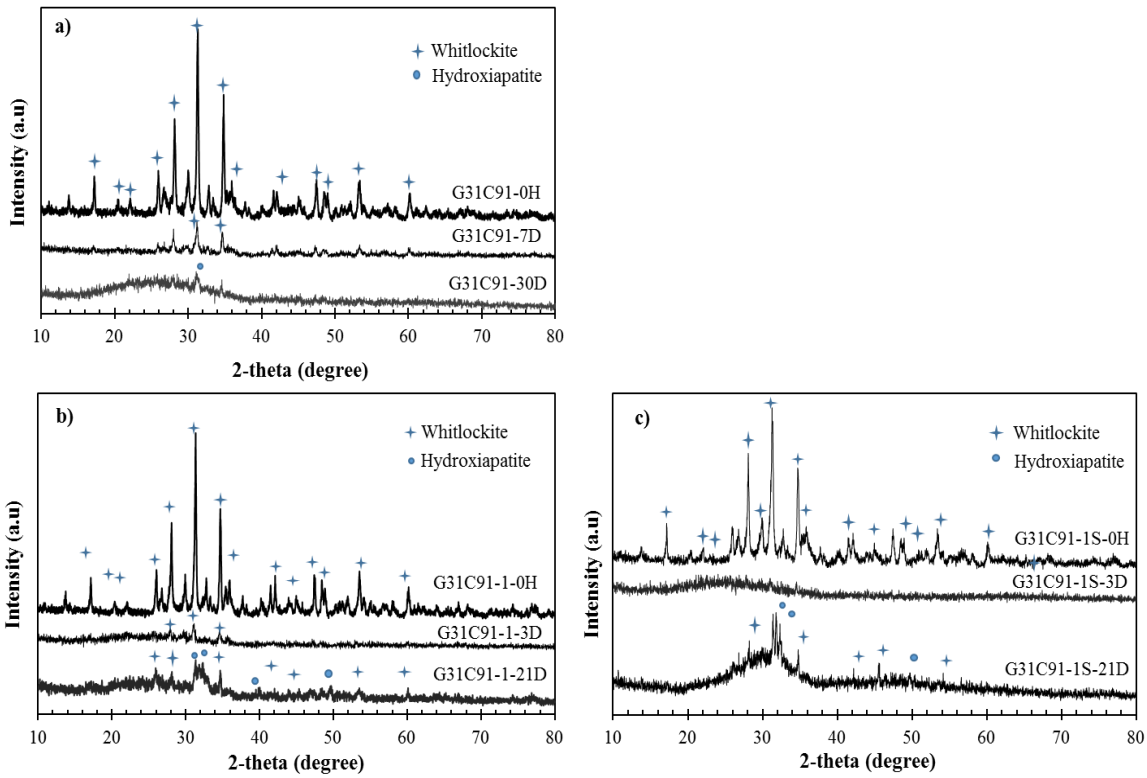

Fig. X.6. XRD spectra of samples (a) as-prepared, (b) surface hydroxylation with acetone and (c) surface-modification with APTES

The microstructural evolution, upon immersion in SBF, of the as prepared glass-ceramic and modified surfaces with acetone and after silanization is illustrated in Fig. X.7.

After soaking in SBF for 1 day, it is clear a faster dissolution of the glass phase in the modified G31C-91-1compared with the as-prepared sample G31C-91.

After 3 weeks, HA-like bulbs were precipitated on the surface of the modified surface (in a ratio close to 1.67) in which the crystalline phase was not clear due to an amorphous glass matrix that embedded the surface, in agreement with the results of XRD analysis (Fig. X.6b and 6c).

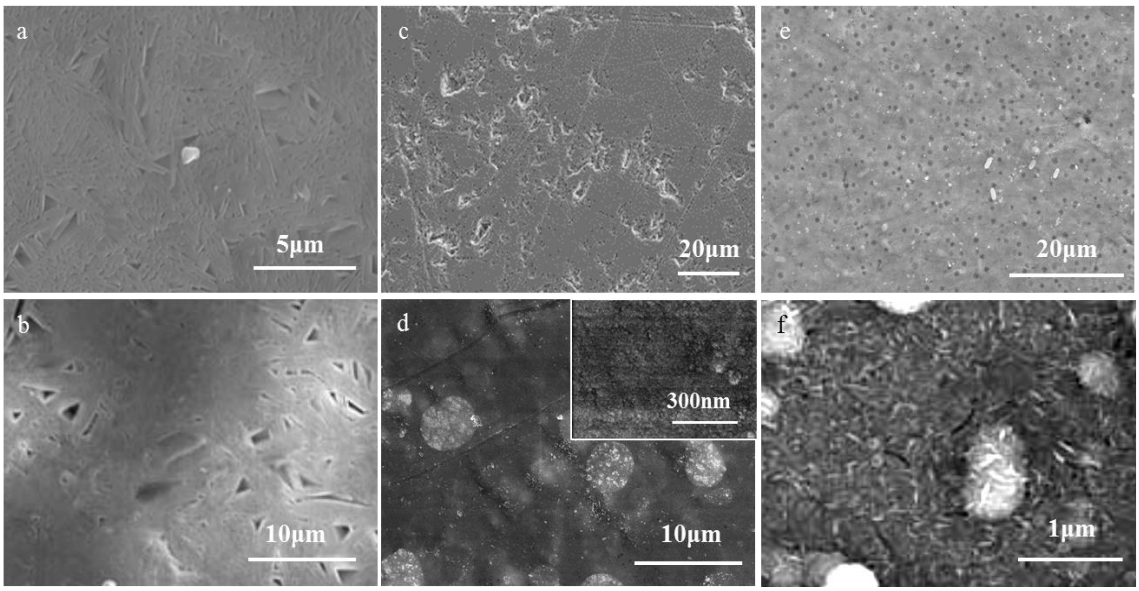

Fig. X.7. Surface microstructure of the as prepared glass-ceramic G31C-91 (a, b), acetone G31C-91-1 (c, d), and acetone + silane G31C-91-1S (e, f) samples after immersion in SBF for 1 day (a, c and e) and 3 weeks (b, d and f)

The surface modification plays a key role in speeding up the formation of HCA layer. The reasons for this behaviour are the faster dissolution of the glass phase compared with the as prepared sample. In the acetone treated surface without APTES (Fig. X.7c), the glass matrix dissolves faster, such that the crystalline particles are exposed on the surface. When modified with APTES (Fig. X.7e), the surface is covered by a layer of APTES molecules, which reduces the dissolution rates of the glass matrix.

Preferential dissolution is observed in the gaps between the glass matrix and crystalline particles. This narrow interstices seems to be attack by the SBF solution, forming cavities indorsing the whitlockite crystals to detached from the matrix, leaving pores (Fig. X.7a, 7c) in the glass matrix.

As confirmed by XRD, the establishment of the HA is not observed in the 3 weeks immersion in SBF of the as-prepared glass-ceramic, G31C-91. However, in the acetone-treated and silane surface-modified samples, the HA formed at almost the same rate, since silanization does not significantly alter material reactivity.

The stability of aminosilane, with a dense surface free amine functional group, is crucial for tissue engineering applications. Currently, APTES is the most widely used aminosaline in the field but it can self-polymerize in humid environments and result in a heterogeneous surface [31,35]. Interestingly, our FTIR analysis did not confirmed this result on the surface of the glass-ceramics using the acetone cleaning treatment.

X.4. Conclusion

Surface modification of the Si-Ca-P-Mg based glass-ceramic monolithic was carried out by different cleaning methods and further chemical functionalization by reaction with the APTES. The washing treatment is necessary to induce surface activation by free –OH exposition. The results of this study indicate that the acetone treatment during the surface-modification process must be considered in the glass–ceramic bioactivity improvement. Both acetone aqueous treatment and APTES molecules surface-functionalization process expedites the subsequent bioreaction of the glass-ceramics in SBF and must be considered in the design of glass-ceramic scaffolds with tailored bioactivity and biodegradability. The surface-functionalized samples are ready for protein immobilization and can be used to fabricate glass-ceramic scaffolds for protein release studies.

References

[1] P. Li, Q. Yang, F. Zhang, T. Kokubo, The effect of residual glassy phase in a bioactive glass-ceramic on the formation of its surface apatite layer in vitro, J Mater Sci Mater Med. 3 (1992) 452–456.

[2] Q.Z. Chen, K. Rezwan, D. Armitage, S.N. Nazhat, A.R. Boccaccini, The surface functionalization of 45S5 Bioglass-based glass-ceramic scaffolds and its impact on bioactivity, J. Mater. Sci. Mater. Med. 17 (2006) 979–87.

[3] M.M. Farag, C. Rüssel, Glass-ceramic scaffolds derived from Bioglass® and glass with low crystallization affinity for bone regeneration, Mater. Lett. 73 (2012) 161–165.

[4] Y. Zhang, J.. Santos, Microstructural characterization and in vitro apatite formation in CaO–P2O5–TiO2–MgO–Na2O glass-ceramics, J. Eur. Ceram. Soc. 21 (2001) 169–175.

[5] E.J.R. Davim, N.A.F. Almeida, A.M.R. Senos, M.H.R. Fernandes, M.H.V. Fernandes, Crystallization effect in the in vitro behaviour of a calcium-phosphate-based glass bulk and scaffold, in preparation.

[6] A. Saboori, M. Rabiee, F. Moztarzadeh, M. Sheikhi, M. Tahriri, M. Karimi, Synthesis, characterization and in vitro bioactivity of sol-gel-derived SiO_2-CaO-P_2O_5-MgO bioglass, Mater. Sci. Eng. C. 29 (2009) 335–340.

[7] M.R. Filgueiras, G. La Torre, L.L. Hench, Solution effects on the surface reactions of a bioactive glass, J. Biomed. Mater. Res. 27 (1993) 445–53.

[8] O. Peitl Filho, G.P. LaTorre, L.L. Hench, Effect of crystallization on apatite-layer formation of bioactive glass 45S5., J. Biomed. Mater. Res. 30 (1996) 509–14.

[9] O.P. Filho, G.P. Latorre, L.L. Hench, Effect of crystallization on apatite-layer formation of bioactive glass 45S5, J Biomed Mater Res. 30 (1996) 509–514.

[10] J.K.M.F. Daguano, K. Strecker, E.C. Ziemath, S.O. Rogero, M.H. V Fernandes, C. Santos, Effect of partial crystallization on the mechanical properties and cytotoxicity of bioactive glass from the 3CaO.P(2)O(5)-SiO(2)-MgO system., J. Mech. Behav. Biomed. Mater. 14 (2012) 78–88.

[11] J.M. Oliveira, R.N. Correia, M.H. Fernandes, Surface modifications of a glass and a glass-ceramic of the MgO-3CaO.P2O5-SiO2 system in a simulated body fluid., Biomaterials. 16 (1995) 849–54.

[12] P. Van Der Voort, I. Gillis-D'Hamers, E.F. Vansant, Estimation of the distribution of surface hydroxyl groups on silica gel, using chemical modification with trichlorosilane, J. Chem. Soc. Faraday Trans. 86 (1990) 3751.

[13] L.M. Alonso, J.Á.D. García-Menocal, M.T. Aymerich, J.Á.Á. Guichard, M. García-Vallés, S.M. Manent, et al., Calcium phosphate glasses: Silanation process and effect on the bioactivity behavior of glass-PMMA composites, J. Biomed. Mater. Res. B. Appl. Biomater. 102 (2013) 205–13.

[14] E.J.C.R. Davim, Suportes porosos vítreos do sistema Si-Ca-P-Mg para aplicações biomédicas, Universidade de Aveiro,(Msc thesis), 2008.

[15] E.J.C. Davim, A.M.R. Senos, M.H.V. Fernandes, Non-isothermal crystallization kinetics of a Si-Ca-P-Mg bioactive glass, J. Therm. Anal. Calorim. 117 (2014) 643–651.

[16] E.J.C. Davim, M.H.V. Fernandes, A.M.R. Senos, Increased surface area during sintering of calcium phosphate glass and sodium chloride mixtures, J. Eur. Ceram. Soc. 35 (2015) 329–336.

[17] S. Jo, K. Park, Surface modification using silanated poly(ethylene glycol)s, Biomaterials. 21 (2000) 605–616.

[18] M. Ma, Y. Zhang, W. Yu, H. Shen, H. Zhang, N. Gu, Preparation and characterization of magnetite nanoparticles coated by amino silane, Colloids Surfaces A Physicochem. Eng. Asp. 212 (2003) 219–226.

[19] E. Verné, C. Vitale-Brovarone, E. Bui, C.L. Bianchi, A.R. Boccaccini, Surface functionalization of bioactive glasses., J. Biomed. Mater. Res. A. 90 (2009) 981–92.

[20] M. Khorami, S. Hesaraki, A.A. Behnamghader, M. Alizadeh, S. Farhangdoust, Effect of Substitution Li_2O for Na_2O on Surface Reactivity and Cellular Properties of 45S5 Bioglass, J. Aust. Ceram. Soc. 46 (2010).

[21] J. Peña, Hydroxyapatite, tricalcium phosphate and biphasic materials prepared by a liquid mix technique, J. Eur. Ceram. Soc. 23 (2003) 1687–1696.

[22] F. Ay, A. Aydinli, Comparative investigation of hydrogen bonding in silicon based PECVD grown dielectrics for optical waveguides, Opt. Mater. (Amst). 26 (2004) 33–46.

[23] S.R. Federman, V.C. Costa, D.C.L. Vasconcelos, W.L. Vasconcelos, Sol-Gel SiO2-CaO-P2O5 biofilm with surface engineered for medical application, Mater. Res. 10 (2007).

[24] X.D. Liu, S. Tokura, M. Haruki, N. Nishi, N. Sakairi, Surface modification of nonporous glass beads with chitosan and their adsorption property for transition metal ions, Carbohydr. Polym. 49 (2002) 103–108.

[25] M.E. Marques, A.A.P. Mansur, H.S. Mansur, Chemical functionalization of surfaces for building three-dimensional engineered biosensors, Appl. Surf. Sci. 275 (2013) 347–360.

[26] N. Lapin, O. Seitz, Y.J. Chabal, Biointerface Characterization by Advanced IR Spectroscopy, Elsevier, 2011.

[27] K.-S. Ma, F. Reza, I. Saaem, J. Tian, Versatile surface functionalization of cyclic olefin copolymer (COC) with sputtered SiO2 thin film for potential BioMEMS applications, J. Mater. Chem. 19 (2009) 7914.

[28] H.S. Mansur, R.L. Oréfice, W.L. Vasconcelos, Z.P. Lobato, L.J.C. Machado, Biomaterial with chemically engineered surface for protein immobilization, J. Mater. Sci. Mater. Med. 16 (2005) 333–40.

[29] Q.-Z. Chen, K. Rezwan, V. Françon, D. Armitage, S.N. Nazhat, F.H. Jones, et al., Surface functionalization of Bioglass-derived porous scaffolds., Acta Biomater. 3 (2007) 551–62.

[30] E. Verné, S. Ferraris, C. Vitale-Brovarone, S. Spriano, C.L. Bianchi, A. Naldoni, et al., Alkaline phosphatase grafting on bioactive glasses and glass ceramics., Acta Biomater. 6 (2010) 229–40.

[31] S. Ferraris, C. Vitale-Brovarone, O. Bretcanu, C. Cassinelli, E. Vernè, Surface functionalization of 3D glass–ceramic porous scaffolds for enhanced mineralization in vitro, Appl. Surf. Sci. 271 (2013) 412–420.

[32] M. Zhu, M.Z. Lerum, W. Chen, How to prepare reproducible, homogeneous, and hydrolytically stable aminosilane-derived layers on silica., Langmuir. 28 (2012) 416–23.

[33] T. Kokubo, H. Kushitani, S. Sakka, T. Kitsugi, T. Yamamuro, Solutions able to reproduce in vivo surface-structure changes in bioactive glass-ceramic A-W, J. Biomed. Mater. Res. 24 (1990) 721–34.

[34] O. Peitl, E. Dutra Zanotto, L.L. Hench, Highly bioactive P2O5–Na2O–CaO–SiO2 glass-ceramics, J. Non. Cryst. Solids. 292 (2001) 115–126.

[35] J.P. Matinlinna, L.V.J. Lassila, M. Ozcan, A. Yli-Urpo, P.K. Vallittu, An introduction to silanes and their clinical applications in dentistry, Int. J. Prosthodont. 17 (2004) 155–64.

Chapter XI

"We ourselves feel that what we are doing is just a drop in the ocean.
But the ocean would be less because of that missing drop."
Madre Teresa de Calcuta (1910 – 1997)

CHAPTER XI

GENERAL CONCLUSIONS & FINAL REMARKS

XI.1. General Conclusions

The main goal of the present thesis was to investigate the fabrication, mechanical properties and in vitro performance of bioactive glass and glass-ceramic scaffolds from compositions of the Si–Ca–P–Na–Mg system using the salt sintering process for applications in bone regeneration.

The sintering behavior of the base $3CaO.P_2O_5$-MgO-SiO_2 system glass was investigated. The glass powder compacts can be densified through viscous sintering, without the present of crystalline phases. Near full densification was reached by a small decrease of the glass particle size from 6.8 μm to 3.5 μm, decreasing the degree of particle orientation and shrinkage anisotropy. In the initial stage of the densification the activation energies of sintering, Es, were comparable for both particle size distributions.

A complex crystallization process was observed in the same glass system, with associated activation energies reflecting the change of behaviour during in-situ crystal precipitation. Whitlockite, forsterite and enstatite were the crystalline phases forming on heat treating the glass. It was found that the crystallization process was affected by the fraction of crystallization (x), giving rise to decreasing activation energy values, Ec(x), with the increase of x, for the first crystalline phase whitlockite. As the crystallization proceeds, and thus the crystallized fraction increases, the Avrami exponent increased, corresponding to a crystallization with one-dimensional growth associated to a bulk nucleation of the whitlockite phase, in agreement with the long needles observed by SEM.

During the scaffold processing a reaction involving the glass network and the alkaline salt was proposed, in which, a structural disruption of the glass surfaces takes place, with formation of chlorine gas that causes an expansion phenomenon responsible for the increase of the SSA by the wrinkling of the surfaces and the creation of preferential crystallization sites at the surface. This phenomenon of salt–glass reaction is of high technological interest for the production of glass based scaffolds for many purposes including bone related biomedical applications where the exceptional surface area available after sintering can provide a high contact surface with the surrounding biological system.

The base glass composition in the $3.CaO.P_2O_5 – SiO_2 – MgO$ system was changed by Na_2O addition, aiming to obtain glass melts of controlled viscosity and workability to enlarge the "working window" for sintering. A small addition of Na_2O to the $3.CaO.P_2O_5 – SiO_2 – MgO$ system was crucial to enhance the densification behaviour and mechanical strength. The partial replacement of MgO by Na_2O enhanced the trend towards depolymerisation, reflected by an increase in Q_2 at the expense of Q_3 and Q_4 units, as supported by MAS-NMR spectra. The selected glass systems allow variation of properties, such as degradation tendency through minor chemical adjustments and adequate heat treatments.

The mechanical reliability of bioactive glass scaffolds remain as limiting factors for applications in loaded bone repair. The crystallization was proposed for improving the toughness of bioactive glass scaffolds. Besides the study of the scaffold processing, the understanding of the effect of crystallization on the mechanical behaviour and surface reactivity in acellular medium and in cell cultures allowed assessing the best compromise in the fabricated scaffolds. The crystallization of glass improved the mechanical properties of the obtained glass-ceramics scaffolds but it compromised their surface chemical reactivity hindering bioactivity, especially on bulk samples. To counterbalance this drawback, surface functionalization of the glass-ceramics appears as a promising solution. Only after 3 weeks, crystalline hydroxyapatite peaks were identified in the surface of glass-ceramic modified samples while the as prepared glass-ceramic had no detected formation of hydroxiapatite up to 5 months.

This possibility seems to be of major importance not only for the manufacturing of implant materials with resorption rates matching the growth rates of bone, but also for satisfying results in cell experiments and tissue engineering having in mind that the optimization of the degradation rate facilitates cell proliferation and improved biocompatibility.

XI.2. Directions for Future Research

For bone regeneration, the biggest challenge is to fabricate scaffolds with suitable mechanical properties capable of load transmission, induction of vascularisation and tailored degradability. Future research is needed to broaden the choice of glass compositions, thermal treatments and porogen so that scaffolds can be tailored to distinctive applications.

Furthermore, another desirable modification to these scaffolds is the incorporation of bioactive substances, like growth factors. However, once these scaffolds undergo fast degradation rates we believed that a significant higher kinetic release of the growth factors will be generated. Therefore it seems essential to develop the adequate techniques to retain an appropriated amount of the incorporated factors for a later release.

A focus of future work should be the creation of strong and tough bioactive glass-ceramic scaffolds and their evaluation in loaded and non-loaded bone defect sites in animal models. Moreover, the application of surface modification and use of protein adsorption provide a scope of tailoring the scaffold biocompatibility.

Based on the biodegradable and biocompatibility results there would be room for simulating the degradation and resorption kinetic of the process and based on these factors, to manufacture scaffolds which could fulfil the desired function properly.